Investigation of the Gas Adsorption Properties in the Metal-Organic Framework: CPO-54-M (M= Co, Mg, Mn, Ni)

Even Storheim

Master Thesis in Renewable Energy

UNIVERSITY OF BERGEN

Supervisor: Professor Pascal D. C. Dietzel

Geophysical Institute

University Of Bergen

August 2019

Preface

This master's thesis is part of the Master's program in Renewable Energy (Energy Materials) at the Geophysical Institute at the University of Bergen. The experimental part of the thesis was carried out at the Department of Chemistry with Prof. Pascal D. C. Dietzel as supervisor. The work started in October 2018, and was completed in August 2019.

Even Storheim

Bergen, 2019-08-05

Acknowledgment

Summary

Climate change and global warming as the result of anthropogenic pollution are among the biggest challenges of our generation. As the world's energy demand is expected to increase in the years to come, carbon capture and storage (CCS) technology may play an essential part in the transition towards zero-emission energy production. The current CCS technology is energy-inefficient. Therefore, one seeks to find new solid materials to use as sorbents in more efficient CCS processes. One such material is the metal-organic framework CPO-54-M (M=Co, Mg, Mn, Ni), which is based on an extended version of the linker molecule used in CPO-27.

This study aims to discover how the extended linker molecule in CPO-54 affect the applicability of these materials for CO_2/N_2, CO_2/CH_4 and CO_2/O_2 separation, how CPO-54 adsorbs N_2O, and whether or not the materials are suitable to separate Xe from Kr. In this work, the gas adsorption capacity of CPO-54-M (M = Mg, Mn, Ni, and Co) have been measured for CO_2, CH_4, N_2, O_2, N_2O, Kr, and Xe. Isosteric heats of adsorption and selectivity coefficients have been calculated based on these adsorption measurements. This work has given new insight into the CPO-54 MOF series and its properties.

The results of this study have shown that CPO-54 is highly selective of CO_2 over N_2, CH_4, and O_2. The essential has also shown that CPO-54 selectively adsorbs Xe over Kr. The selectivity factors were found to be highly temperature-dependent, and the selectivity was found to be highest at lower temperatures. The results indicate that the extended linker molecule in CPO-54 decreases the MOF's CO_2, CH_4, N_2 and O_2 adsorption capacity, and the CO_2/N_2, and CO_2/CH_4 selectivity, compared to CPO-27. The Xe/Kr selectivity, on the other hand, was found to increase.

The Q_{st} at the open metal sites in both CPO-54 and CPO-27 were found to be of similar magnitude and the Q_{st} was found to be lower at the secondary adsorption site in CPO-54. The study has, furthermore, shown that CPO-54 have high uptakes of N_2O and a high selectivity of N_2O over N_2.

Sammendrag

Klimaendringer og global oppvarming som resultat av antropogene utslipp er blant de største utfordringene denne generasjonen står ovenfor. Verdens energibehov er forventet å stige i de kommende årene, og CCS-teknologi kan komme til å spille en viktig rolle i overgangen til en null-utslipp-energiproduksjon. Dagens CCS-teknologi er energi-ineffektiv og en ønsker derfor å finne nye materialer som kan brukes som adsorbent i mer energieffektive prosesser. Et slikt materiale er det metall-organiske nettverket CPO-54-M (M=Co,Mg,Mn,Ni), som er basert på en utvidet versjon av linker-molekylet fra CPO-27.

Denne studien tar sikte på å finne ut hvordan den utvidede linkeren i CPO-54 påvirker disse materialenes anvendbarhet for CO_2/N_2, CO_2/CH_4 og CO_2/O_2 seperasjon, hvordan CPO-54 adsorberer N_2O og hvorvidt disse materialene kan brukes til å separere xenon og krypton fra hverandre. I dette arbeidet har gass-adsorpsjonskapasiteten til CPO-54-M (M = Mg, Mn, Ni og Co) blitt undersøkt for gassene CO_2, CH_4, N_2, O_2, N_2O, Kr og Xe. Basert på disse målingene har de isokore adsorpsjonsentalpiene og selektivitetskoeffisientene blitt beregnet. Denne studien har gitt ny innsikt i CPO-54 MOF-serien og dens egenskaper.

Resultatene fra denne studien har vist at CPO-54 selektivt adsorberer CO_2 fremfor CH_4, N_2 og O_2. Studien har også vist CPO-54 er selektiv mot Xe fremfor Kr. Studien viste at selektivitetsfaktorene var meget temperaturavhengig og at de var høyest ved lavere temperaturer. Resultatene indikerer at det utvidede linker-molekylet i CPO-54 fører til lavere opptak av CO_2, CH_4, N_2 og O_2, samt lavere CO_2/N_2- og CO_2/CH_4-selektivitet. Derimot viste det seg at Xe/Kr-selektiviteten økte.

Det ble vist at Q_{st} ved de umettede matall-kationene var av lik størrelsesorden i både CPO-54 og CPO-27, og at den var lavere ved de sekundere adsorpsjonsplassene i CPO-54. Studien har videre vist at CPO-54 har et høyt opptak av N_2O og en høy selektivitet av N_2O fremfor N_2.

Abbreviations

UN	United Nations
OECD	The Organisation for Economic Co-operation and Development
NOAA	National Oceanic and Atmospheric Administration
IUPAC	International Union of Pure and Applied Chemistry
CCS	Carbon Capture and Storage
PV	Photovoltaic
DAC	Direct Air Capture
MOF	Metal-Organic Framework
CPO	Coordination Polymer of Oslo
SBU	Secondary Building Unit
OMS	Open Metal Sited
XRD	X-Ray Diffraction
PXRD	Powder X-Ray Diffraction
SCXRD	Single-Crystal X-Ray Diffraction
IAST	Ideal adsorption Solution Theory
BET	Brunauer, Emmett and Teller
NMR	Nuclear Magnetic Resonance Spectroscopy
DSL	Dual-Site Langmuir
N_2	Nitrogen
O_2	Oxygen

CO$_2$ Carbon dioxide

CH$_4$ Methane

N$_2$O   Nitrous Oxide

Xe   Xenon

Kr   Krypton

Ar   Argon

He   Helium

H$_2$O   Water

Co   Cobalt

Mg   Magnesium

Mn   Manganese

Ni   Nickel

NMP   N-Methyl-2-pyrrolidone

DMSO   Dimetylsulfoxid

DMF   Dimetylformamid

TMS   Tetramenthylsilane

THF   Tetrahydrofuran

BHT   Butylated Hydroxytoluene

dobpdc   4,4'-dioxidobiphenyl-3,3'-dicarboxylate

DHNDC   1,5-Dihydroxy-2,6-naphthalene-dicarboxylic acid

Symbols

ΔE Energy gap / J

h Planck's constant / Js

γ Gyromagnetic ratio (unique to each nucleus) / $rads^{-1}T^{-1}$

B_0 Magnetic field / T

π Pi

N_α Number of nuclei in energy level α

N_β Number of nuclei in energy level β

k Boltzmann constant / JK^{-1}

T Temperature / K

δ Chemical shift / ppm

ν Frequency (measured) / Hz

ν_0 Frequency (reference material) / Hz

ν_s Frequency (instrument) / Hz

h, k, l Miller indices

λ Wavelength / nm

n^* Integer in Bragg's equation

Θ Angle between lattice plane and X-ray / $degrees$

d Lattice spacing / nm

z_{ij} Distance between the two molecules i and j / m

V Intermolecular potential / J

P Pressure / Pa

p_0 Saturation pressure / Pa

P_T Total pressure / Pa

K Equilibrium constant

K_a Adsorption constant

K_b Desorption constant

Θ_L Fraction of surface covered by adsorbate

S_L Langmuir surface area / $m^2 g^{-1}$

v_m Volume of adsorbed molecules / m^3

m_v Molar volume of adsorbed gas / $m^3 mol$-1

s Cross-section of adsorbate / m^2

N_a Avogadro's number / mol-1

C BET constant

v Adsorbed amount / m^3 at STP

V_M Specific monolayer capacity / m^3 at STP

a Intercept

b Slope

S_{BET} BET surface area / $m^2 g^{-1}$

Q_{st} Isosteric heat of adsorption / $kJmol^{-1}$

ΔH_{ads} Isosteric enthalpy of adsorption / $kJmol^{-1}$

R Universal gas constant / $JK^{-1}mol^{-1}$

q_i Saturation pressure at adsorption site i / Pa

b_i Langmuir parameter at adsorption site i

v_i Freundlich parameter at adsorption site i

a_i Equation parameter

b_i Equation parameter

n Adsorbed amount / $molg^{-1}$

x_i Mole fraction in fluid phase

y_i Mole fraction in adsorbed phase

Π Spreading pressure

π^* Reduced spreading pressure

A Specific surface area of adsorbent

S_{ij} Selectivity of component i over component j

Contents

Chapter 1

Introduction

1.1 Background

Climate change and global warming are generally considered to be some of the biggest challenges of our generation. With growing global population and an increasing energy use per capita in many countries in Asia and Africa, the world is close to reaching its limit for sustainability. There is a consensus among the scientists of the world that a significant part of climate change is the direct result of human activities.[1]

The Paris Agreement of 2016 marked a turning point for global climate and energy politics. For the first time, all of the UN were brought together and unanimously agreed to undertake significant and ambitious actions to combat climate change and to keep the temperature rise of this century below 2°C compared to pre-industrial times.[2]

The atmospheric CO_2 concentration is rising at an alarming rate.[3,4] By now, it is a well-established fact that human activity and anthropogenic pollution are the causes of this increase as we continue to burn coal, oil and gas.[5] The economic sectors that contribute most to the world's total CO_2 emissions are the electricity and heat producing sectors.[6] 85% of the global energy in 2017 was produced by burning fossil fuels, and by that emitting 35 billion tons of CO_2 per year.[7]

The world's energy consumption is not expected to decrease. On the contrary, global energy demand will increase as non-OECD countries become more and more developed. As a result of this, the energy consumption per capita is growing at a faster rate in developing countries
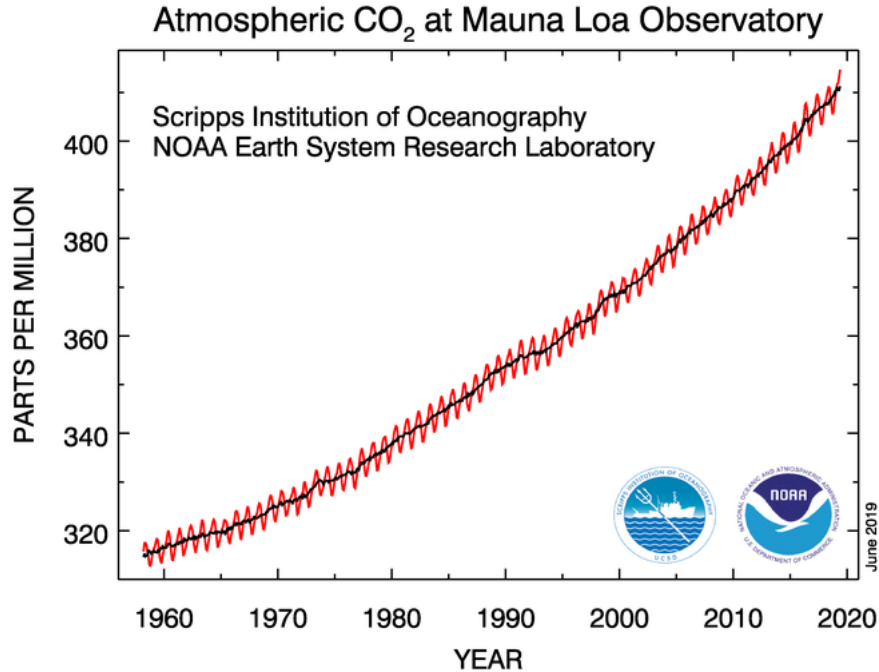
Figure 1.1: Atmospheric CO_2 concentration measured at the Mauna Loa Observatory, Hawaii. The **red line** is carbon dioxide level, measured as the mole fraction in dry air. The **black line** shows the same data after correction for the average seasonal cycle.[3]

compared with OECD countries.[8, 9] A global reduction in energy consumption may seem futile. Therefore one has to put greater emphasis on finding new, more efficient technologies, and utilize renewable energy sources to a more considerable extent than today. Energy production from renewable energy sources, such as wind and solar power, has seen exponential growth over the last decades and is still growing.[10, 11] However, it is not enough at the present time to replace all fossil fuel based energy production.

Carbon capture and storage (CCS) is a controversial topic. To capture and store CO_2, rather than emitting it, is in itself a good thing, but it comes with some considerable disadvantages. The problem with today's CCS technology is the massive energy penalty it comes with. A gas power plant with CCS technology requires significantly more energy to run and be operational, thus raising the production costs of the power plant. For this reason CCS technology is considered by many to be an inefficient way to reduce emissions of climate gases. Nevertheless, if new energy-efficient CCS technologies are implemented, it can make the transition towards a zero emission energy production, based on renewable energy,[14] easier. There are already several

large-scale CCS facilities around the world, and some, like Sleipner and Snøhvit in Norway,[12] have been operational for several decades. Another is the new direct air capture (DAC) plant that recently opened in Hinwil, Switzerland[13] in May 2017.

If CCS is to play a part in the solution, new materials must be developed and new processes designed based upon these. A new class of solids that have shown promising properties for CO_2 capture is metal-organic frameworks (MOFs). MOFs are a class of nanoporous crystalline solids. Due to their large internal surface area, they are promising adsorbent materials. MOFs are a relatively new class of solids, and they have both the largest surface area and the lowest density of any known crystalline solids. In addition to the large surface area, MOFs have an exceptionally free diffusion through the channels.[15, 16, 17, 18] These properties have given scientists all over the world hope that a MOF may just be that new material CCS technology needs. There are several materials that have good potential, and this thesis will look more closely at one of these candidates.

1.2 Objectives

This study deals with the investigation of the gas adsorption properties in the CPO-54 MOF series, which is based on an extended version of the linker used in construction of the CPO-27 compounds, a series of MOFs that performs exceptionally well in CO_2 adsorption and have been studied extensively for application in separation processes. The extended linker leads to an isostructural framework with larger pores. These allow adsorption of larger amounts of gas, so the focus of the thesis will be on investigating how this affects the potential of these materials for CO_2/N_2, CO_2/CH_4 and CO_2/O_2 separation, which are among the most relevant separation processes in energy technology. I will, in addition, look into N_2O adsorption in CPO-54 and also investigate whether or not CPO-54 can be suitable for Xe/Kr separation.

1.3 Approach

In this work, I have synthezised CPO-54-M using four different metal compounds: Co, Mg, Mn and Ni. Gas sorption measurements with N_2, CO_2, CH_4, O_2, N_2O, Kr and Xe were conducted in order to investigate the adsorption properties. This thesis will firstly give a brief introduction to metal-organic frameworks and a short overview of MOFs for gas separation processes in Chapter 2. In Chapter 3, I describe the different syntheses I have used in details, and give an overview of the instrumentation and chemicals used in the experimental work. The results of my experimental work and computational analysis will thereafter be presented in Chapter 4 and discussed in Chapter 5. Lastly, in Chapter 6, I present my conclusions of the study and give some recommendations for further work.

1.4 Limitations

This study is restricted to the experimental measurement of the gas adsorption capacity for CPO-54-M, and the investigation by IAST (ideal adsorption solution theory) of CPO-54-M's gas separation properties. It is beyond the scope of this study to cover the economical issues of CCS-technology, or the question of how MOF's, such as CPO-54, can be implemented into new or existing processes.

Chapter 2

Background

2.1 Metal-Organic Frameworks

Metal-organic frameworks is an incredibly versatile class of crystalline materials, and they are known to possess some remarkable properties. Their ultra-high porosity and flexibility, due to a vast diversity of different building units, make them an ideal material class for heterogeneous catalysis and gas adsorption processes.[19] The many possibilities of different organic linker molecules and metal cations possible, allow scientists to make new MOFs tailored for specific purposes and applications. At this point, the only limitation is one's imagination. Since MOFs consist of an inorganic connector and an organic linker, the study of MOFs involves several branches of chemistry, and bridges the traditional gap between organic and inorganic chemistry. Theory from both fields as well as computational models are needed to understand this class of crystalline materials entirely.

2.1.1 The discovery of MOFs

Metal-organic frameworks are generally considered to be a relatively new class of materials, but materials that fit the general criteria for MOFs have existed for a long time. The very first discovery of materials that resembled a metal-organic framework was *Prussian Blue (Hexacyanoferrate)* and *Zeise's salt*, back in the early 18th century.[20,21] Only since the 1990s has the reaserch field of metal-organic frameworks developed and grown explosively. The discovery of the frame-

work $Cu(4,4\text{-bpy})_{1.5}NO_3(H_2O)_{1.25}$ by Yagi and coworkers in 1995[22] and the seminal report of MOF-5 in 1999 by Li et al.[23,24] (Figure 2.1), marked the start of an intensive search for new MOFs.[23] MOF-5 was porous, relatively stable, had a well-defined crystal structure and a vast internal surface area. It was, in other words, the first material to fit the modern definition of a MOF.
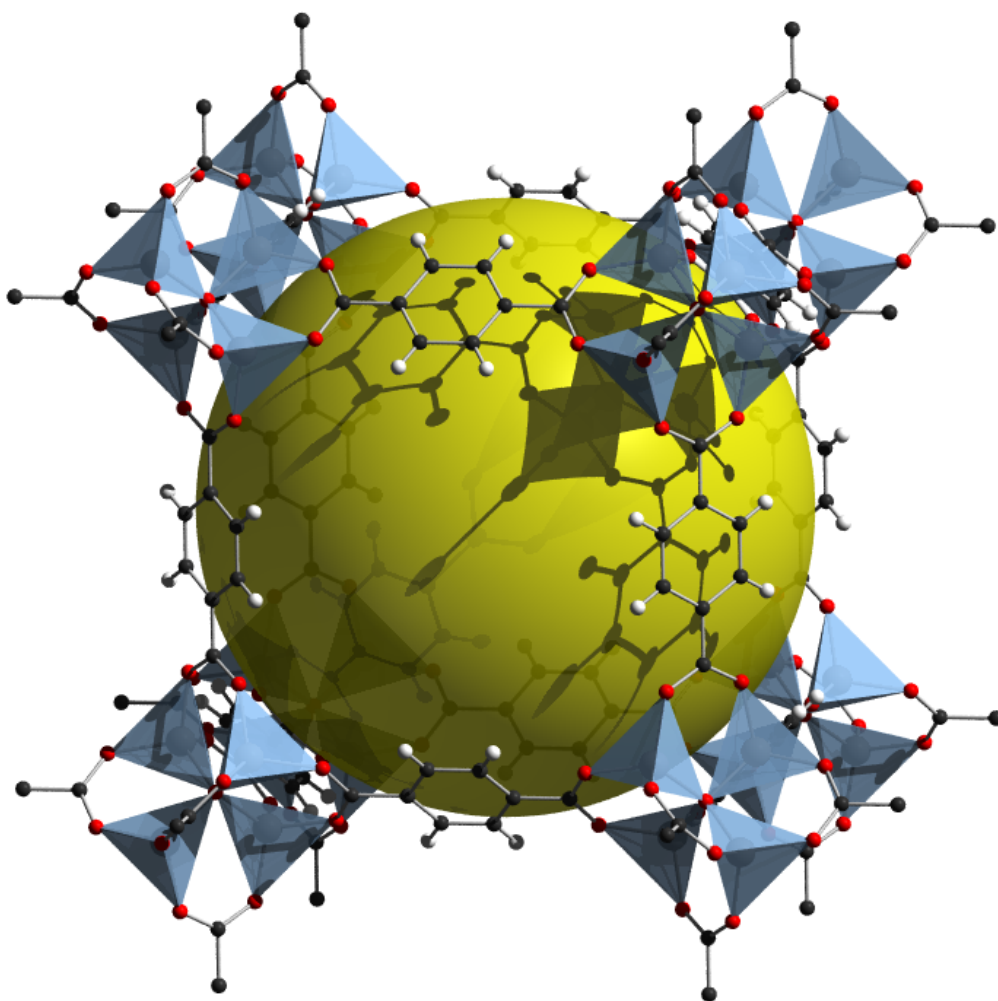

Figure 2.1: The famous MOF-5 / IRMOF-1, discovered in 1999. This is considered to be the MOF that really sparked the international research interest in the MOF-area.

Since then, there has been an exploding research activity in the MOF field. The new material class received enormous interest, not only from a scientific point of view but also from commercial and industrial interests. Tens of thousands of different structures have been discovered in the last decades, and the number of publications concerning metal-organic frameworks has seen exponential growth. New MOFs are still discovered every week, but even though there are

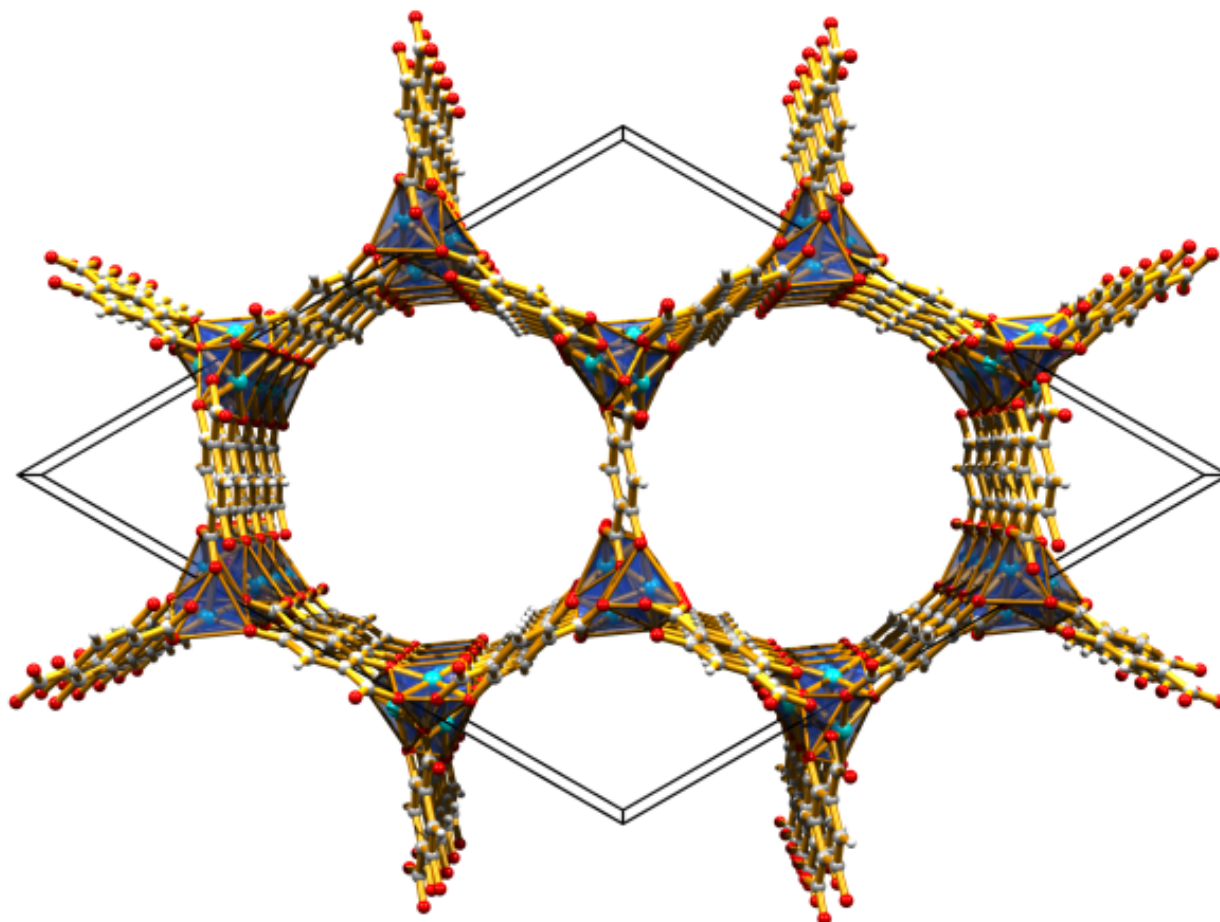so many of them, only a few have sparked scientific interest.

Figure 2.2: MOF-74/CPO-27, discovered in 2005. An isostructural MOF series where M can be Mg, Fe, Co, Ni, Cu or Zn. The MOF has honeycomb-like structure and the highest reported number of open metal sites when activated.

In 2005, a new series of isostructural compounds, M-MOF-74 (CPO-27-M), with a honeycomb-like structure and large one-dimensional pores (11-12 Å) were discovered (figure 2.2). The CPO-27-M MOFs are a series of isostructural compounds formed by the reaction of 2,5-dihydroxy-terephthalic acid and a number of salts of divalent cations (M=Mg, Mn, Fe, Co, Ni, Cu, Zn). Yagi et. al reported the Zn-MOF-74[25] and Dietzel et. al presented CPO-27-Co.[26] They found that this structure was stable after the removal of all the solvent molecules and, more importantly, that there was a very high concentration of unsaturated metal cations in the structure.[17] These open metal sites (OMS) in the CPO-27 have furthermore been identified as the primary adsorption

site for guest molecules.[27,28] The CPO-27 series is among the most investigated MOFs due to its excellent properties in several application areas, and the record high concentration of open metal sites. They are also particularly promising for CO_2 capture and CH_4 storage.[17,18]

2.1.2 Structure Of MOFs

Metal-organic Frameworks consist of two main components - secondary building units (SBUs). There is always an organic *linker* and a metal *connector*. Both of these have preferred coordination modes, which make out the foundation for the MOF structure (Figure 2.3).
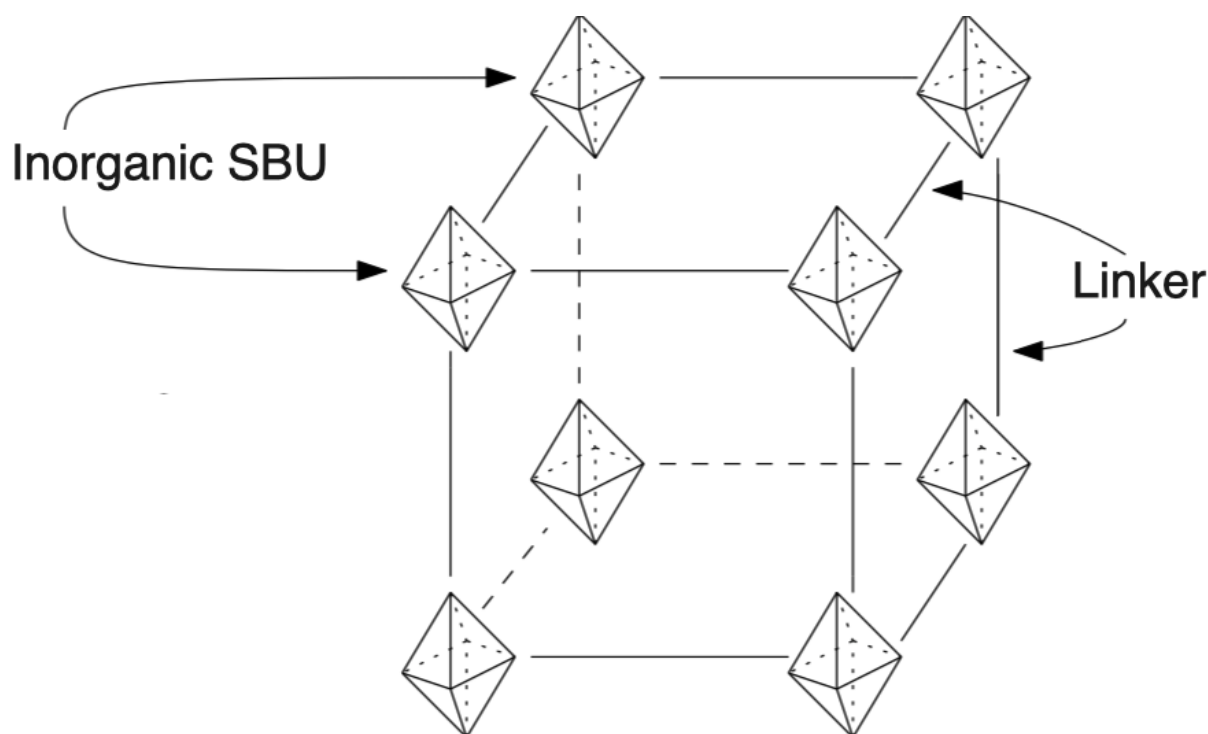

Figure 2.3: A simplified illustration of how the linkers and metals coordinate to one-another. The organic linkers are represented by straight lines while the metal connectors are represented as octahedrons.

The linkers are typically planar or linear molecules, generally with 2-4 electron donating functional groups that can form bonds to the metal connector (bi-, tri- or ploy dentate). Aromatic linkers are the most used because of their rigidity and stability.

The metal connector is usually small metal oxide clusters, a diatomic or a single metal cation. The connector can be seen as the *signature part* of the MOF. There is a constant race between
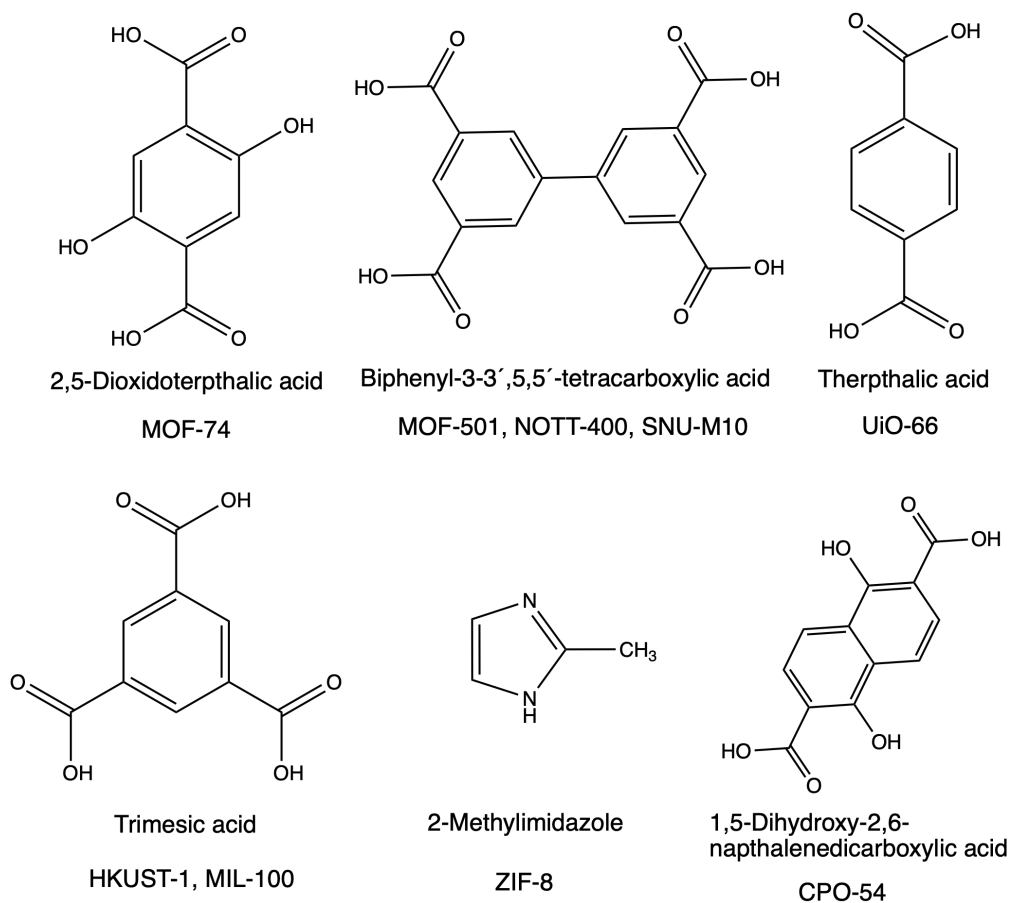
Figure 2.4: Some typical organic linker molecules used for a number of metal-organic frameworks.

researchers to find new connectors to make new MOFs and be the first to investigate their properties. Computational methods are often used to investigate possible new compounds before they are ever synthesized. Some MOFs, like the ones in the CPO-27 series, are all made with the same linker but with different metal cations. They all have the same honeycomb-like structure and similar properties, and the series is therefor an iso-reticular one.

2.1.3 MOF Synthesis In General

There are several different methods for synthesizing MOFs. The most common of these are the solvothermal approach.[29] In this method, the precursors are dissolved in a polar solvent that has a high boiling point and can dissolve both organic and inorganic materials. This allows the reactants to be homogeneously mixed before the reaction. Typical solvents for MOF syntheses

are, e.g. DMF, DMSO and NMP. The crystallization normally happens in a closed vessel at elevated temperatures and pressures. The temperature range can vary from room temperature up to 250°C, and the reaction vessels are typically heated in electric furnaces.

The solvothermal method offers several advantages: It is easy to perform, has a small chance of failure due to falsely workup, and it does not require any advanced instruments. The disadvantage is, of course, the reaction time, which can range from hours to several days. Other methods, such as microwave-assisted synthesis, electro- and mechanochemical synthesis and sonochemical synthesis are also used to make MOFs.

MOF synthesis is dynamic, and thereby very sensitive to small changes in the reaction mixture. A trial-and-error approach is often used to optimize reaction conditions. Parameters that can be changed are temperature, reaction time, solvent, pressure, concentrations, pH and the nature of the precursors.

Some times it is beneficial to use a *modulator* in the reaction. Modulators are used to control the crystallization process and prevent unwanted and rapid precipitation of amorphous product. These modulators are nonstructural, mono-topic linkers (e.g. acetic acid, benzoic acid, hydrochloric acid) that make dynamic bonds with the metal precursor. This helps to slow down the growth, due to the fact that the modulator and the linker compete for the same metal coordination sites.[30]

The synthesized product should always be washed with the same solvent that was used for the synthesis, in order to remove any byproduct and excess linker left in the reaction mix. To be able to remove all the solvent molecules from the structure entirely, one frequently performs a solvent exchange where the polar solvent is replaced by a more volatile solvent (e.g. methanol). The MOF is then filtered and dried under reduced pressure in order to evaporate all the solvents. To fully activate the entire surface area one can heat the material under vacuum to speed up the process. This, of course, requires a structure that is thermally stable within the heating range in question. Materials are only permanently porous if the solvent molecules can be removed from the pores without the structure collapsing. Not all MOFs survive this step, and that decreases their framework crystallinity, while other MOFs change their structural properties when the solvents are removed.[31]

2.1.4 MOFs For Gas Separation

MOFs have a very high surface-to-volume ratio. The highest reported surface area to date is 7000 m^2/g (experimentally measured) and the highest theoretical surface area is 14600 m^2/g.[32] With numbers like these, together with their high porosity, it is no wonder that MOFs are seen as an exiting material class for a wide range of industrial applications - CCS being one of them.

Carbon capture has been a hot topic in recent years, and it is still one of the most intensively studied gas separation processes. Today's carbon capture technology is mainly CO_2 scrubbers with aqueous alkanolamine solutions. The problem with these is that the regeneration energy is too high for an efficient process, in terms of energy demand and cost, due to large portions of water in their composition.[33] This has been a huge motivation to finding new solid sorbents that can be used in a more energy efficient way, and at a lower cost. MOFs are considered a promising sorbent material for dry separation processes, where one seeks to utilize the difference in the interaction between the MOF and different gas species.[27] Because of this difference in MOF/gas interaction, one can design an MOF to have a higher affinity towards a specific gas, and thus be able to separate it from a given gas mixture. MOFs are normally synthesized as powders, so consequently, one has to find a practical solution for incorporating MOFs into industrial processes.

Making materials with open metal sites is a commonly used strategy for selective gas sorption in solid sorbents. The benchmark MOF with OMS is, by far, CPO-27-Mg (Mg-MOF-74). This has been reported by several groups.[26,34]CPO-27-Mg has been found to be the porous physisorbent with the highest CO_2 uptake of them all (8.1 $mmol g^{-1}$ at 298K and 1 bar) and has among the best CO_2-selectivities for any MOF.[35,36] However, CPO-27-Mg requires dry conditions to reach these high values, because the OMSs are more preferably occupied by water. This water-sensitivity is a challenge when it comes to application in real processes, because of the difficulties of running a large-scale separation process in completely dry conditions. McDonald et al. showed in 2012 that one could somewhat overcome this problem for Mg2(dobpdc) by functionalization with N,N-dimethylethylenediamine, and still get good CO_2-selectivity - even in the presence of water.[37] One possible way of utilizing the open metal-site MOFs are by incorporating them into membranes, as suggested by Bae and Long in 2013.[38]

Other materials, such as the MOF CuBTTri, 2011,[39] and the zeolite 13X have shown very

good properties for CO_2/N_2 separation. Even carbon materials, such as carbon nanotubes and graphene, have been intensively studied for possible use in CCS. These carbon materials do not achieve CO_2 uptakes or heats of adsorption at the same level as MOFs and zeolites at lower pressures. They can, however, survive harsher conditions than both MOF's and zeolites, and they have a good uptake at higher pressures.[40]

MOFs are also interesting for other separation processes. One of them being separation of the two noble gases xenon and krypton. Xenon is used and/or produced in many areas; ranging from medicine to commercial lighting, from scientific analysis methods to bi-product of nuclear reactors. Xe capture from "air" might be of interest for recycling of medically used Xe. Xe/Kr separation is related to nuclear fuel processing where both occur and one wants to remove the radioactive 85Kr isotope. CPO-27 have shown interesting potential for Xe capture and separation from Kr. Better, in fact, than MOF-5.[41,42]

Although carbon dioxide is generally considered to be the main contributing anthropogenic pollutant towards global warming, other gases, such as methane and nitrous oxide, have a higher global warming potential per formula unit. From a climate and energy perspective, it is also of great interest to be able to capture these gases. MOFs have already shown potential to selectively capture both of these gasses.[43]

2.1.5 CPO-54-M

In 2010, Dietzel et. al. made a new compound: CPO-54.[44] They discovered that the CPO-54 MOFs crystallized with the same honeycomb-like structure and network topology as CPO-27 (Figure 2.5) and that they could synthesize it with several of the same divalent cations; Co^{2+}, Fe^{2+}, Mg^{2+}, Mn^{2+} and Ni^{2+}. CPO-54 also possesses a high concentration of open metal sites in - the second highest reported and second only to CPO-27. The structure consists of six-coordinated divalent metal centers, each coordinated to three carboxyl groups, two oxide groups and one solvent molecule at the open metal site. This makes up helical M(II)-O-C rods in the structure.[25]
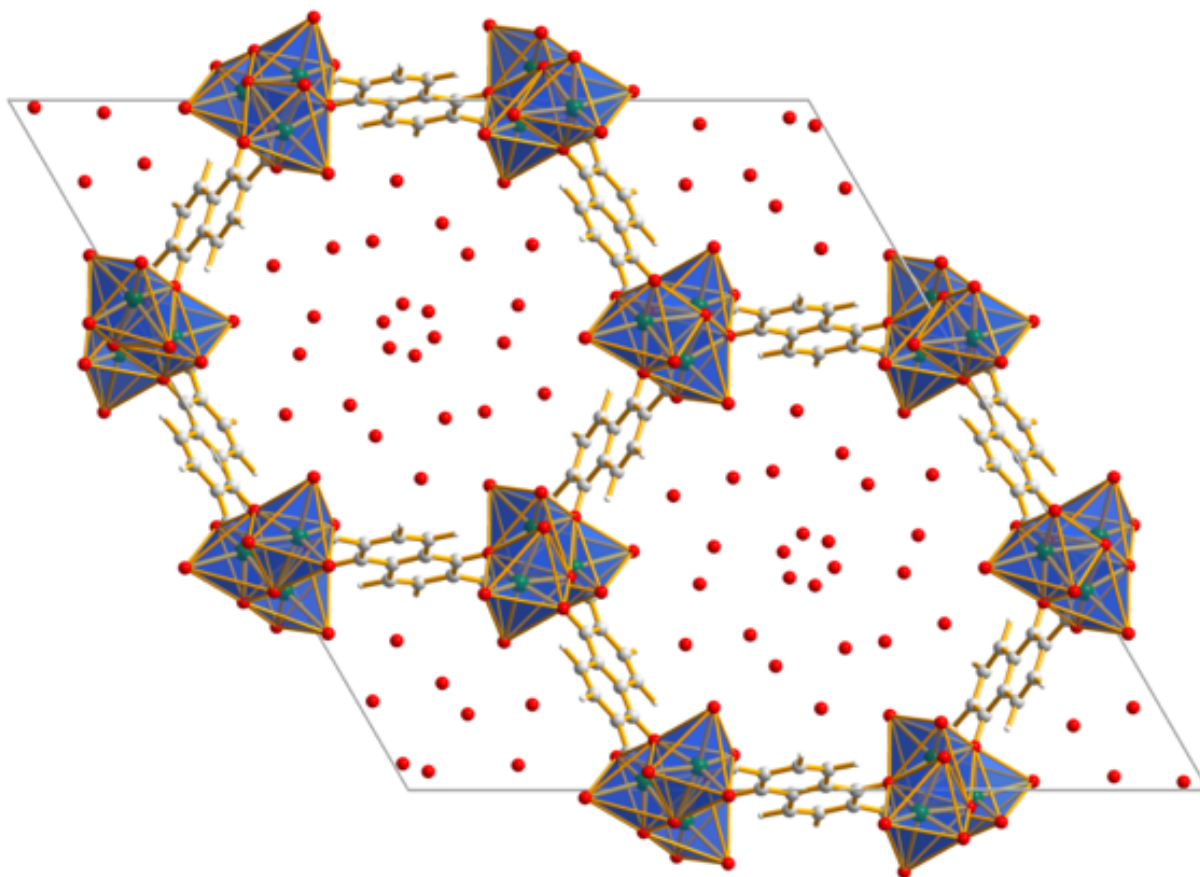

Figure 2.5: The solvated framework structure of CPO-54-M before activation of the open metal sites.

The big difference between the two MOFs is the organic linker. The CPO-54 series is made

with a an extended version of the linker molecule used in the CPO-27 MOFs (Figure 2.6). The pore diameter of CPO-54 is approximately 1 Å larger, compared to its predecessor.
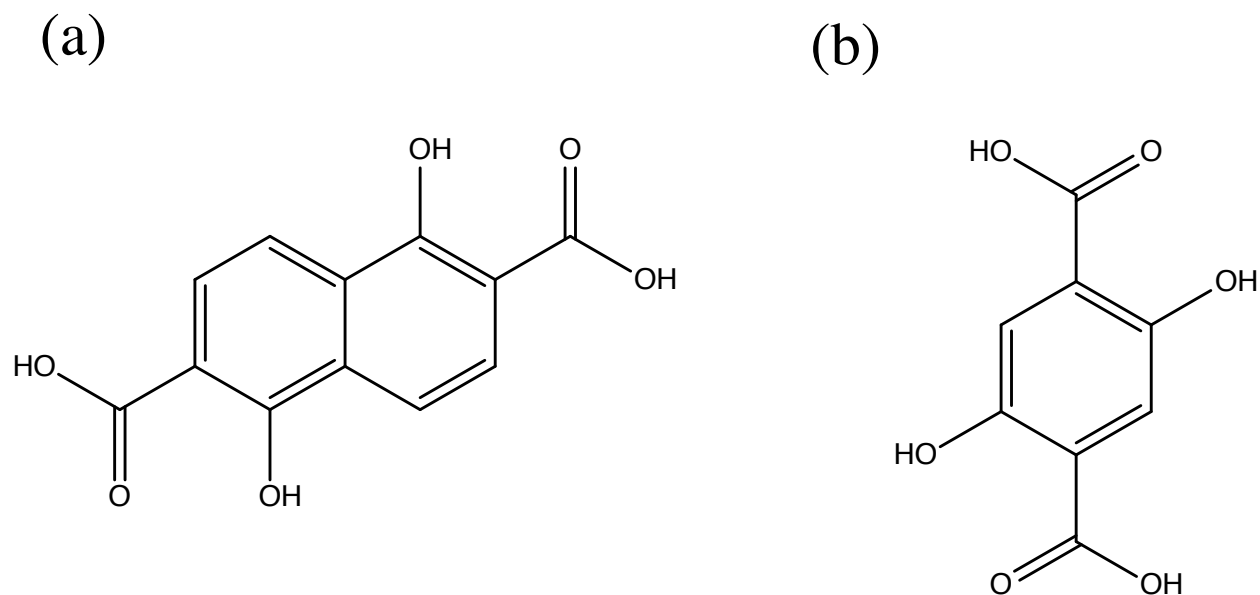
(a)

(b)

Figure 2.6: These are the organic linker-molecules used in the two MOFs **a)** Used in CPO-54: 1,5-Dihydroxy-2,6-naphthalene-dicarboxylic acid, and **b)** used in CPO-27: 2,5-dihydroxytterephhalic acid

2.2 Motivation

While CPO-27 is widely known and studied in detail by researchers all over the world, the CPO-54 series still remains an unchartered field. It is therefore of scientific interest to investigate the adsorption properties of these MOFs and see how they compare to CPO-27 and other metal-organic frameworks.

2.3 Characterisation

This section gives a brief description of the various characterization techniques used in this work.

2.3.1 Nuclear Magnetic Resonance

Nuclear Magnetic Resonance (NMR) is a conventional analysis technique, especially in organic chemistry. This powerful technique is used for characterization of materials and to determine their purity. Many atomic nuclei have an intrinsic magnetic moment due to an odd number of protons or neutrons. In NMR the sample is subjected to a magnetic field, thus inducing an energy gap between the spin states, here described in equation (2.1):

$$\Delta E = \frac{h\gamma B_0}{2\pi} \tag{2.1}$$

where h is Planck's constant, γ is the magnetogyric ratio (unique to each nucleus) and B_0 is the applied magnetic field.

The distribution of nuclei in the different energy states (α and β) are given in the Boltzmann equation, (2.2):

$$\frac{N_\alpha}{N_\beta} = e^{\frac{-\Delta E}{kT}} \tag{2.2}$$

The sample is subjected to short pulses of radiation, causing the spin state to resonate between the energy states (α and β) when the energy of the radiation matches the energy gap, ΔE. These interactions can further be measured and processed by Fourier Transformations to produce a NMR spectrum.

The dispersion of NMR signals will, of course, be influenced by electrons that protect the nuclei, and by the chemical environment on the neighboring atom. It also depends on the magnetic field and radiation frequency. Because of that, one uses a *proton reference frequency*, normally that of tetramethylsilane (TMS). Equation 2.3 uses the measured frequency (v), the reference frequency for TMS (v_0) and the spectrometer frequency (v_s) to define the *chemical shift* (δ), which is more convenient to work with.

NMR can be used on solid samples, but it is most common (as done in this thesis) to measure materials in solution, where the dissolved molecules can rotate freely.

$$\delta = \frac{\nu - \nu_0}{\nu_s} \tag{2.3}$$

2.3.2 Powder X-Ray Diffraction

Powder X-ray diffraction is an analytic technique using monochromatic X-rays to collect information on crystalline materials. When the x-ray radiation is directed through a crystal, it interacts with the regular arrays of electron densities in the crystal lattice, causing it to scatter in many directions. The scattered x-rays will interact with each other, and, if the path length of the x-rays between the reflective planes is equal, create constructive interference and thus maximums. These maximums can be detected. Destructive interference will occur when the path length difference is not an integer multiple of incident wave length. The intensity of the interference distribution is a function of the wavelength of the incident light and the scattering centers involved in the particular *hkl* plane. This means that the electron density of the atoms contributes to the intensity of different reflections. The Braggs equation (2.4) describes the angle at which a beam of X-rays of a particular wavelength diffracts form a crystalline surface:

$$n\lambda = 2d \sin\Theta \tag{2.4}$$

Where d is the spacing between the crystal lattice planes, Θ is the angle between the lattice plane and the beam of incident X-rays, n is an integer and λ is the wavelength of the incident X-ray radiation.

By varying the angle of the centered sample one can attain all possible diffraction directions of the lattice. The plot of the intensity of the scattered X-rays as a function of the angle (2Θ) produce the PXRD patterns. It is evident from the Bragg equation that a perfect crystal would produce a perfect pattern without noise and with infinitely thin peaks. Peak broadening have a variety of causes, for example that the radiation is not perfectly monochromatic, crystal lattice distortion, stacking faults, etc... It is therefore essential to consider the signal-to-noise ratio,
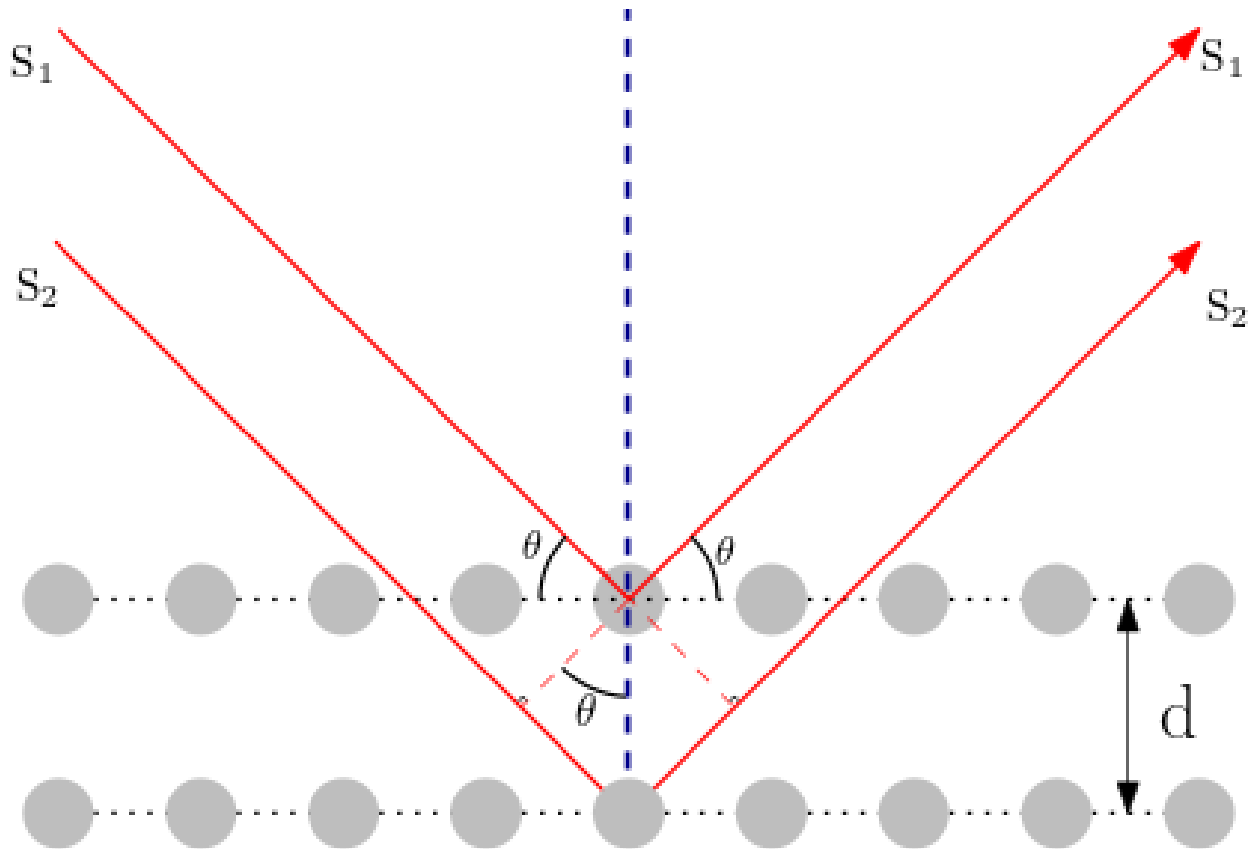
Figure 2.7: An illustration of how the radiation interact with the lattice planes in X-ray diffraction. The notations are related to the Bragg equation 2.4.

counts per second and FWHM when determining the crystalline quality of a material.

X-ray diffraction can be performed in two ways: Either on a single crystal or a powder consisting of many randomly orientated crystals. Single-crystal XRD (SCXRD) is beneficial for crystal structure determination. It requires crystals that are large enough to be measured. PXRD is a powerful tool and is the technique used in this thesis. The diffraction pattern can reveal information on the crystal systems and unit cell parameters and is an excellent method to confirm that one has produced the correct product.

2.4 Adsorption

Gas adsorption is a ubiquitous process in chemical science, and these measurements are widely used to determine the surface area of solid materials and their pore size.

The adsorption process takes place at the interface between a solid material (adsorbent) and a gas molecule (adsorbate). All molecules will interact with each other through weak van der-Waal forces. If a gas molecule is far from the surface of the adsorbent, it will not "feel" any attracting forces. If, however, a surrounding gas molecule gets close enough to a solid material, it will start to "feel" the actracting force. The potential energy between the adsorbent and adsorbate will decrease exponentially with decreasing distance, to a point where it will be in an energetic minimum. At this point, the gas molecule is neither pushed away nor pulled further towards the adsorbent. This is called adsorption equilibrium point. This can be illustrated trough the Lenard-Jones potential curve (Figure 2.8), where the potential energy between the gas and the solid is a function of distance between the two molecules. This overall process is called *physisorption*.[45]Chemisorption, where the adsorptive binds chemically to the adsorbate, will not be discussed in this thesis, as only physisorption is relevant to the MOFs in question.
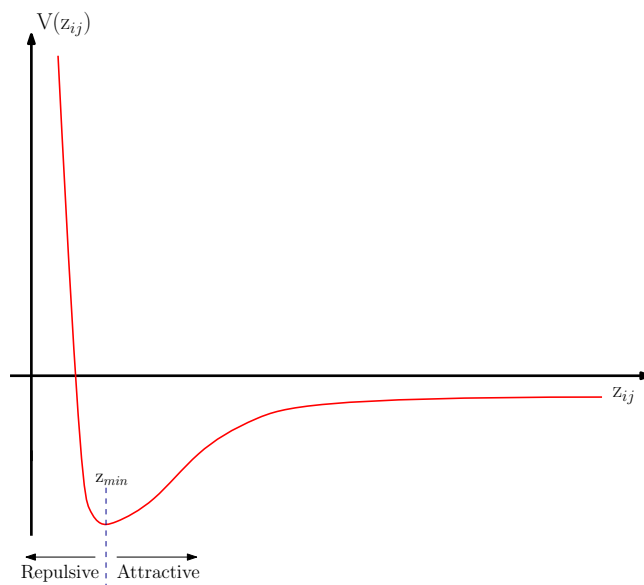

Figure 2.8: The Lenard-Jones potential describes the potential energy between two molecules, i and j as a function of the distance between them, z. The attractive and repulsive forces working between them are minimised at a given distance, z_{min}.

One of the motivations for studying MOFs is their very large specific surface area. Because of the spacing between the metal cations, created by the organic linkers, MOFs are often, but not always, porous. This porosity gives MOFs great applicability for gas adsorption. Pores can, in general, take many different forms: They can be regularly shaped as circles, rectangles, and

polygons, or be shaped at random. Some materials have randomly distributed pores, while others have pores in well-defined patterns that create channels through the material or make up two-dimensional and three-dimensional voids within the structure. A convention is that pores have to be deeper than they are wide to be defined as a pore.

All adsorption measurements in this work are measured as excess adsorption. *Excess adsorption* is the amount of gas taken up by the adsorbent beyond what it could have contained, under the same conditions, in a *free volume* equivalent to the total pore volume of the sample material. The excess adsorption isotherm will deviate from the *absolute adsorption* isotherm. The deviation will get more significant as the pressure increases. Absolute adsorption is the total amount of a gas species that is confined within the material. In a material, the pores will restrict how efficient gas molecules can be packed within them.

Adsorption measurement at low pressures (up to 1 bar) is standard procedure in many labs. At such low pressures, the difference between excess and absolute adsorption is so small that it can be neglected. Since most industrial processes happen at pressures higher than 1 bar, adsorption measurements at elevated pressures (up to 100 bar) have become more and more common. In these high-pressure measurements it is of crucial importance to correct for absolute adsorption before one uses the data for further analysis (e.g. isosteric heat of adsorption). The excess adsorption is, however, often sufficient for performance comparison because it reflects the usable capacity.

IUPAC have defined six main isotherm types (Figure 2.9).[46] *Type I* is reversible and typical for microporous solids. It approaches a limiting value as $\frac{p}{p_0} \to 1$. *Type II* is reversible, typical for non- or macroporous adsorbents. The intermediate flat region corresponds to the monolayer. *Type III* is not common. *Type IV* is irreversible, has characteristic hysteresis loop associated with capillary condensation in mesopores, and the initial part is similar to the type II behaviour. *Type V* is not common. *Type VI* is a stepwise multilayer adsorption on a uniform non-porous surface. Step height represents the monolayer capacity.
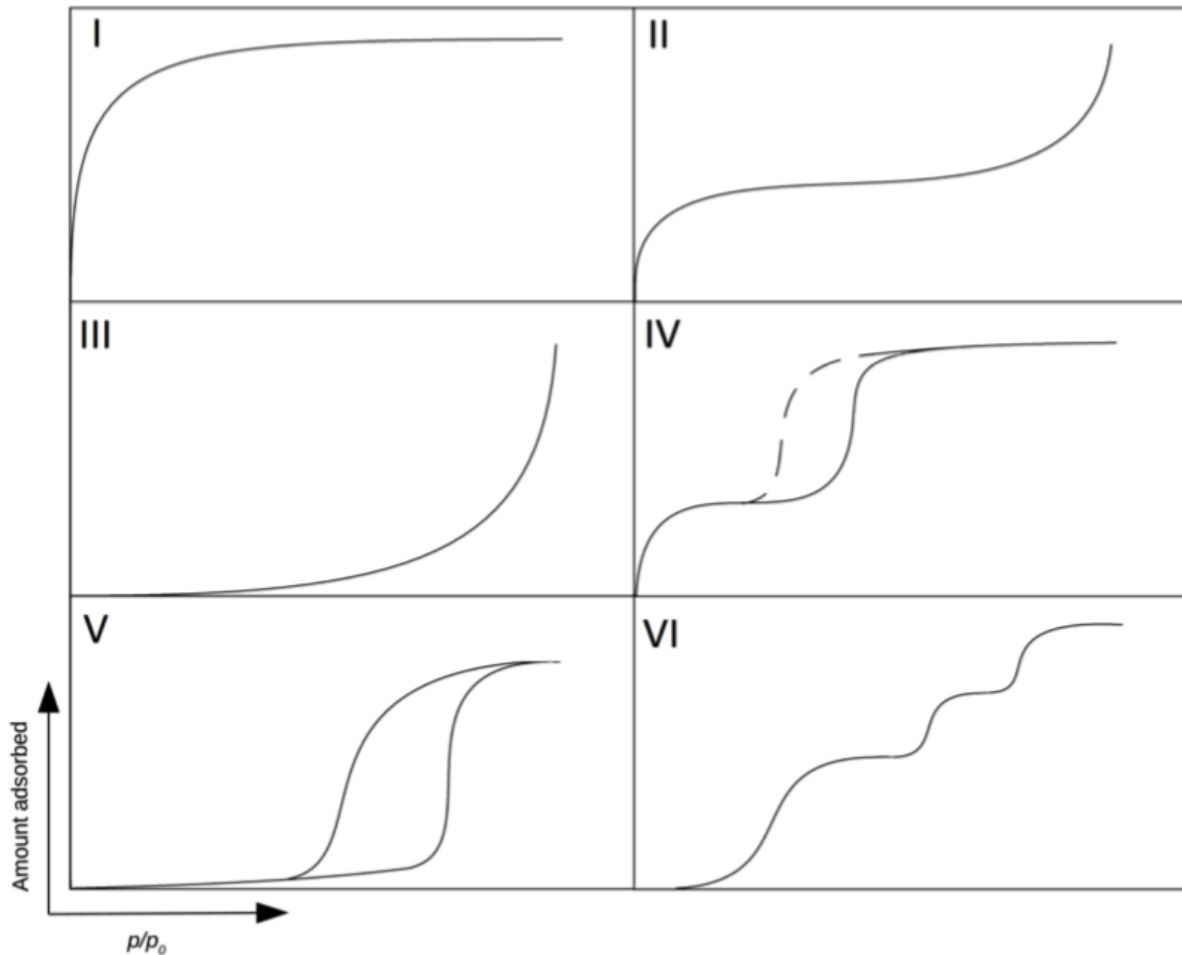
Figure 2.9: The different isotherm types as defined by IUPAC. Type *Type I* isotherm is typical for MOFs.

2.4.1   Langmuir Theory

In 1918 Langmuir proposed a model for describing the physisorption process. In this model, he made several assumptions. Langmuir assumed that the rate of adsorption equals the rate of desorption at equilibrium and that the adsorption energy is equal for all the adsorption sites. He further assumed that there was a defined number of adsorption sites, where only one molecule could occupy one adsorption site and that these molecules do not interact with each other. The Langmuir theory accounts only for formation of a monolayer on the adsorbent surface. The type I isotherm is therefore often referred to as the *Langmuir isotherm*, because they are typical for monolayer adsorption.[47] This relation is shown in the Langmuir equation, (2.5):

$$K_a P(1 - \Theta_L) = K_b \Theta_L \tag{2.5}$$

where P is the pressure, K_a is the adsorption rate constant and K_b is the desorption rate constant. Θ_L is the fraction of the surface that is occupied by the adsorbate. Equation 2.5 can be used further to derive the Langmuir model, (2.6):

$$\Theta_L = \frac{KP}{1 + KP}, \qquad K = \frac{K_a}{K_b} \tag{2.6}$$

The Langmuir surface area can be calculated from equation (2.7).

$$S_L = \frac{v_m N_a s}{m_v} \tag{2.7}$$

N_a is Avogadro's number, v_m is the volume of adsorbed gas molecules, m_v is the molar volume of adsorbed gas at standard pressure and temperature and s is the cross-section of the adsorbing species.

2.4.2 Brunauer–Emmett–Teller Theory

In 1938 Brunauer, Emmett and Teller (BET) made an extension of the Langmuir model, so that they could describe multilayer adsorption isotherms, and not only monolayer isotherms.[48] Brunauer, Emmett and Teller assumed that the first adsorption layer could act as a substrate for further adsorption. It is what we know as *multilayer adsorption*, where every absorbed molecule can in turn act as an adsorption site. BET assume that all of these sites are energetically equal. However, the interactions between the solid surface and the first adsorption layer will have stronger interactions than that of the 2nd and 3rd layer. In other words, the heat of adsorption will be higher for the first layer and then lower and constant from the 2nd layer and onwards. As in the Langmuir case, BET assume that there are no lateral interactions between the adsorbed molecules. BET further assume that the Langmuir theory is valid for each layer. The adsorption process, according to BET, is presented in equation (2.8) and given in a linear form in equation (2.9).

$$v = \frac{v_m C p}{(p_0 - p)[1 + (C-1)(\frac{p}{p_0})]} \tag{2.8}$$

Where p is the equilibrium pressure, p_0 is the saturation pressure, and v is the adsorbed amount of gas. The expression holds two constants, v_m and C. V_M is the specific monolayer capacity and C is the BET constant.

$$\frac{p}{v(p_0 - p)} = \frac{C-1}{V_M C}(\frac{P}{P_0}) + \frac{1}{V_M C} \tag{2.9}$$

In order to find the two constants, V_M and C, one can plot $\frac{p}{v(p_0-p)}$ vs. $(\frac{P}{P_0})$ and use the intercept a and the slope b from the straight line in equation (2.9)

$$v_m = \frac{1}{a+b} \tag{2.10}$$

$$C = 1 + \frac{b}{a} \tag{2.11}$$

Normally in BET theory, one uses the intervall where $0.05 < \frac{p}{p_0} < 0.35$. This is not the case for MOFs. Multilayer adsorption has strong restrictions in microporous materials, due to the small dimensions of the pores.[49] Instead one uses the Rouquerol criteria, where C must always be positive and $v(1 - \frac{p}{p_0})$ are monotonically increasing with $\frac{p}{p_0}$.[50]

The BET surface area is calculated from equation (2.12), where m_v is the volume occupied by one mole of adsorbent at standard temperature and pressure.

$$S_{\text{BET}} = \frac{v_m N_a s}{m_v} \tag{2.12}$$

BET surface area is the typical surface area that is most frequently reported in the literature for microporous materials.[49]

2.4.3 Isosteric Heat Of Adsorption

One of the fundamental quantities in adsorption measurements is the *isosteric enthalpy of adsorption.* The common therm for this, which is most often used, is *isosteric heat of adsorption*

$(Q_{st} = -\Delta H_{ads.})$. Heat of adsorption is, in conjunction with gas separation processes, a substantial quantity, because it describes how well a gas species will adsorb onto a material. It can, furthermore, be used to look at a material's affinity towards certain gasses over others. The heat of adsorption is a measure of the negative enthalpy of adsorption at a given volume. In order to calculate the heat of adsorption for a material, one needs a minimum of two isotherms collected at two different temperatures not too far apart (a difference of 10 K is a good rule of thumb). The isosteric heat of adsorption can be calculated from equation (2.13):

$$Q_{st} = -\Delta H_{ads.} = R\left(\frac{\partial ln(p)}{\partial \frac{1}{T}}\right)_{\Theta_L} \tag{2.13}$$

where p is the pressure corresponding to the loading Θ_L, T is temperature, R is the universal gas constant and Q_{st} is the isosteric enthalpy of adsorption. Θ_L indicates the surface coverage is kept constant (thereby *isosteric*).

The isosteric method requires perfectly spaced n intervals. However, for experimentally measured isotherms, this is not the case. The n intervals might well be approximately equally spaced, but this is not good enough for the purpose of calculating the heat of adsorption. One can approach this problem in several ways. One can either extrapolate to the correct n value from the experimentally measured datapoint, or one can fit the isotherm to an appropriate function. The latter is by far the more preferable method.

If, for example, the isotherms fit well with the dual-site Langmuir model (Equation 2.14), the parameters from the fitted model can be used to calculate the equilibrium pressures for a given set of regularly spaced n values. This can further be used, together with the Clausius-Clapeyron equation (Equation 2.15) to determine the heat of adsorption,

$$n = \frac{q_1 b_1 p^{v_1}}{1 + b_1 p^{v_1}} + \frac{q_2 b_2 p^{v_2}}{1 + b_2 p^{v_2}} \tag{2.14}$$

$$RT^2\left[\frac{\partial ln(p)}{\partial T}\right]_n = Q_{st} \tag{2.15}$$

Equation 2.15 can be re-written as:

$$[ln(p)]_n = -(\frac{Q_{st}}{R})(\frac{1}{T}) + C \qquad (2.16)$$

The Q_{st} can then be obtained from the slop of *ln (p)* vs. *(1/T)* plot from equation (2.16).

A difficulty can sometimes arise when trying to fit an analytical model to an isotherm's low pressure region, or to isotherms which display a stepwise behavior. Because of that, a virial-type equation is often used to determine the Q_{st}. In this approach, one uses a virial equation to fit several experimental isotherms, presented as $ln(\frac{p}{n})$ vs. n, simultaneously to the equation:

$$ln(p) = ln(n) + \frac{1}{T}\sum_{i=0}^{m} a_i n^i + \sum_{i=0}^{l} b_i n^i \qquad (2.17)$$

Where p is equilibrium pressure, n is loading, T is temperature and a_i and b_i is temperature independent parameters. The a_i parameters from equation (2.17) are further used in the following equation to obtain the heat of adsorption,

$$Q_{st} = -R\sum_{i=0}^{m} a_i n^i \qquad (2.18)$$

It follows that the heat of adsorption at zero-coverage is given by:

$$Q_{st} = -Ra_0 \qquad (2.19)$$

2.4.4   Ideal Adsorption Solution Theory

When considering a material's applicability for gas separation, it is of crucial importance to know its selectivity towards certain gases over others. However, producing binary or multi-phase isotherms experimentally by direct measurement is a complicated and challenging task.

In 1965, Meyers et al. found a way to get around this problem. They purposed the *Ideal Adsorption Solution Theory* (IAST), where they constructed multi-phase isotherms from single-compound measurements.[51] Today, IAST is widely used and is considered a powerful tool for sidestepping time consuming and laborious adsorption measurements with mixed gasses, and it has the advantage that one can determine multicomponent isotherms directly from the single-component isotherms without any additional parameters. The accuracy of the IAST model has

been well documented by comparison with Configurational Bias Monte Carlo simulations of mixed adsorption[52]

IAST is founded on two basic assumptions:[50, 51]

1. The adsorbate acts like an ideal solution in equilibrium with the gas phase. This is considered to be equal to the equilibrium between a liquid and a vapor phase, analogous to Raoult´s law.

2. The spreading pressure for each component is equal to that of the mixture.

These assumptions lead to the following two equations:

$$py_i = x_i p_i^0(\pi) \qquad (i = 1, 2) \tag{2.20}$$

and

$$\frac{A\Pi}{RT} = \frac{A\pi_i}{RT} = \int\limits_0^p \frac{n_i^a}{p_i} \mathrm{d}p_i \tag{2.21}$$

where $p_i^0(\pi)$ is the hypothetical pressure of the component in the gas phase that gives the spreading pressure π. y_i and x_i are y_i are the mole fractions in the fluid and adsorbed phase, respectively.

In this work, a Python Package (pyIAST), released in 2015 under a MIT-licence by M. Simon and co-workers, was used to perform the IAST-calculations and to obtain separation coefficients for several different mixed gases.[53] In order to perform the IAST-calculation, one needs to obtain the spreading pressure, π_i of a pure component i at the pressure p_i^0. For IAST, the spreading pressure are given as:

$$\pi_i(p_i^0) = \frac{RT}{A} \int_0^{p_i^0} \frac{q_i^0(p)}{p} dp \tag{2.22}$$

$$\pi^* = \frac{A\pi}{RT} = \int_0^{p_i^0} \frac{q_i}{p} dp \tag{2.23}$$

π^* and π are the reduced spreading pressure and the spreading pressure, respectively, A is

the specific surface area of the adsorbent, and q_i is the the saturation capacity of component i. The spreading pressure of single components is equal at constant temperatures:

$$\pi_1^* = \pi_1^* = ... = \pi^* = \pi \tag{2.24}$$

In order to compute the spreading pressures from equation (2.22) pyIAST needs the adsorption isotherm of the pure-component first. Again, this can be done in one of two ways: Either by fitting the experimental isotherm to an analytic model, or by linear interpolation. For a more detailed discussion on the choice of method, the reader is referred to [Simon, Smit, Haranczyk 53, p. 371].

By passing initial values for mole fractions for the gas components (two gasses in the case of this work), pyIAST returns their respective partial pressures:

$$y_1 P_T = x_1 p_1 \tag{2.25}$$

$$(1 - y_1) p_T = (1 - x_1) p_2 \tag{2.26}$$

This is further used to calculate the selectivity coefficient for component *1* over component *2*:

$$S_{12} = (\frac{x_1}{x_2})(\frac{y_2}{y_1}) \tag{2.27}$$

Where p_T is the total pressure. The selectivity is normally presented as a function of the total pressure in the computed mixed-gas system.

Chapter 3

Experimental Section

3.1   Chemicals

This chapter describes the syntheses, experiments and chemicals used in this work. All chemicals, reagents and solvents used in this work were purchased from Sigma Aldrich and used as received without further purification.

Metal Sources

- Cobalt (II) acetate tetrahydrat, ACS reagent, ≥ 98.0%

- Magnesium (II) acetate tetrahydrat, ACS reagent, 99.5%

- Manganese (II) acetate tetrahydrat, Purum p.a, ≥ 99.0% (KT)

- Nickel (II) acetate tetrahydrat, Purum p.a, ≥ 99.0% (KT)

Solvents

- N-Methyl-2-pyrrolidone, anhydrous, 99.5% (NMP).

- Distilled water (distilled in the home lab using an Aquatron A4000 water distiller).

- Tetrahydrofuran, ACS reagent ≥ 99.9% (Contained 250 ppm BHT as inhibitor).

Other Chemicals

Acetic acid	Ethanol	1,5-dihydroxynapthalene
Benzoic acid	Liquid nitrogen	Dry ice
Hydrochloric acid	Dimethyl sulfoxide	Methanol (anhydrous, 99.8%)
Acetone	Potassium bicarbonate	

Gases

The gases used for gas adsorption measurements, and the inert gas used for the Schlenk-line, were all bought from Yara Praxair and had a minimum purity of 99.999%

N_2	CH_4	He	Xe	Ar
CO_2	O2	N_2O	Kr	

3.2 Procedures

Ligand Synthesis

The linker in CPO-54 is 1,5-dihydroxy-2,6-naphthalene-dicarboxylic acid (DHNDC). To produce it, potassium bicarbonate 27 g, 0.27 mol) was mixed with 1,5-dihydroxynaphthalene (13 g, 0,08 mol) by use of pestle and mortar. This homogenous mixture was transferred to a teflon lined autoclave and reacted at 230°C in a pre-heated electric furnace for 20hr. No overpressure was observed.

After cooling, 2M hydrochloric acid was added to the solid mixture, resulting in a furious evolution of CO_2. Addition of hydrochloric was stopped when the evolution of CO_2 stopped. The resulting suspension was filtered, affording a green solid. The solids were dissolved in a saturated solution of potassium bicarbonate. To this, concentrated HCl was added, again resulting in the evolution of CO_2. The mixture was filtered, dissolved in THF (roughly 1.5L) and filtered one more time to remove any inorganic impurities. The THF was then removed by use of a rotor evaporator at 30°C and 268 mbar. The brown solid was suspended in water, filtered again and dried.

The dried powder was further dissolved in acetone. The acetone was removed by evaporation at 30°C and 300mbar. The resulting yellow-brown solid material was washed with acetone and dried again. Finally, to get a pure powder, it was washed in a 1:1 mixture of ethanol and water, then dried, producing a yellow powder. This powder was placed in a sealed Schlenk-flask, put under dynamic vacuum and heated to 90°C overnight to remove all solvents from the final product.
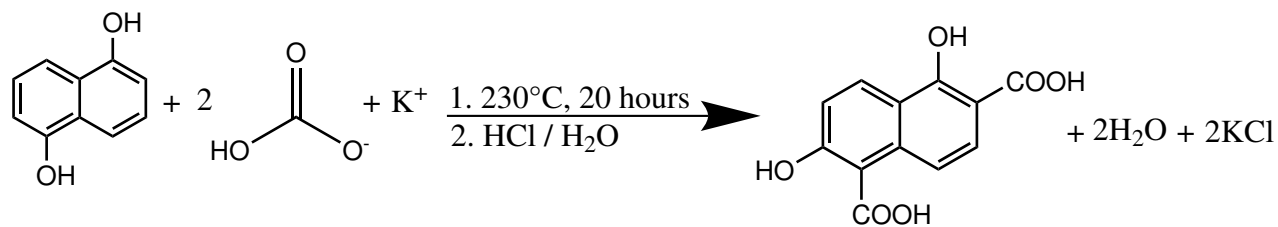

Figure 3.1: Overall reaction equation for the reaction used to make the 1,5-dihydroxy-2,6-naphthalene-dicarboxylic acid.

MOF Synthesis

CPO-54-Mg

1,5-dihydroxy-2,6-naphthalene-dicarboxylic acid (0.25 mmol, 0.0620 g) and ml n-methylpyrolidone (8 ml) was combined in a 23 ml Teflon liner and stirred for 10 minutes. Magnesium (II) acetate tetrahydrate (0.5 mmol, 0.1073 g) and water (1 ml) was added to this solution while stirring. The solution was stirred for a further 5 minutes. The autoclave was sealed and put into a pre-heated furnace to react for 24 hours at 140°C. The sample was taken out of the furnace and cooled down (approximately one hour) before it was washed with NMP and water.

The pale yellow powder was filtered under inert conditions by use of a Schlenk-line. The sample was soaked in 50 ml of methanol to replace any potential solvent molecules left in the structure. This was repeated three times. The methanol was exchanged after 1 and 2 hours before it was left soaking in methanol overnight. Lastly, the dried and filtered product was transferred to an argon-filled Schlenk-flask and heated at 110°C under dynamic vacuum for 24 hours. The finished material was stored in an argon-filled glove box.

CPO-54-Ni

1,5-dihydroxy-2,6-naphthalene-dicarboxylic acid (0.3 mmol, 0.0745 g) and n-methylpyrolidone (9 ml) were combined in a 23 ml Teflon liner and stirred for 10 minutes. Nickel (II) acetate tetrahydrate (0.6 mmol, 0.1493 g) and water (1 ml) was added to this solution whilst stirring. To this, Benzoic acid (3.0 mmol, 0.3664 g) was added, and the solution was stirred for another 5 minutes. The autoclave was sealed and put into a pre-heated furnace to react for 24 hours at 140°C. The sample was taken out of the furnace and cooled down (approximately one hour) before it was washed with NMP and water.

The dark yellow powder was filtered under inert conditions by use of a Schlenk-line. The sample was soaked in 50 ml of methanol to replace any potential solvent molecules left in the structure. This was repeated three times. The methanol was exchanged after 1 and 2 hours before it was left soaking in methanol overnight. Lastly, the dried and filtered product was transferred to an argon-filled Schlenk-flask and heated at 110°C under dynamic vacuum for 24 hours. The finished material was stored in an argon-filled glove box.

CPO-54-Co

1,5-dihydroxy-2,6-naphthalene-dicarboxylic acid (0.25 mmol, 0.0620 g) and ml n-methylpyrolidone (8 ml) was combined in a 23 ml Teflon liner and stirred for 10 minutes. Cobalt (II) acetate tetrahydrate (0.5 mmol, 0.1250 g), water (1 ml) and acetic acid (0.5 mL) were added to this solution while stirring. The solution was stirred for a further 5 minutes. The autoclave was sealed and put into a pre-heated furnace to react for 16 hours at 140°C. The sample was taken out of the furnace and cooled down (approximately one hour) before it was washed with NMP and water.

   The dark brown powder was filtered under inert conditions by use of a Schlenk-line. The sample was soaked in 50 ml of methanol to replace any potential solvent molecules left in the structure. This was repeated three times. The methanol was exchanged after 1 and 2 hours before it was left soaking in methanol overnight. Lastly, the dried and filtered product was transferred to an argon-filled Schlenk-flask and heated at 110°C under dynamic vacuum for 24 hours. The finished material was stored in an argon-filled glove box.

CPO-54-Mn

1,5-dihydroxy-2,6-naphthalene-dicarboxylic acid (0.25 mmol, 0.0620 g) and ml n-methylpyrolidone (8 ml) was combined in a 23 ml Teflon liner and stirred for 10 minutes. Manganese (II) acetate tetrahydrate (0.5 mmol, 0.1230 g) and water (1 ml) was added to this solution whilst stirring. The solution was stirred for a further 5 minutes. The autoclave was sealed and put into a pre-heated furnace to react for 24 hours at 110°C. The sample was taken out of the furnace and cooled down (approximately one hour) before it was washed with NMP and water.

   The dark orange powder was filtered under inert conditions by use of a Schlenk-line. The sample was soaked in 50 ml of methanol to replace any potential solvent molecules left in the structure. This was repeated three times. The methanol was exchanged after 1 and 2 hours before it was left soaking in methanol overnight. Lastly, the dried and filtered product was transferred to an argon-filled Schlenk-flask and heated at 110°C under dynamic vacuum for 24 hours. The finished material was stored in an argon-filled glove box.

Powder X-Ray Diffraction

PXRD measurements were carried out on a Bruker AXS D8 Advance, with a 9-position sample changer. Data collection was performed using monochromatic Cu $K_{\alpha 1}$ radiation in Bragg-Brentano geometry.

Nuclear Magnetic Resonance Spectroscopy

A 1H-NMR spectrum was measured on a Burker Biospin AV 500 instrument with broadband observe probe and field strength of 500MHz. DMSO was used as the solvent in the measurement.[54]

Gas Adsorption at Standard-Pressure

The standard-pressure gas adsorption measurements were conducted on a BELSORP-max instrument equipped with a low-pressure transducer and a turbo-molecular pump, allowing measurements with high precision from very low pressures ($\frac{p}{p_0} = 10^{-8}$).

The samples were prepared under inert conditions and transferred to the sample cell inside an argon-filled glove box. The sample cells were closed with quick-connectors. Before the measurements, the samples were activated at 110 °C for 8 hours in a dynamic vacuum on the instrument itself. A span adjustment was performed between all the measurements. The samples were kept under dynamic vacuum on a Belprep-vacII pre-treatment station between the measurements. The samples were purged with nitrogen before they were transferred back onto the instrument. An overview of the measured gases and temperatures are presented in Table 3.1.

A slush of dry ice and ethanol was used as coolant for the measurements at 195 K. The purpose of adding ethanol was to enable the gas sample holders to be pressed down into it, without too much resistance from the dry ice, in case the impact would break them.

Table 3.1: Overview of the measured temperatures and gases at standard-pressure for CPO-54-Mg, CPO-54-Ni and CPO-54-Co.

Adsorptive	Temperature / K				
N_2	77		278	288	298
CO_2		195	278	288	298
CH_4		195	278	288	298
O_2			278	288	298
N_2O		195	278	288	298
Xe			278	288	298
Kr			278	288	298

Gas Adsorption at High-pressure

The high-pressure gas adsorption measurements were carried out on a Belsorp-HP instrument. Several dead volume measurements were performed on the empty sample cell and filter cap, both at room temperature and 77K, to determine its total volume. The dead volume was further measured after the sample was weighed and filled into the sample cell, in order to determine the final dead volume. This was further used to calculate the *true density* of the sample, a parameter used in the measurement by the Belsorp software. The dead volume of the sample was measured again after all the planned measurements were conducted. The sample was weighted again after all the measurements, to ensure that the correct mass was used to convert the measured data from *excess* to *absolute* adsorption.

The sample was heated to 110 °C for 24 hours in a dynamic vacuum prior to the first adsorption measurement, and again for 8 hours in-between all the following measurements, using the instrument's external heating cap. Three parallells were measured for each temperature. An overview of the gases and temperatures measured for CPO-54-Ni and CPO-54-Mn are shown in Table 3.2 and Table 3.3, respectively.

Table 3.2: Overview of the measured temperatures and adsorptives at high-pressure for CPO-54-Ni.

Adsorptive	Temperature / K				
N_2	77		288	298	303
CO_2		278	288	298	
CH_4		278	288	298	
O_2		278	288	298	

Table 3.3: Overview of the measured temperatures and adsorptives at high-pressure for CPO-54-Mn.

Adsorptive	Temperature / K			
N_2	77	278	288	298
CO_2		278	288	298
CH_4		278	288	298
O_2		278	288	298

Chapter 4

Results

This chapter summarises the results of the experimental work and the data analysis for all of the explored materials: CPO-54-M (M= Co, Mg, Mn and Ni). Here, the powder X-ray diffraction patterns of all the MOF's are presented, as well as a NMR spectrum for the ligand used to synthesise them. Sorption isotherms and their accompanying analyses and calculations are shown for all compounds, as are the isosteric heats of adsorption. Finally, the gas separation properties are presented.

4.1 PXRD

All the material was examined by powder X-ray diffraction. Patterns were collected at angles $3° \leq 2\Theta \leq 70°$ and wavelength $\lambda = 1.54$Å. Please note that the intensities are normalized between 0 and 100 for easier comparison.
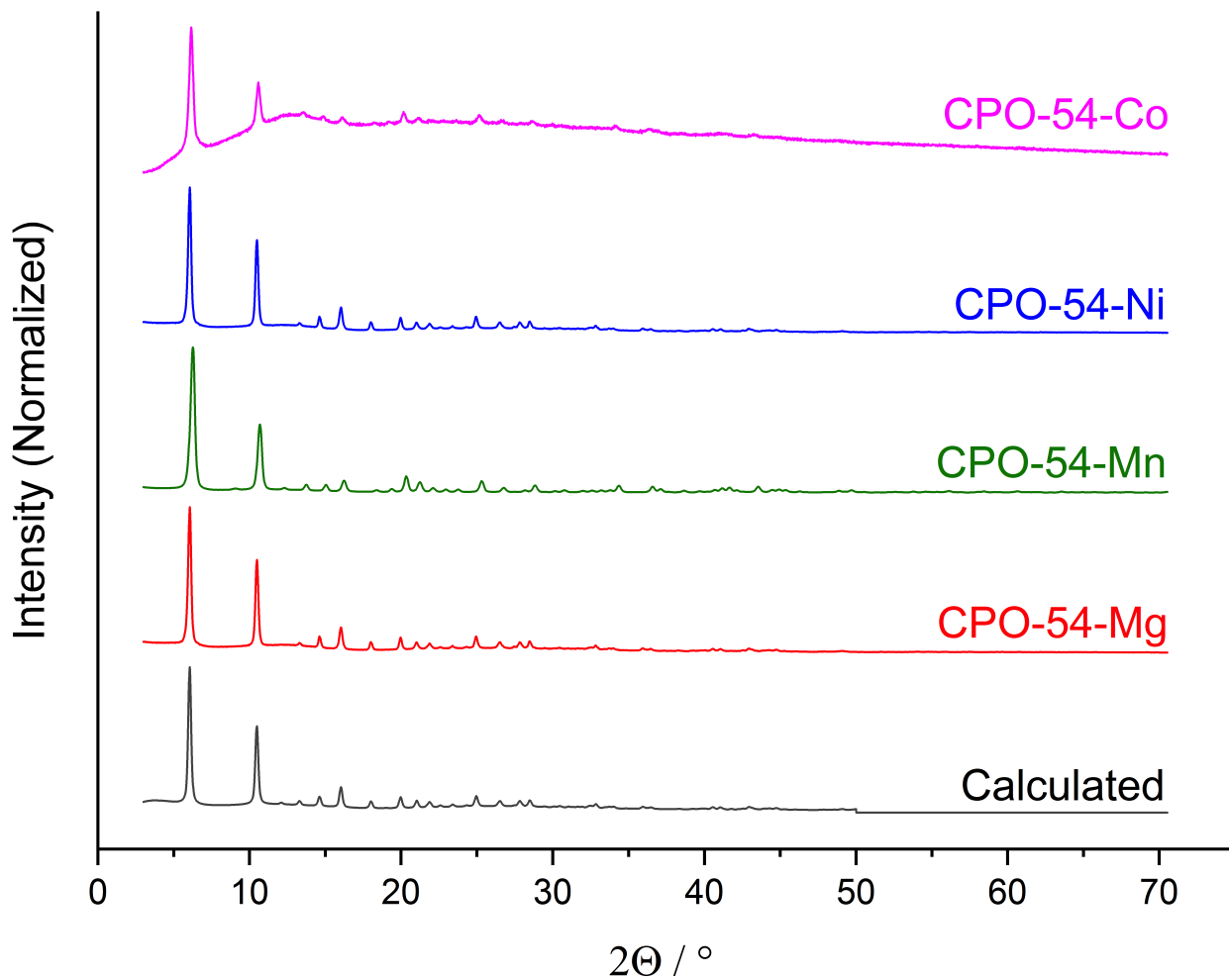
Figure 4.1: Experimentally measured powder X-ray patterns for CPO-54-Mg **(red)**, CPO-54-Mn **(green)**, CPO-54-Ni **(blue)**, CPO-54-Co **(magenta)**, and one calculated pattern **black**.

4.2 NMR

A ^{1}H-NMR spectrum was recorded of the synthesized 1,5-dihydroxynapthalene-2,6-dicarboxylic acid using DMSO as solvent (Figure 4.2). One can see the signals from the aromatic hydrogen atoms at 7.70 ppm to 7.81 ppm, whilst signals from the alcohol and acid groups appear at 12.61 and 14.14. Signals from the solvent (DMSO) are clearly visible at lower shifts, as is acetone and THF. Both of these were used to purify the product after the synthesis.
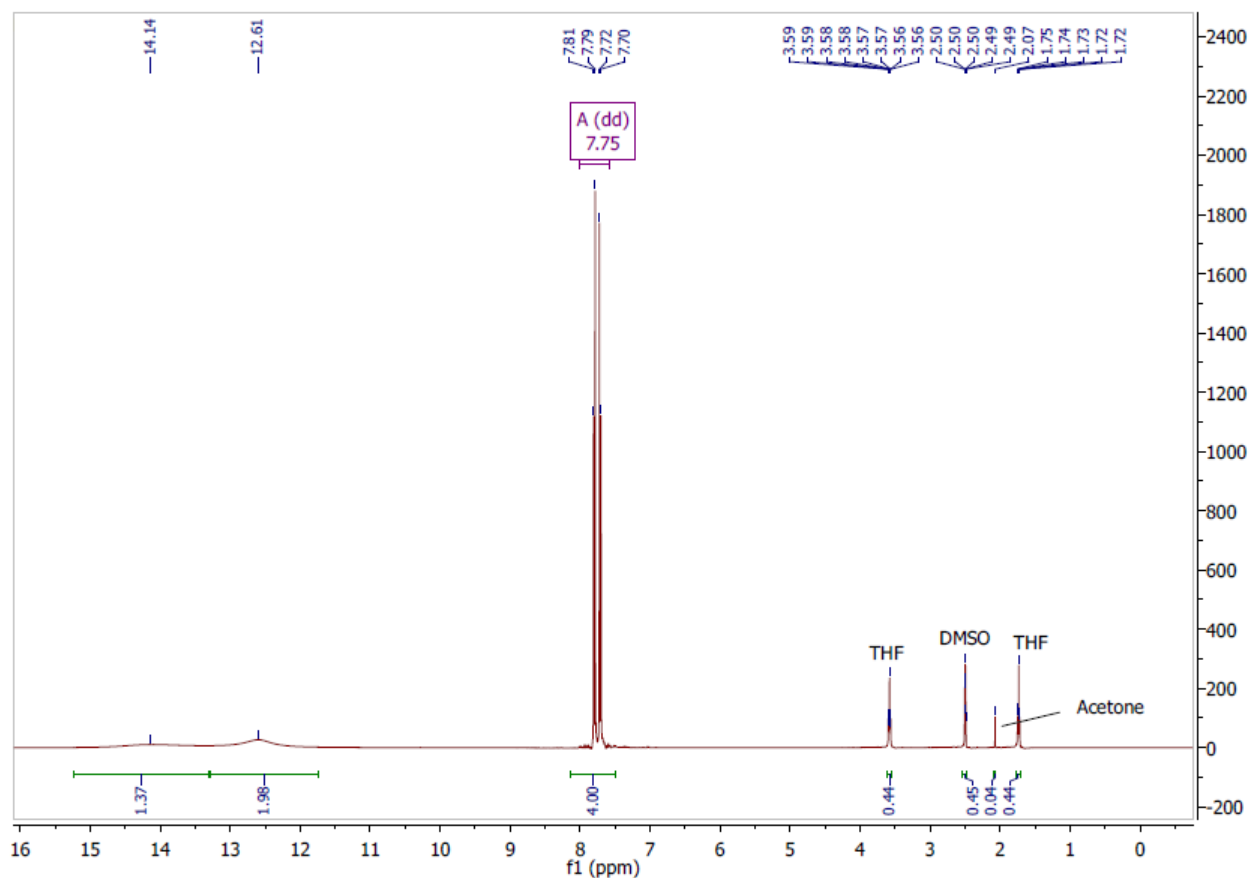
Figure 4.2: H-NMR spectrum of 1,5-dihydroxynapthalene-2,6-dicarboxylic acid.

4.3 Sorption

In order to investigate the gas separation properties of CPO-54, adsorption isotherms were measured at several temperatures and with the following adsorptives: CO_2, CH_4, N_2, O_2, Xe and Kr. Unfortunately, due to the very untimely breakdown of the Belsorp-HP instrument, only one of the compounds (CPO-54-Ni) was measured with the full range of gasses at high pressures, and it was only possible to collect a few isotherms for CPO-54-Mn (CO_2 and N_2). In this section the resulting adsorption and desorption isotherms are presented.

4.3.1 CPO-54-Mg

An N_2 isotherm was measured for CPO-54-Mg at 77K to determine the maximum capacity for N_2 uptake, the pore volume and the surface area of the material (Figure 4.3).

BET-theory was applied to the isotherm in order to find the surface-area and pore volume. By use of the Rouquerol criteria, the linear range for the BET-plot was identified as $0 \leq p/p_0 \leq 0.0396$ (Figure 4.4) and used in the BET analysis (Figure 4.5). The calculated pore volume and surface area are presented in Table 4.1.
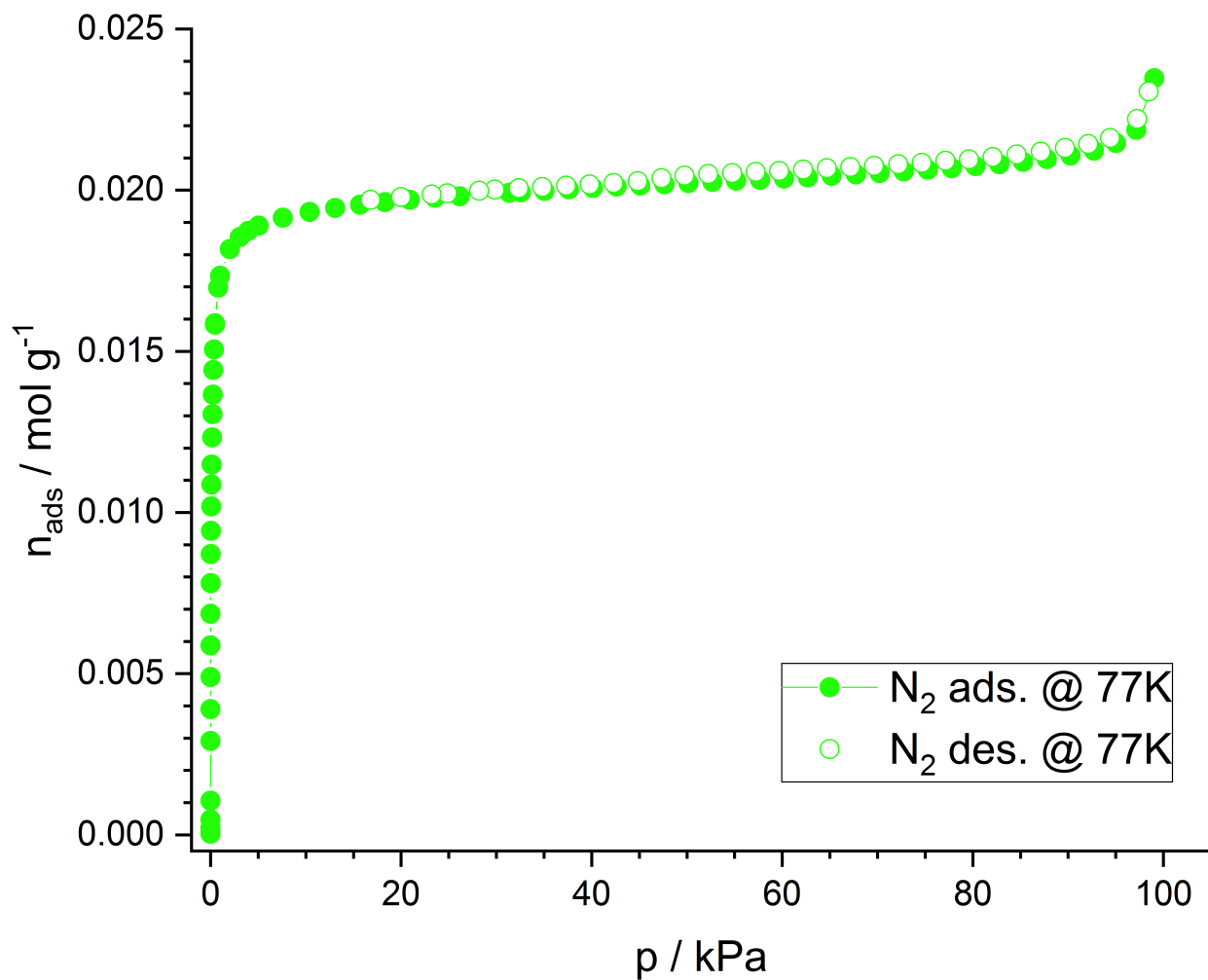
Figure 4.3: Adsorption (circles with colour fill) and desorption (circles without colour fill) isotherm for the material CPO-54-Mg, measured at 77K. The sample was pre-heated under dynamic vacuum at 388K for 8 hours prior to the measurement. The line between the data points is meant only as a *guide for the eye.*
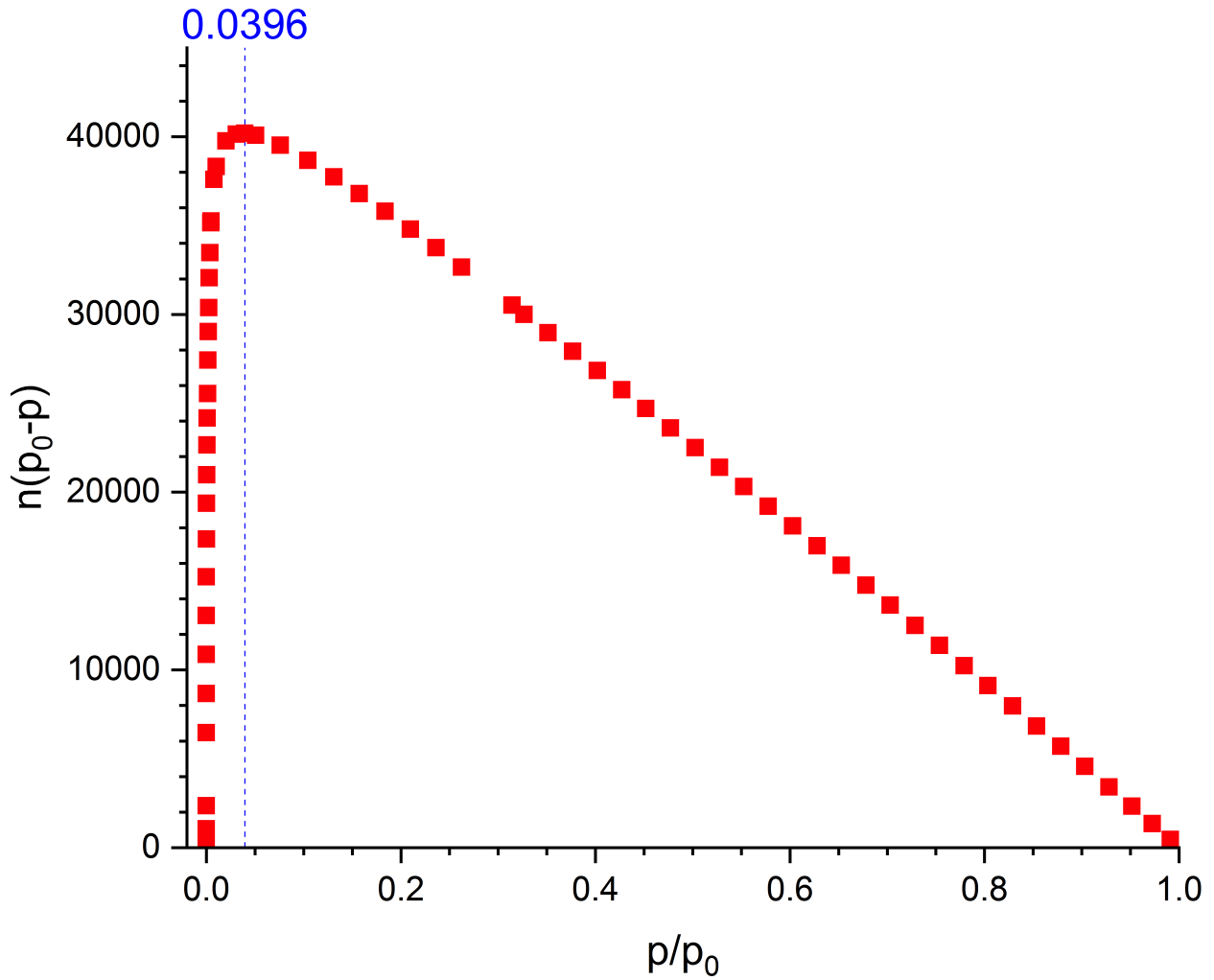
Figure 4.4: The Rouquerol criteria was used to define the linear range for the N_2 measurement at 77K prior to the BET-analysis. The **red** point represent the experimental data, whilst the **blue** line indicates the final point where $v/(1 - p/p_0)$ is increasing monotonically with p/p_0. The upper limit for p/p_0 was found to be 0.00396.
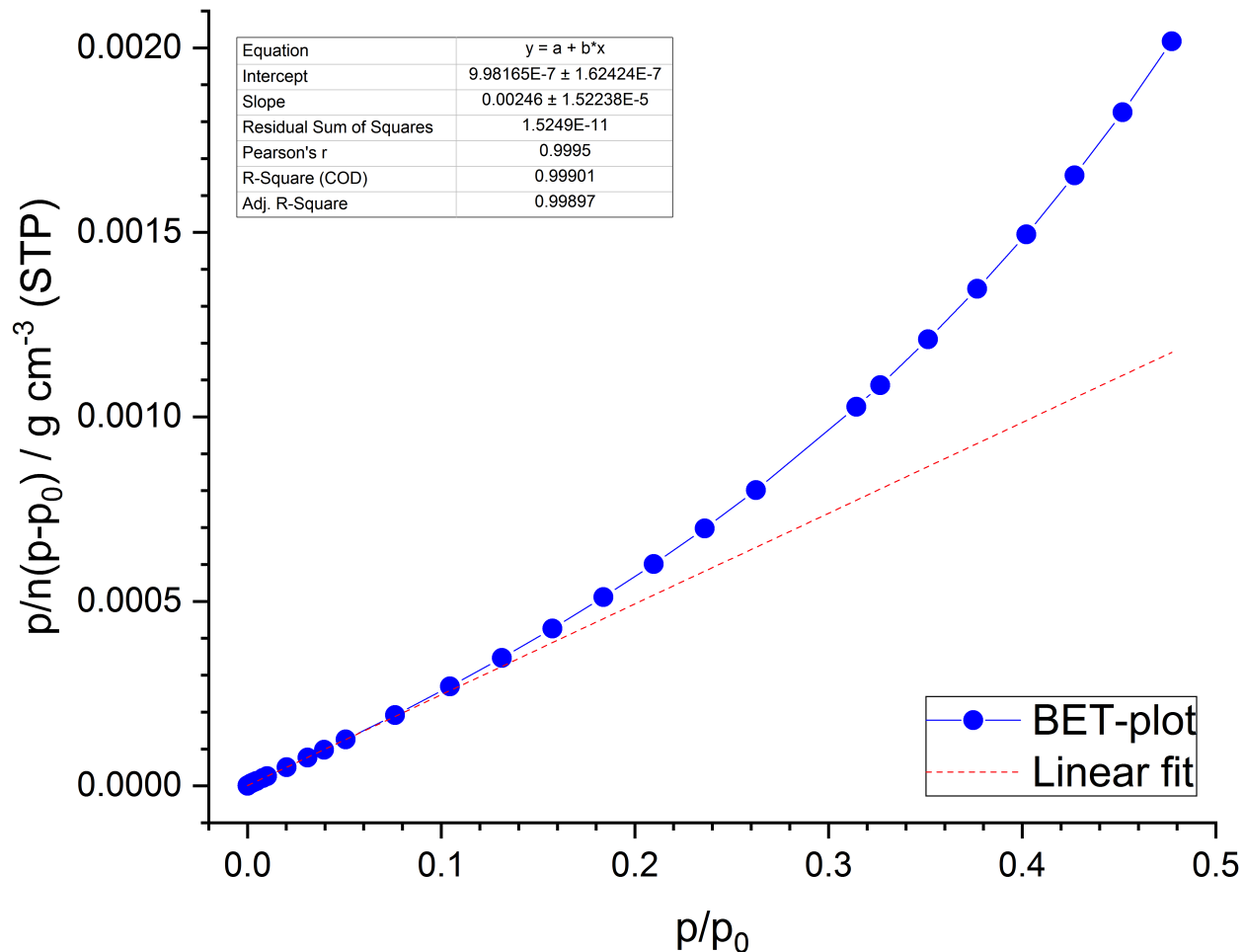
Equation	y = a + b*x
Intercept	9.98165E-7 ± 1.62424E-7
Slope	0.00246 ± 1.52238E-5
Residual Sum of Squares	1.5249E-11
Pearson's r	0.9995
R-Square (COD)	0.99901
Adj. R-Square	0.99897

Figure 4.5: BET-plot used in the BET analysis of the N_2 at 77K measurement on CPO-54-Mg. The linear regression (represented by the dashed red line) was performed on the experimental data **(blue)** in its linear region, as defined by the Rouquerol criteria.

Table 4.1: Overview of calculated pore volume and surface area for CPO-54-Mg.

Material	Pore volume / cm^3g^{-1}	BET surface area / m^2g^{-1}	Langmuir surface area / m^2g^{-1}
CPO-54-Mg	0.7281	1819.4	1994.4

Further, adsorption isotherms were measured at room temperature, and temperatures close to room temperature, for CPO-54-Mg (Figure 4.6). The temperatures 278 K, 288 K and 298 K were chosen so that the isosteric heat of adsorption could be calculated based upon them (see section 2.4.3). In order to illustrate the interactions between the different gases and the open metal-sites, the isotherms are plotted on a semi-logarithmic scale.

It was also of interest to investigate the maximum capacity for CO_2 uptake. Therefor, a measurement of CO_2 adsorption at 195 K was conducted. The CH_4 uptake was also measured at 195K, to make it possible to calculate the separation factor between the two gases at that temperature. In addition, N_2O was also measured at 195K to show how its uptake compared to the CO_2 uptake.
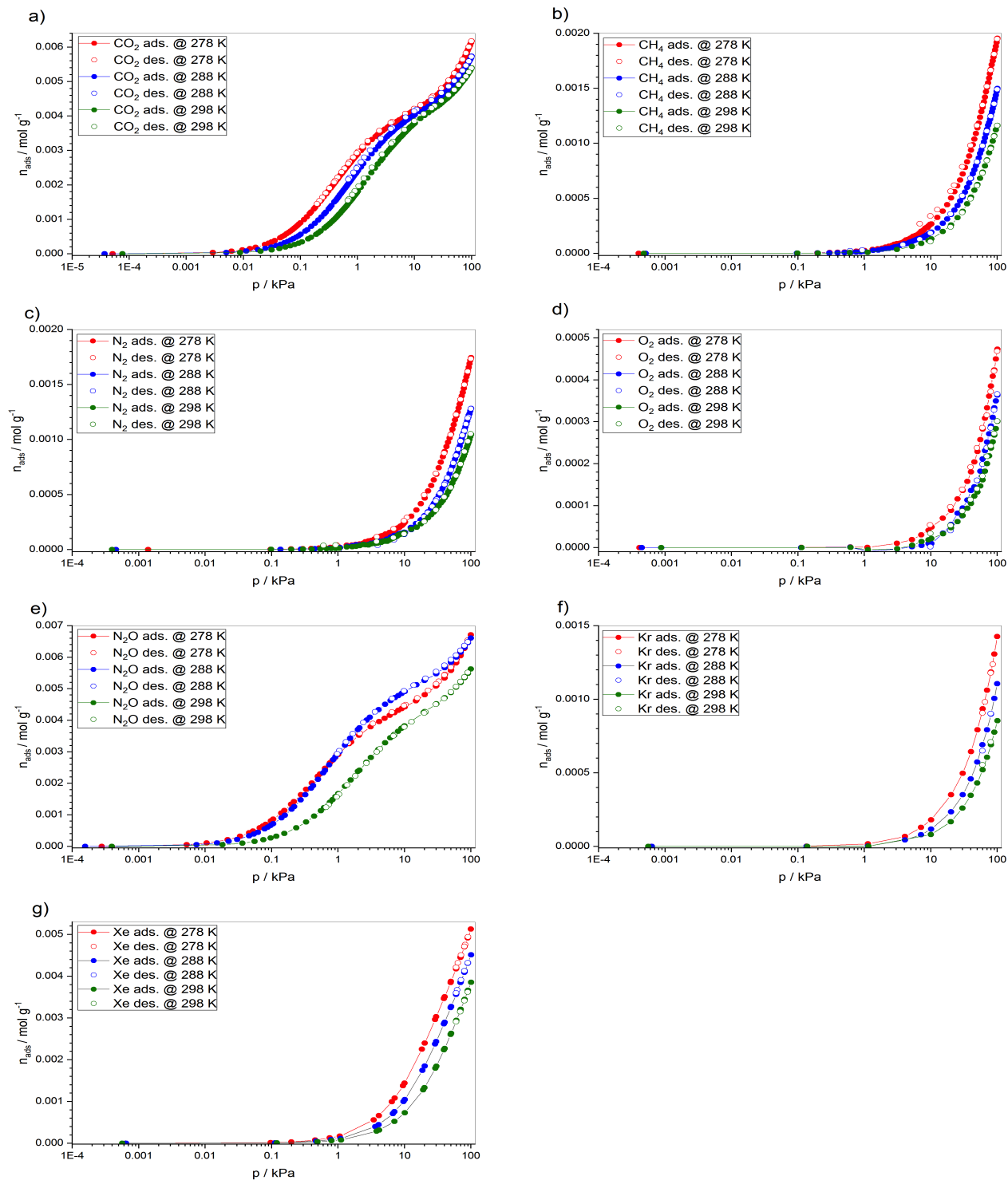
Figure 4.6: Adsorption and desorption isotherms for CPO-54-Mg. The sample was pre-heated under dynamic vacuum at 388K for 8 hours prior to the measurement. **a)** CO_2, **b)** CH_4, **c)** N_2, **d)** O_2, **e)** N_2O, **f)** Kr, and **g)** Xe. The **red** data points represent the 278 K isotherms, the **blue** data points represent the 288 K isotherms, and the **green** data points represent the 298 K isotherms. The line between the data points is meant only as a *guide for the eye*.
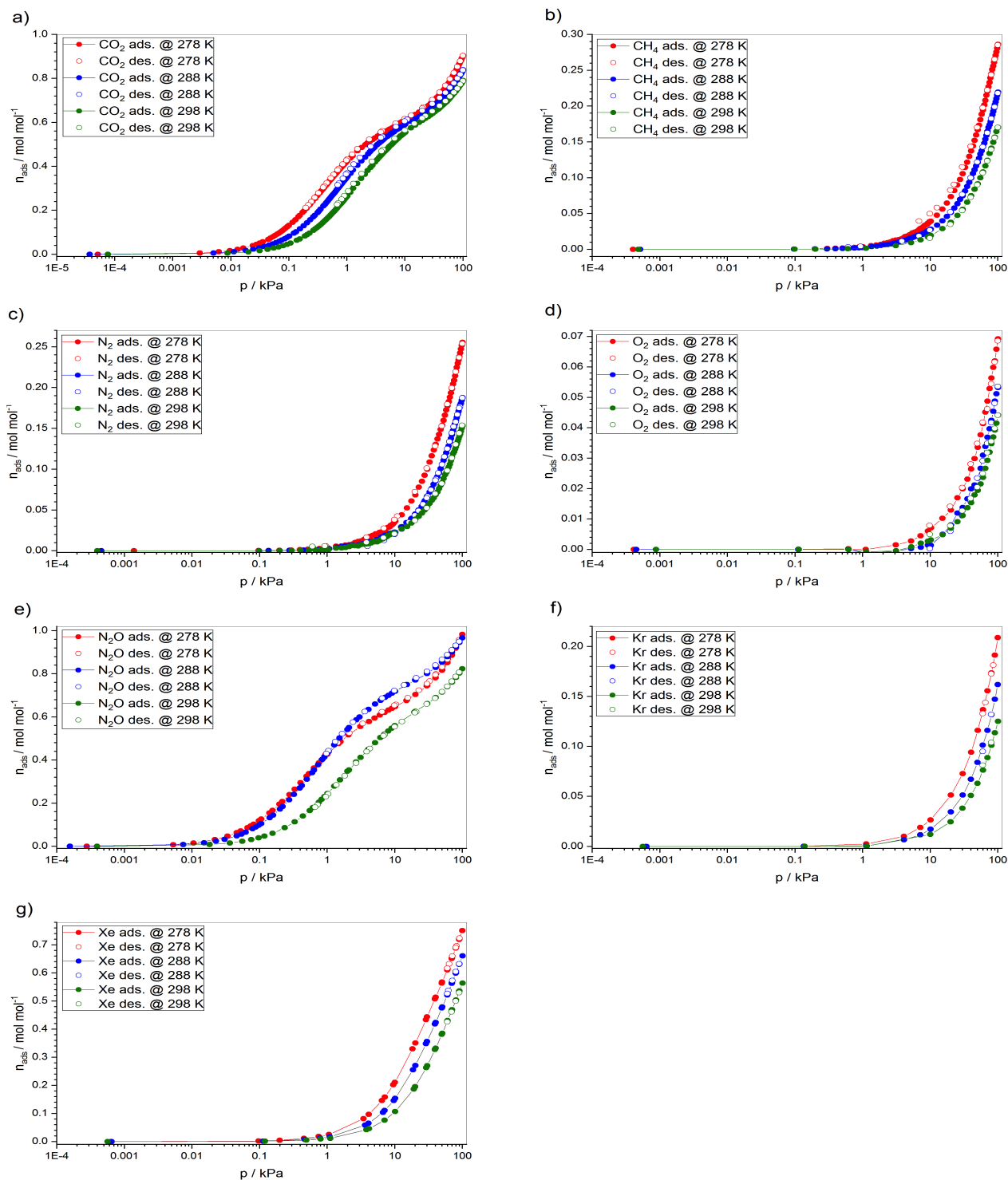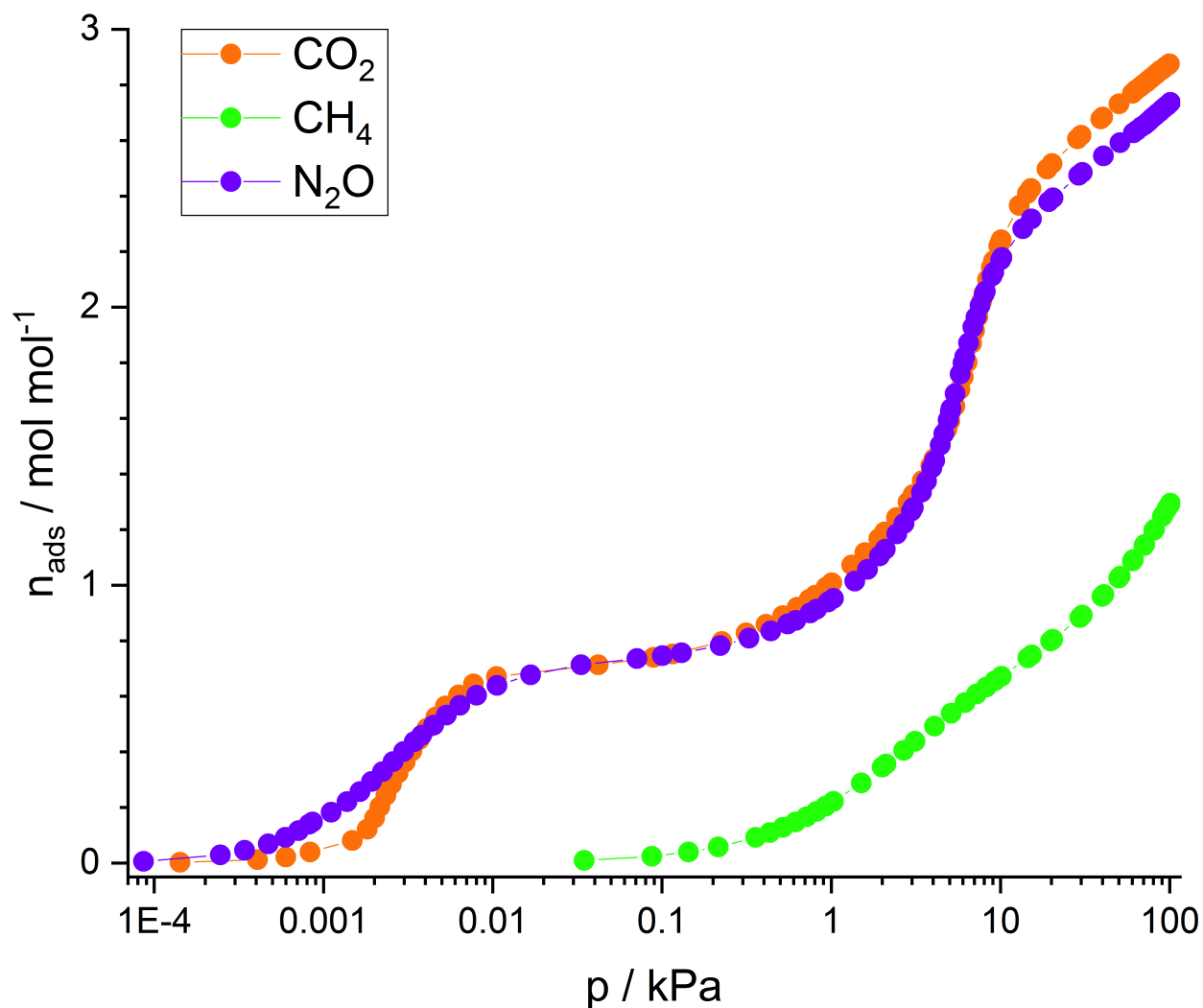
Figure 4.7: Isotherms for CPO-54-Mg plotted as number of molecules adsorbate per mole adsorbent on a semi-logarithmic scale. **a)** CO_2, **b)** CH_4, **c)** N_2, **d)** O_2, **e)** N_2O, **f)** Kr, and **g)** Xe. The **red** data points represent the 278 K isotherms, the **blue** data points represent the 288 K isotherms, and the **green** data points represent the 298 K isotherms. The line between the data points is meant only as a *guide for the eye.*

Figure 4.8: Isotherms for CPO-54-Mg at 195 K, plotted as the number of molecules adsorbate per mol adsorbent on a semi-logarithmic scale. The **orange line** represents CO_2, the **green line** represents CH_4 whilst the **purple line** represents N_2O. The line between the data points is meant only as a *guide for the eye*.

4.3.2 CPO-54-Ni

An N_2 isotherm was measured at standard-pressure (0<p<1 bar) for CPO-54-Ni at 77K to determine the maximum capacity for N_2 uptake, the pore volume and the surface area of the material, figure 4.9.
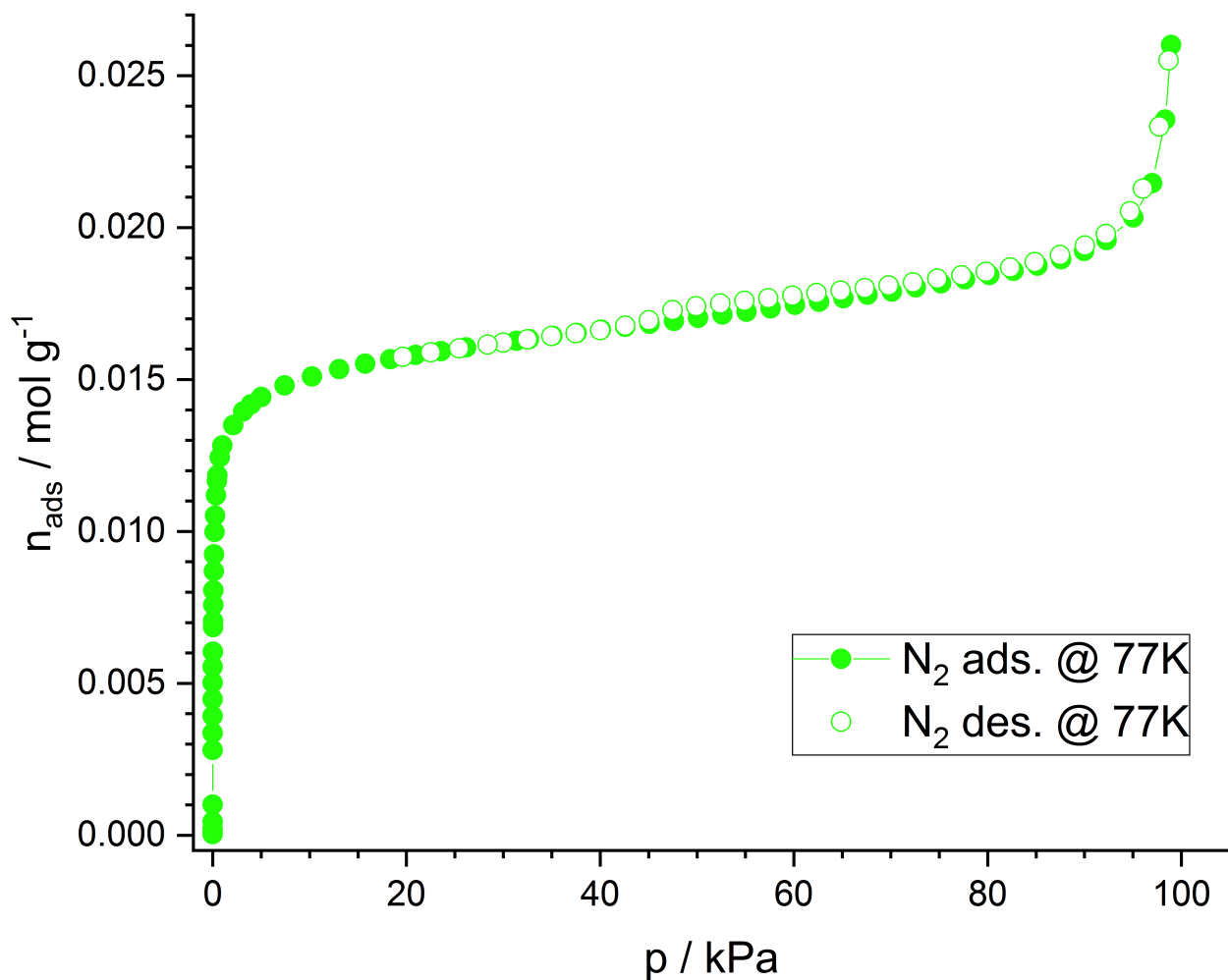

Figure 4.9: Adsorption and desorption isotherm for the material CPO-54-Ni, measured at 77K. The isotherm was measured using liquid nitrogen as coolant, and the sample was pre-heated under dynamic vacuum at 388K for 8 hours prior to the measurement. The line between the data points is meant only as a *guide for the eye*.

Again, the isotherm (Figure 4.9) correspons well with a type I isotherm as defined by IUPAC (see Figure 2.9), which validates the use of BET-theory for pore volume and surface area determination. The Rouquerol criteria (Figure 4.10) was used to define the linear range of the BET-plot

(Figure 4.11) to be $0 \leq 0.0747$. The calculated pore volume are shown in Table 4.2. Adsorption isotherms for CPO-54-Ni were also measured at standard-pressure and at three different temperatures (Figure 4.12 and 4.13).
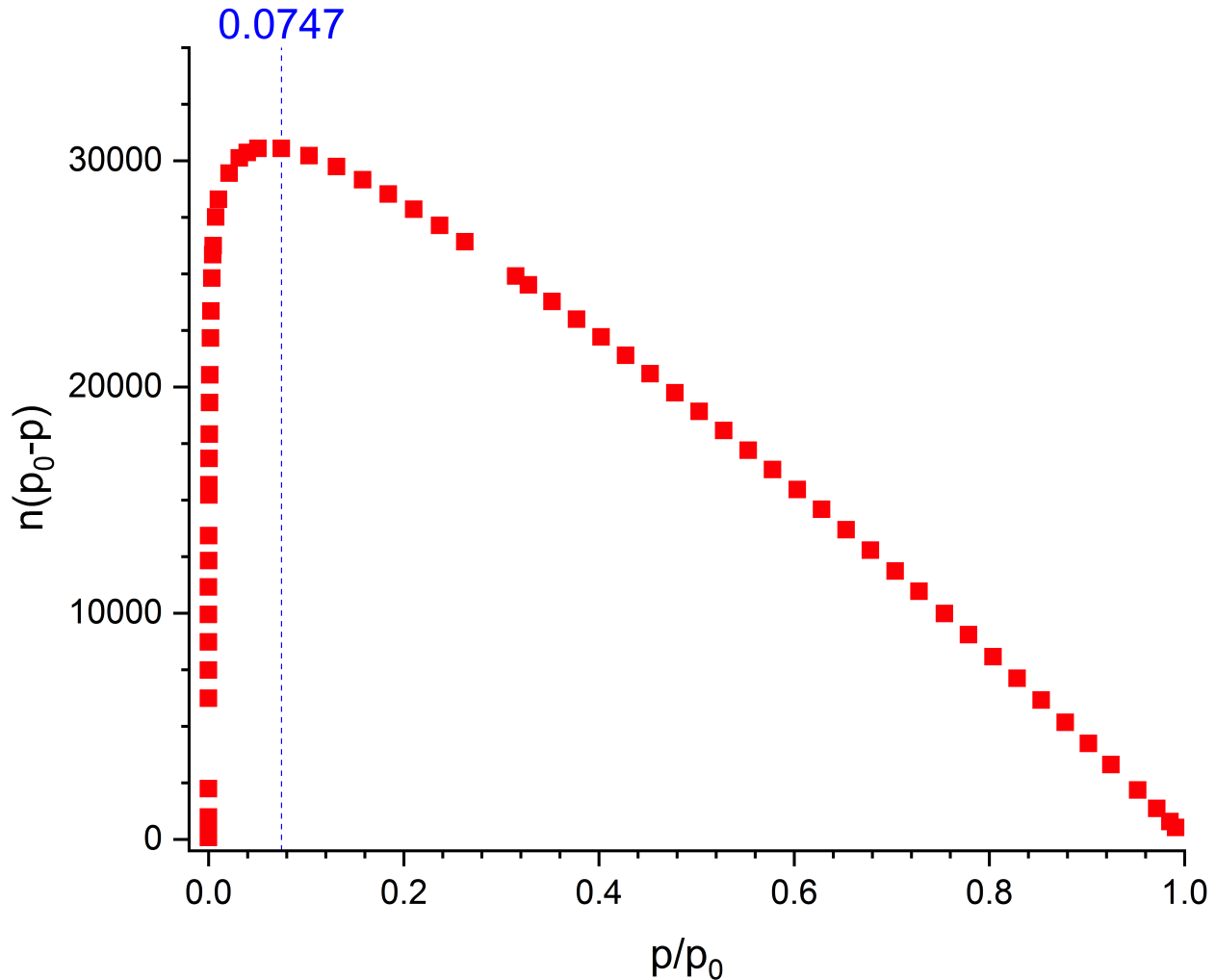

Figure 4.10: The Rouquerol criteria was used to define the linear range for the N_2 measurement at 77K prior to the BET-analysis. The **red** point represent the experimental data, whilst the **blue** line indicates the final point where $v/(1 - p/p_0)$ is increasing monotonically with p/p_0. The upper limit for p/p_0 was found to be 0.0747.

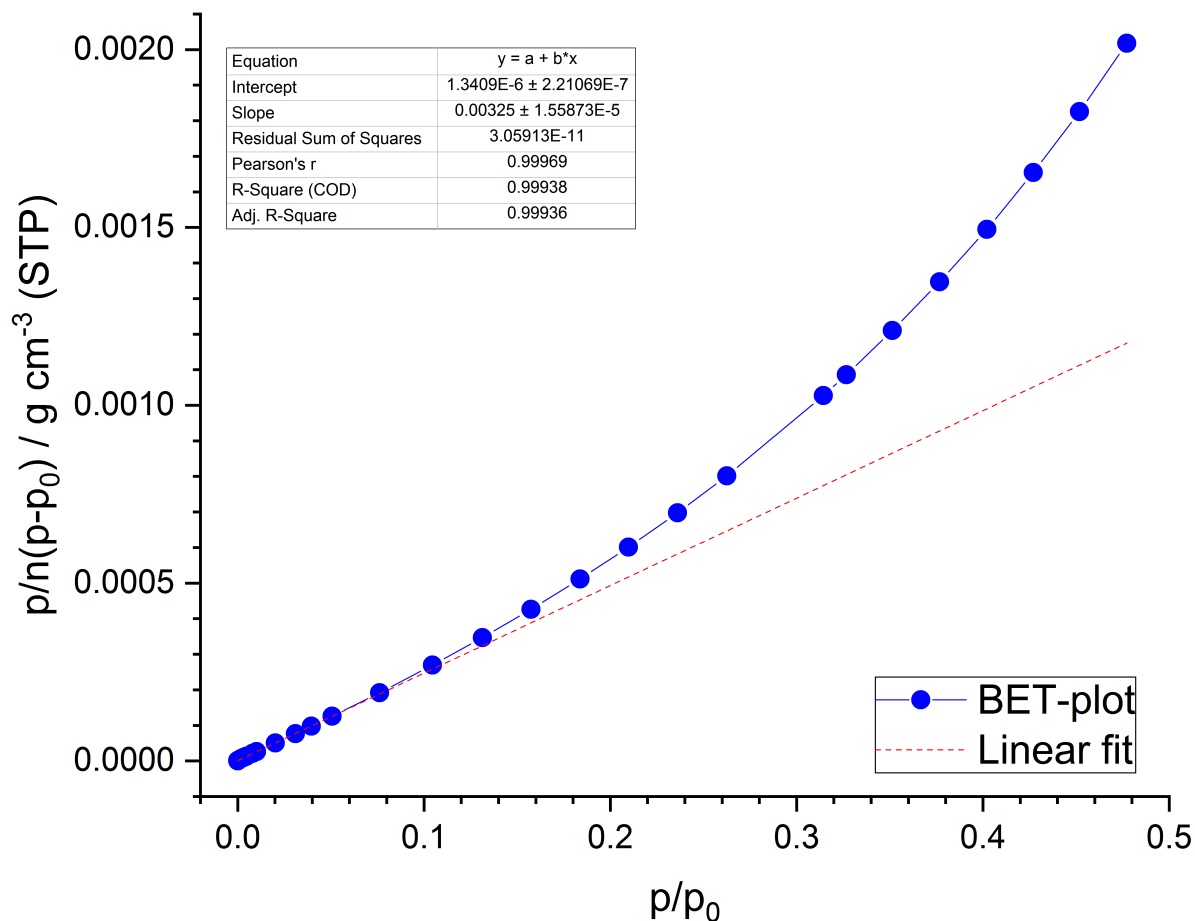| Equation	y = a + b*x
Intercept	1.3409E-6 ± 2.21069E-7
Slope	0.00325 ± 1.55873E-5
Residual Sum of Squares	3.05913E-11
Pearson's r	0.99969
R-Square (COD)	0.99938
Adj. R-Square	0.99936

Figure 4.11: The BET-plot used in the BET analysis of the N_2 at 77K (standard-pressure) measurement on CPO-54-Ni . The linear regression (represented by the dashed red line) was performed on the data **(blue)** in its linear region, as defined by the Rouquerol criteria.

Table 4.2: Overview of calculated pore volume and surface area for CPO-54-Ni based on the standard-pressure N2 77K measurement.

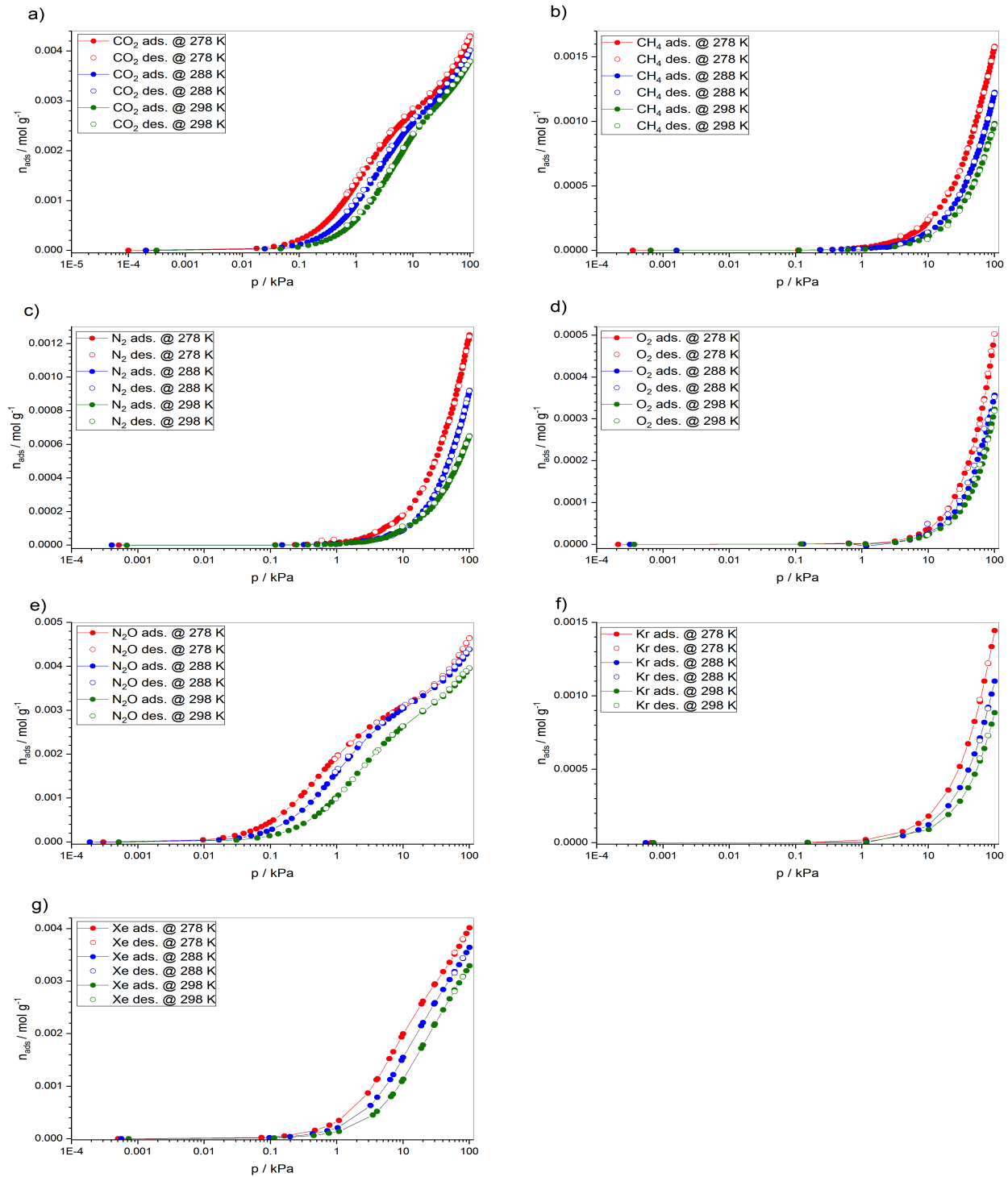| Material	Pore volume / cm^3 g^\textrm{-1}$	BET surface area / m^2 g^{-1}	Langmuir surface area / m^2 g^{-1}	Instrument used
CPO-54-Ni	0.5275	1180.1	1272.4	Belsorp-MAX
CPO-54-Ni	0.3814	915.9	1003.3	Belsorp-HP

Figure 4.12: Isotherms measured on CPO-54-Ni at three different temperatures. A water bath was used to keep the materials at a constant temperature whilst measured. The sample was pre-heated under dynamic vacuum at 388K for 8 hours prior to the measurement. **a)** CO_2, **b)** CH_4, **c)** N_2, **d)** O_2, **e)** N_2O, **f)** Kr **and g)** Xe. The **red** data points represent the 278 K isotherms, the **blue** data points represent the 288 K isotherms, and the **green** data points represent the 298 K isotherms. The lines are meant only as a *guide for the eye.*
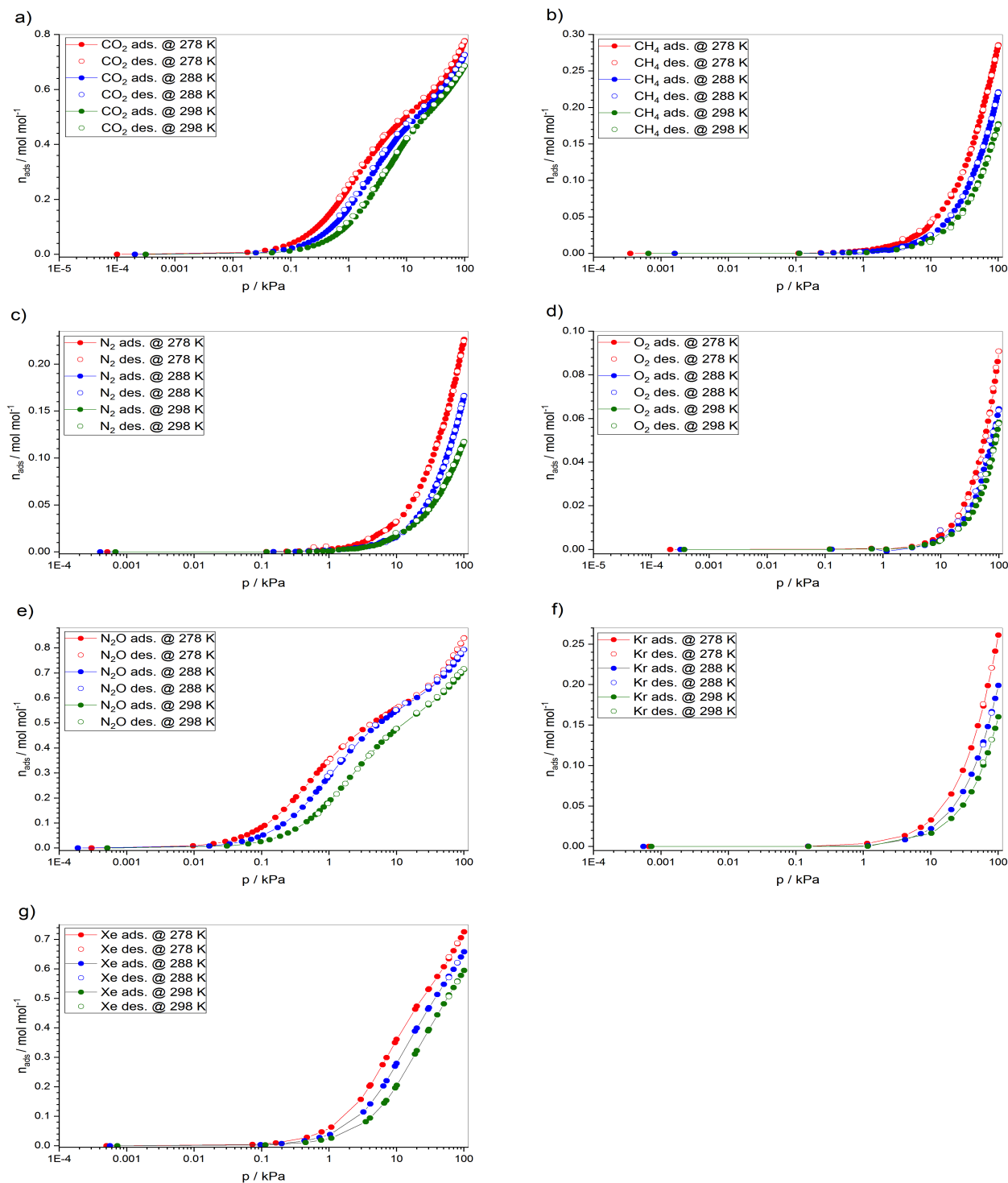
Figure 4.13: Isotherms for CPO-54-Ni plotted as the number of molecules adsorbate per mole adsorbent on a semi-logarithmic scale. **a)** CO_2, **b)** CH_4, **c)** N_2, **d)** O_2, **e)** N_2O, **f)** Kr, **and g)** Xe. The **red** data points represent the 278 K isotherms, the **blue** data points represent the 288 K isotherms, and the **green** data points represent the 298 K isotherms. The line between the data points is meant only as a *guide for the eye*.
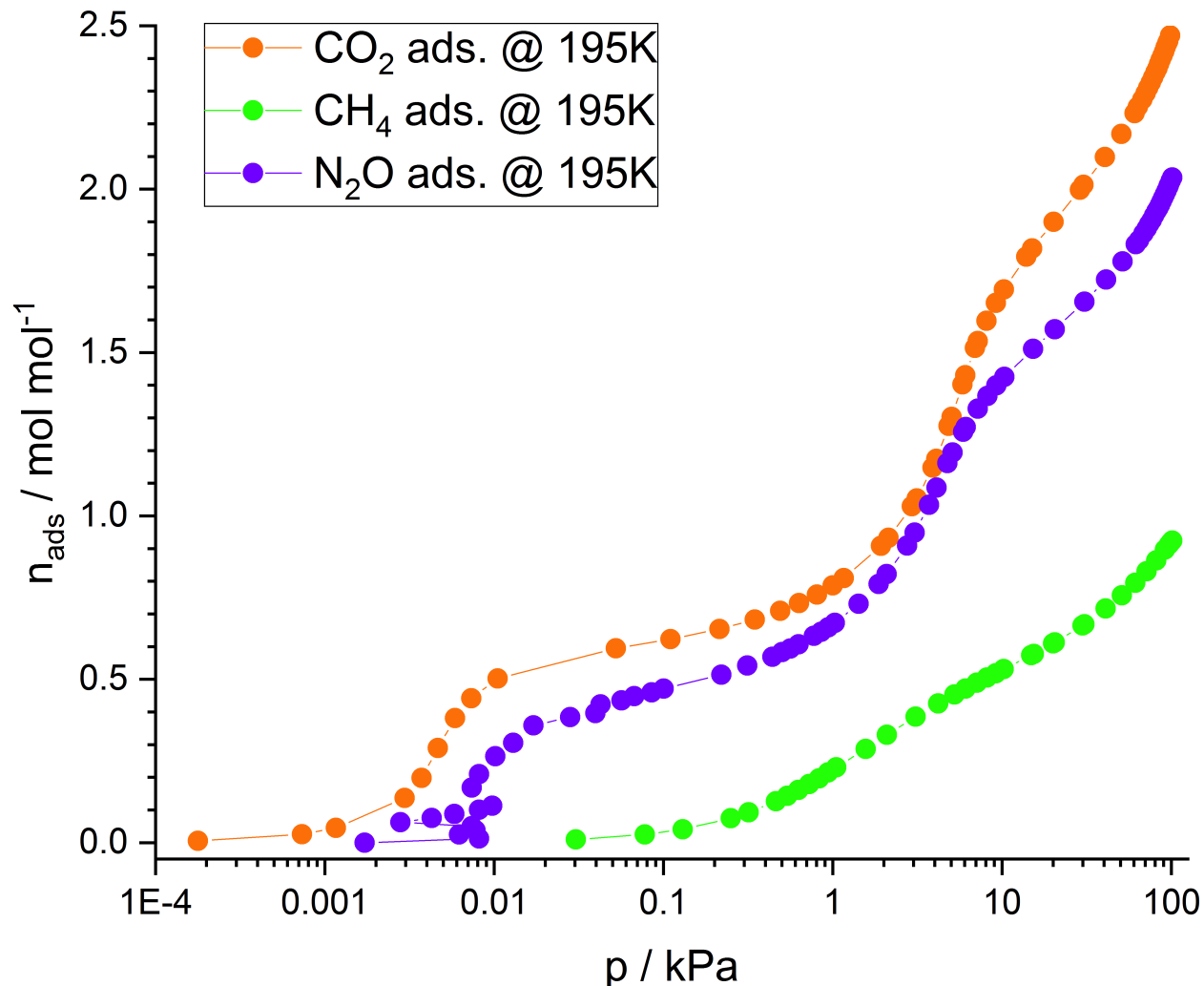
Figure 4.14: Isotherms for CPO-54-Ni at 195 K, plotted as the number of molecules adsorbate per mole adsorbent on a semi-logarithmic scale. The **orange line** represents CO_2, the **green line** represents CH_4 whilst the **purple line** represents N_2O. The line between the data points is meant only as a *guide for the eye*.

High-Pressure Gas Adsorption Measurements on CPO-54-Ni

Gas adsorption on CPO-54-Ni was measured at high pressures for a number of adsorptives at different temperatures. A new N_2 isotherm at 77K was also measured - this time at a BELSORP-HP instrument (Figure 4.15). Even though a standard-pressure N_2 isotherm at 77K had already been measured, it was essential to start the high-pressure measurement series by doing one more for comparison reasons. By doing that, there was now a reference uptake, a reference pore

volume and a reference surface area that could be compared with future N_2 at 77K measurements, to check that the material still performed at its initial level during the course of measurements.
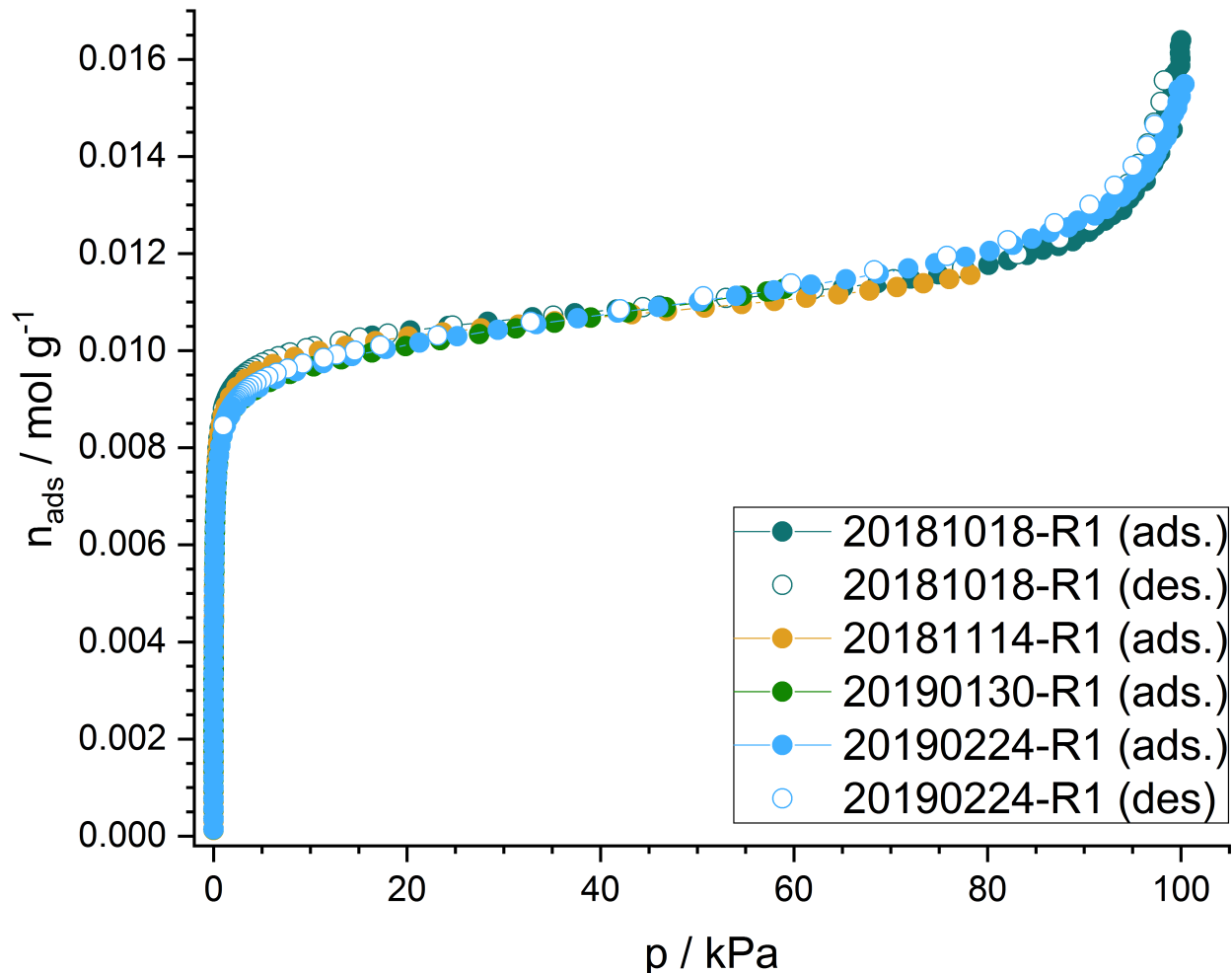

Figure 4.15: High-pressure N_2 isotherms 77K for CPO-54-Ni. Two of the isotherms were measured in between measurements with other gases, whilst the other two were measured at the start and the end, respectively. **Dark cyan**: the initial measurement, **yellow**: after the N_2 measurements, **green**: after the CO_2 and CH_4 measurements, **blue**: measurement after O_2 - final. The lines between the data points are meant only as a *guide for the eye.*

The linear range of the isotherm was, again, defined by the Rouquerol criteria (Figure 4.16). The linear ranges are listed in Table 4.3. This was used to produce a BET-plot (Figure 4.17). The surface areas and pore volume were calculated using equations 2.5, 2.7, 2.10, 2.11 and 2.12 (see Table 4.4.)

Table 4.3: Overview of the linear ranges for BET-analysis of the N_2 77K adsorption isotherms.

Experiment-ID	20181018-R1	20181114-R1	20190130-R1	20190224-R1
Linear range	0<p/p_0<0.05480	0<p/p_0<0.04441	0<p/p_0<0.05707	0<p/p_0<0.06345

Table 4.4: Overview of the calculated pore volumes and surface areas from all the different high pressure measurements of N_2 at 77K on CPO-54-Ni.

Experiment-ID	Pore volume / cm^3 g^{-1}	BET area / m^2 g^{-1}	Langmuir area / m^2 g^{-1}	Comment
20181018-R1	0.3814	915.9	1003.3	First measurement.
20181114-R1	0.3794	911.1	1002.8	After N_2 measurements.
20190130-R1	0.3817	896.3	991.21	After CO_2 and CH_4 measurements.
20190224-R1	0.3825	899.0	995.01	After O_2 measurements. Final.

Isotherms for N_2, CH_4 and O_2 adsorption were measured at three different temperatures (intervals of 10 K), in order to calculate the heat of adsorption and the separation factors (Figure 4.18).
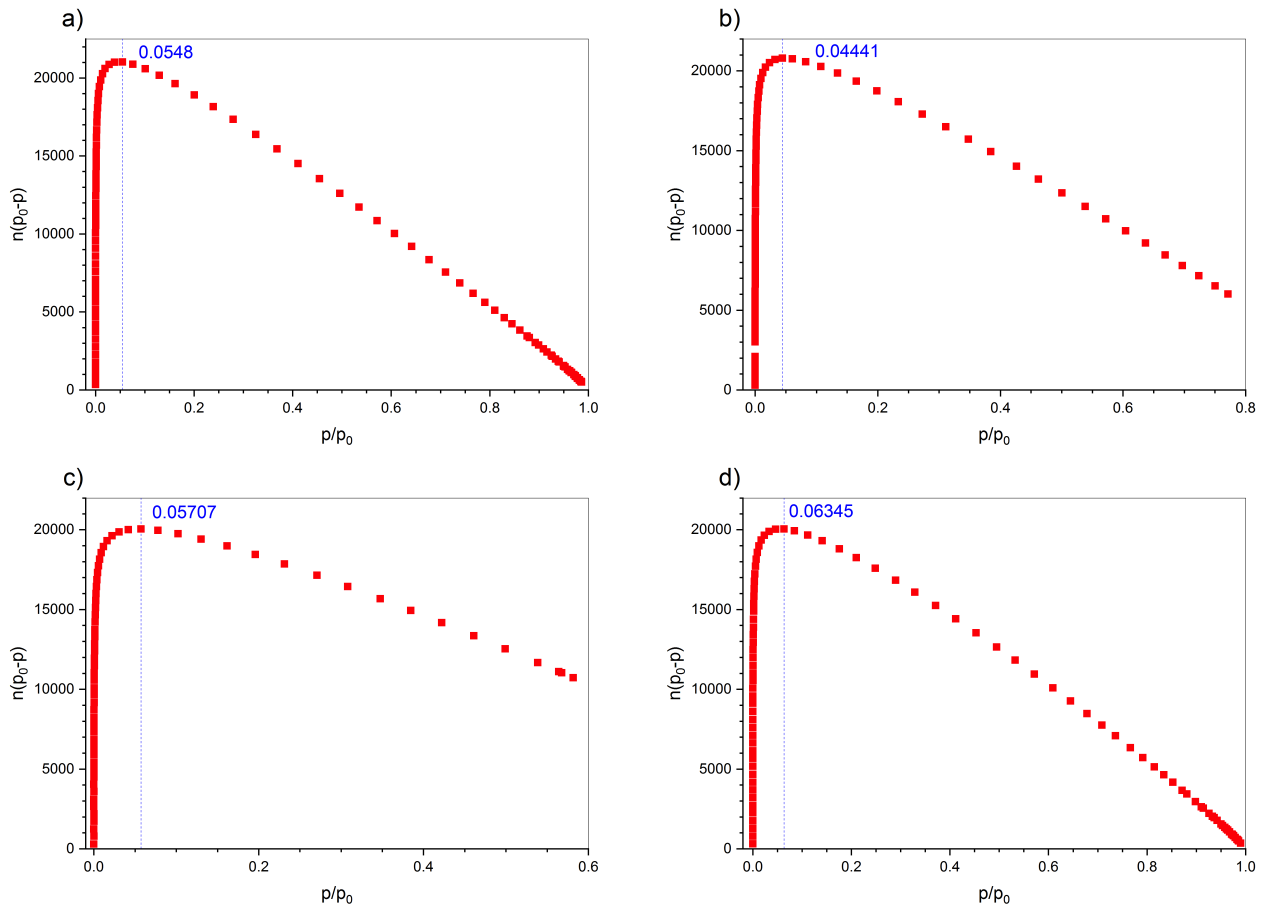
Figure 4.16: Rouquerol criteria for N_2 isotherms at 77K. **a)**: 20181018-R1, **b)**: 20181114-R1, **c)**: 20190130-R1, **d)**: 20190224-R1.
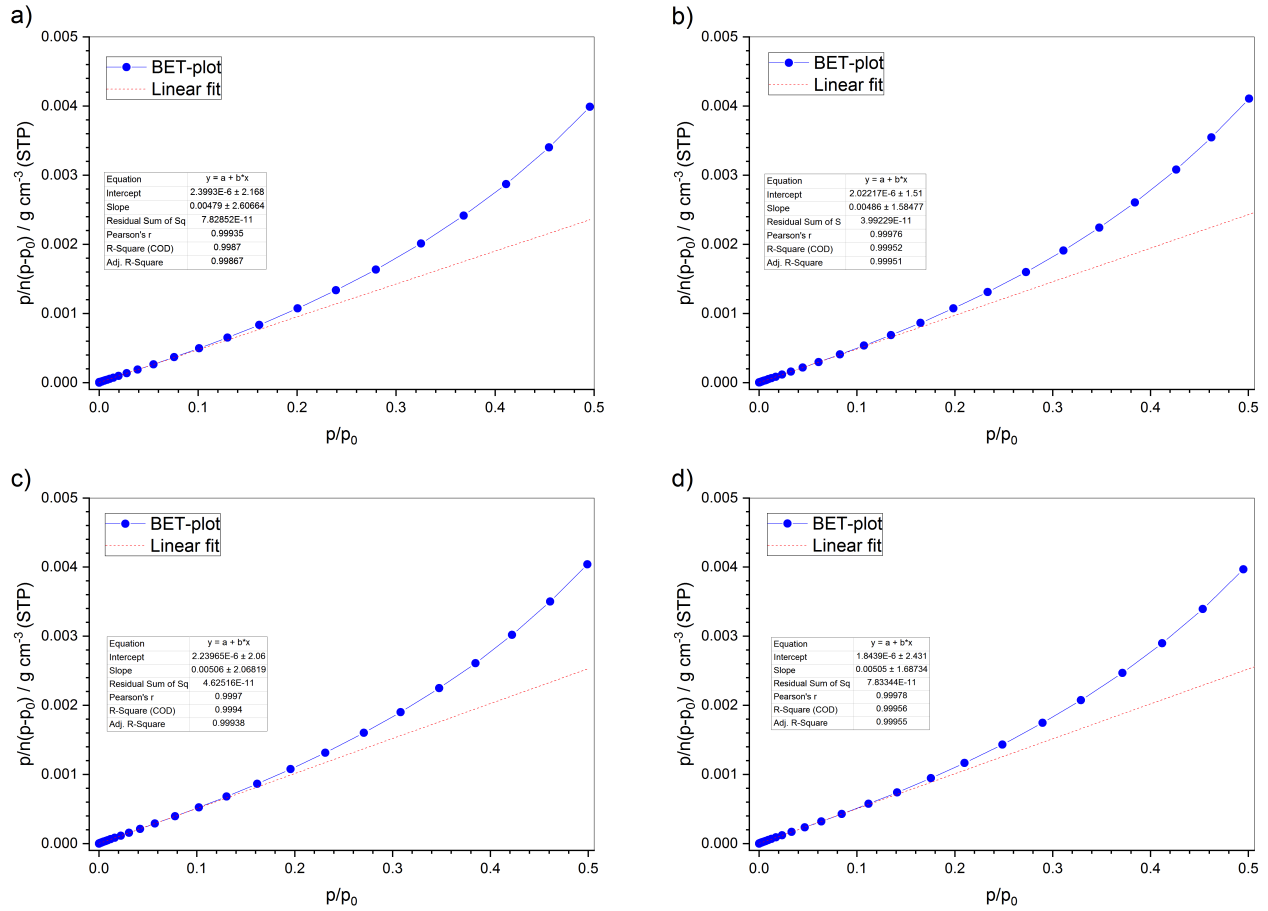
Figure 4.17: BET-plots for all the high-pressure N_2 measurements. **a)**: 20181018-R1, **b)**: 20181114-R1, **c)**: 20190130-R1, **d)**: 20190224-R1.
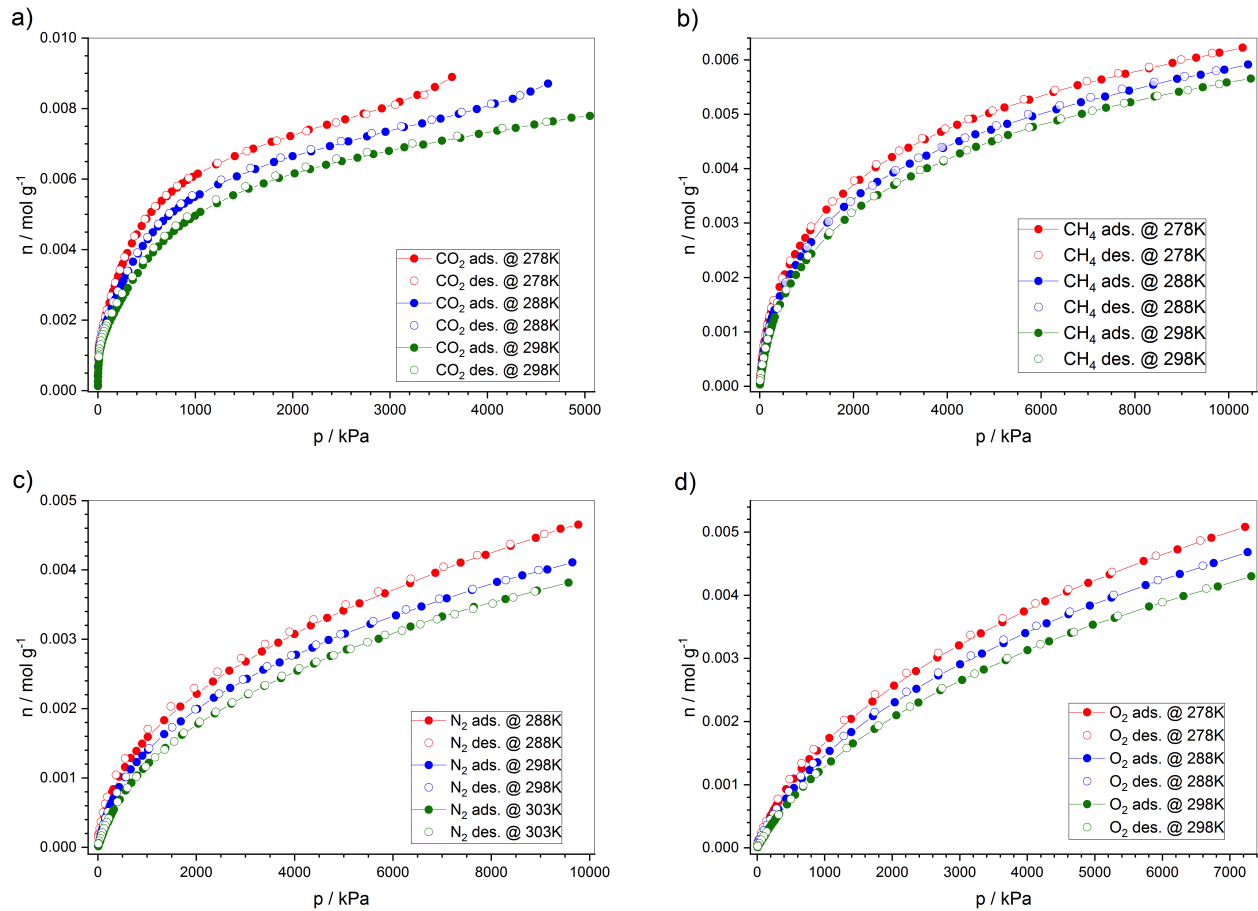
Figure 4.18: Excess adsorption N_2, CO_2, CH_4 and O_2 isotherms measured at three different temperatures. **a)** CO_2 isotherms. **b)** CH_4 isotherms. **c)** N_2 isotherms. **d)** O_2 isotherms. The **red** data points represent the 278 K isotherms, the **blue** data points represent the 288 K isotherms, and the **green** data points represent the 298 K isotherms. The line between the data points is meant only as a *guide for the eye*.

4.3.3 CPO-54-Co

N_2, CH_4 and O_2 adsorption isotherms were measured for CPO-54-Co at three different temperatures, whilst CO_2 was measured at two (Figure 4.22). A water bath was used to keep the samples temperature constant during the measurement. The Belsorp-Max instrument, on which all the standard-pressure sorption measurements were performed, has only got two sample ports with high precision pressure sensors. The third one has a lower precision. The measurements at near-room-temperature were all carried out on three materials in parallel: CPO-54-Mg and CPO-54-Ni on the high precision ports, and CPO-54-Co on the port with lower precision. One measurement on CPO-54-Co was, however, measured with a high-precision sensor: 77K N_2 (Figure 4.19).

The calculated pore volume and surface area are presented in Table 4.5.

Table 4.5: Overview of calculated pore volume and surface area for CPO-54-Co.

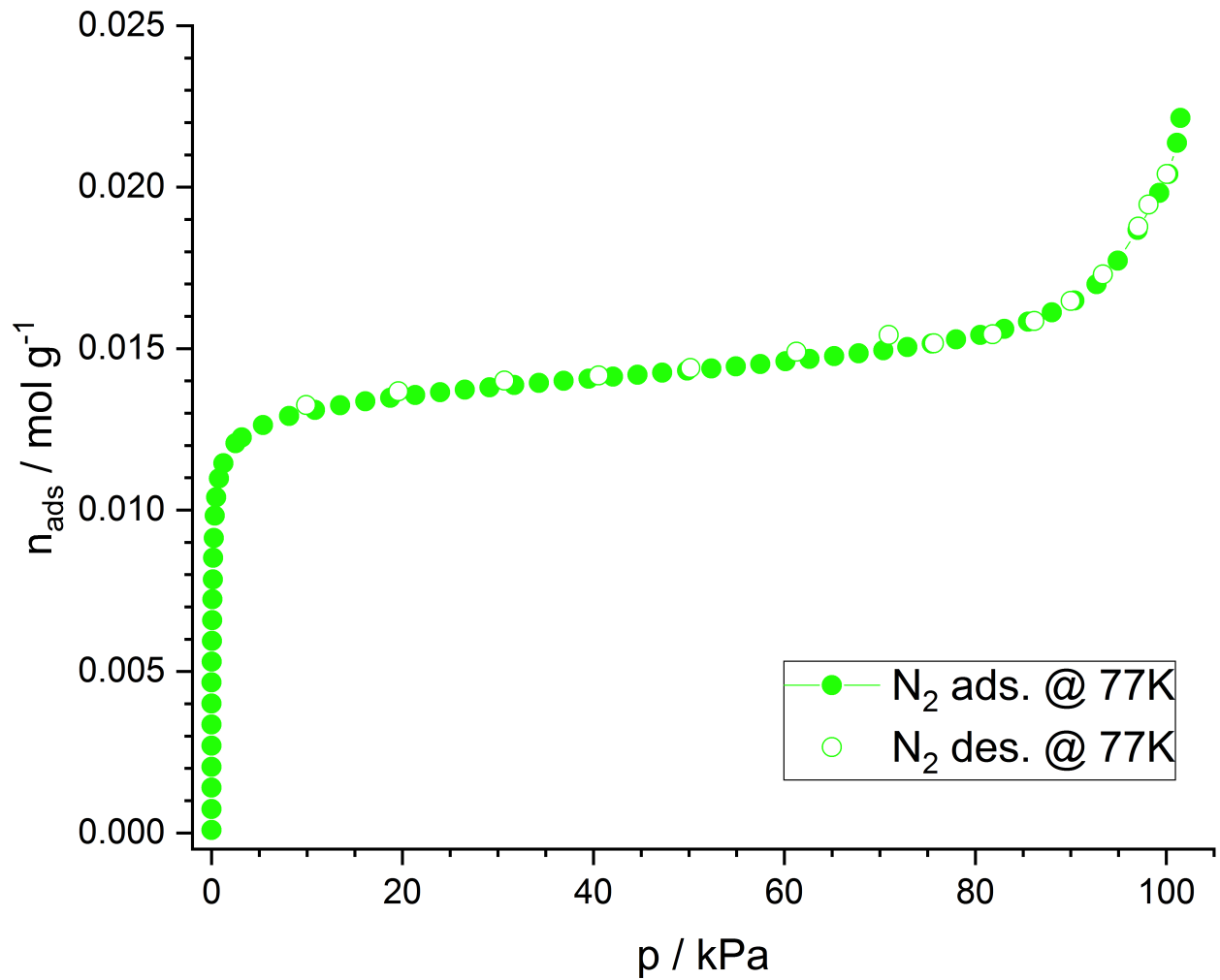| **Material**	**Pore volume / cm^3g^{-1}**	**BET surface area / m^2g^{-1}**	**Langmuir surface area / m^2g^{-1}**
CPO-54-Co	0.4979	1275.5	1342.2

Figure 4.19: Adsorption and desorption isotherm for N_2 at 77 K for CPO-54-Co. The lines are meant only as a *guide for the eye*.
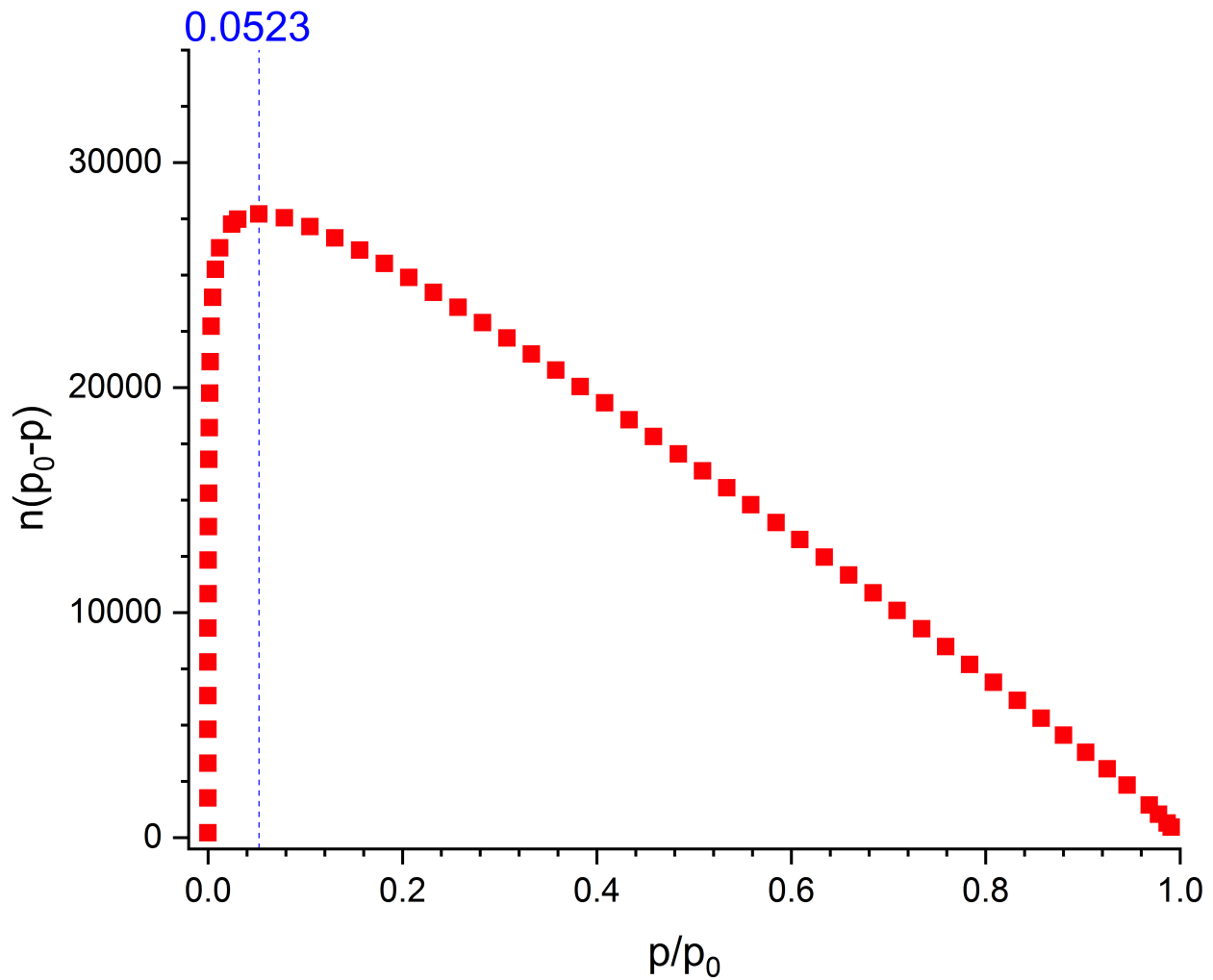
Figure 4.20: The Rouquerol criteria was used to define the linear range for the N_2 measurement at 77K prior to the BET-analysis. The *red* point represents the experimental data, whilst the *blue* line indicates the final point where $v/(1 - p/p_0)$ is increasing monotonically with p/p_0. The upper limit for p/p_0 was found to be 0.0523.

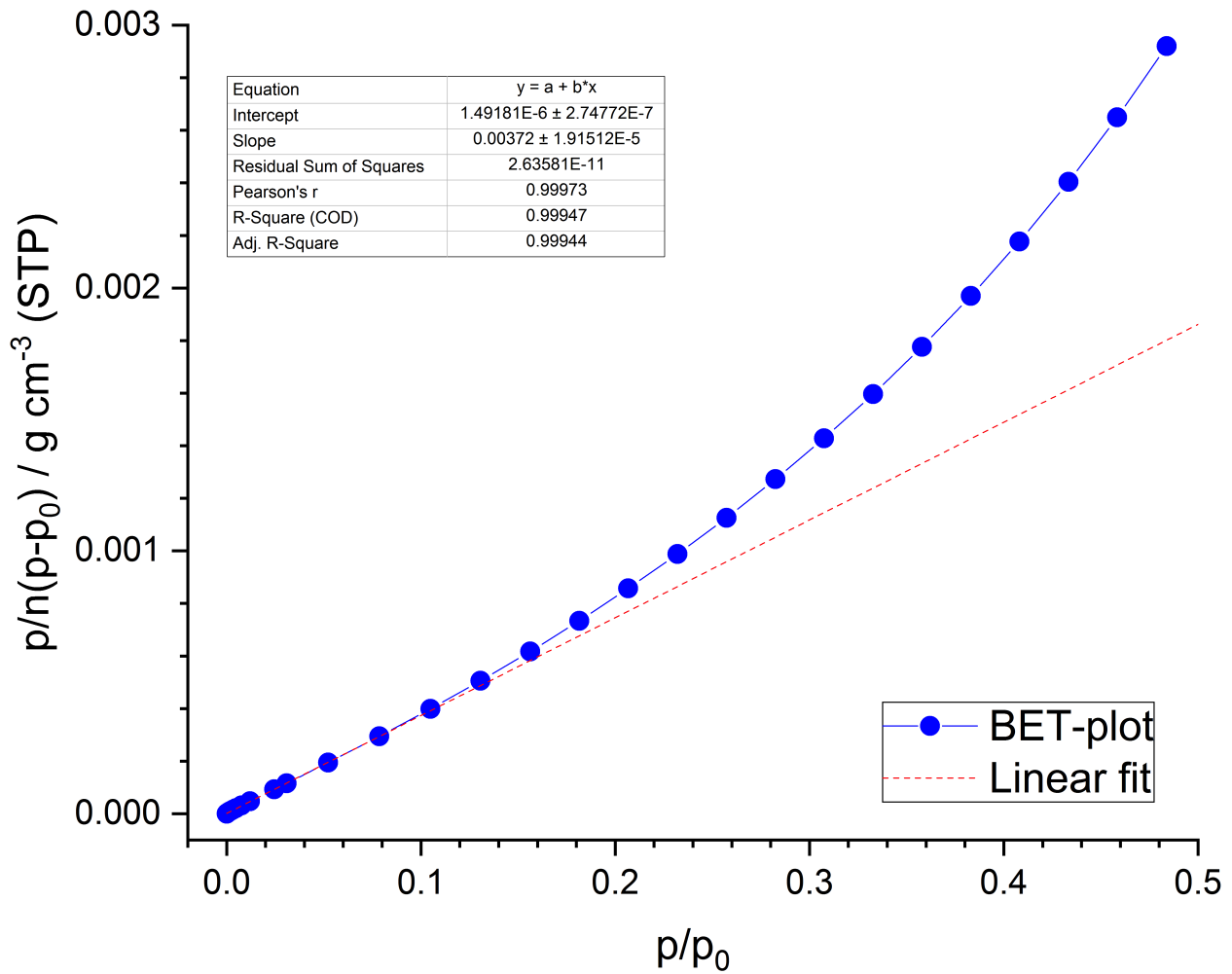| Equation	y = a + b*x
Intercept	1.49181E-6 ± 2.74772E-7
Slope	0.00372 ± 1.91512E-5
Residual Sum of Squares	2.63581E-11
Pearson's r	0.99973
R-Square (COD)	0.99947
Adj. R-Square	0.99944

Figure 4.21: The BET-plot used in the BET analysis of the N_2 at 77K (low pressure) measurement on CPO-54-Ni . The linear regression (represented as the dashed red line) was performed on the data *(blue)* in its linear region, as defined by the Rouquerol criteria.
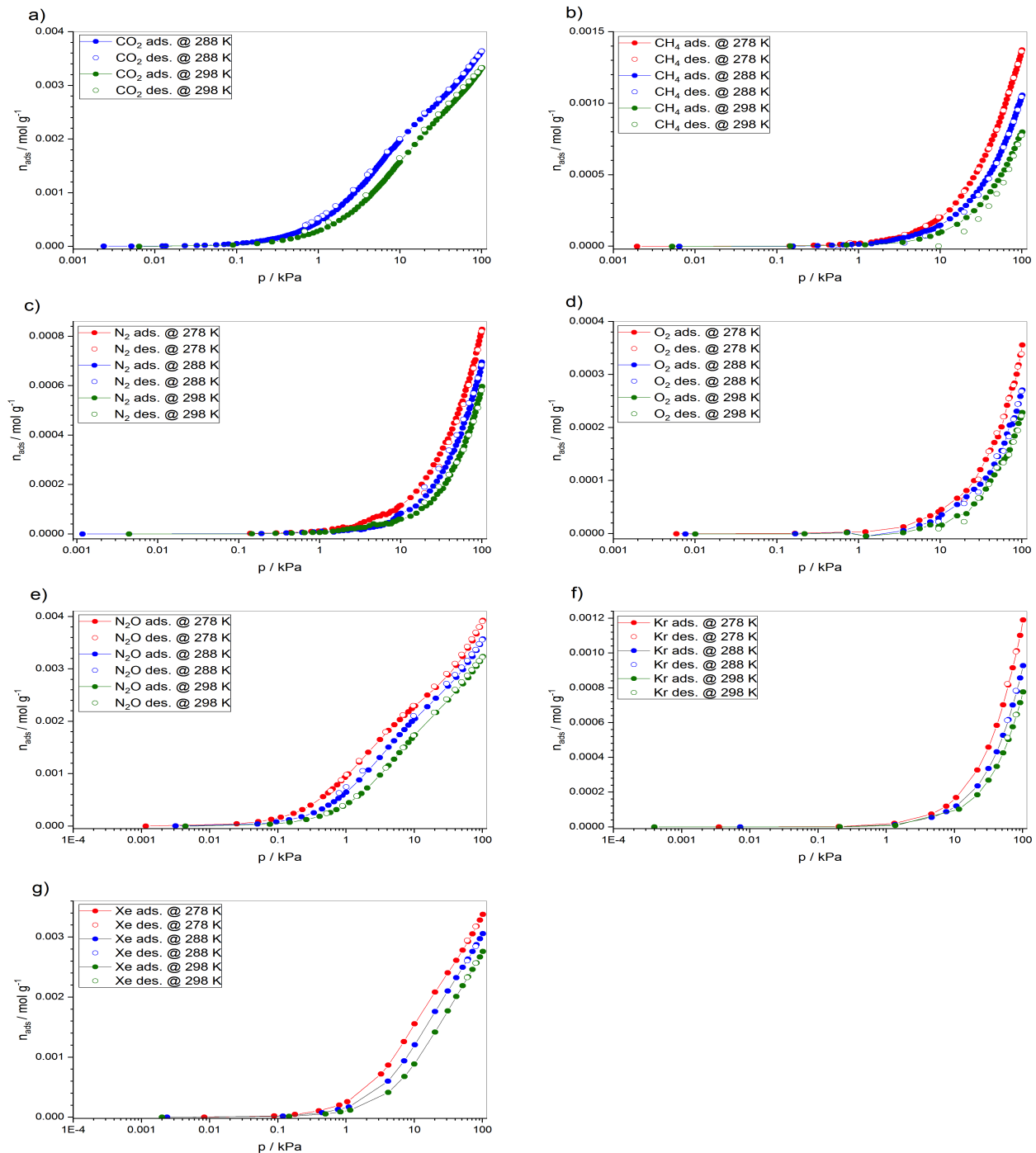
Figure 4.22: Isotherms measured on CPO-54-Co at three different temperatures. A water bath was used to keep the materials at a constant temperature whilst measured. The samples were pre-heated under dynamic vacuum at 388K for 8 hours prior to the measurement. **a)** CO_2, **b)** CH_4, **c)** N_2, **d)** O_2, **e)** N_2O, **f)** Kr and **g)** Xe. The **red** data points represent the 278 K isotherms, the **blue** data points represent the 288 K isotherm, and the **green** data points represents the 298 K isotherms. The lines are meant only as a *guide for the eye*.

Figure 4.23: Isotherms for CPO-54-Co plotted as the number of molecules adsorbate per mol adsorbent on a semi-logarithmic scale. **a)** N_2O isotherms. **b)** Xe isotherms. **c)** Kr isotherms. The **red** data points represent the 278 K isotherms, the **blue** data points represent the 288 K isotherms, and the **green** data points represent the 298 K isotherms. The lines are meant only as a *guide for the eye.*
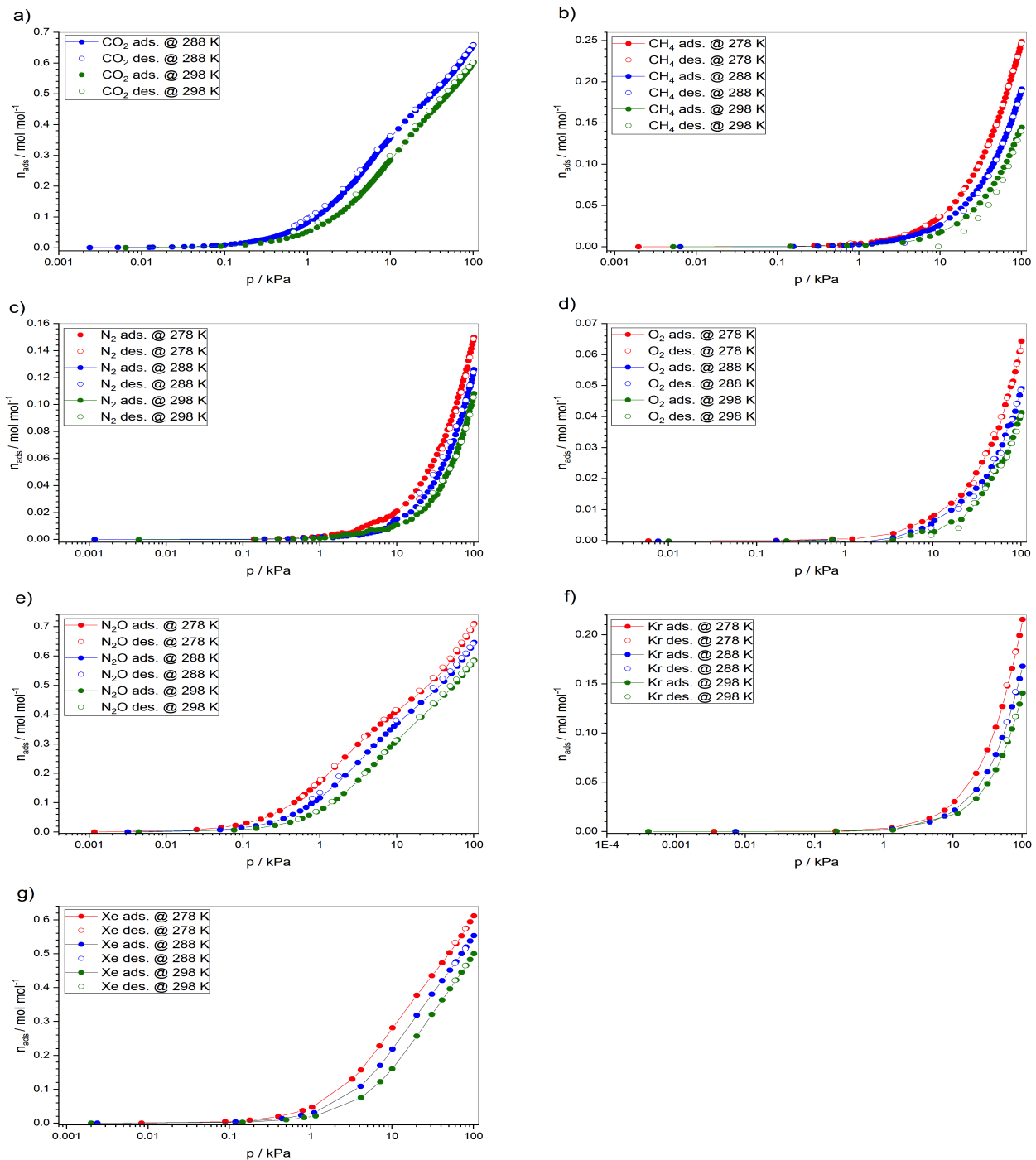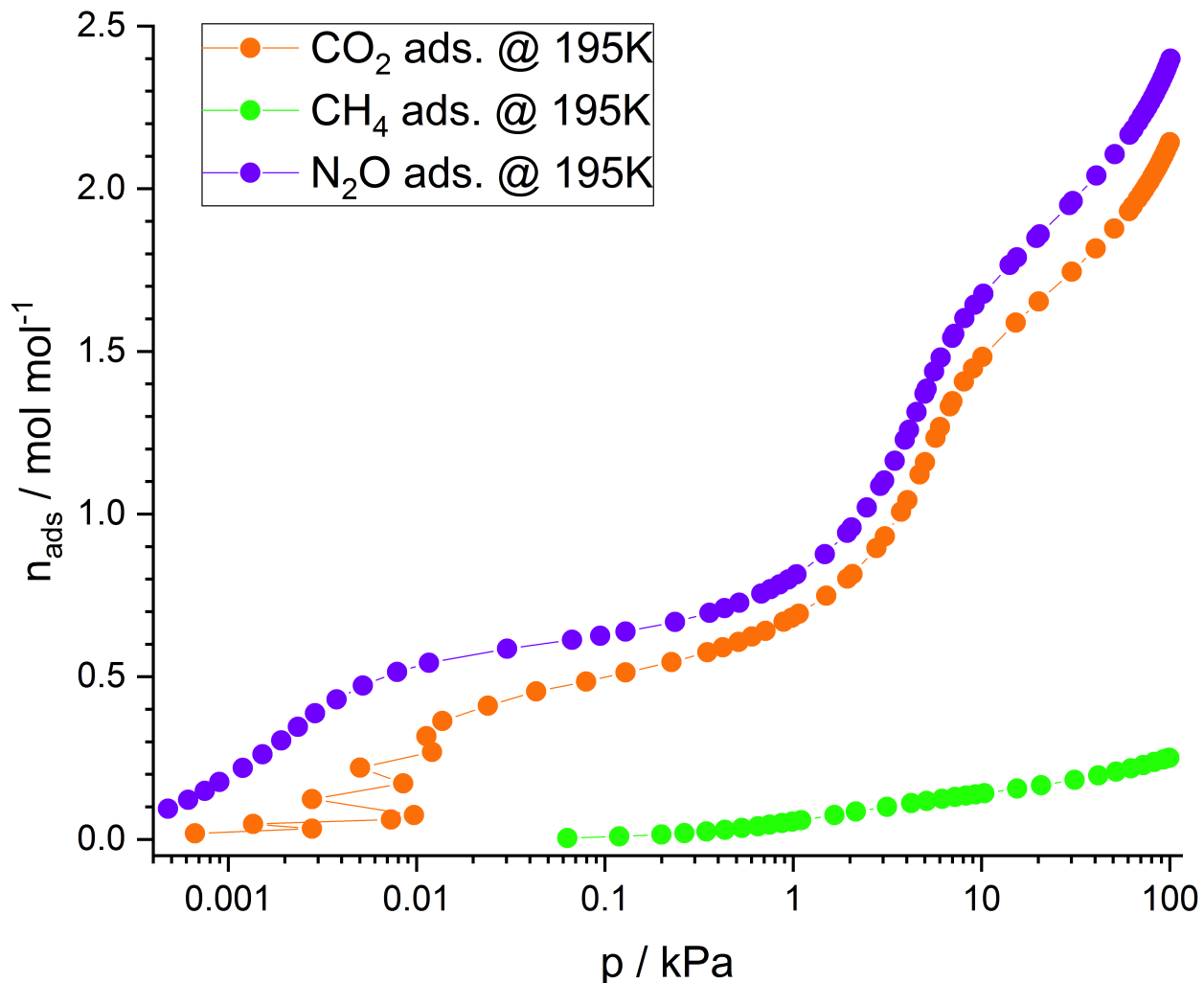
Figure 4.24: Isotherms for CPO-54-Co plotted as the number of molecules adsorbent per mol adsorbate on a semi-logarithmic scale. **a)** CO_2 isotherms, **b)** CH_4 isotherms, **c)** N_2 isotherms, **d)** O_2 isotherms. A slush of dry ice and ethanol was used to cool the samples during the measurement. The line between the data points is meant only as a *guide for the eye*.

4.3.4 CPO-54-Mn

The CPO-54-Mn material was measured both at high-pressure and standard-pressure. Very unfortunately, the measurements were forced to stop, due to instrumentation failure shortly after they had started. The high-pressure measurements were continued after the broken vents on the BELSORP-HP instrument had been replaced. The sample had, by that time, been stored in the instruments sample holder, under a N_2 atmosphere, for approximately three and a half

months. The three isotherms that were measured at 77K are presented in Figure 4.25.
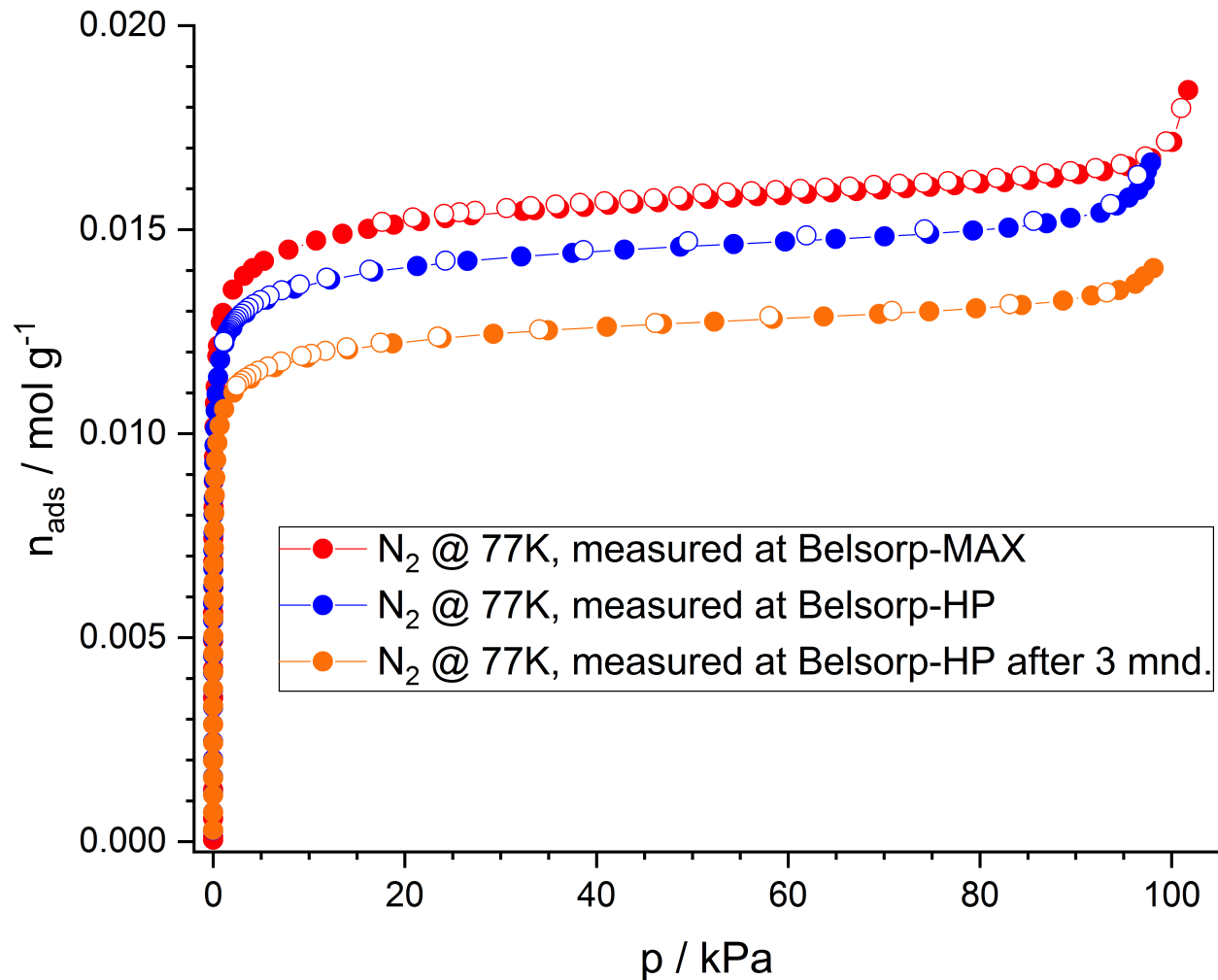
Figure 4.25: Isotherms measured at 77K for CPO-54-Mn. **Red:** shows the very first measurement of the sample, collected at a BELSORP-MAX instrument. **Blue:** shows the first measurement on the high-pressure instrument, BELSORP-HP. **Orange:** shows the isotherm that was measured three months after the other two, after the BELSORP-HP had been repaired.

A BET-analysis was performed on all of the three isotherms to find their pore volume and surface area. The Rouquerol criteria was used to define the linear ranges (Figure 4.26). The BET-plots are presented in Figure 4.27, whilst the pore volumes and surface areas are displayed in Table 4.6.
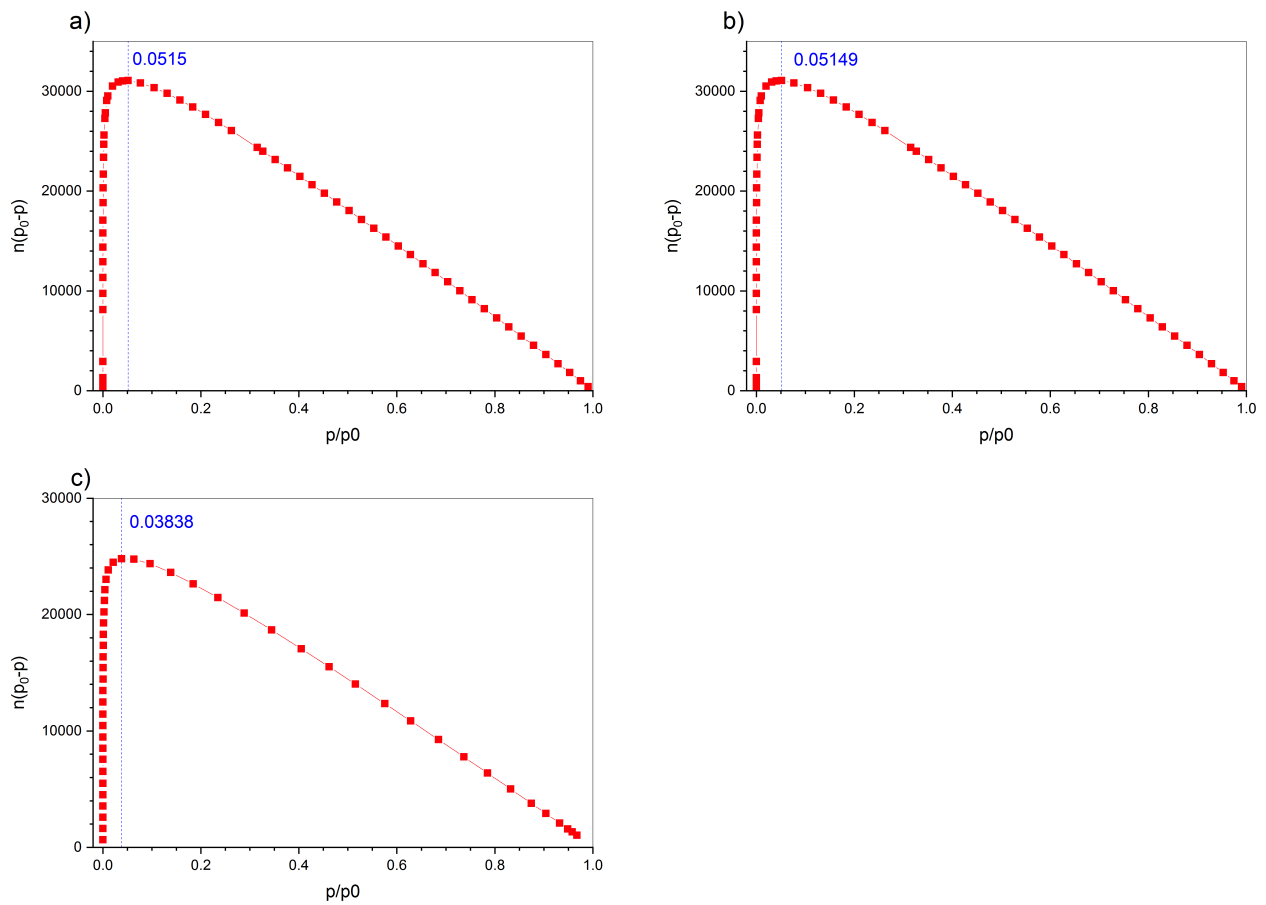
Figure 4.26: Linear ranges defined by the Rouquerol criteria for CPO-54-Mn. **a):** ES-1-041-20190211 (BELSORP-MAX). **a):** ES-1-041-20190306 (BELSORP-HP). **a):** ES-1-041-20190620 (BELSORP-HP).

a)

b)

c)
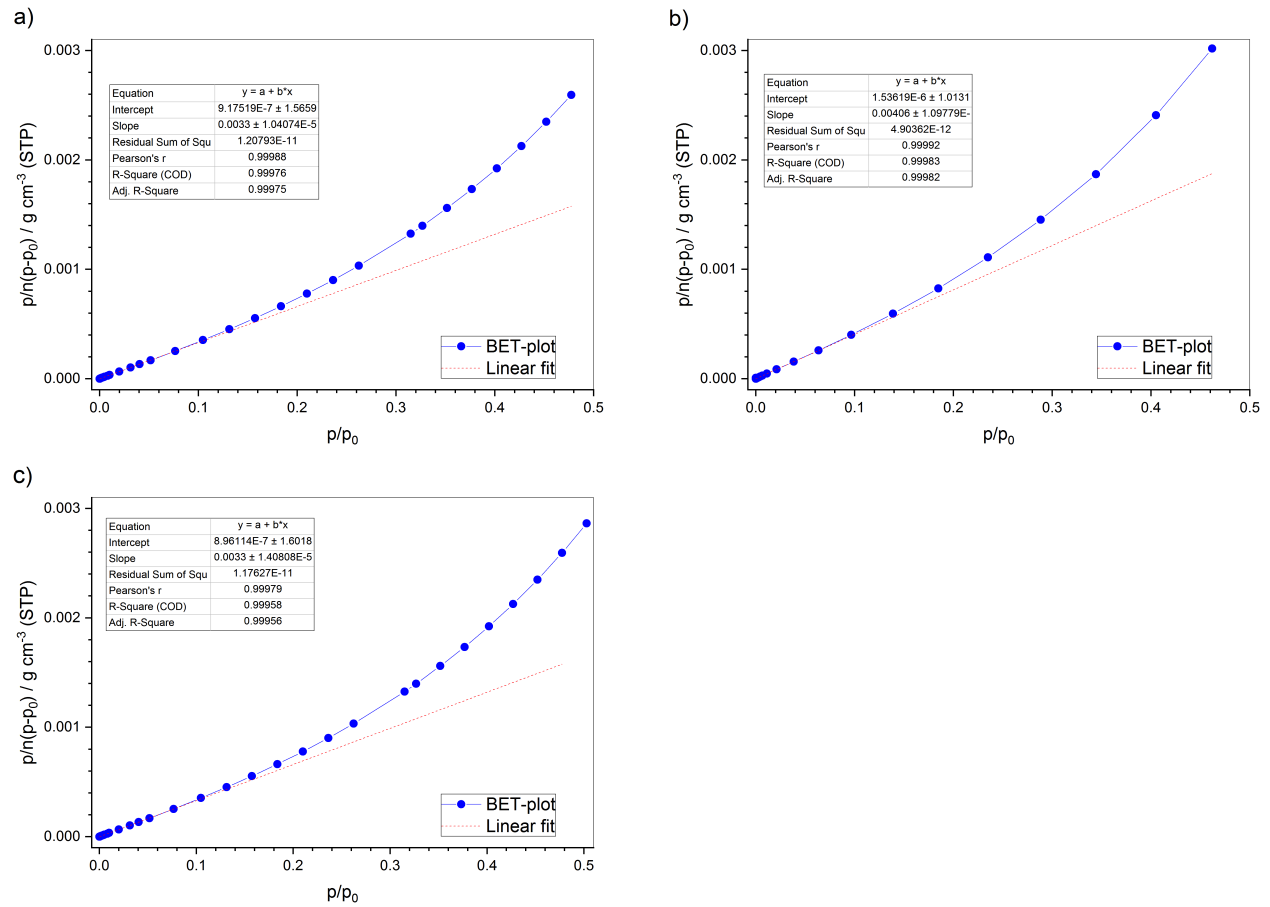
Figure 4.27: BET-plots for CPO-54-Mn. **a):** ES-1-041-20190211 (BELSORP-MAX). **b):** ES-1-041-20190306 (BELSORP-HP). **c):** ES-1-041-20190620 (BELSORP-HP).

Table 4.6: Overview of the pore volumes and surface areas from the different N_2 measurements at 77K for CPO-54-Mn.

Experiment-ID	Pore volume / $m^3 g^{-1}$	BET-area / $m^2 g^{-1}$	Langmuir area / $m^2 g^{-1}$
ES-1-041-20190211 BELSORP-MAX	0.5459	1354.4	1402.3
ES-1-041-20190306 BELSORP-HP	0.5063	1323.6	1352.4
ES-1-041-20190620 BELSORP-HP	0.4413	1081.7	1208.0

Figure 4.25 and Table 4.6 clearly shows a drop in performance for the material.

A total of two gases was measured for CPO-54-Mn: CO_2 and N_2 (Figure 4.28). The isotherms are presented in a semi-logarithmic plot Figure 4.29 as moles adsorbed gas pr. mol adsorbent.
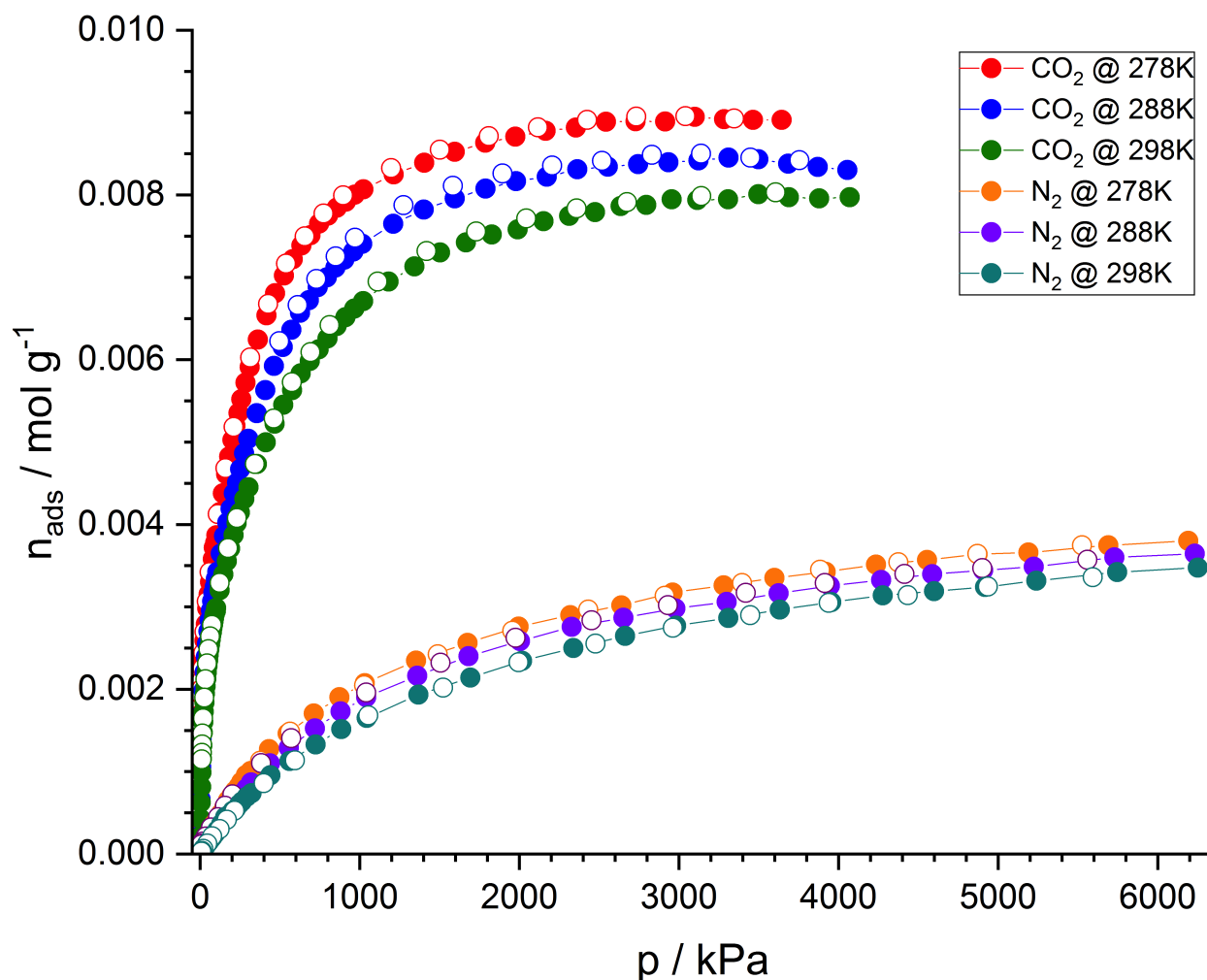
Figure 4.28: Excess adsorption isotherms measured at high-pressure for CPO-54-Mn at three different temperatures. A water bath was used to keep the materials at a constant temperature whilst measured. The sample was pre-heated under dynamic vacuum at 388K for 8 hours prior to the measurement. **Red)** CO_2 at 278 K, **blue)** CO_2 at 288 K, **green)** CO_2 at 298 K, **orange)** N_2 at 278 K, **purple)** N_2 at 288 K, and **dark cyan)** N_2 at 298 K. The lines are meant only as a *guide for the eye.*
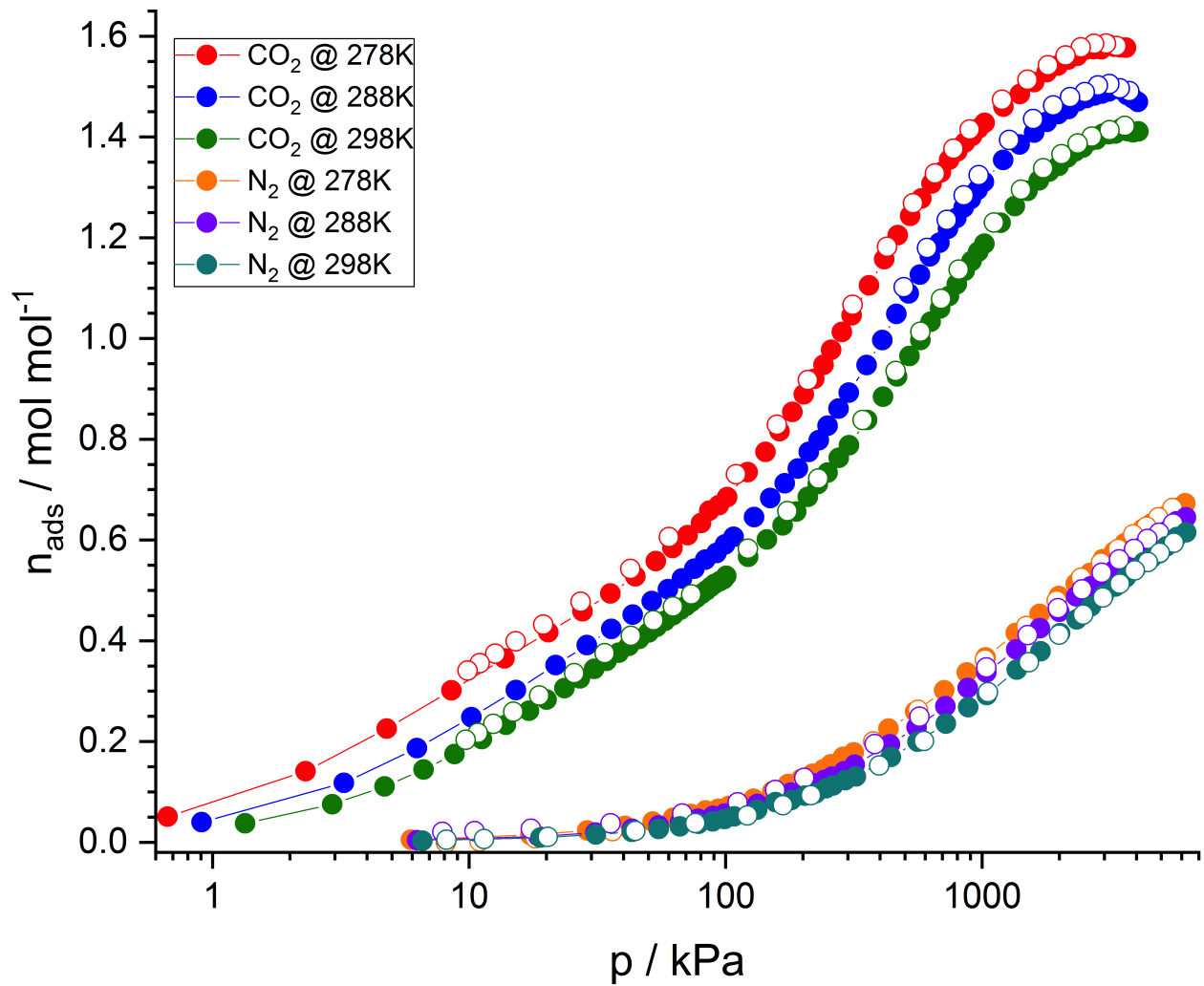
Figure 4.29: Gas uptake of CO_2 and N_2 in CPO-54-Mn presented as moles adsorbed pr. mole adsorbent (excess adsorption). **Red)** CO_2 at 278 K. **Blue)** CO_2 at 288 K. **Green)** CO_2 at 298 K. **Orange)** N_2 at 278 K. **Purple)** N_2 at 288 K. **Dark cyan)** N_2 at 298 K. The lines are meant only as a *guide for the eye.*

4.4 Isosteric Heat of Adsorption

A dual-site Langmuir model (Equation 2.14) was fitted to all the experimental isotherms for CPO-54-Mg, CPO-54-Ni and CPO-54-Co, CPO-54-Mn. A MATLAB code was written in order to calculate the Q_{st} from the dual-site Langmuir fit-parameters . The MATLAB code is included as Appendix A and the DSL fits are presented in Appendix C.

As mentioned in Section 2.4.3, a small error in the isotherm fit can give large errors in the calculated Q_{st}. Therefore, the heat of adsorption was calculated by means of two additional methods: an *akimia interpolation method* and a *virial-type method*. The interpolation method was performed by the software provided by Belsorp (*BELMASTER*). For the virial method, the model from Equation 2.17 was fitted to the experimental isotherms. The resulting fit-parameters were used in the MATLAB code, together with Equation 2.18, to calculate the heats of adsorption. The MATLAB code is included as Appendix B and the virial equation fit-parameters as Appendix E.

4.4.1 CPO-54-Mg

The heat of adsorption for CPO-54-Mg was calculated using three different methods. The resulting Q_{st} from the dual-site Langmuir method are presented in Figure 4.30, whilst the results of all the three methods are compared in Figure 4.31.

Figure 4.30: Isosteric heat of adsorption for CPO-54-Mg. **Red:** CO_2, **blue:** CH_4, **green:** N_2, **orange:** O_2, **violet:** N_2O, **cyan:** Xe, **magenta:** Kr in CPO-54-Mg. The values were calculated by fitting a dual-site Langmuir model to the experimental isotherms and applying the Clausius-Clapeyron equation.
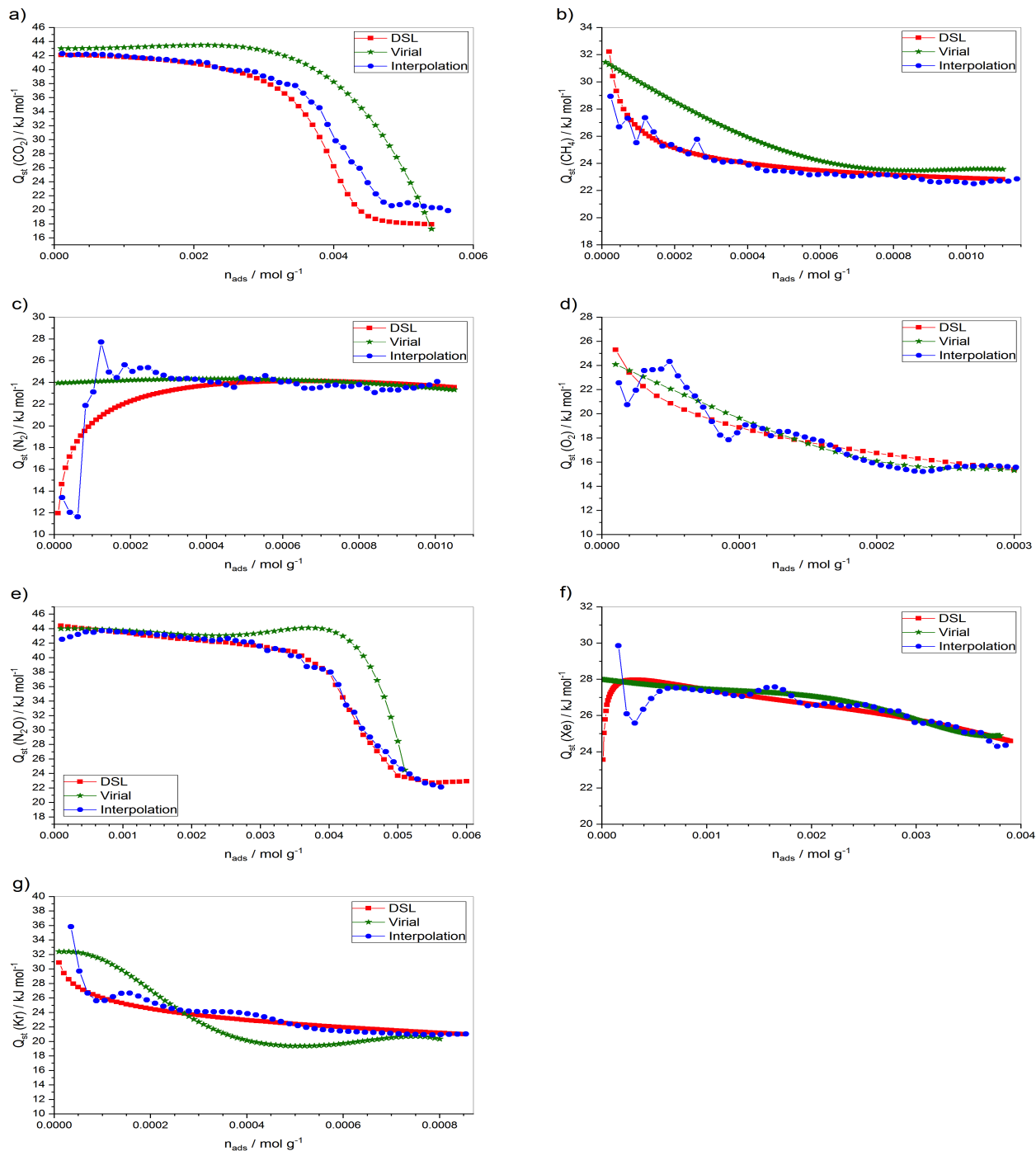
Figure 4.31: Comparison of the isosteric heat of adsorption for CPO-54-Mg. **(a)** CO_2, **(b)** CH_4, **(c)** N_2, **(d)** O_2, **(e)** N_2O, **(f)** Xe, and **(g)** Kr, calculated using three different methods to describe the isotherms: DSL-fit **(red)**, virial equation **(green)** and spline interpolation **(blue)**.

Some deviations between the three methods can be observed in both Figure 4.30 and Figure 4.31.

4.4.2   CPO-54-Ni

For both the high- and low-pressure isotherms the Q_{st} was calculated using three methods. The heat of adsorption was calculated by the dual-site Langmuir model and the Clausius-Clapeyron equation for the standard- pressure and the high-pressure measurements (Figure 4.36 and Figure 4.33, respectively).
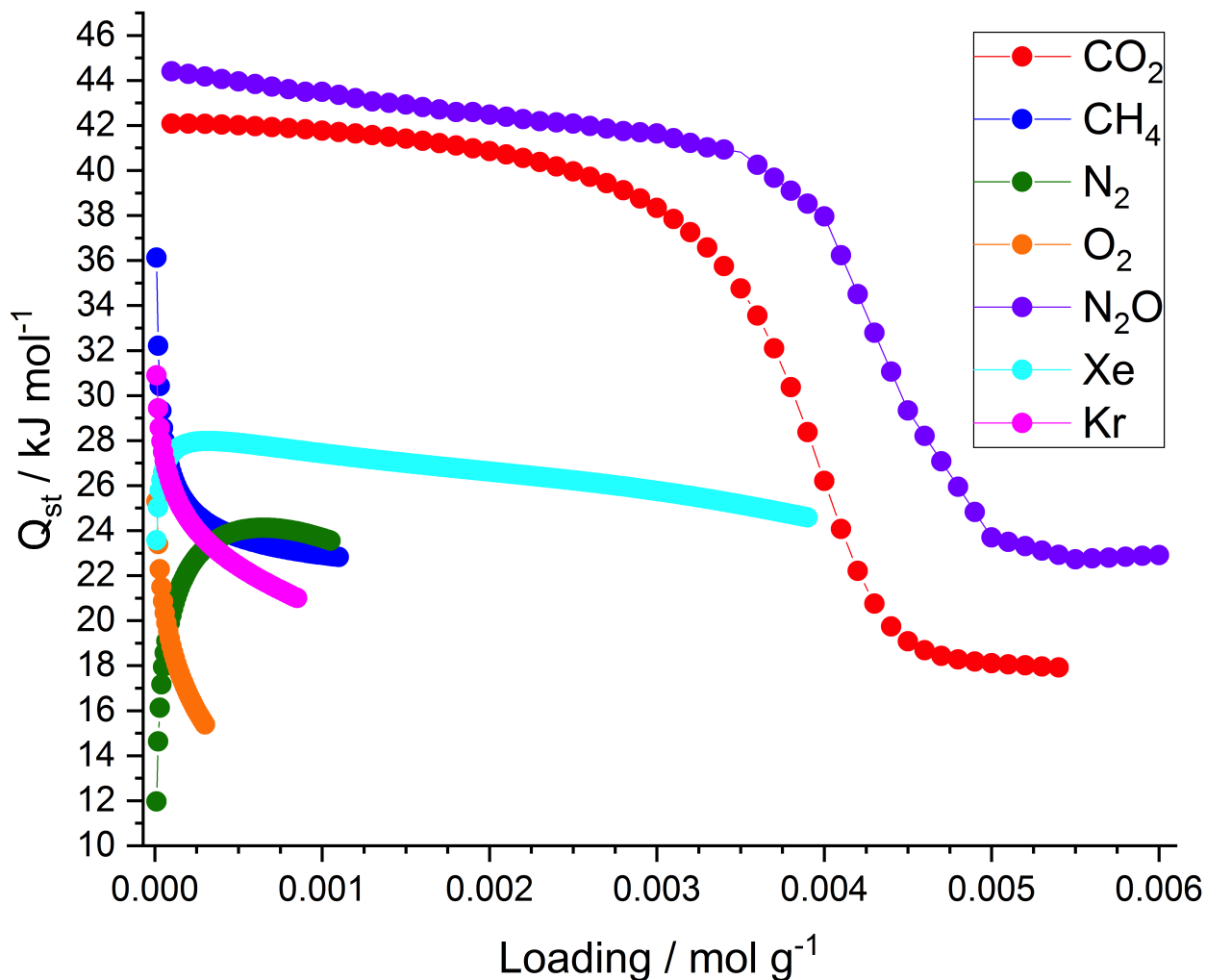
Figure 4.32: Isosteric heat of adsorption for CPO-54-Ni. **Red**: CO_2, **blue**: CH_4, **green**: N_2, **orange**: O_2, **violet:** N_2O, **cyan:** Xe, **magenta:** Kr. The values were calculated by fitting a dual-site Langmuir model to the experimental standard-pressure isotherms and applying the Clausius-Clapeyron equation.
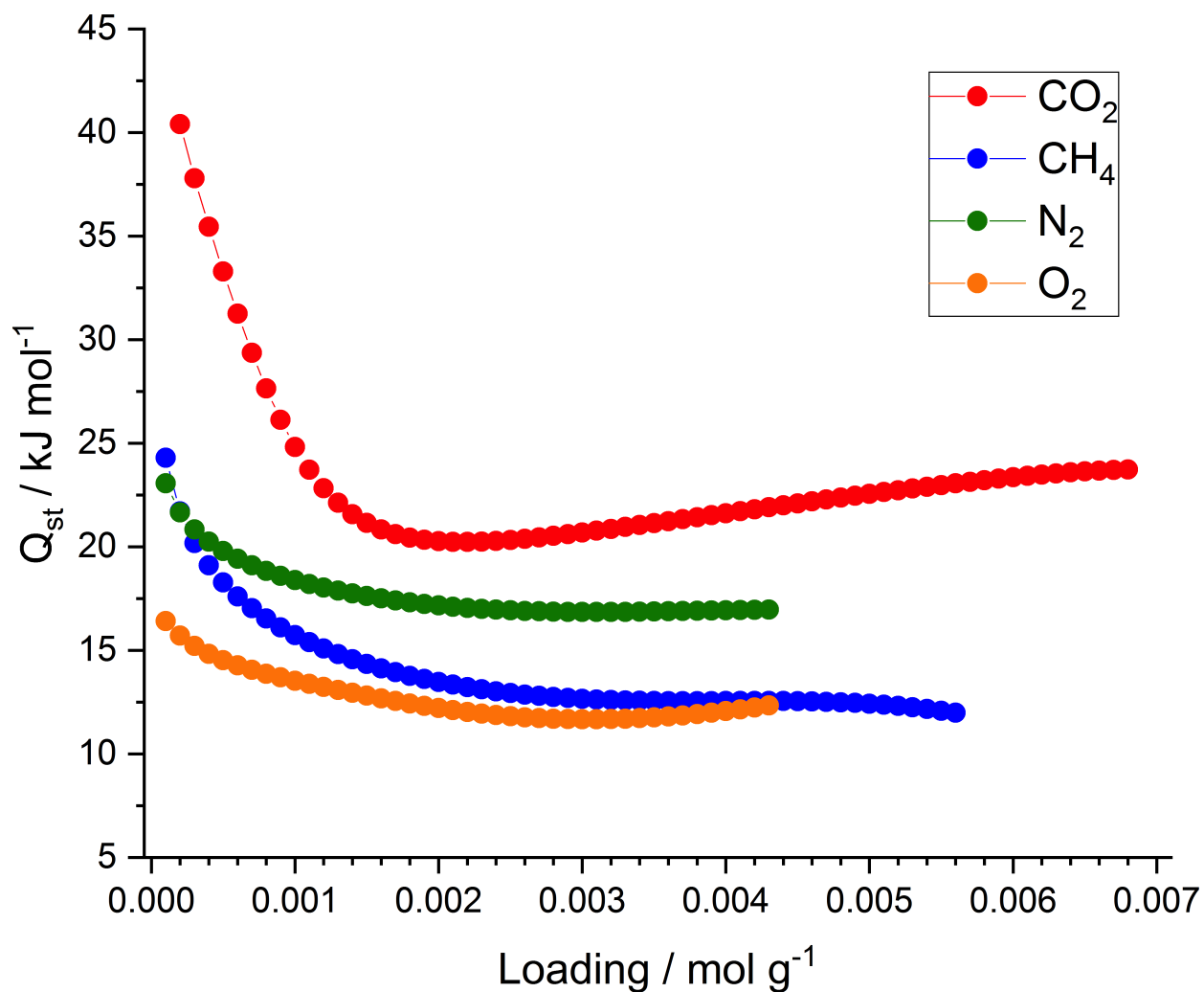
Figure 4.33: Isosteric heat of adsorption for CPO-54-Ni **Red**: CO_2, **blue**: CH_4, **green**: N_2, and **orange**: O_2. The values were calculated by fitting a dual-site Langmuir model to the experimental high-pressure absolute adsorption isotherms and applying the Clausius-Clapeyron equation.

The three methods are compared in Figure 4.35 (standard-pressure) and Figure 4.34. In theory, the high-pressure and low-pressure experiments should result in equal heats of adsorption. However, this is not the case. By comparing the values and trends in Figure 4.32 and 4.33 one can clearly see significant differences. Dual-site Langmuir functions were used to fit to the experimental isotherms.
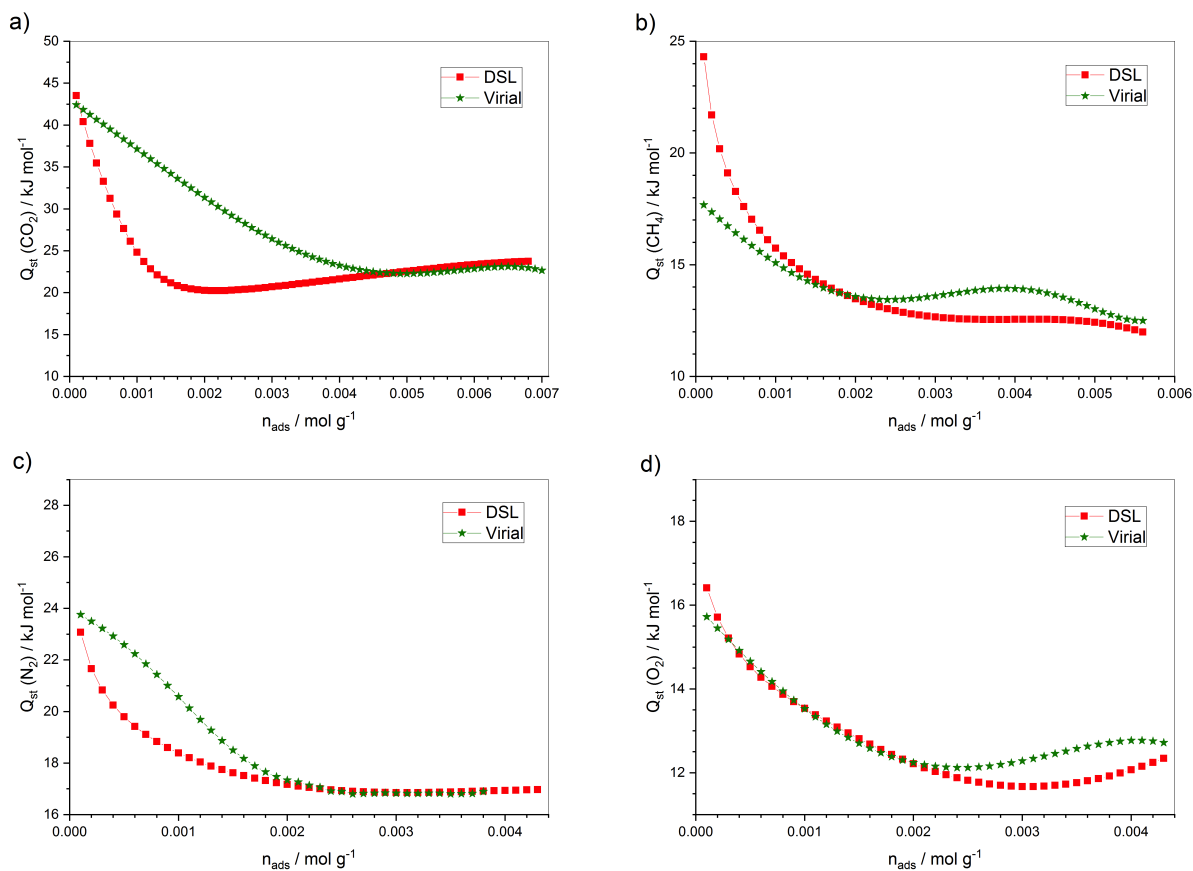
Figure 4.34: Isosteric heats of adsorption for four different gases in CPO-54-Ni: CO_2 **(a)**, CH_4 **(b)**, N_2 **(c)** and O_2 **(d)**. These values have been calculated based on absolute adsorption isotherms from the high-pressure measurements of CPO-54-Ni.
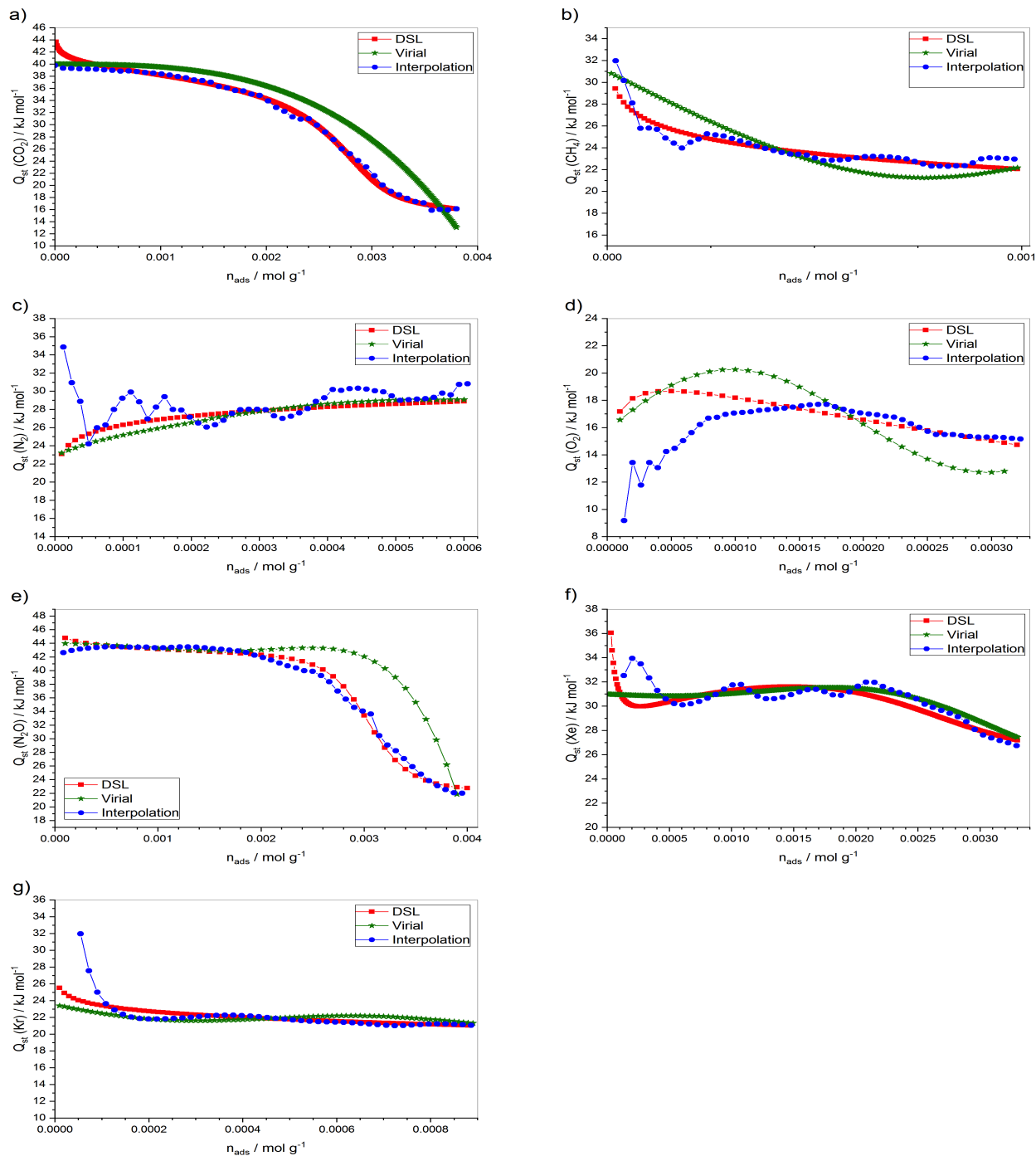
Figure 4.35: Isosteric heats of adsorption for CPO-54-Ni, calculated in three different ways for several gases. **(a)** CO_2, **(b)** CH_4, **(c)** N_2, **(d)** O_2, **(e)** N_2O, **(f)** Xe, and **(g)** Kr. These heats of adsorptions are based on adsorption measurements at standard-pressure.

4.4.3 CPO-54-Co

All three methods were used to calculate the heat of adsorption for CPO-54-Co. The results from the DSL-method are shown in Figure 4.36, and compared to the two other methods in Figure 4.37.
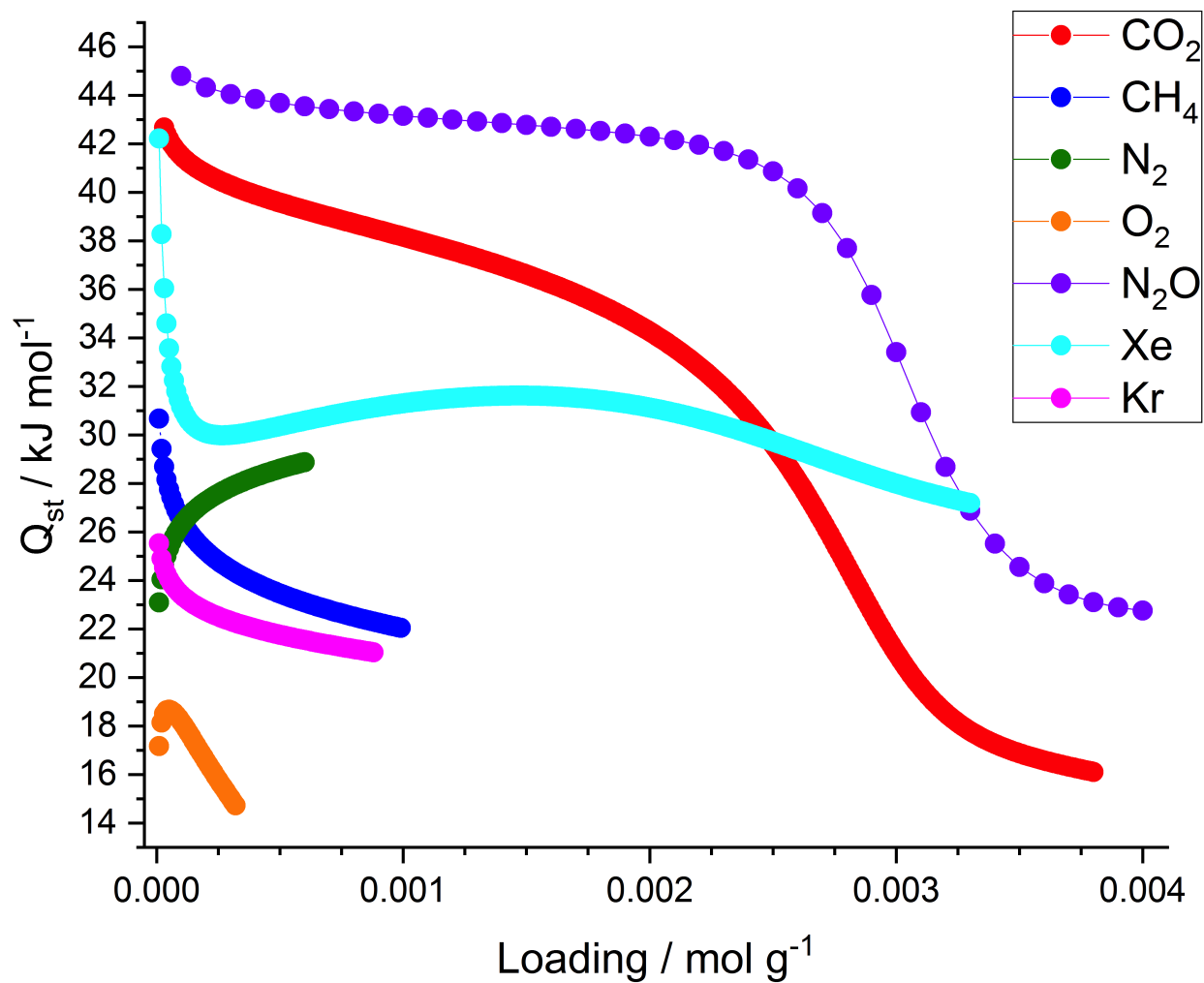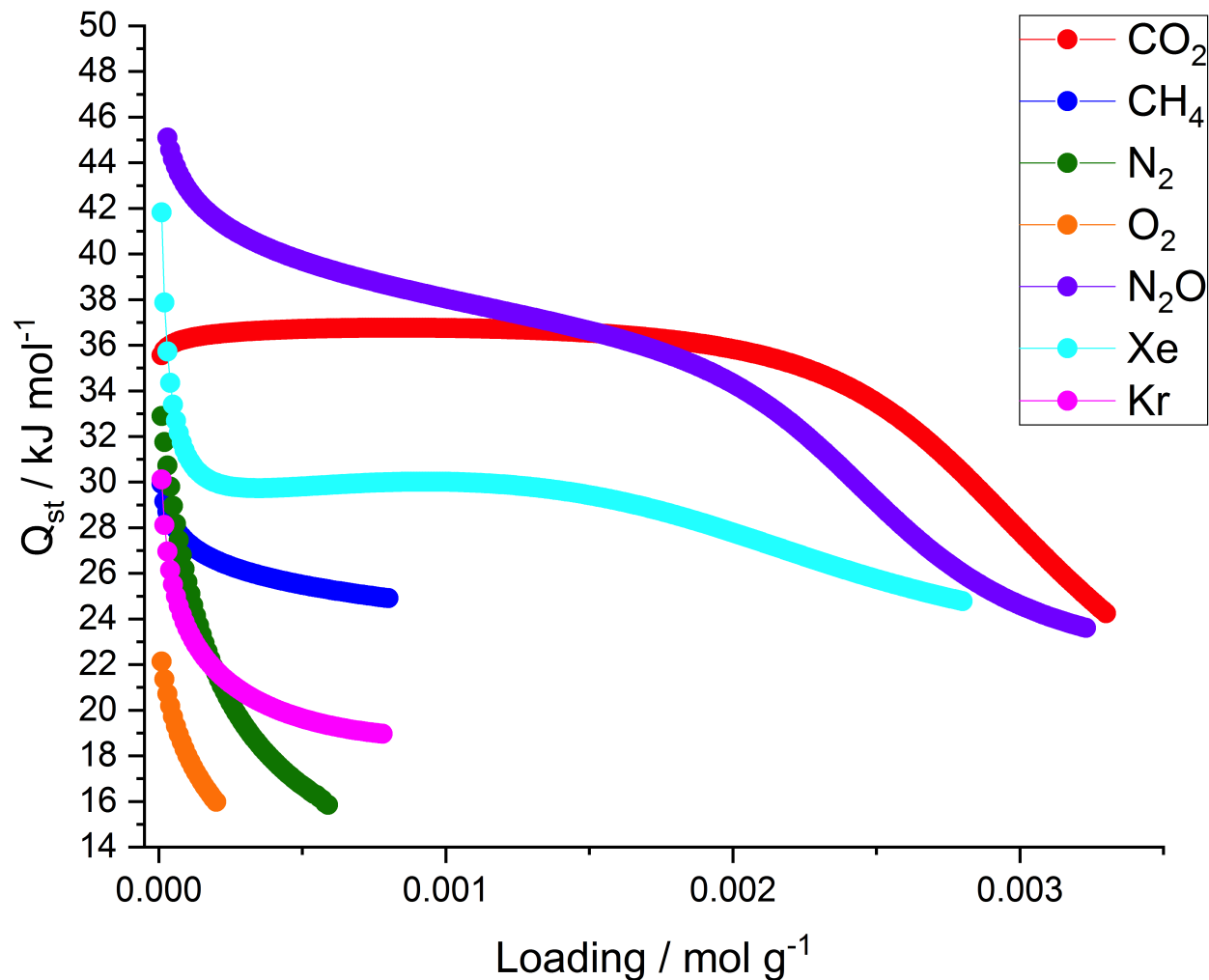

Figure 4.36: Isosteric heat of adsorption for **Red**: CO_2, **Blue**: CH_4, **Green**: N_2, **Orange**: O_2, **violet:** N_2O, **cyan:** Xe, **magenta:** Kr in CPO-54-Co. The values were calculated by fitting a dual-site Langmuir model to the experimental isotherms and applying the Clausius-Clapeyron equation.

Again, there are some deviations between the results that the three methods produce. The virial method for N_2 deviates quite a lot from the two others, whilst the results from the virial and interpolation methods are fluctuating around the results of the DSL method for O_2.
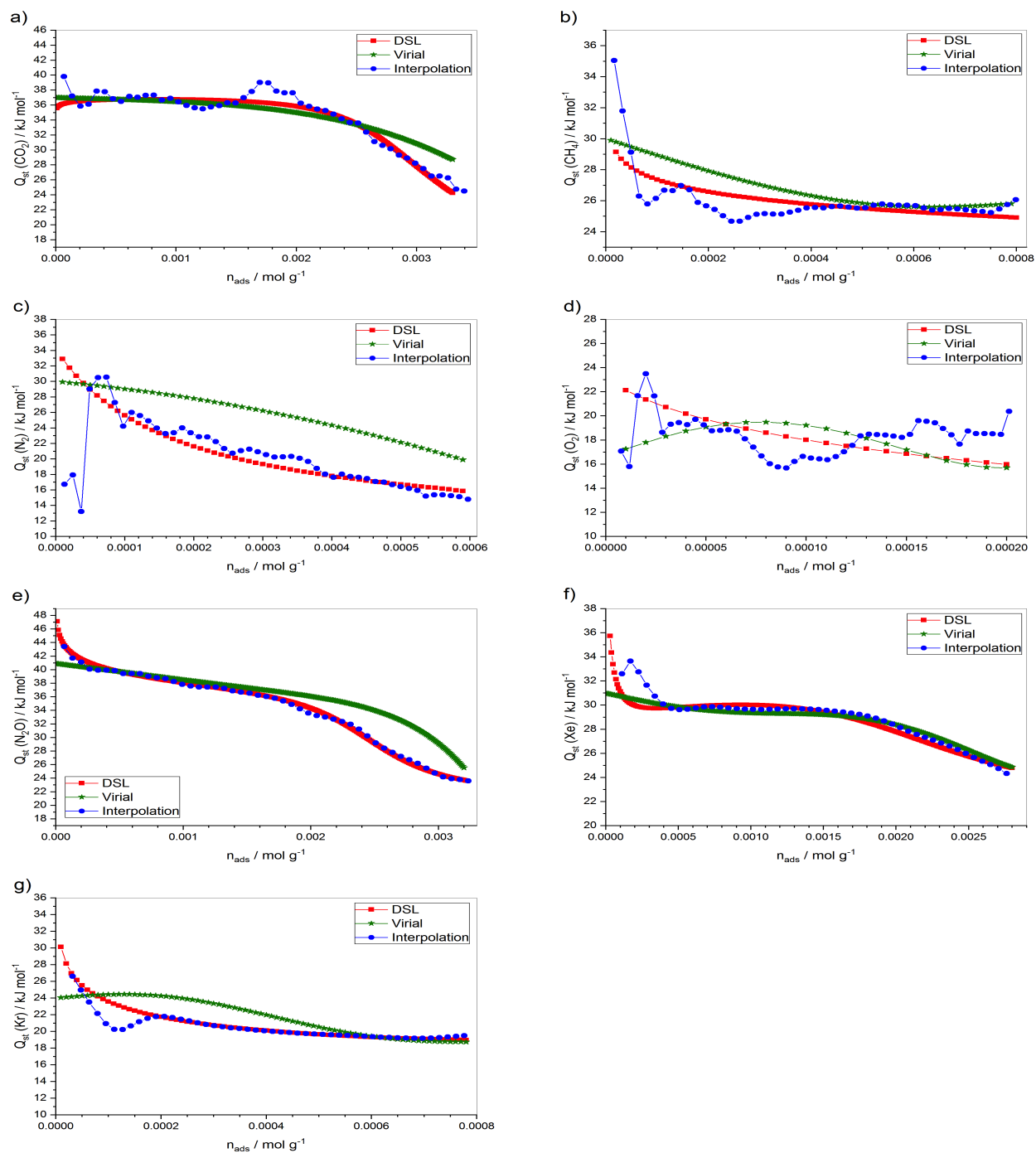
Figure 4.37: Comparison of the isosteric heat of adsorption in CPO-54-Co, using three different methods to describe the isotherms: DSL-fit **(red)**, virial equation **(green)** and spline interpolation **(blue)**, for the gasses: **(a)** CO_2, **(b)** CH_4, **(c)** N_2, **(d)** O_2, **(e)** N_2O, **(f)** Xe, and **(g)** Kr.

4.4.4 CPO-54-Mn

The CPO-54-Mn high-pressure adsorption isotherms were used to calculate the isosteric heat of adsorption for CO_2 and N_2 (Figure 4.38). Both a virial equation and a dual-site Langmuir model were used describe the experimental isotherms.
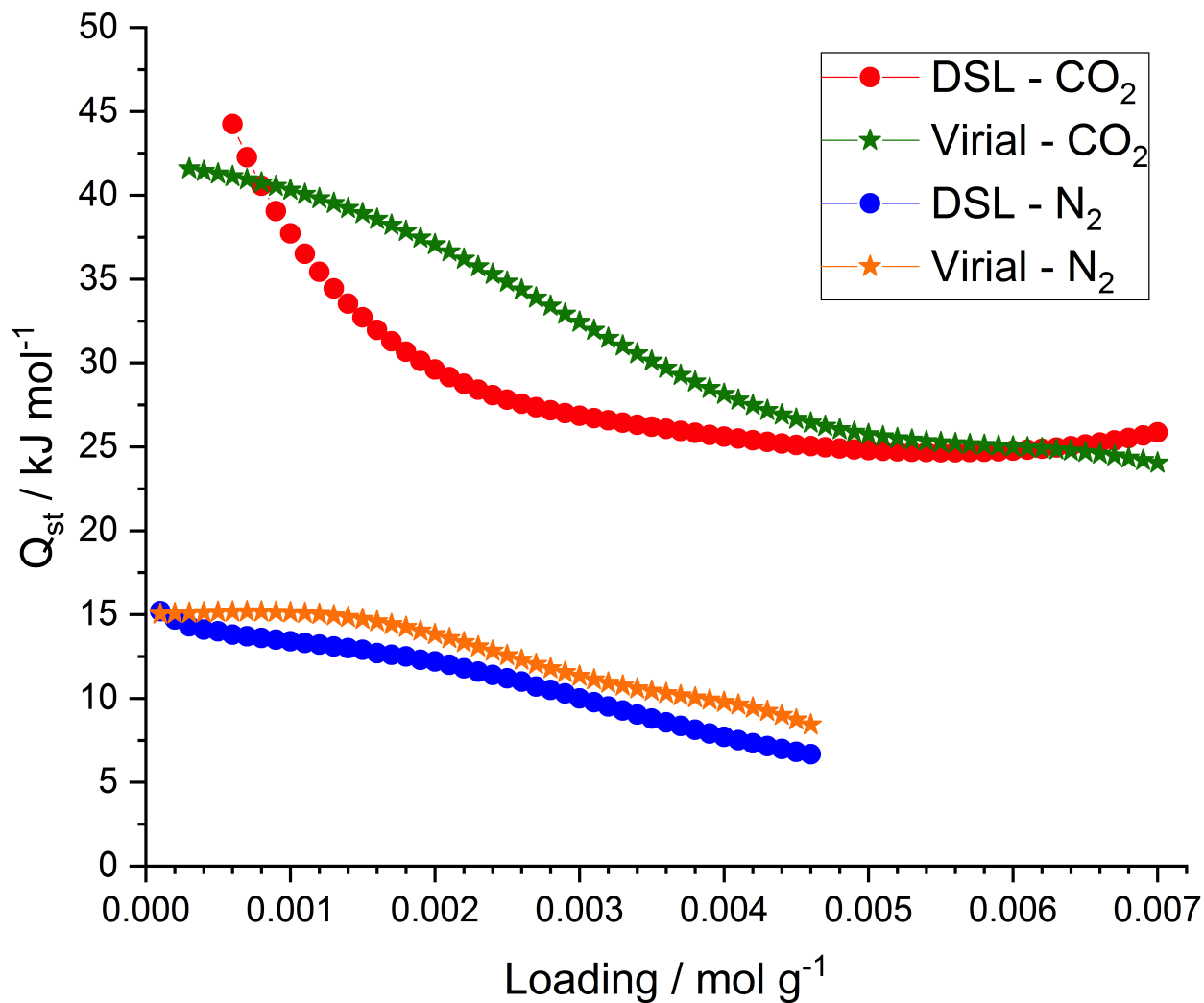
Figure 4.38: The isosteric heat of adsorption for CO_2 andN_2 in CPO-54-Mn. The Q_{st} are calculated from high-pressure absolute adsorption isotherms measured at three different temperatures (278K, 288K and 298K). Two different methods have been used. **Red:** is the Q_{st} for CO_2 where a DSL-fit was used to describe the isotherm. **Green:** Q_{st} for CO_2 where a virial equation was used to calculated it. **Blue:** the Q_{st} for N_2 calculated by use of a DSL model. **Orange:** the Q_{st} for N_2 where a virial equation was used to describe the experimental isotherms.

4.5 Gas Selectivity

A code was written for *Python 3* in order to run the pyIAST package on the experimental isotherms (previously described in Section 2.4.4). The python code is attached as Appendix D. The focus has been on investigating the selectivity of CO_2/N_2, CO_2/CH_4, CO_2/O_2, N_2O/N_2 and Xe/Kr.

4.5.1 CPO-54-Mg

CO_2/N_2 (Figure 4.39), CO_2/CH_4 (Figure 4.40), CO_2/O_2 (Figure 4.41) and Xe/Kr (Figure 4.42) separation were investigated for CPO-54-Mg at 278K, 288K and 298K. A dual-site Langmuir function was used to describe all the experimental isotherms.

Figure 4.39: Separation factors for CO_2/N_2 in a binary gas mixture, computed from single-component isotherms by use of IAST for CPO-54-Mg at three different temperatures; **(a)** 278K, **(b)** 288K, and **(c)** 298K.

Figure 4.40: Separation factors for CO_2/ CH_4 in a binary gas mixture, computed from single-component isotherms by use of IAST for CPO-54-Mg at three different temperatures; **(a)** 195K,**(b)** 278K, **(b)** 288K, and **(d)** 298K.
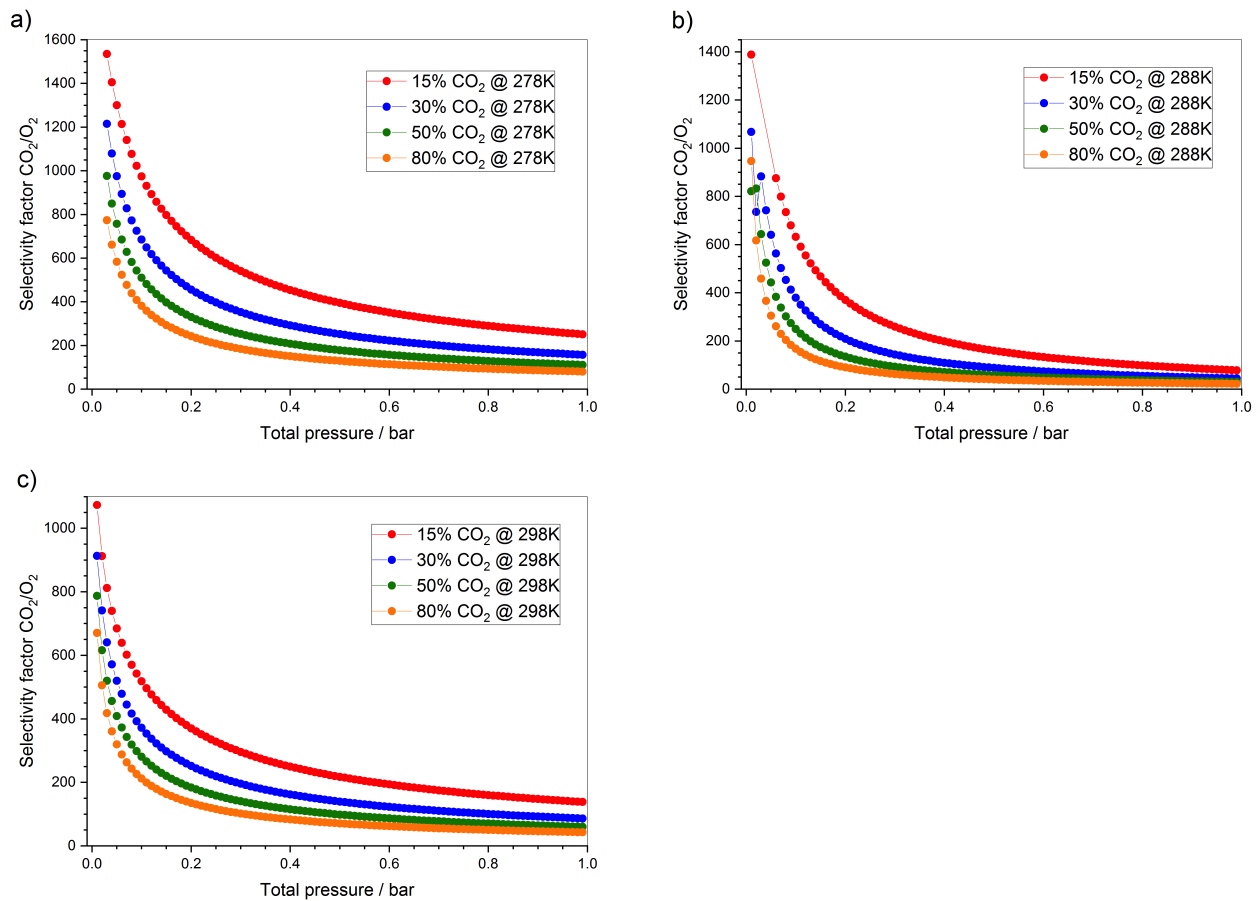
Figure 4.41: Separation factors for CO_2/O_2 in a binary gas mixture, computed from single-component isotherms by use of IAST for CPO-54-Mg at three different temperatures; **(a)** 278K, **(b)** 288K, and **(c)**: 298K.

Figure 4.42: Separation factors for Xe/Kr in a binary gas mixture, computed from single-component isotherms by use of IAST for CPO-54-Mg at three different temperatures; **(a)** 278K, **(b)** 288K, and **(c)** 298K.

Figure 4.43: Separation factors for N_2O/N_2 in a binary gas mixture, computed from single-component isotherms by use of IAST for CPO-54-Mg at three different temperatures; **(a)** 278K, **(b)** 288K, and **(c)** 298K.

4.5.2 CPO-54-Ni

For CPO-54-Ni, selectivity coefficients were calculated using both the high-pressure and standard-pressure experimental data. A dual-site Langmuir function was used in both cases to fit to the adsorption isotherms. Selectivity was calculated for CO_2/N_2 (Figure 4.44), CO_2/CH_4 (Figure 4.45), CO_2/O_2 (Figure 4.46) and Xe/Kr (Figure 4.47) using data from the standard-pressure experiments. Selectivity for CO_2/N_2 (Figure 4.49), CO_2/CH_4 (Figure 4.50), CO_2/O_2 (Figure 4.51) was also calculated based on the high-pressure data.

Figure 4.44: Separation factors for CO_2/N_2 in a binary gas mixture, computed from the single-component isotherms by use of IAST for CPO-54-Ni at three different temperatures; **(a)** 278K, **(b)** 288K, and **(c)** 298K.

Figure 4.45: Separation factors for CO_2/CH_4 in a binary gas mixture, computed from the single-component isotherms by use of IAST for CPO-54-Ni at three different temperatures; **(a)** 278K, **(b)** 288K, and **(c)** 298K.
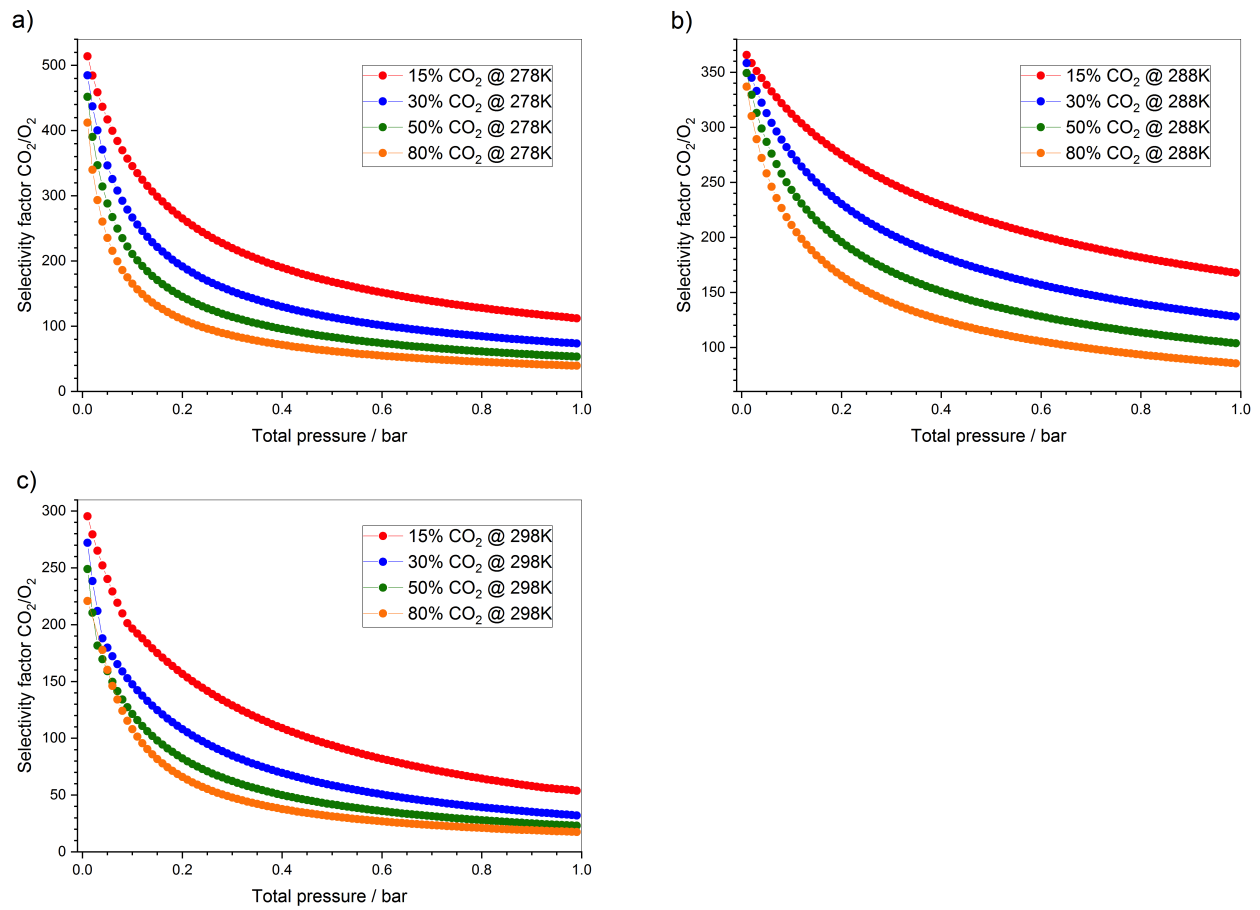
Figure 4.46: Separation factors for CO_2/O_2 in a binary gas mixture, computed from the single-component isotherms by use of IAST for CPO-54-Ni at three different temperatures; **(a)** 278K, **(b)** 288K, and **(c)** 298K.
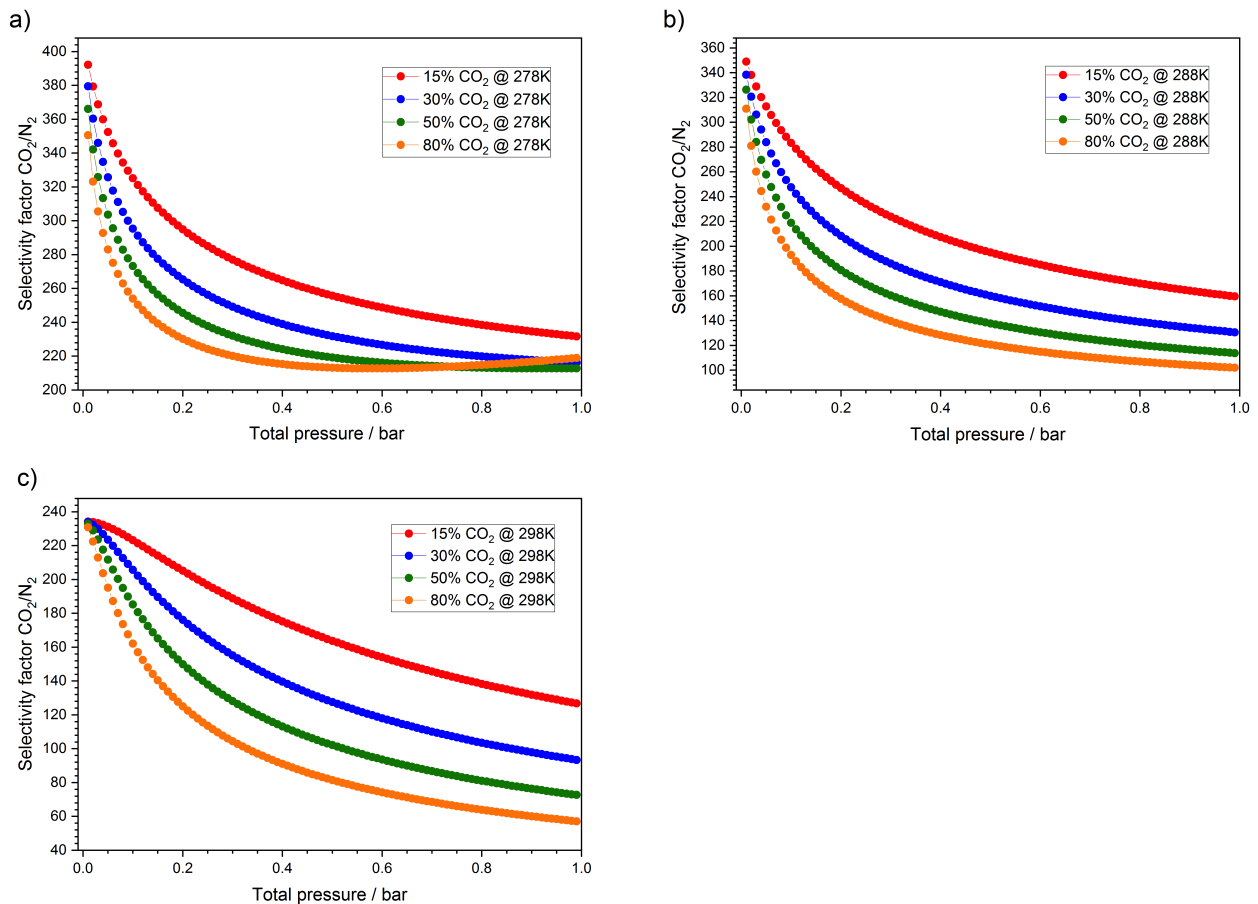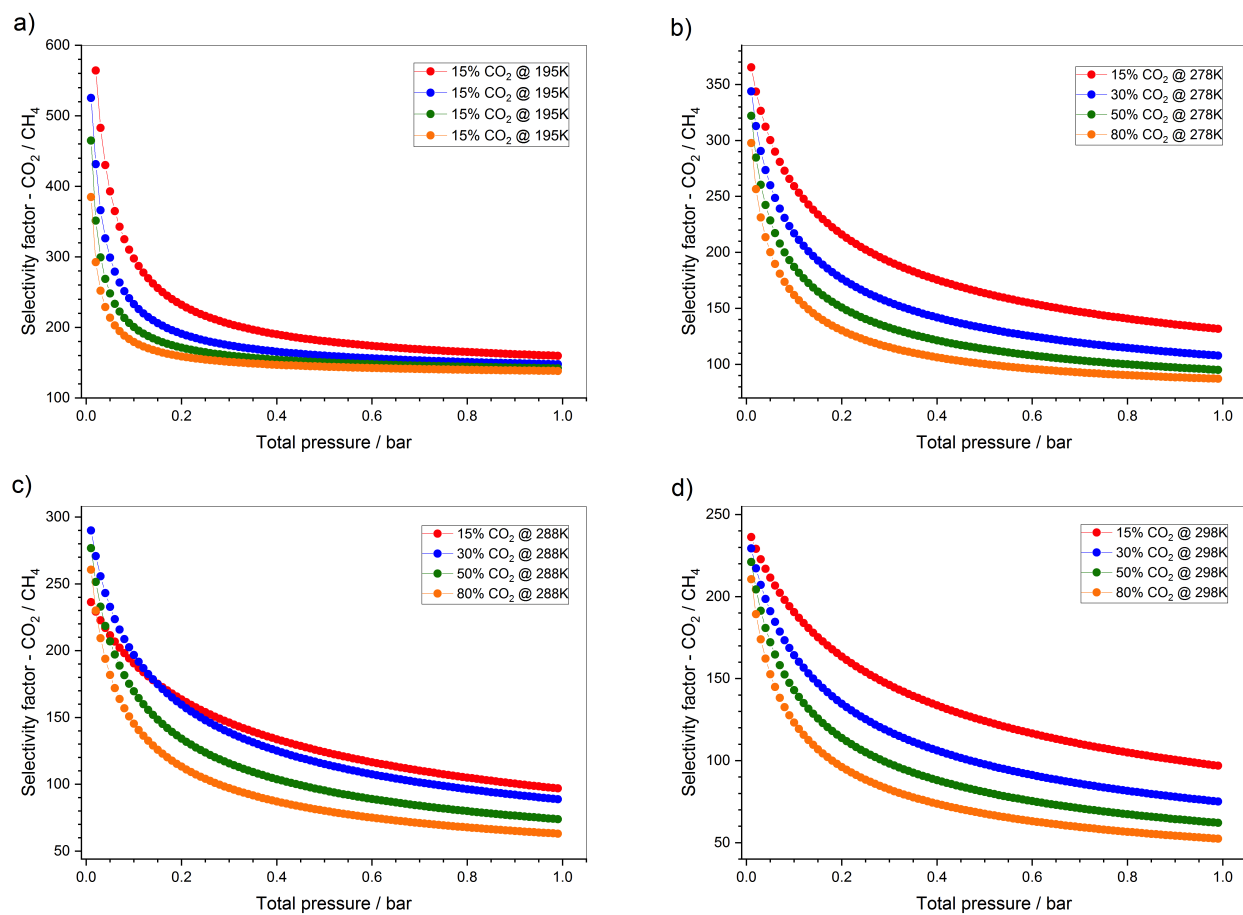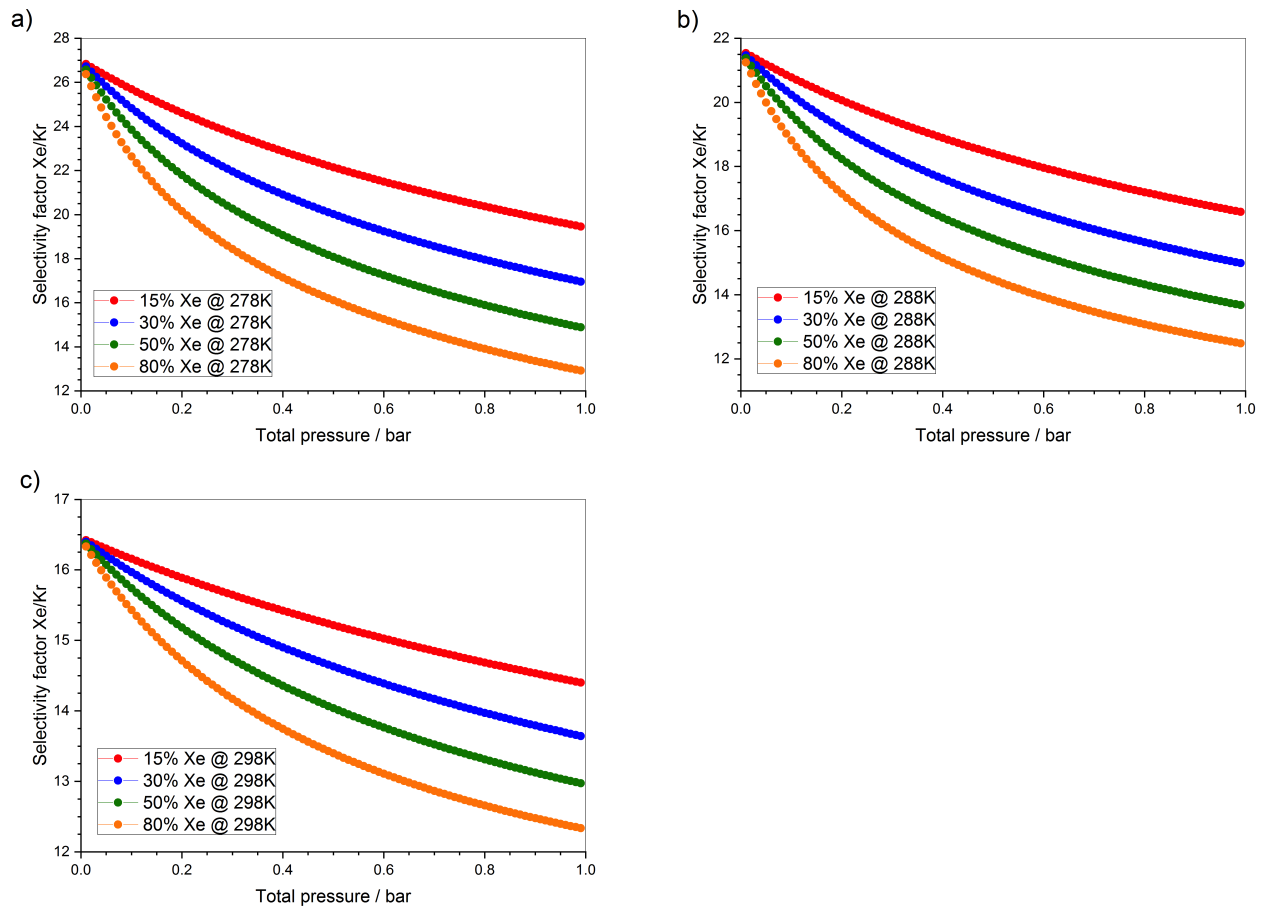
Figure 4.47: Separation factors for Xe/Kr in a binary gas mixture, computed from the single-component isotherms by use of IAST for CPO-54-Ni at three different temperatures; **(a)** 278K, **(b)** 288K, and **(c)** 298K.
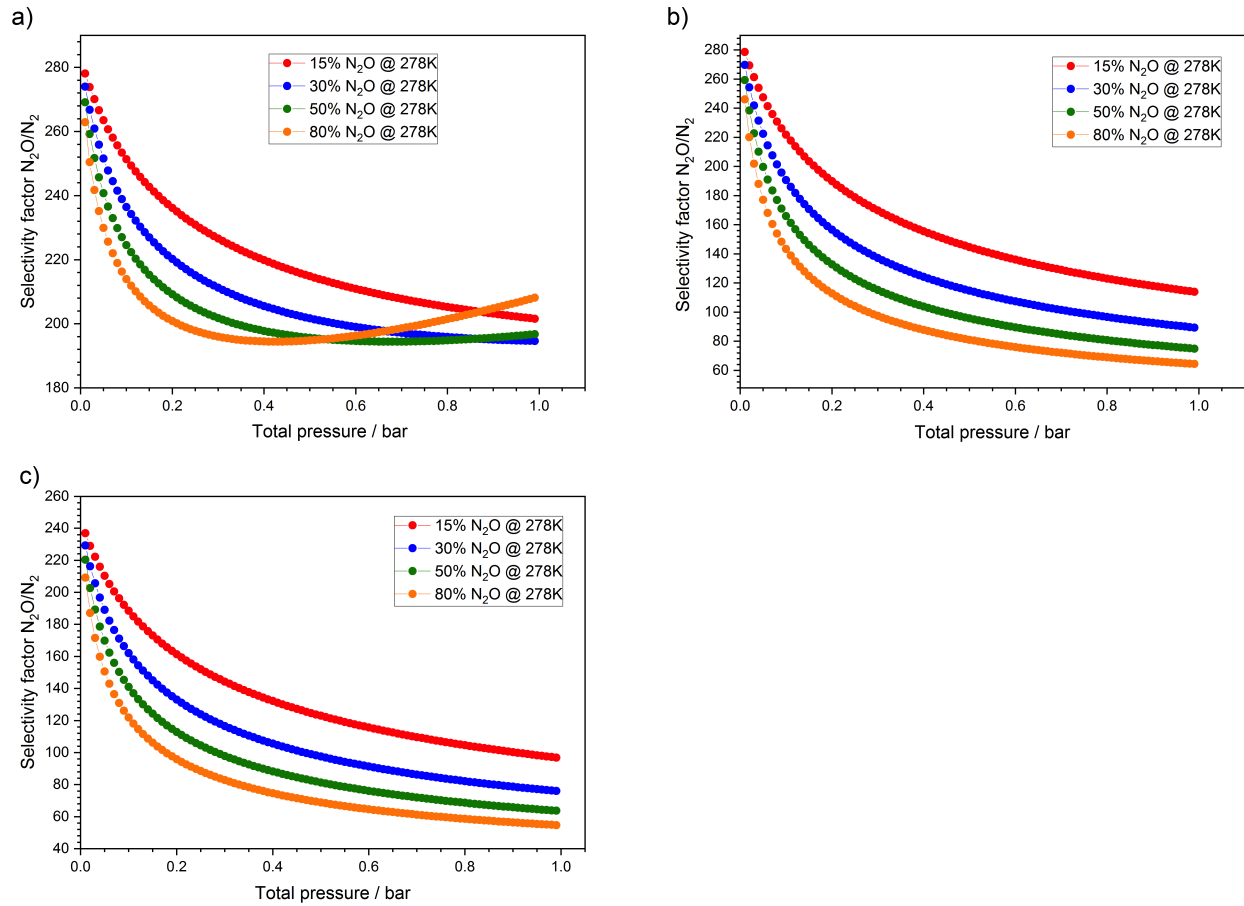
Figure 4.48: Separation factors for N_2O/N_2 in a binary gas mixture, computed from the standard-pressure single-component isotherms by use of IAST for CPO-54-Ni at three different temperatures; **(a)** 278K, **(b)** 288K, and **(c)** 298K.
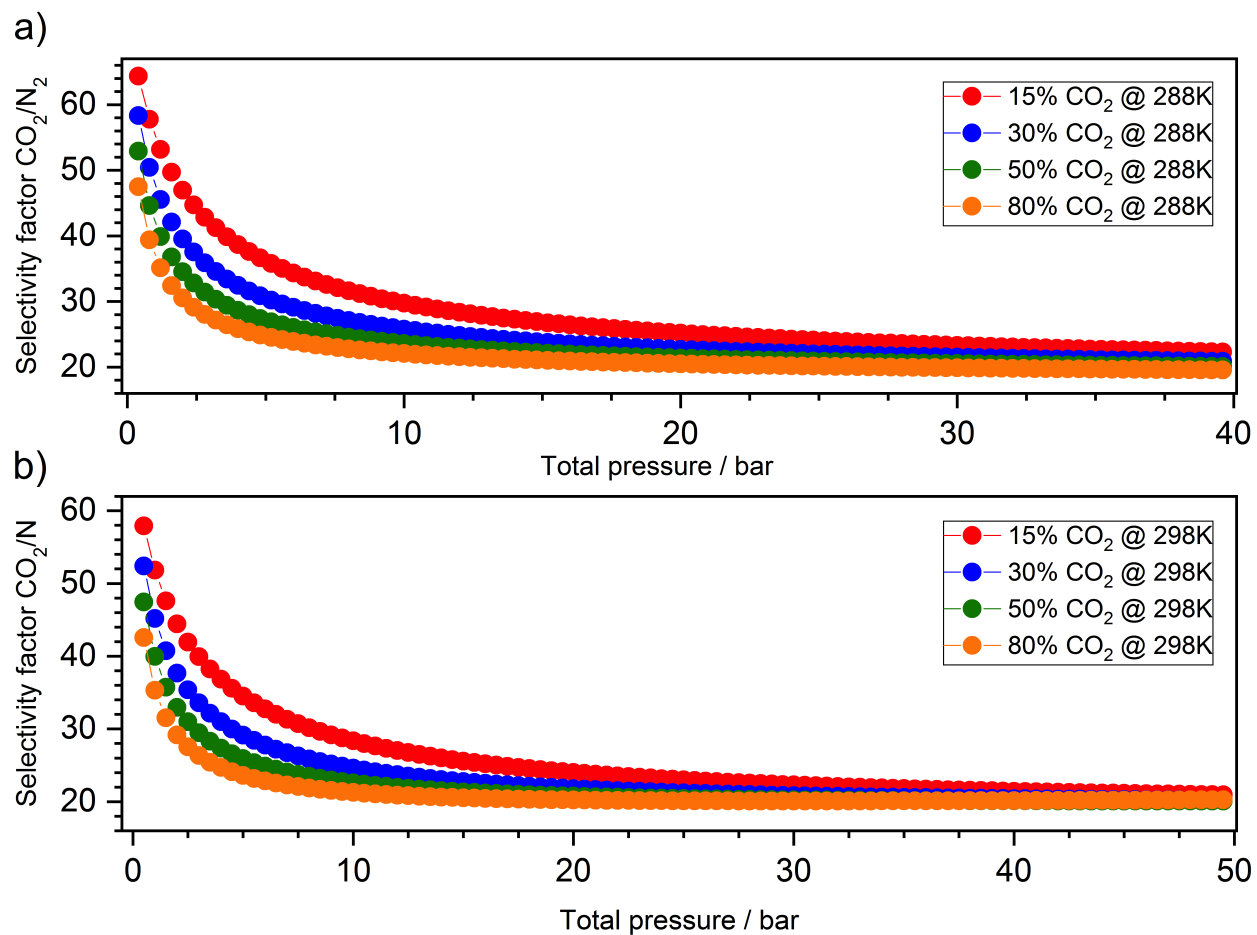
Figure 4.49: Separation factors for CO_2/N_2 in a binary gas mixture, computed from high-pressure single-component absolute adsorption isotherms by use of IAST for CPO-54-Ni at two different temperatures; **(a)** 288K, and **(b)** 298K.
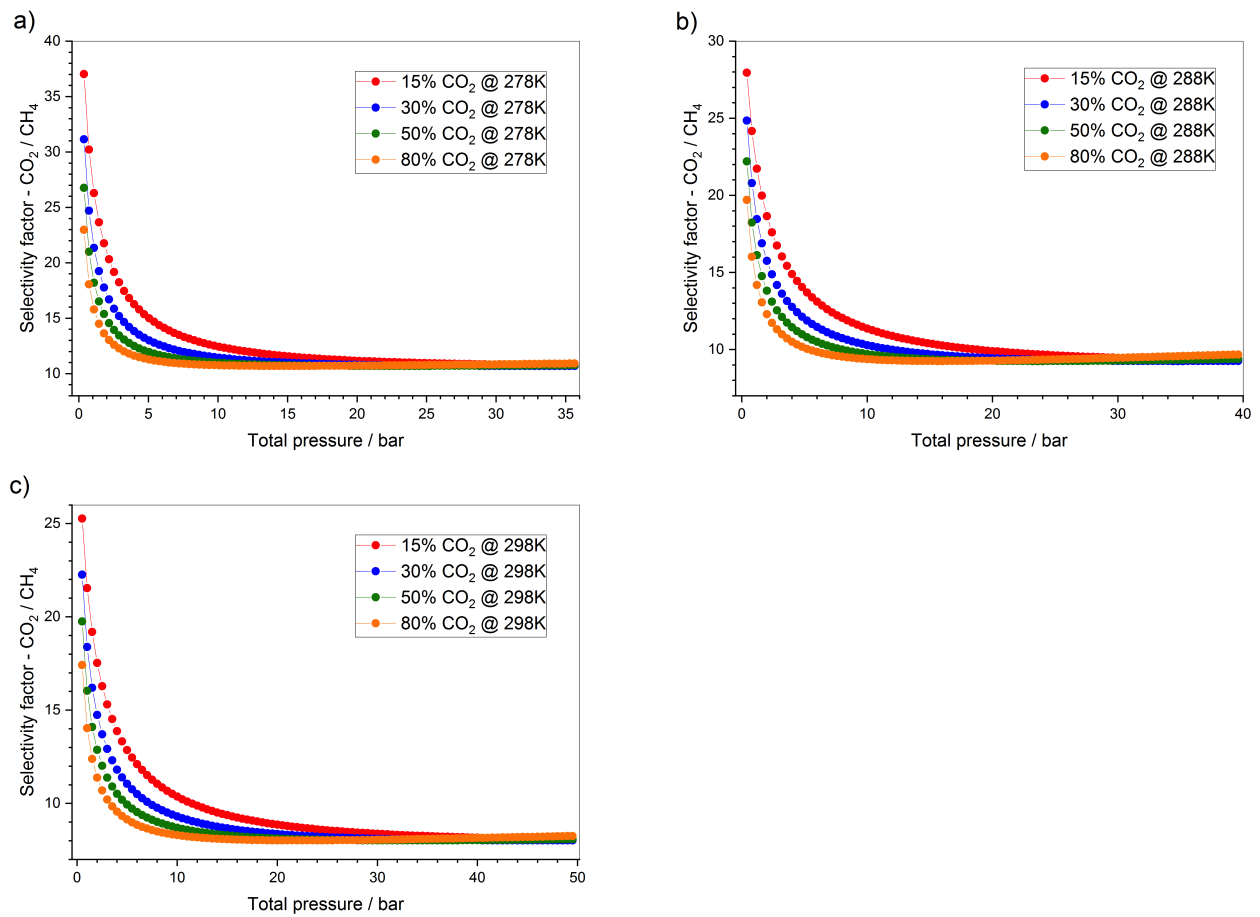
Figure 4.50: Separation factors for CO_2/CH_4 in a binary gas mixture, computed from high-pressure single-component absolute adsorption isotherms by use of IAST for CPO-54-Ni at three different temperatures; **(a)** 278K, **(b)** 288K, and **(c)** 298K.
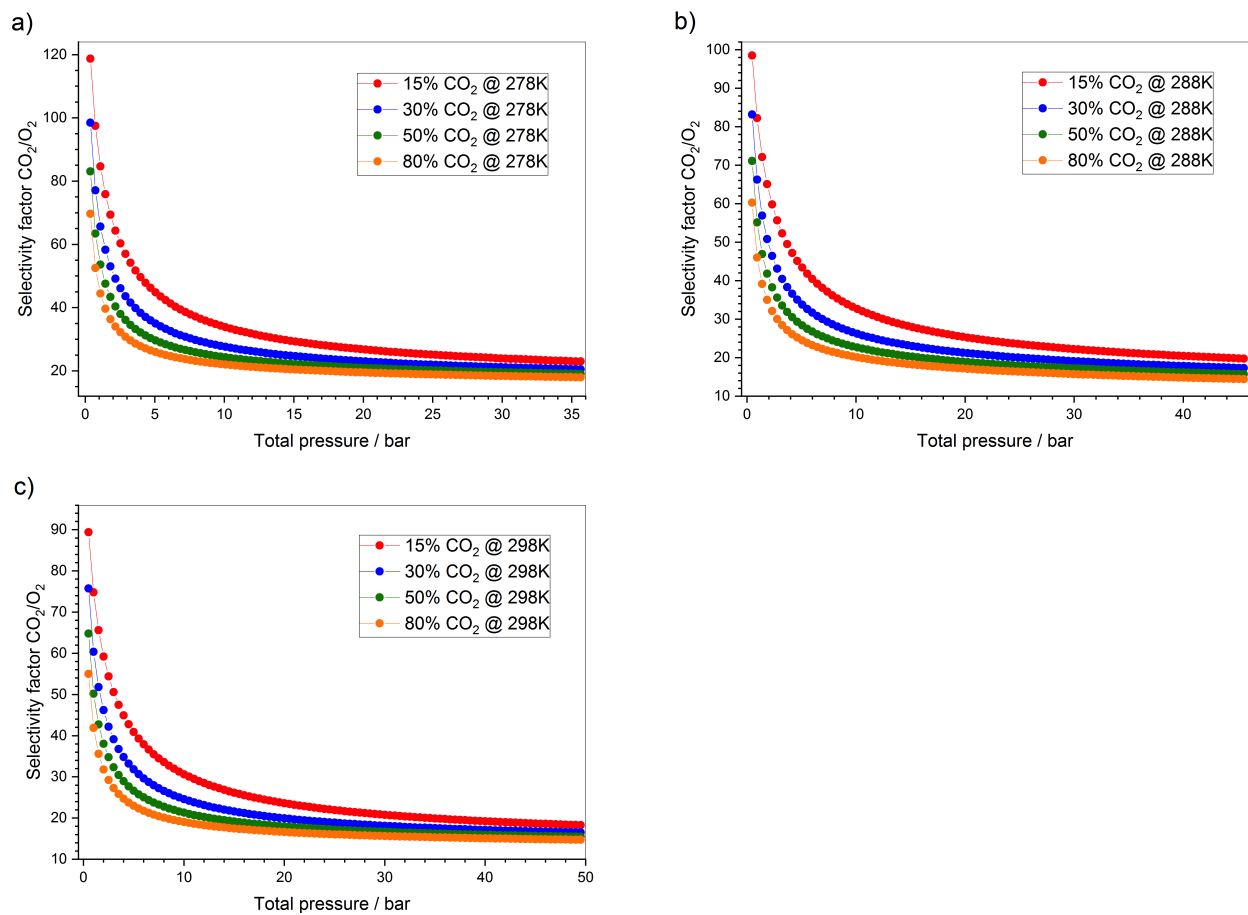
Figure 4.51: Separation factors for CO_2/O_2 in a binary gas mixture, computed from high-pressure single-component absolute adsorption isotherms by use of IAST for CPO-54-Ni at three different temperatures; **(a)** 278K, **(b)** 288K, and **(c)** 298K.

4.5.3 CPO-54-Co

The separation coefficients were calculated for CPO-54-Co at different temperatures and using different compositions of the investigated gases. The values for CO_2/N_2 separation are shown in Figure 4.52, CO_2/CH_4 separation in Figure 4.53, CO_2/CH_4 separation in Figure 4.53 and Xe/Kr separation in Figure 4.55.
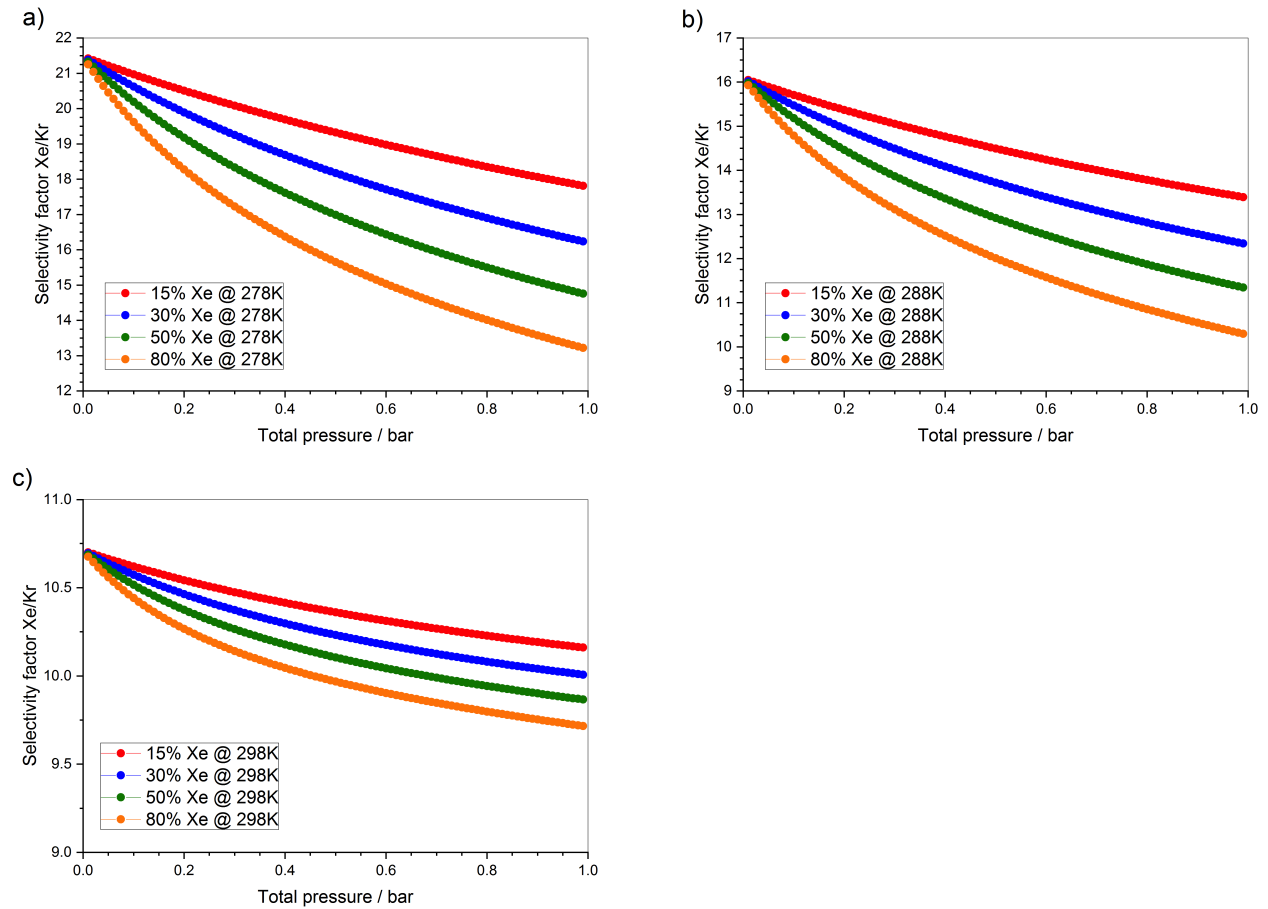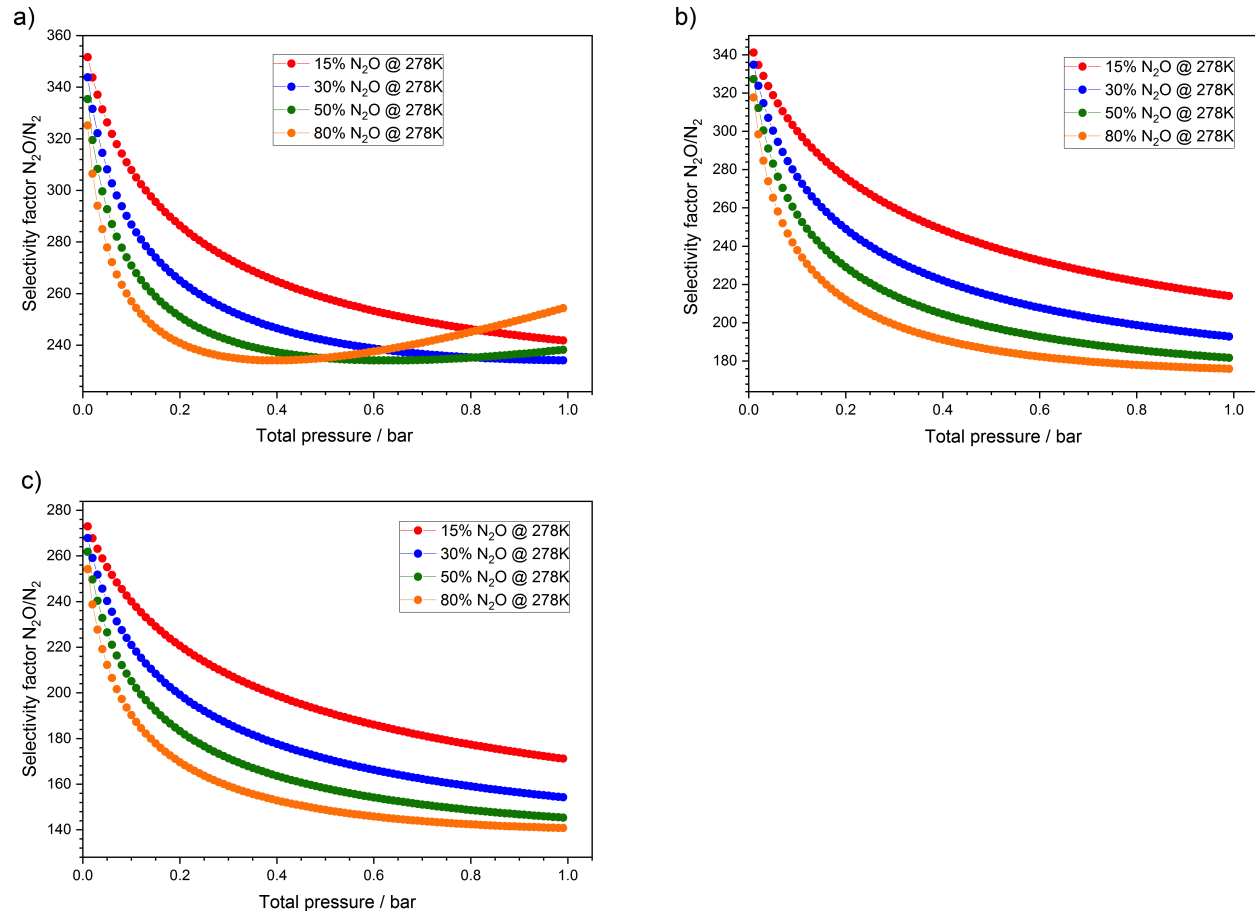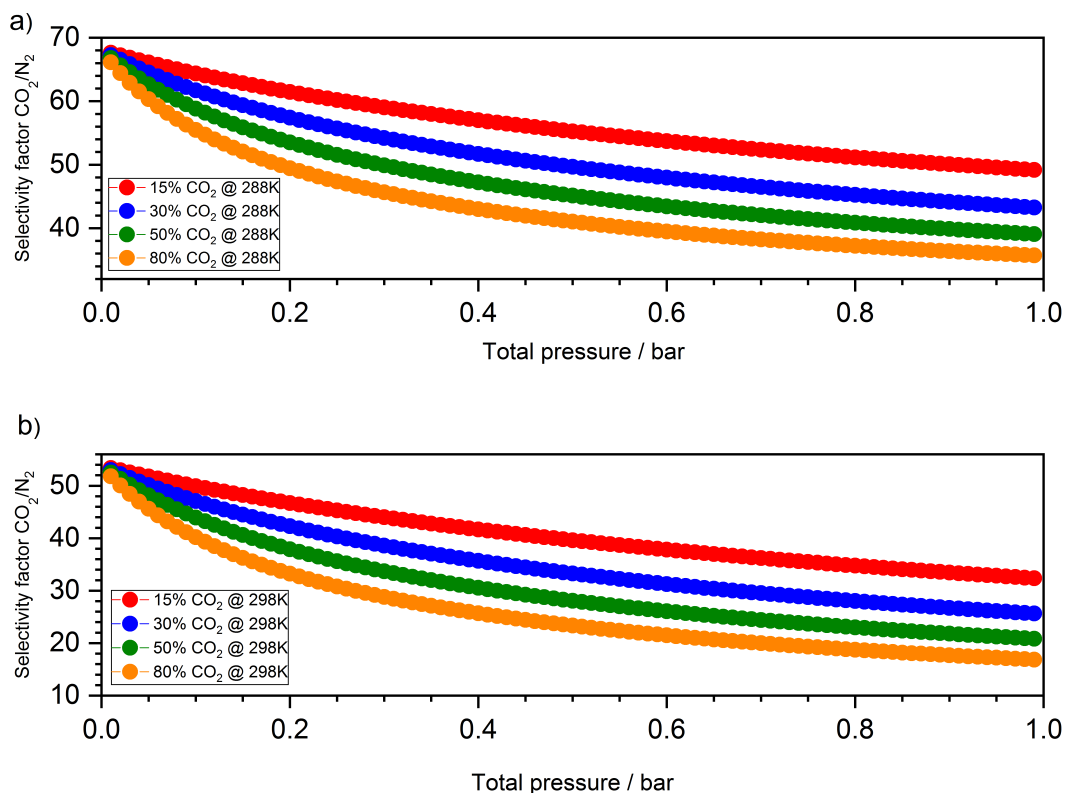

Figure 4.52: Separation factors for CO_2/N_2 in a binary gas mixture, computed from single-component isotherms by use of IAST for CPO-54-Co at two different temperatures; **(a)** 288K, and **(b)** 298K.
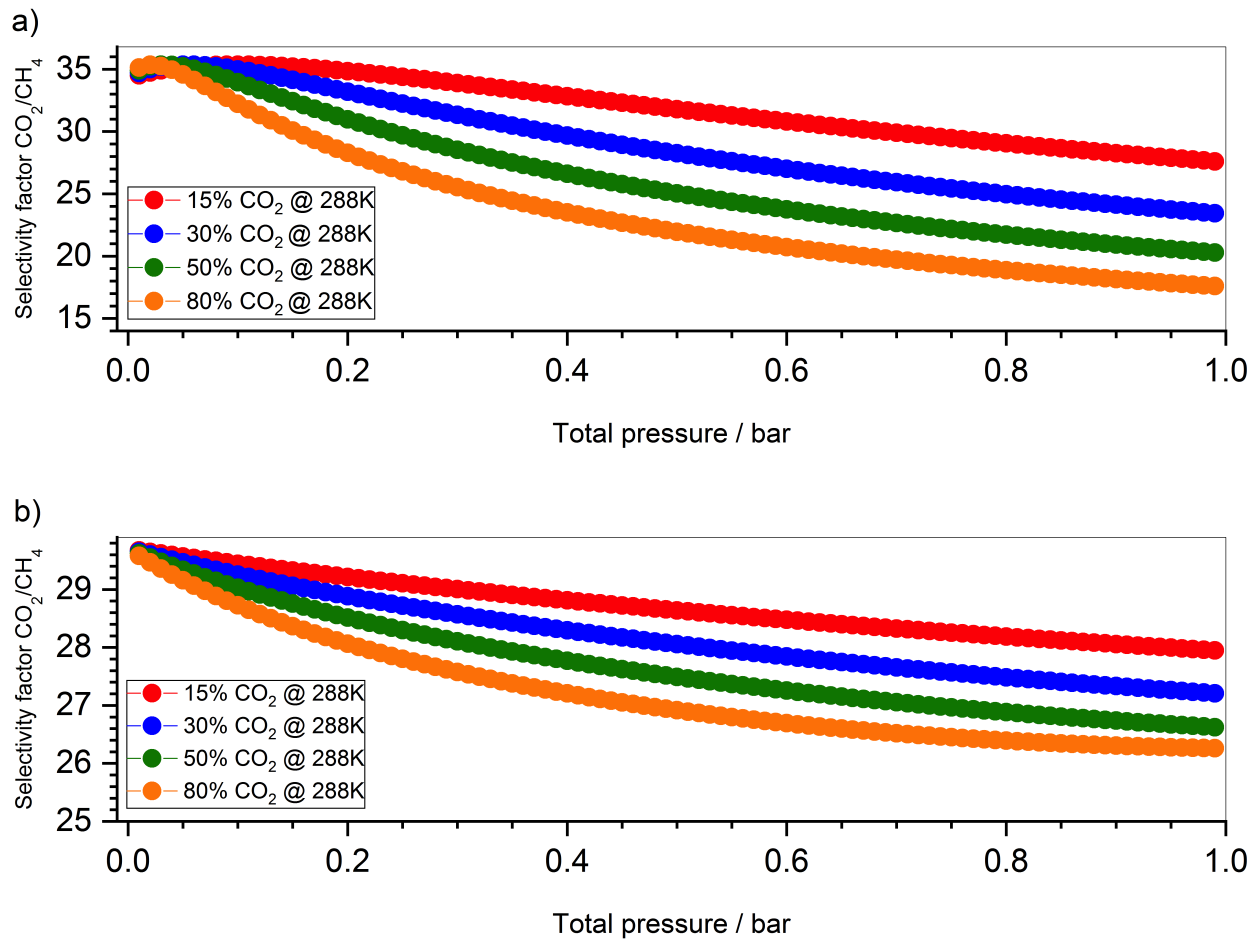
Figure 4.53: Separation factors for CO_2/CH_4 in a binary gas mixture, computed from single-component isotherms by use of IAST for CPO-54-Co at two different temperatures; **(a)** 288K, and **(b)** 298K.
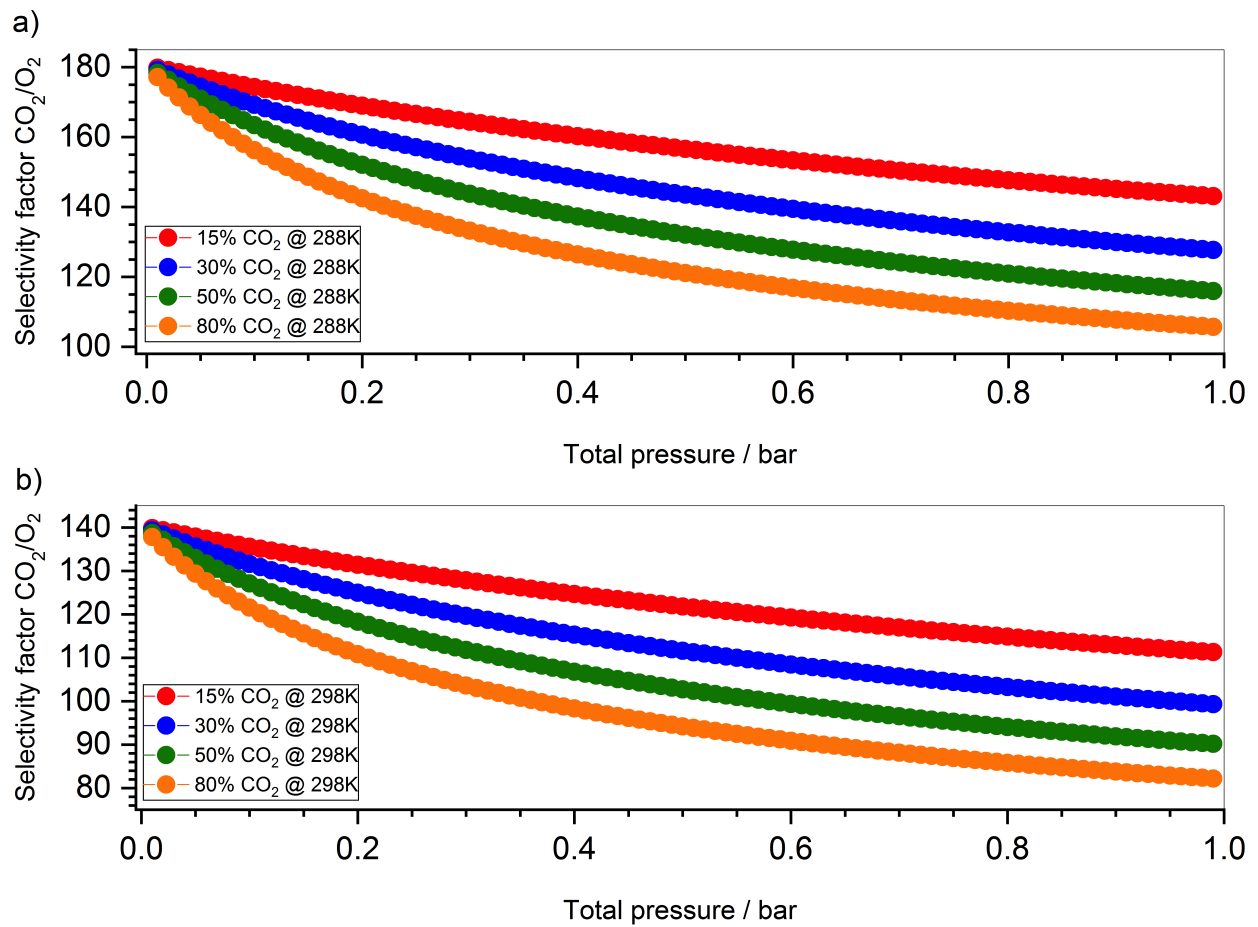
Figure 4.54: Separation factors for CO_2/O_2 in a binary gas mixture, computed from single-component isotherms by use of IAST for CPO-54-Co at two different temperatures; **(a)** 288K, and **(b)** 298K.
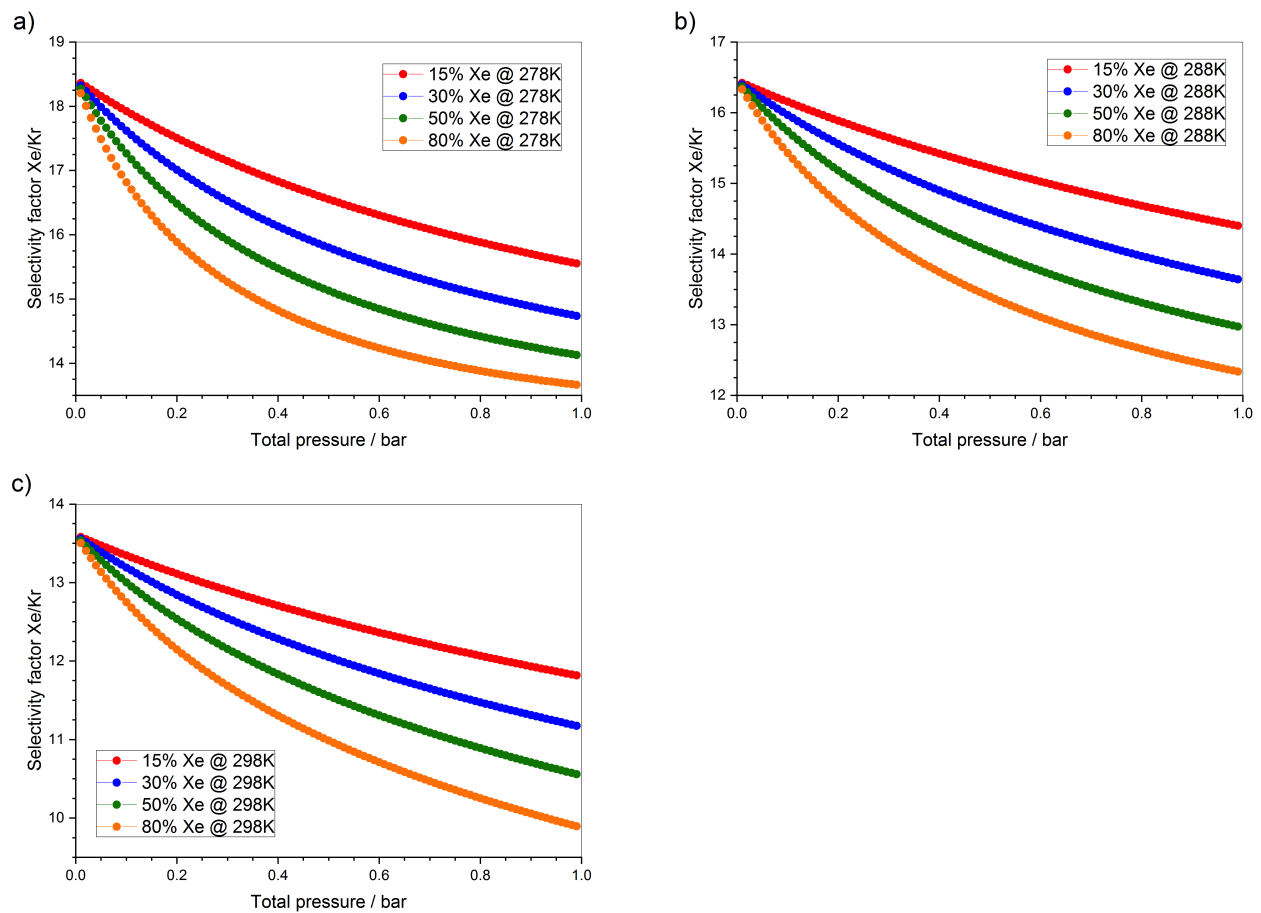
Figure 4.55: Separation factors for Xe/Kr in a binary gas mixture, computed from single-component isotherms by use of IAST for CPO-54-Co at three different temperatures; **(a)** 278K, **(b)** 288K, and **(c)** 298K.
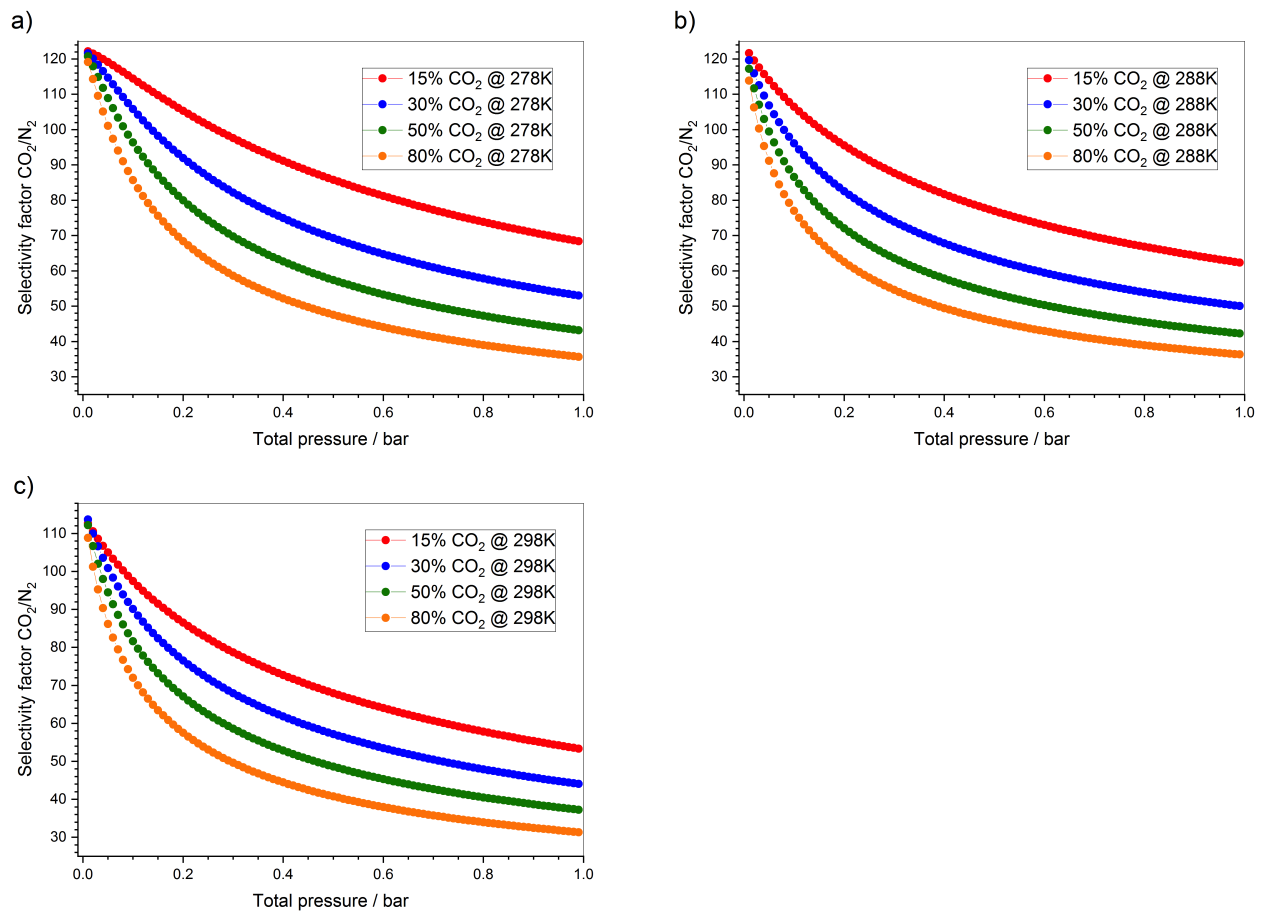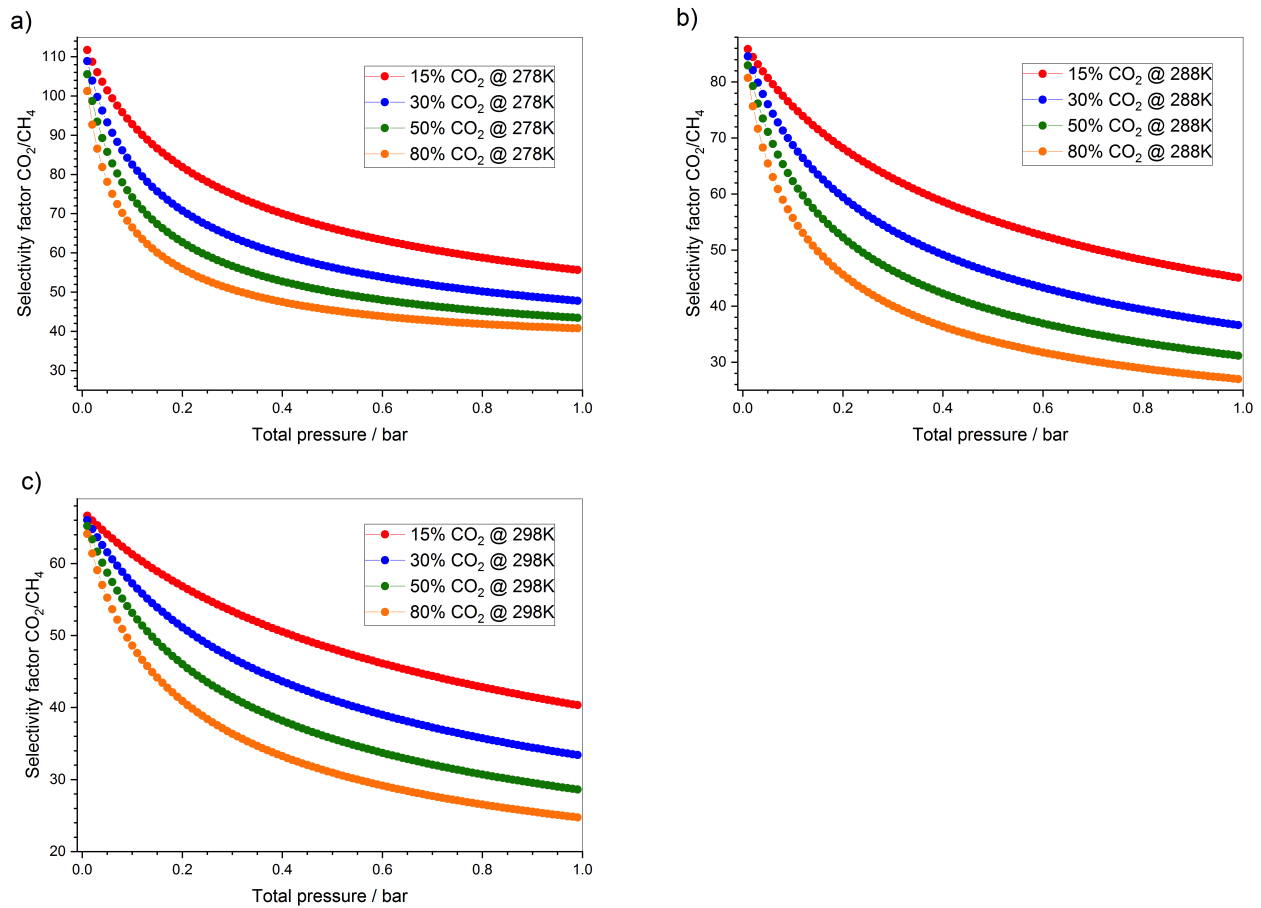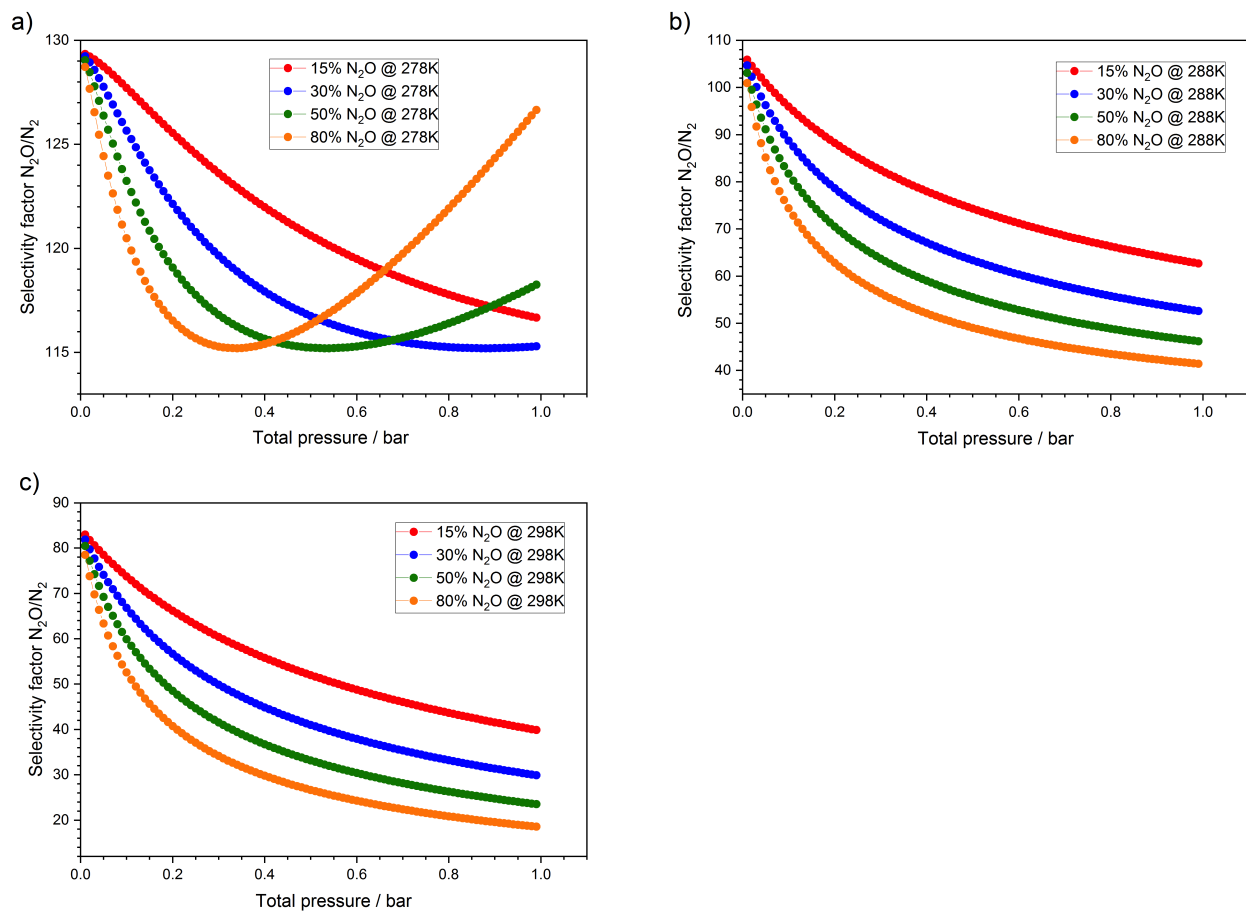
Figure 4.56: Separation factors for N_2O/N_2 in a binary gas mixture, computed from single-component isotherms by use of IAST for CPO-54-Co at three different temperatures; **(a)** 278K, **(b)** 288K, and **(c)** 298K.

4.5.4 CPO-54-Mn

The CO_2/N_2 selectivity coefficients (Figure 4.57) were calculated for CPO-54 using the high-pressure experimental data. A dual-site Langmuir function was used to fit to the adsorption isotherms.
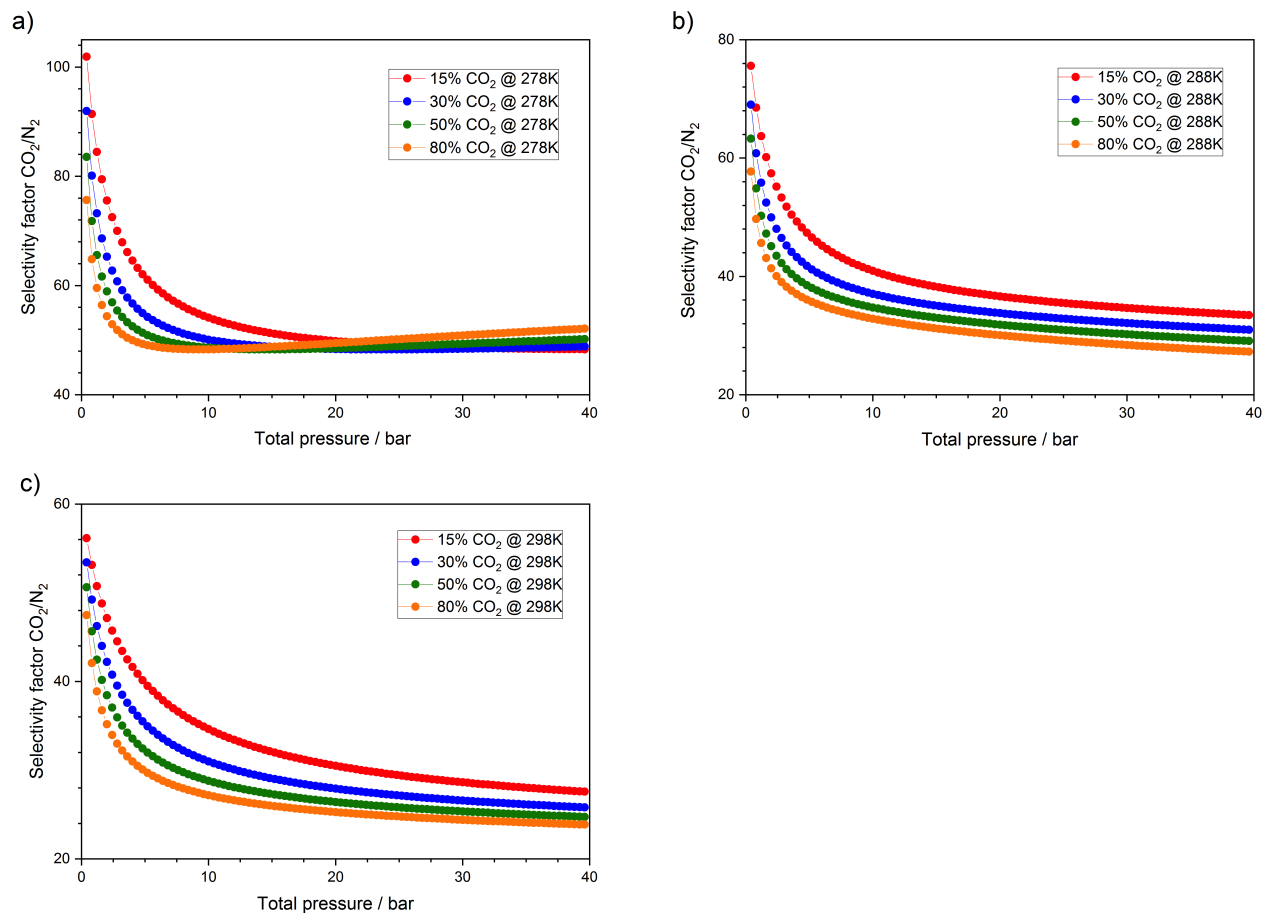
Figure 4.57: Separation factors for CO_2 and N_2 in a binary gas mixture, computed from single-component high-pressure absolute adsorption isotherms by use of IAST for CPO-54-Mn at three different temperatures; **(a)** 278K, **(b)** 288K, and **(c)** 298K.

Chapter 5

Discussion

This chapter deals with the discussion of the results presented in Chapter 4. It will present an interpretation of the key findings, a comparison with literature, and an evaluation of the methods used to obtain the results.

5.0.1   PXRD

The experimental PXRD-patterns (Figure 4.1) compared well to the calculated pattern. This confirmed that the synthesized materials were indeed CPO-54-M. The elevated background in the CPO-54-Co pattern was due to the fact that the data were collected using Cu-monochromatic radiation, which leads to an absorbance of radiation in the Co-compound.

5.0.2   CPO-54-Mg

From the results in Chapter 4, it is clear that the CPO-54-Mg material outperformed all the rest in terms of uptake. The maximum capacity (Figure 4.3) of CPO-54-Mg are of similar magnitude to what Queen et al. (2014) have found for CPO-27-Mg (20.9 mmol g^{-1} and 19.5 mmol g^{-1}, respectively).[55] The isotherm was recognised as a type I isotherm, is confirms the assumed micro-porous structure of the material. The calculated BET surface area and pore volume were found to be 1819.4 m^2g^{-1} and 0.7281 cm^3g^{-1}, respectively, which is significantly larger than the previously reported BET surface area of CPO-54-Mn (1409 m^2g^{-1} and 0.59 cm^3g^{-1}) by Dietzel et al. (2010).[44] This is an expected result because of the difference in formula weight.

The O_2 and N_2O isotherms of CPO-54-Mg have different curvature than the other gases (Figure 4.6). The CO_2 and N_2O isotherms display a defined stepwise behavior, as opposed to all the other measured gases. If one puts this into context with the heat of adsorption for CO_2 and N_2O, it becomes obvious that the step in the isotherm corresponds to the filling of the open metal sites. This effect is even more profound at 195 K (Figure 4.8).

The CO_2 uptake, measured at 195K (the sublimation temperature of CO_2), shows the maximal capacity for CO_2 adsorption in CPO-54-Mg, which is more than three times as high as the uptake at ambient temperature. The stepwise behavior is also more defined, compared to measurements close to room temperature, and the step occurs at lower pressure. The CH_4 isotherm at 195K, on the other hand, does not exhibit such a prominent step, compared to CO_2, nor such a high uptake. This behavior is not unexpected, of course, since one would expect the van der Waals interaction between CH_4 and the adsorbent to be much lower, compared to CO_2. CH_4 also has a much lower melting point (90.7 K), meaning that one would not get the full CH_4 uptake at this temperature.

The reason for the different shaped isotherms becomes evident from the calculated isosteric heat of adsorption (Figure 4.30). The Q_{st} values at low loadings compare well to what both Dietzel et. al and Queen et al. (2014) reported for CPO-27-Mg (Table 5.1), although it drops at a significantly lower loading compared to their results. CPO-54-Mg displays two well-defined heat of adsorption levels for CO_2 gas, and only one for the remaining gases.[18,55] These levels are caused by the difference in how the gases interact with the open metal sites within the pores. As mentioned earlier, incorporation of open metal-sites in MOF's is a well-established method for enhancing carbon-dioxide uptake. Because of the quadrupole moment of the CO_2 molecule, it will interact strongly with the OMS. CH_4, N_2, and O_2, however, do not interact as strongly with the OMS, resulting in an even Q_{st} over the full range of uptake. The Q_{st} value for CO_2, on the other hand, will drop from 42 to 19 kJ mol⁻¹ after all of the OMSs have been occupied.

Table 5.1: A comparison of the CO2 isosteric adsorption for CPO-54-Mg found in this work, and values for CPO-27-Mg reported by Yu et al. (2013) and Queen et al. (2014).

	CPO-54-Mg (This work)	CPO-27-Mg (Yu et al. 2013)	CPO-27-Mg (Queen et al. 2014)
Q_{st} / kJ mol⁻¹ (at 0.1 mol mol⁻¹)	42.1	42.0	43.5

The heat of adsorption at 43 kJ mol⁻¹ indicates an adsorbate/adsorbent interaction. With a heat of adsorption as high as this, one could ask whether this is actually a chemisorption, and not a physisorption. However, based on the isotherm and how the gas species desorb (reversible process), this is clearly a physisorption process. This is an important point, considering an application in CCS processes. It is, of course, essential to have sufficiently strong interaction between the adsorbent and CO_2. However, in order to be a realistic option for use in CCS, the interaction cannot be too strong. The stronger the interaction (or chemical bond), the more energy is needed to regenerate the adsorbent material and rerelease the CO_2 after the separation process is complete.

The difference in heats of adsorption forms the basis for the material's separation properties. The CO_2/N_2 selectivity, as calculated by use of IAST (Figure 4.39), shows that CPO-54-Mg has a very high affinity for CO_2 over N_2 gas. Based on the fact that CPO-54 have open metal sites, this

behavior is expected. As far as CO_2 selectivity goes, CPO-54-Mg has a superb selectivity of CO_2 over N_2. However, not as high as CPO-27-Mg.[18]

CPO-54-Mg also shows a high affinity towards CO_2 over CH_4 (Figure 4.40). However, the CO_2/CH_4 selectivity in CPO-54-Mg is lower than what has previously been reported for CPO-27-Mg (63 and 135, respectively)[18] . It is also lower than what has previously been found as CH_4/N_2 selectivity in CPO-27-Mg.[18]

One can see that the N_2O/N_2 separation, just as the CO_2/N_2 separation, is at a very high level (Figure 4.43). It follows from the similarities between CO_2 and N_2O that they should interact with the MOF in a similar manner, and the selectivity factors show just that. The N_2O/N_2 selectivities are just below the CO_2/N_2 selectivities at 278K and 288K. At room temperature, the order is reversed. In fact, CPO-54-Mg has a slightly higher uptake of N_2O than of CO_2 at temperatures near room temperature (Figures 4.6). This is reflected in the heat of adsorption, which is significantly higher for N_2O than for CO_2 (Figure 4.30). At 195K, on the other hand, it adsorbs more CO_2 than N_2O (Figure 4.8).

One can also observe that the heat of adsorption for Xe far exceeds that of Kr (Figure 4.30). Xe is a heavier noble gas, and will therefore interact more strongly with the OMS within the pores. The difference in Q_{st} is large enough to give high selectivity factors for selection of Xe over Kr (Figure 4.42). Both the heat of adsorption and Xe/Kr selectivity are higher for CPO-54-Mg than for CPO-27-Mg. The total uptakes, however, are lower for CPO-54-Mg than what Lee et al. (2013) have reported for CPO-27-Mg.[42]

The selectivity of CO_2 over O_2 was found to be the highest of them all. Not surprising, since the O_2 uptake was by far the lowest of all the measured gases. This indicates that CPO-54-Mg has a very good potential for CO_2 from O_2.

5.0.3 CPO-54-Ni

The standard-pressure isotherm in Figure 4.9 displayed a micro-porous behavior in the form of a type I isotherm, as defined by IUPAC. The BET-theory could hence be used to find the pore volume and surface area, which were found to be 0.5275 cm^{3}g^{-1} and 1180.1 m^{2}g^{-1}. As expected, this is significantly lower than the surface area and pore volume found for CPO-54-Mg. In fact, it corresponds well with trends in surface area for varying metal-centers in the CPO-27 series,

where it has been shown that the surface area is higher in the compounds with lighter metals (Mg>Mn>Co>Ni).

The CPO-54-Ni material investigated in this work display somewhat lower uptakes for all the measured gases, compered to results previously reported for standard-pressure CPO-27-Ni measurements in the literature (Table 5.2).[18,55] Just as the pore volume and surface area, the uptakes in the nickel compound are significantly lower than that of the magnesium one (see Figure 4.12). If one compares the CO_2 uptake in CPO-54-Ni and CPO-54-Mg (Figures 4.14 and 4.8, respectively), one can see that the uptake is approximately 30% lower for the nickel material than the magnesium one.

CPO-54-Ni generally exhibited lower uptake and surface area, compared to CPO-54-Mg. The full CO_2 capacity at 195 K are approximately 30% less in CPO-54-Ni than in CPO-54-Mg (Figures 4.14 and 4.8. The uptakes for CPO-54-Ni found in this work are also lower than what others have reported in the literature for CPO-27-Ni (Table 5.2).[18,55]

Table 5.2: Comparison of the CO_2 uptakes at 298 K (100 kPa) for CPO-54-Ni found in this work and the results reported by Queen et al. (2014) for CPO-27-Ni.

Material	CO_2 uptake at 298 K, 100 kPa / mmol g^{-1}
CPO-54-Ni (This work)	7.1
CPO-27-Ni (Queen et al. 2014)	3.8

The lower uptake (at standard pressure) for CPO-54-Ni, compared to CPO-54-Mg, also reflects in the isosteric heat of adsorption. The Q_{st} at zero-loading for CPO-54-Ni was found to be 40 kJ mol^{-1}, which is 3 kJ mol^{-1} lower than that of CPO-54-Mg. Also, the heat of adsorption for the secondary adsorption site in CPO-54-Ni is lower, compared to CPO-54-Mg. This in turn, means that both the primary adsorption site (the OMS) and the secondary adsorption site in CPO-54-Mg will adsorb more readily than the corresponding sites in CPO-54-Ni.

The N_2O adsorption in CPO-54-Ni was similar to CPO-54-Mg. Although CPO-54-Ni had lower total uptake of N_2O than CPO-54-Mg, the heat of adsorption was at the same level in both materials. The Q_{st} for N_2O was also generally higher than the Q_{st} for CO_2 in both CPO-54-Ni and

Table 5.3: Comparison of Xe/Kr the calculated selectivity in equimolar mixtures at 298 K (0.05 bar and 0.5 bar) for CPO-54

Material	Xe/Kr selectivity in equimolar mixture (0.05 bar, 298 K)	Xe/Kr selectivity in equimolar mixture (0.5 bar, 298 K)
CPO-54-Mg	10.6	10.1
CPO-54-Ni	16.2	14.3
CPO-54-Co	13.5	11.6

CPO-54-Mg.

From Figure 4.32 one can also see that the heat of adsorption for Xe gas is much higher than for Kr. This indicates a high selectivity for Xe over Kr. The IAST selectivity for Xe/Kr of CPO-54-Ni is, in fact, even higher than that of CPO-54-Mg (Table 5.3).

The picture changed somewhat when CPO-54-Ni were measured at high pressures. The first thing one should note (Figure 4.18 compared to Figure 4.12) is that the uptake of CH_4, N_2, and O_2 are much closer to that of CO_2 compared to the standard-pressure measurements. One can observe that the CO_2 uptake has doubled, while the CH_4 and N_2 uptake have almost five-doubled. Interestingly, it is the O_2 uptake that has increased the most from standard-pressure to high-pressure, by a factor of thirteen. It has even surpassed that of N_2. The curvature of the isotherms also suggests that the uptakes are closer to the maximum capacity, since the increase in uptake, as a function of pressure, subsides in the higher pressure range.

Also, the isosteric heats of adsorption, calculated from the high-pressure absolute adsorption isotherms, deviates a great deal from the resulting Q_{st}s from the standard-pressure measurements (Figure 4.33). It is especially worth noticing how the Q_{st} for CO_2 changes with respect to loading. Where there were two clearly defined levels in the standard-pressure Q_{st} (one for the open metal site and one for the secondary site), the graph now starts to decrease immediately instead of behaving in a stepwise manner. Even though both the starting and end values are within what one could expect, the total Q_{st} curve is unexpected. This may indicate that a large number of the open nickel sites were not open at all, but instead blocked by something else (e.g. water), hindering the CO_2 molecules from adsorbing onto them.

Thus, the difference in behavior from the high-pressure to the standard-pressure isotherms

resulted directly into differences in separation properties. By comparison of the calculated CO_2/N_2 selectivity (Figures 4.44 and 4.49), one will see that the selectivities from the high-pressure measurement are only half of the selectivities for the standard-pressure measurements. To explain this decrease, one must look at how the uptakes and surface area changed in the high-pressure experiments (Table 4.2). Firstly, a drop in BET-surface area was observed, compared to what was measured at the Belsorp-MAX. The cause of that might be how the sample was handled when it was installed onto the high-pressure instrument, where the sample was exposed (unavoidable) to the room-atmosphere for a short time before being installed. Secondly, the increase in uptake was higher for N_2 than for CO_2 at high pressure, which directly decreased the CO_2/N_2 selectivity, compared to standard-pressure. This is disappointing, because, despite the all time consuming work, it is now impossible to determine with certainty how good the separation properties for CPO-54-Ni are at high pressure with the full surface area available.

5.0.4 CPO-54-Co

CPO-54-Co displayed the lowest N_2 (77K) uptake of all the investigated materials in this study (Figure 4.19). The isotherm was recognized as a type I and BET-theory was applied to calculate surface area and pore volume. Although CPO-54-Co had a lower N_2 uptake at 77K than CPO-54-Ni, it has a higher surface area (Table 4.5). Again, this corresponds to the observed trend in surface area in CPO-27 (Mg>Mn>Co>Ni).

As for both CPO-54-Mg and CPO-54-Ni, the CO_2 isotherms for CPO-54-Co have a different curvature than those of CH_4, N_2, and O_2 (see Figure 4.22), and one do not see the stepwise behavior as profound as for CPO-54-Mg and CPO-54-Ni. No step can be observed for CH_4, N_2, and O_2. The N_2O isotherm, on the other hand, displays a stepwise behavior (most clearly shown in the 195 K isotherms, Figure 4.24). In fact, this material shows a higher uptake of N_2O than CO_2. Similar values for the uptake of N_2O and CO_2 are expected, based on the similarities of the two gases.

The similarities between N_2O and CO_2 are reflected in the isosteric heats of adsorption. The curvature of the Q_{st} for N_2O and CO_2 are similar, although the Q_{st} for N_2O is slightly higher than for CO_2 at the lower loadings (Figure 4.36). Interestingly, the heat of adsorption for N_2O has the same value at zero loadings for all three materials (Mg, Ni and Co). Whereas the CO_2

heat of adsorption for CPO-54-Co was significantly lower than for the magnesium and nickel materials, it now has the same value at zero loadings (44 kJ mol^{-1}). This may indicate that the Co-OMS interacts stronger with N_2O than with CO_2, or it could merely be that the material was better activated (meaning that more of the OMS might have been available) prior to the N_2O measurements, compared to the CO_2 measurements. The samples were, however, pre-treated in the same manner before both measurements, which points in the direction of N_2O adsorbing stronger onto the Co^{2+} open metal site compared to CO_2.

An interesting point is that, although CPO-54-Co has a much lower total uptake than CPO-27-Co, the CO_2 heat of adsorption is higher in CPO-54-Co, compared to what has been reported by both Yu et al. (2013) and Queen et. al (2014) for CPO-27-Co (Table 5.4).[18,55] Further more, the CO_2/N_2 selectivity is low, compared to CPO-54-Mg, CPO-54-Ni and CPO-27-Co.[18] Based on the trends in selectivity from CPO-27, it was expected that the cobalt material should have a lower CO_2/N_2 selectivity than the magnesium and nickel materials.

Table 5.4: A comparison of the CO2 uptake and Qst found for CPO-54-Co in this work, and values for CPO-27-Co reported by Yu et al. (2013) and Queen et al. (2014)

	CPO-54-Co (This work)	CPO-27-Co (Yu et al. 2013)	CPO-27-Co (Queen et al. 2014)
CO_2 uptake / mmol g^{-1}	6.0	6.8	6.7
Q_{st} / kJ mol^{-1} (at 0.1 mol mol^{-1})	36.1	34.5	33.8

Both the uptake and Q_{st} are higher for Xe than for Kr in CPO-54-Co (Figures 4.22 and 4.36). Furthermore, the heat of adsorption for the cobalt material is higher than that of the magnesium material (Figure 4.30). This is in agreement with previously reported trends in CPO-27-Co and CPO-27-Mg Lee et al. (2016)[42] The Q_{st} found in this work is higher than those reported for CPO-27-Co by both Lee et al. (2016) and Thallapally et al. (2012), indicating a good potential for Xe/Kr separation in CPO-54-Co.[41,42]

That potential was confirmed by IAST calculations (Figure 4.55), yielding selectivities similar to what has previously been reported for CPO-27-Co.[41] The Xe/Kr selectivity was lower compared to CPO-54-Ni, but higher than for CPO-54-Mg. This indicates that the trend for how

strongly Xe interacts with the open metal sites in CPO-54 is Ni>Co>Mg, and that CPO-54-Co are an interesting material for use in Xe/Kr separation processes.

5.0.5   CPO-54-Mn

The N_2 77K isotherm for CPO-54-Mn was identified as a type I, which confirmed the expectation that synthesized material was microporous. Following from that, BET-theory could be applied and used to calculate the specific surface area and pore volume. The initial N_2 measurement at 77K (standard-pressure) resulted in a pore volume of 0.5459 cm^3g^{-1} and a BET-area of 1354.4 m^2g^{-1}. The surface area is lower than for CPO-54-Mg, but higher than CPO-54-Co and CPO-54-Ni, thus joining the previously described trend from CPO-27
(Mg>Mn>Co>Ni). The surface area is, in other words, directly scaled with the materials formula weight. The surface is for CPO-54-Mn are slightly lower than what was previously reported by Dietzel et al. (2010) for the same material (approximately 10%), but higher than for CPO-27-Mn.[44]

If one examines the uptake in Figure 4.25, one will see that CPO-54-Mn has a high N_2 uptake at 77K. Higher than the cobalt material, but lower than the magnesium and nickel compounds. Due to the lower surface area, compared to Dietzel et al. (2010), it also has approximately 12% lower total N_2 uptake at 77K than what they have previously reported (Table 5.5).[44]

Table 5.5: Comparison of the maximum N2 uptake at 77 K and the BET surface areas for the different CPO-54 materials.

Material	Maximum N_2 uptake at 77 K, 1 bar / mmol g^{-1}	BET surface area / m^{2}g^{-1}
CPO-54-Mg	21.4	1819
CPO-54-Mn Dietzel et al.(2010)	19.2	1409
CPO-54-Mn	17.0	1354
CPO-54-Co	15.8	1276
CPO-54-Ni	19.1	1180

Unfortunately, the same drop in uptake and surface area as were observed for the nickel material was also observed here when the material was installed onto the BELSOR-HP instrument

for high-pressure measurements. The drop in surface area was approximately 10%. Again, this may be due to the way the sample is installed on the instrument, where it is briefly exposed to an open atmosphere.

CPO-54-Mn also had a second drop in performance. As mentioned in chapter 4, the high-pressure instrument broke down shortly after the measurements had begun. That resulted in a three-month-long period, where the sample was kept on the instrument under a N_2 atmosphere, before the instrument was repaired. A new N_2 measurement at 77K was completed to check how the material had kept its properties. The result showed that it had experienced a new drop in both surface area and uptake, now displaying approximately 80% of its initial surface area.

In other words, the surface area was down by 20% by the time the CO2 measurements had started. Consequently, the measured CO_2 uptakes in CPO-54-Mn were not as high as they potentially could have been if the material had been in it's original condition. The CO_2 uptake found for CPO-54-Mn in this work is significantly lower than what Yu et al. (2013) have previously reported for CPO-27-Mn at high-pressure.[18] The CO_2 uptake in CPO-54-Mn in this work is, however, significantly higher than what Dietzel et al. (2010) reported for CPO-54-Mn at standard-pressure.[44] (Table 5.6). Unfortunately there are no CO_2 measurements at standar pressure in this work, which makes it difficult to compare the results of Dietzel et al. (2010) directly to the results of this work.

Table 5.6: A comparison of the CO2 uptake and Qst found for CPO-54-Mn in this work, and values for CPO-54-Mn reported by Dietzel et al. (2010), and for CPO-27-Mn reported by Yu et al. (2013)

	CPO-54-Mn high-pressure (This work)	CPO-54-Mn standard-pressure (Dietzel et al. 2010)	CPO-27-Mn high-pressure (Yu et al. 2013)
CO_2 uptake / mmol g^{-1} 298 K	8.0	6.5	11.5
Q_{st} / kJ mol^{-1}	40.7	36.0	33.9

It was not only the CO_2 uptake that was lower for CPO-54-Mn, compared to CPO-27-Mn,

but also the selectivity. Yu et al. (2013) reported generally higher CO2/N_2 selectivity for CPO-27-Mn than what has been found for CPO-54-Mn in this work (Table 5.7). It is interesting to note that the CO_2/N_2 selectivity for CPO-54-Mn are decreasing as the pressure increases, whilst it is opposite for CPO-27-Mn.

Table 5.7: Comparison of CO2/N2 selectivity for CPO-54-Mn and CPO-27-Mn at high pressures.

Material	CO2/N2 selectivity in equimolzr mixtures at 298 K, 1 bar	CO2/N2 selectivity in equimolzr mixtures at 298 K, 8 bar
CPO-54-Mn (This work)	65	30
CPO-54-Mn (Yu work)	61	89

Another interesting point is the CO_2 Q_{st} for CPO-54-Mn, which has higher values than expected. Dietzel et al. (2010) have already shown that the Q_{st} are higher for CPO-54-Mn than for CPO-27-Mn.[44] However, the values found in this work are even higher than what Dietzel et al. (2010) reported for the same material. A difference between the two studies is the pressure at which the isotherms were measured (standard-pressure vs. high-pressure). The curvature of the CO_2 Q_{st} is also deviating from what one would expect. One normally see two levels: one representing the OMS and one representing the secondary adsorption site. Here, however, there are no defined levels. The curvature for CPO-54-Mn at high-pressure is similar to that of CPO-54-Ni at high-pressure. These results may indicate that the adsorbate/adsorbent interaction for the Mn^{2+} site are more profound at high pressures and low loadings. However, further studies are needed to confirm this.

Table 5.8: Comparison of the isosteric heat of adsorption (at 0.1 CO2 per M2+) for CPO-54-Mn and CPO-27-Mn.

	CPO-54-Mn High-pressure (This work)	CPO-54-Mn Standard-pressure (Dietzel et al. 2010)	CPO-27-Mn High-pressure (Yu et al. 2013)	CPO-27-Mn Standard-pressure (This work)
Q_{st} kJ mol^{-1}	40.5	36.1	31.3	31.7

5.0.6 Potential for application

All in all, the CPO-54 materials in this work have shown very similar behaviour to CPO-27. The isosteric heats of adsorptionn for the open metal sites are in the same order of magnitude in both MOFs for CO_2, CH_4, N_2, and O_2. However, the Q_{st} at the secondary adsorption sites are in general lower for CPO-54 than for CPO-27. This suggest that the extended linker in CPO-54 results in a lower heat of adsorption for adsorption sites other than the OMSs.

The total gas uptakes of CO_2, CH_4, N_2, and O_2 are lower in CPO-54 than in CPO-27. Although the CO_2/N_2, and CH_4/N_2 are somewhat lower in CPO-54, it is still in the same order of magnitude.

These results suggest that CPO-54 is a suitable MOF-candidate for use in CO_2/N_2, and CH_4/N_2 separation processes and N_2O-capture from air. However, CPO-27 still remains the better material of the two for carbon capture.

The point where CPO-54 differs most from CPO-27, in terms of sorption properties, is the ability to separate Xe and Kr. The Xe/Kr are, to the best of my knowledge, better than what has been reported for any CPO-27 material. The open magnesium-site generally showed the highest heats of adsorption, especially for CO_2 and N_2O. However, for Xe adsorption, the highest Q_{st} was on the open nickel-site. CPO-54-Ni also displayed the highest Xe/Kr selectivity. Thus making CPO-54-Ni a most interesting material for Xe/Kr separation.

It is evident from the IAST calculations that the selectivity factors for all the different adsorbates in all the CPO-54 materials are highly temperature-dependent. This indicates that it would be favourable to run potential selectivity processes with CPO-54 at lower temperatures, where one would have a more selective and efficient separation proses.

5.0.7 Work Evaluation

A large part of the practical work was spent in the laboratory, trying to produce perfect CPO-54 samples. This proved to be more challenging than expected, mainly due to the water-sensitivity of the CPO-54 series. The inert filtration process was time consuming, and it never worked quite as it was intended to in the beginning, because some air (and thereby also water) seemed to get into the system every time. This problem was resolved by using a brand new Schlenk-line, as we suspected that there might be some contamination in the old one. The materials made after that were fine. In fact, the CPO-54-Mg and CPO-54-Mn samples produced in this work are the best-preforming CPO-54 materials made by anyone in this research group since the CPO-54-Mn material that Prof. Dietzel et al. reported in 2010.[44] It might, however, be possible to synthesis even better CPO-54-Ni and CPO-54-Co samples than those who were made in this work.

A weakness in the gas sorption measurements is their sensitivity to error in mass. If one has an error of 1% when weighing the sample, one will get a 1% error in the isotherm. It will, consequently, result in errors in the calculated heats of adsorption and selectivity. To insure that the correct mass was used, the samples were weighed both before and after the measurements. That is, with the exception of the high-pressure measurements of CPO-54-Mn. That sample is, at precent time, still being measured, and has therefore only been weighed prior to the measurements. Measurements of this sample will be continued by the research group after the submission of this thesis.

Another potential source of error that stands out, is the fits used to describe the experimental data. Both the Q_{st} and selectivity are highly sensitive to errors in the isotherm-fits. Especially in the lower pressure areas. I have therefore used three different methods to calculate the isosteric heat of adsorption. However, the fits obtained by the dual-site Langmuir model were highly acceptable (Appendix C). The virial equation generally did not fit the experimental data as well as the DSL, and this reflects in many of the calculated Q_{st}. Whereas the DSL and interpolation yield similar results, the results from the virial equations deviate more from the other two.

Chapter 6

Conclusions

6.1 Conclusions

This study aimed to discover how the extended linker in CPO-54 would affect the applicability of these materials for CO_2/N_2, CO_2/CH_4 and CO_2/O_2 separation, how CPO-54 adsorbed N_2O, and whether or not the materials were suitable to separate Xe from Kr.

In this work, the gas adsorption capacity of CPO-54-M (M = Mg, Mn, Ni, and Co) has been measured for CO_2, CH_4, N_2, O_2, N_2O, Kr, and Xe. Isosteric heats of adsorption and selectivity coefficients have been calculated based on these adsorption measurements. This work has given new insight into the CPO-54 MOF series and its properties.

The results of this study have shown that CPO-54 is highly selective of CO_2 over N_2, CH_4, and O_2. The selectivity factors were found to be highly temperature-dependent, where the selectivity was highest at lower temperatures. The results indicate that the extended linker molecule in CPO-54 decreases the MOF's CO_2, CH_4, N_2 and O_2 adsorption capacity and the CO_2/N_2, and CO_2/CH_4 selectivity, compared to CPO-27.

It has been shown that the Q_{st} at the open metal sites in both CPO-54 and CPO-27 are of similar magnitude. The Q_{st} was found to be lower at the secondary adsorption site in CPO-54. The study has, furthermore, shown that CPO-54 has a high uptake of N_2O and a high selectivity of N_2O over N_2.

The study has also shown that CPO-54 can indeed, based on selectivity, be used to separate Xe and Kr, and that it has a significantly higher Xe/Kr selectivity than CPO-27.

6.2   Recommendations For Further Work

This thesis has given new insight into the CPO-54 series. However, there is still more to learn about the CPO-54 MOFs, and the following points might be of interest for further research:

- High-pressure gas adsorption has now been studied for CPO-54-Mn and CPO-54-Ni. A natural progression from this work will, therefore, be to investigate high-pressure adsorption for the remaining materials: CPO-54-Mg, CPO-54-Co, and CPO-54-Fe.

- To better understand how suitable CPO-54 actually is for CCS technology, further studies could address the efficiency (both energetically and economically) of a potential CCS process with CPO-54 as adsorbent.

- Based on the high Xe/Kr selectivity of CPO-54-Ni, it may be interesting to investigate further whether this property can be utilized in a separation process.

Appendix A

Matlab Code - Calculating The Isosteric Heat Of Adsorption From A Dual-Site Langmuir Model

```
clear all
clc
% Information required from user
% Name of input file with dual Langmuir-Freundlich parameters (without
% mandatory ending "_fitparam.dat"
FNBase = "ES-1-048_CO2";
% Format T q(sat)1 b1 v2 q(sat)2 b2 v2
% Temperature and dual Langmuir function parameters
% New row for each set
nmax = 0.0055;          % Max amount adsorbed (at highest T) / mol g-1
nstepwidth = 0.0001;    % Step width / mol g-1
nstep = double ( int32 ( nmax / nstepwidth ) );% Number of data points to calculate
% Had to use the double(int32()) construct because of some weird behavior
% of MATLAB that results in 0.0026 / 0.0001 = 26.0000 (instead of 26) whereupon the arra
% definitions further down result in an error.
Q = load(FNBase+'_fitparam.dat','-ascii')   % Don't forget to change the output
```

```matlab
% filename at the end!

[nTemp, ncol] = size(Q); % nTemp is the number of temperatures

T =  Q(:,1);

q1 = Q(:,2);

q2 = Q(:,5);

b1 = Q(:,3);

b2 = Q(:,6);

v1 = Q(:,4);

v2 = Q(:,7);

syms p real              % p / kPa

S=ones(nstep,1);

result=ones(nstep,nTemp+5); % Number of columns = nTemp plus 1 for n and 4 for output

%from linear regression

for i = 1:nstep

    n = nstepwidth*i;

    result(i,1)=n;

    for k = 1:nTemp

        eqn = [n == (q1(k) * b1(k) .* p^v1(k))/(1+b1(k) .* p^v1(k)) +

        (q2(k) * b2(k) .* p^v2(k))/(1+b2(k) .* p^v2(k))];

        S(i,1)=solve(eqn, p);

        result(i,1+k)=S(i);

    end

end

%Debugging

disp(result)

%plot(result(:,2),result(:,1),'bo',result(:,3),result(:,1),

%'go',result(:,4),result(:,1),'ro')

%set(gca, 'XScale','log')


% Now for the linear regression
```

```matlab
R = 8.314462;              % Universal gas constant / J K-1 mol-1

k = nTemp+2;               % Index for adding Q(st) data to 'result' array

Tinv = 1./T;               % x values = 1/T

for i = 1:size(result,1)

    parray = log(result(i,2:(1+nTemp)).*1000);  % ln p for all pressure values
%in a row, note conversion from kPa to Pa!

    parray = transpose(parray);

    b = polyfit(Tinv, parray, 1);        % Linear regression

    result(i,k) = b(1);      % Slope

    result(i,k+1) = b(2);    % Intercept

    yfit = polyval(b,Tinv);   % Compute R2 residual

    yresid = parray - yfit;

    SSresid = sum(yresid.^2);

    SStotal = (length(parray)-1) * var(parray);

    rsq = 1 - SSresid/SStotal;

    result(i,k+2) = rsq;

    Qst = -b(1)*R/1000;       % Qst / kJ mol-1

    result(i,k+3) = Qst;

end

%disp(result)

plot(result(:,1),result(:,k+3),'bo')

save(FNBase + '.mat','result')

save(FNBase + '.csv','result','-ascii')
```

Appendix B

Matlab Code - Calculating The Isosteric Heat Of Adsorption From A Virial Model

```
clear all
clc
% Information required from user
FNBase = "ES-1-048_CO2";
nmax = 0.0054;             % Max amount adsorbed (at highest T) / mol g-1
nstepwidth = 0.0001;    % Step width / mol g-1
%nstep =( nmax / nstepwidth );
nstep = double ( int32 ( nmax / nstepwidth ) );% Number of data points to calculate
% Had to use the double(int32()) construct because of some weird behavior
% of MATLAB that results in 0.0026 / 0.0001 = 26.0000 (instead of 26)
%whereupon the array
% definitions further down result in an error.
% Parameters from virial fitting.
%Number of parameters (ai) depends on the curve fitting.
a0 = ;
a1 = ;
a2 = ;
a3 = ;
```

```matlab
a4 = ;

a5 = ;

a6 = ;

a7 = ;

a8 = ;

a9 = ;

% Equation for calculating the Qst:

syms Qst                % Define variables

R = 8.314462;           % Universal gas constant / J K-1 mol-1

S=ones(nstep,1);

result=(nstep); % Number of columns

for i = 1:nstep

    n = nstepwidth*i;

    result(i,1)=n;

    for k = 1

        eqn = Qst == -R*(a0 + a1.*n + a2.*n^2 + a3.*n^3 + a4.*n^4 + a5.*n^5 +
        a6.*n^6+ a7.*n^7 + a8.*n^8+ a9.*n^9);

        S(i,1)=solve(eqn, Qst);

        result(i,1)=S(i);

    end

end

plot(result)

disp(result)

save(FNBase + '.csv','result','-ascii')
```

Appendix C

Dual-site Langmuir fits
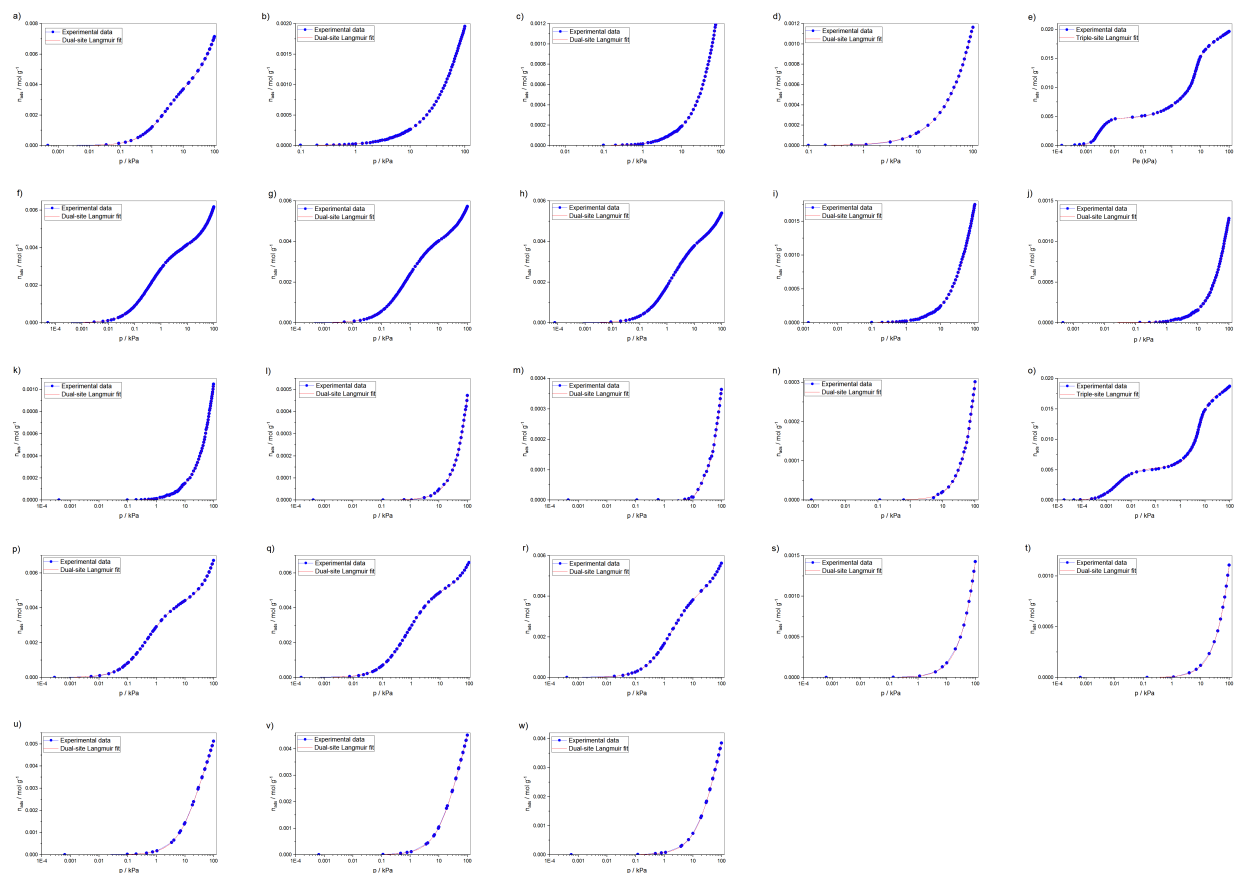
Figure C.1: Dueal-site Langmuir model fitted to experimental data for CPO-54-Mg. **a)** CH_4 195 K, **b)** CH_4 278 K, **c)** CH_4 288 K, **d)** CH_4 298 K, **e)** CO_2 195 K, **f)** CO_2 278 K, **g)** CO_2 288 K, **h)** CO_2 298 K, **i)** N_2 278 K, **j)** N_2 288 K, **k)** N_2 298 K, **l)** O_2 278 K, **m)** O_2 288 K, **n)** O_2 298 K, **o)** N_2O 195 K, **p)** N_2O 278 K, **q)** N_2O 288 K, **r)** N_2O 298 K, **s)** Kr 278 K, **t)** Kr 288 K, **v)** Kr 298 K, **v)** Xe 288 K and **w)** Xe 298 K.

Table C.1: Parameters from the dueal-site Langmuir model fitted to experimental data for CPO-54-Mg.

| Gas / Temp	q1	b1	v1	q2	b2	v2	R-squared
CH4, 195 K	0.0068 ± 0	9.9386E-4 ± 6.59264E-5	1.42958 ± 0.01164	0.0068 ± 0	0.35075 ± 0.0031	0.98965 ± 0.00538	0.99999
CH4, 278 K	0.0068 ± 0	0.00354 ± 1.04456E-4	1.01861 ± 0.00662	0.0068 ± 0	8.99548E-4 ± 2.40912E-4	0.52319 ± 0.19652	0.99991
CH4, 288 K	0.0068 ± 0	0.00169 ± 1.25634E-4	1.0514 ± 0.00757	0.0068 ± 0	0.00161 ± 1.62961E-4	0.61949 ± 0.09707	0.9999
CH4, 298 K	0.0068 ± 0	0.00178 ± 6.1154E-5	1.03281 ± 0.007	0.0068 ± 0	0 ± 7.35834E-12	12.28088 ± 0	0.99992
CO2, 195 K	0.0068 ± 0	1.25559E7 ± 6674550.87712	2.80287 ± 0.08887	0.0068 ± 0	4.6309E-5 ± 1.90724E-5	5.24781 ± 0.21359	0.99998
CO2, 278 K	0.0068 ± 0	0.0022 ± 1.11876E-4	1.13897 ± 0.01029	0.0068 ± 0	2.22758 ± 0.01778	0.91099 ± 0.0033	0.9999
CO2, 288 K	0.0068 ± 0	0.00167 ± 9.20551E-5	1.11657 ± 0.01084	0.0068 ± 0	1.27136 ± 0.00707	0.91805 ± 0.00266	0.99998
CO2, 298 K	0.0068 ± 0	8.36089E-4 ± 8.49371E-5	1.19222 ± 0.01961	0.0068 ± 0	0.70139 ± 0.00447	0.91186 ± 0.00312	0.99998
N2, 278 K	0.0068 ± 0	0.00427 ± 7.66323E-5	0.9564 ± 0.00358	0.0068 ± 0	2.46169E-15 ± 3.10459E-4	0 ± 2.18903E10	0.9997
N2, 288 K	0.0068 ± 0	0.00229 ± 1.39898E-4	1.00391 ± 0.00971	0.0068 ± 0	6.79539E-4 ± 2.22247E-4	0.20261 ± 0.35252	0.99977
N2, 298 K	0.0068 ± 0	0.00285 ± 1.07138E-4	0.86509 ± 0.04481	0.0068 ± 0	1.34461E-5 ± 5.96119E-5	1.60339 ± 0.738	0.99965
O2, 278 K	0.0068 ± 0	9.86745E-5 ± 1.48104	1.1825 ± 2264.04844	0.0068 ± 0	9.62295E-5 ± 1.48083	1.18271 ± 2323.09523	0.99899
O2, 288 K	0.0068 ± 0	9.65839E-14 ± 2.03269E-4	1.64004 ± 3.14504E8	0.0068 ± 0	5.0969E-4 ± 7.06696E-5	1.0836 ± 0.36585	0.99947
O2, 298 K	0.0068 ± 0	9.86745E-5 ± 1.48104	1.1825 ± 2264.04844	0.0068 ± 0	9.62295E-5 ± 1.48083	1.18271 ± 2323.09523	0.99899
N2O, 195 K	0.0068 ± 0	0.1974 ± 0.04577	0.62672 ± 0.36189	0.0068 ± 0	0.02323 ± 0.00925	2.24451 ± 0.25374	0.99937
N2O, 278 K	0.0068 ± 0	0.00166 ± 1.54125E-4	1.25073 ± 0.01859	0.0068 ± 0	1.81705 ± 0.02493	0.00451 ± 1.91518E-5	0.99995
N2O, 288 K	0.0068 ± 0	0.00197 ± 2.7045E-4	1.09189 ± 0.02697	0.0068 ± 0	1.32269 ± 0.01401	0.93698 ± 0.00443	0.99996
N2O, 298 K	0.0068 ± 0	0.0013 ± 1.87395E-4	1.14815 ± 0.02739	0.0068 ± 0	0.59881 ± 0.00553	0.93941 ± 0.00441	0.99998
Kr, 278 K	0.0068 ± 0	0.00271 ± 6.16627E-5	1.01108 ± 0.00529	0.0068 ± 0	2.88526 ± 0	1.37007 ± 0	0.9999
Kr, 288 K	0.0068 ± 0	0.00151 ± 3.78991E-5	1.06902 ± 0.00578	0.0068 ± 0	3.37421 ± 0	1.87307 ± 0	0.99989
Kr, 298 K	0.0068 ± 0	0.02739 ± 2.43123E-4	1.02441 ± 0.00311	0.0068 ± 0	2.84127E-8 ± 2.5601E-8	3.12934 ± 0.18777	0.99998
Xe, 278 K	0.0068 ± 0	0.02739 ± 2.43123E-4	1.02441 ± 0.00311	0.0068 ± 0	2.84127E-8 ± 2.5601E-8	3.12934 ± 0.18777	0.99998
Xe, 288 K	0.0068 ± 0	0.01746 ± 1.53139E-4	1.04486 ± 0.0028	0.0068 ± 0	4.99195E-10 ± 9.45166E-10	3.8411 ± 0.39076	0.99999
Xe, 298 K	0.0068 ± 0	0.00974 ± 0.00102	0.92131 ± 0.05266	0.0068 ± 0	0.00939 ± 8.96125E-4	1.25101 ± 0.03217	0.99999
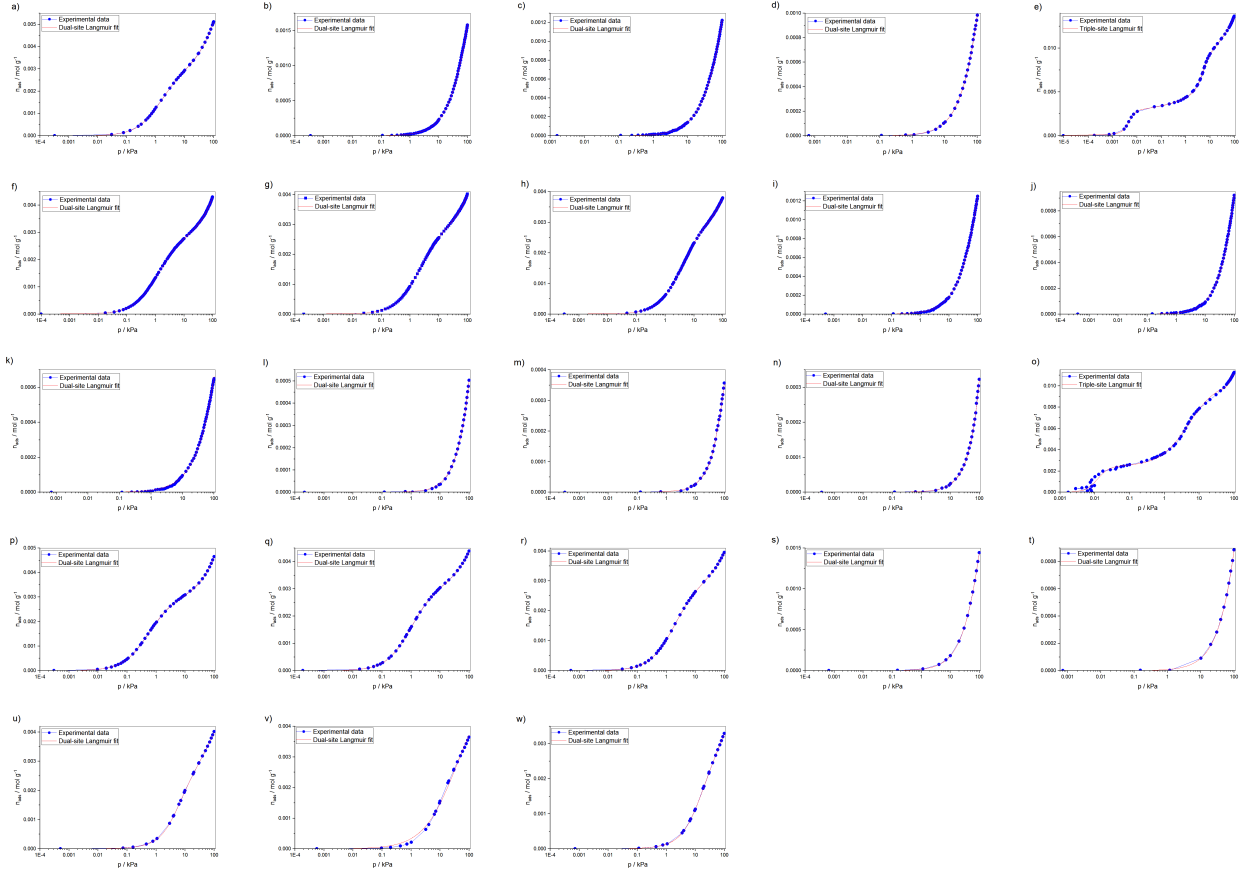
Figure C.2: Dueal-site Langmuir model fitted to experimental data for CPO-54-Ni. **a)** CH_4 195 K, **b)** CH_4 278 K, **c)** CH_4 288 K, **d)** CH_4 298 K, **e)** CO_2 195 K, **f)** CO_2 278 K, **g)** CO_2 288 K, **h)** CO_2 298 K, **i)** N_2 278 K, **j)** N_2 288 K, **k)** N_2 298 K, **l)** O_2 278 K, **m)** O_2 288 K, **n)** O_2 298 K, **o)** N_2O 195 K, **p)** N_2O 278 K, **q)** N_2O 288 K, **r)** N_2O 298 K, **s)** Kr 278 K, **t)** Kr 288 K, **v)** Kr 298 K, **v)** Xe 288 K and **w)** Xe 298 K.

Table C.2: Parameters from the dueal-site Langmuir model fitted to experimental data for CPO-54-Ni.

Gas / Temp	q1	b1	v1	q2	b2	v2	R-squared
CH4, 195 K	0.0055 ± 0	0.0032 ± 2.41256E-4	1.1306 ± 0.01316	0.0055 ± 0	0.63893 ± 0.00829	1.01814 ± 0.00766	0.99998
CH4, 278 K	0.0055 ± 0	0.00455 ± 5.8778E-5	0.97665 ± 0.00307	0.0055 ± 0	2.54726E-17 ± 8.15173E-4	0.29949 ± 9.58432E12	0.99979
CH4, 288 K	0.0055 ± 0	3.56855E-21 ± 0	0.97099 ± 0	0.0055 ± 0	0.00255 ± 2.99229E-5	1.02577 ± 0.00275	0.99986
CH4, 298 K	0.0055 ± 0	0.00192 ± 7.27111E-5	1.02857 ± 0.01013	0.0055 ± 0	6.59036E-21 ± 1.66855E-9	3.40274 ± 4.78884E10	0.99979
CO2, 195 K	0.0055 ± 0	0.00681 ± 0.00201	3.14318 ± 0.18562	0.0055 ± 0	3.17407E7 ± 6.52686E7	3.22091 ± 0.3815	0.9998
CO2, 278 K	0.0055 ± 0	0.00191 ± 1.17449E-4	1.11404 ± 0.01162	0.0055 ± 0	0.79753 ± 0.00564	0.99735 ± 0.00391	0.99997
CO2, 288 K	0.0055 ± 0	0.00149 ± 1.42998E-4	1.10669 ± 0.0177	0.0055 ± 0	0.44311 ± 0.00313	1.01769 ± 0.004	0.99998
CO2, 298 K	0.0055 ± 0	4.89734E-4 ± 8.45867E-5	1.25772 ± 0.03238	0.0055 ± 0	0.2382 ± 0.00156	1.0242 ± 0.00375	0.99998
N2, 278 K	0.0055 ± 0	0.00416 ± 6.77491E-5	0.92693 ± 0.00385	0 ± 0	0 ± 0	0 ± 0	0.99966
N2, 288 K	0.0055 ± 0	0.00174 ± 3.88526E-5	1.03304 ± 0.0052	0 ± 0	0 ± 0	0 ± 0	0.99952
N2, 298 K	0.0055 ± 0	0.00225 ± 4.9226E-5	0.89144 ± 0.00513	0 ± 0	0 ± 0	0 ± 0	0.99938
O2, 278 K	0.0055 ± 0	7.88069E-18 ± 5.94353E-4	0.01319 ± 1.32151E13	0.0055 ± 0	5.89598E-4 ± 1.92225E-5	1.11497 ± 0.00748	0.99965
O2, 288 K	0.0055 ± 0	4.01088E-4 ± 2.71228E-5	1.09938 ± 0.01878	0.0055 ± 0	2.12781E-11 ± 7.70387E-10	6.40343 ± 9.50719	0.99943
O2, 298 K	0.0055 ± 0	3.71989E-4 ± 7.92337E-5	1.03026 ± 0.16787	0.0055 ± 0	4.06091E-6 ± 1.97038E-5	1.82435 ± 0.75544	0.99963
N2O, 195 K	0.0055 ± 0	8.92227E-24 ± 1.0839E-22	12.27862 ± 2.81835	0.0055 ± 0	88888.37826 ± 203830.87339	2.56875 ± 0.48597	0.9994
N2O, 278 K	0.0055 ± 0	0.00339 ± 3.60242E-4	1.04127 ± 0.02087	0.0055 ± 0	1.74642 ± 0.0285	0.98797 ± 0.007	0.99995
N2O, 288 K	0.0055 ± 0	0.00362 ± 3.45641E-4	0.95926 ± 0.01795	0.0055 ± 0	0.99624 ± 0.00971	1.01177 ± 0.00497	0.99998
N2O, 298 K	0.0055 ± 0	0.00243 ± 1.79036E-4	0.98621 ± 0.01341	0.0055 ± 0	1.00708 ± 0.00276	0 ± 0	1
Kr, 278 K	0.0055 ± 0	0.00334 ± 6.55452E-5	1.0274 ± 0.00773	0 ± 0	0.33251 ± 0	0.81539 ± 0	0.99998
Kr, 288 K	0.0055 ± 0	0.00219 ± 5.29342E-5	1.02945 ± 0.00559	0 ± 0	2.18193 ± 0	2.54032 ± 0	0.99989
Kr, 298 K	0.0055 ± 0	0.00148 ± 3.68693E-5	1.0561 ± 0.00573	0 ± 0	6.40361 ± 0	-0.46114 ± 0	0.9999
Xe, 278 K	0.0055 ± 0	0.02928 ± 0.00544	0.67206 ± 0.01489	0.0055 ± 0	0.09368 ± 0.00883	1.41488 ± 0.08108	0.99994
Xe, 288 K	0.0055 ± 0	0.06504 ± 0.00395	0.75187 ± 0.01719	0 ± 0	1.45251 ± 0	1.44225 ± 0	0.9996
Xe, 298 K	0.0055 ± 0	0.01194 ± 9.97806E-4	0.70077 ± 0.00691	0.0055 ± 0	0.03208 ± 0.00102	1.26318 ± 0.01963	0.99999

Table C.3: Parameters from the dueal-site Langmuir model fitted to experimental high-pressure data for CPO-54-Ni.

Gas / Temp	q1	b1	v1	q2	b2	v2	R-squared
CH4, 278 K	0.0055 ± 0	2.44321E-4 ± 1.16239E-4	0.8187 ± 0.04778	0.0055 ± 0	0.00591 ± 1.69806E-4	0.70949 ± 0.0086	0.9999
CH4, 288 K	0.0055 ± 0	2.42539E-5 ± 1.02733E-5	1.03133 ± 0.04336	0.0055 ± 0	0.00411 ± 1.32695E-4	0.75871 ± 0.00675	0.99992
CH4, 298 K	0.0055 ± 0	2.41198E-5 ± 1.42459E-5	1.01742 ± 0.0601	0.0055 ± 0	0.00324 ± 1.26024E-4	0.77107 ± 0.00828	0.99989
CO2, 278 K	0.0055 ± 0	0.12188 ± 0.00511	0.27713 ± 0.00879	0.0055 ± 0	6.3906E-4 ± 6.22212E-5	1.16614 ± 0.01711	0.9995
CO2, 288 K	0.0055 ± 0	0.11924 ± 0.00465	0.25271 ± 0.00835	0.0055 ± 0	5.65656E-4 ± 4.86371E-5	1.14011 ± 0.01484	0.99958
CO2, 298 K	0.0055 ± 0	0.08819 ± 0.00364	0.30083 ± 0.00898	0.0055 ± 0	5.66099E-4 ± 5.51392E-5	1.07172 ± 0.01613	0.99942
N2, 288 K	0.0055 ± 0	2.00459E-8 ± 2.27061E-8	1.7659 ± 0.11694	0.0055 ± 0	0.00281 ± 1.49526E-4	0.71587 ± 0.00875	0.99978
N2, 298 K	0.0055 ± 0	1.25263E-9 ± 2.59917E-9	2.00092 ± 0.21397	0.0055 ± 0	0.00192 ± 1.03522E-4	0.74699 ± 0.00839	0.99975
N2, 303 K	0.0055 ± 0	5.53764E-11 ± 1.67915E-10	2.29691 ± 0.31163	0.0055 ± 0	9.97569E-4 ± 5.16916E-5	0.80997 ± 0.00768	0.99979
O2, 278 K	0.0055 ± 0	3.67238E-7 ± 2.02062E-7	1.533 ± 0.05811	0.0055 ± 0	9.72953E-4 ± 3.95521E-5	0.87283 ± 0.00733	0.99996
O2, 288 K	0.0055 ± 0	2.41041E-8 ± 1.98886E-8	1.79423 ± 0.08763	0.0055 ± 0	6.1847E-4 ± 2.68322E-5	0.9178 ± 0.00719	0.99995
O2, 298 K	0.0055 ± 0	5.14332E-4 ± 2.12875E-5	0.91969 ± 0.00712	0.0055 ± 0	7.16684E-8 ± 6.701E-8	1.6394 ± 0.09821	0.99996

Figure C.3: Dueal-site Langmuir model fitted to high-pressure experimental data for CPO-54-Ni **a)** CH_4 278 K, **b)** CH_4 288 K, **c)** CH_4 298 K, **d)** CO_2 278 K, **e)** CO_2 288 K, **f)** CO_2 298 K, **g)** N_2 288 K, **h)** N_2 298 K, **i)** N_2 303 K, **j)** O_2 278 K, **k)** O_2 288 K and **l)** O_2 298 K.
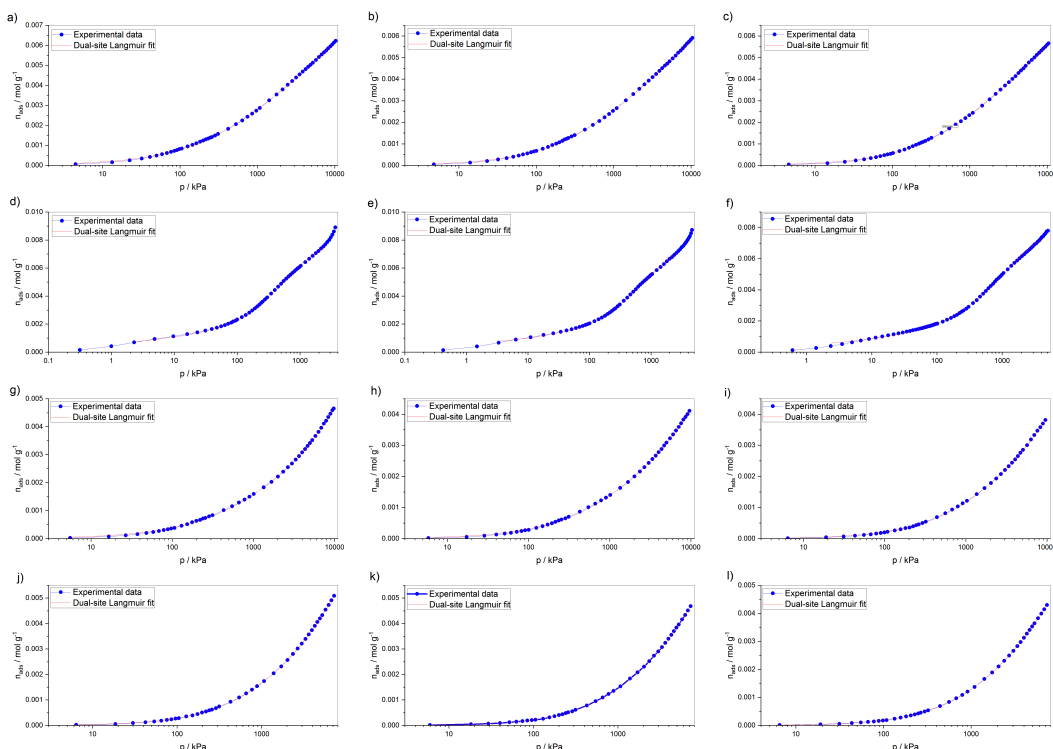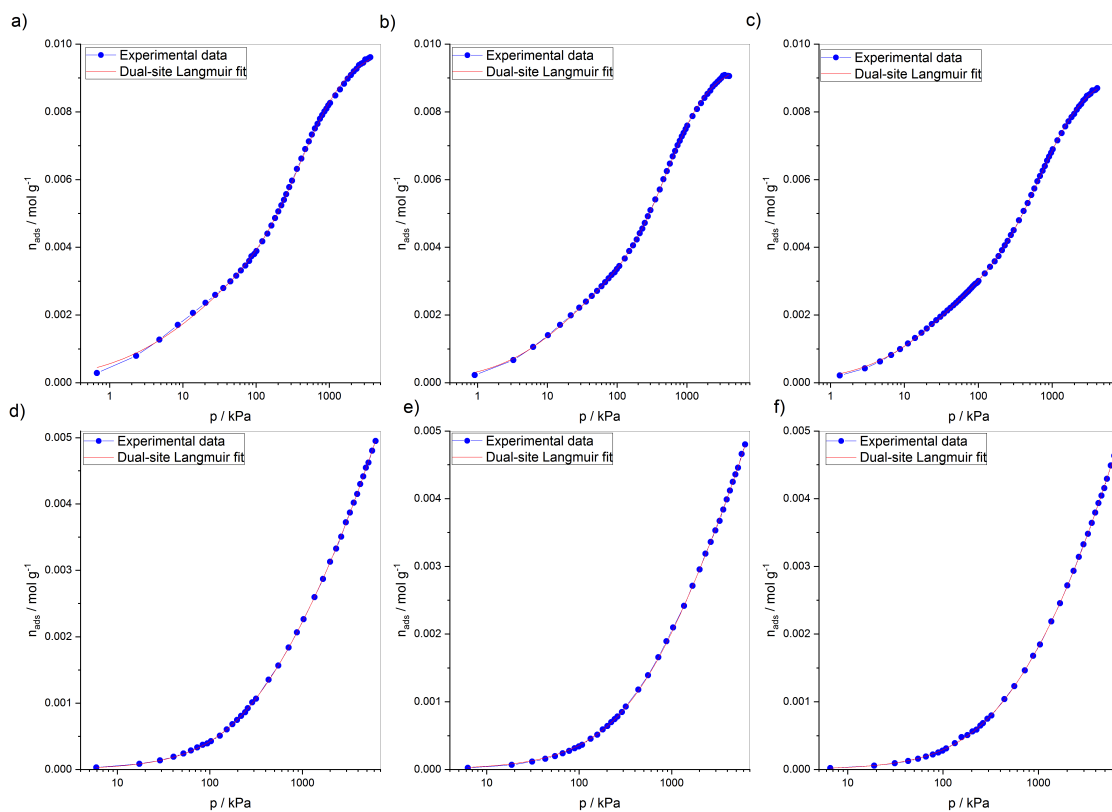
Figure C.4: Dueal-site Langmuir model fitted to high-pressure experimental data for CPO-54-Mn **a)** CO_2 278 K, **b)** CO_2 288 K, **c)** CO_2 298 K, **d)** N_2 278 K, **e)** N_2 288 K and **f)** N_2 298 K.

Table C.4: Parameters from the dueal-site Langmuir model fitted to experimental high-pressure data for CPO-54-Mn.

Gas / Temp	q1	b1	v1	q2	b2	v2	R-squared
CO2, 278 K	0.0056 ± 0	3.12664E-4 ± 5.6	1.32842 ± 0.029	0.0056 ± 0	0.14477 ± 0.007	0.63484 ± 0.024	0.99959
CO2, 288 K	0.0056 ± 0	1.29472E-4 ± 1.4	1.41717 ± 0.017	0.0056 ± 0	0.09109 ± 0.004	0.76402 ± 0.016	0.99985
CO2, 298 K	0.0056 ± 0	1.37438E-4 ± 9.7	1.35175 ± 0.011	0.0056 ± 0	0.06198 ± 0.001	0.82175 ± 0.010	0.99992
N2, 278 K	0.0056 ± 0	3.35364E-5 ± 1.3	1.12196 ± 0.032	0.0056 ± 0	0.00157 ± 6.127	0.97202 ± 0.014	0.99997
N2, 288 K	0.0056 ± 0	0.00106 ± 6.941	0.90465 ± 0.013	0.0056 ± 0	1.02553E-7 ± 1.7	1.53423 ± 0.620	0.99992
N2, 298 K	0.0056 ± 0	2.43613E-5 ± 1.0	1.16892 ± 0.030	0.0056 ± 0	0.00107 ± 7.411	0.99474 ± 0.022	0.99994
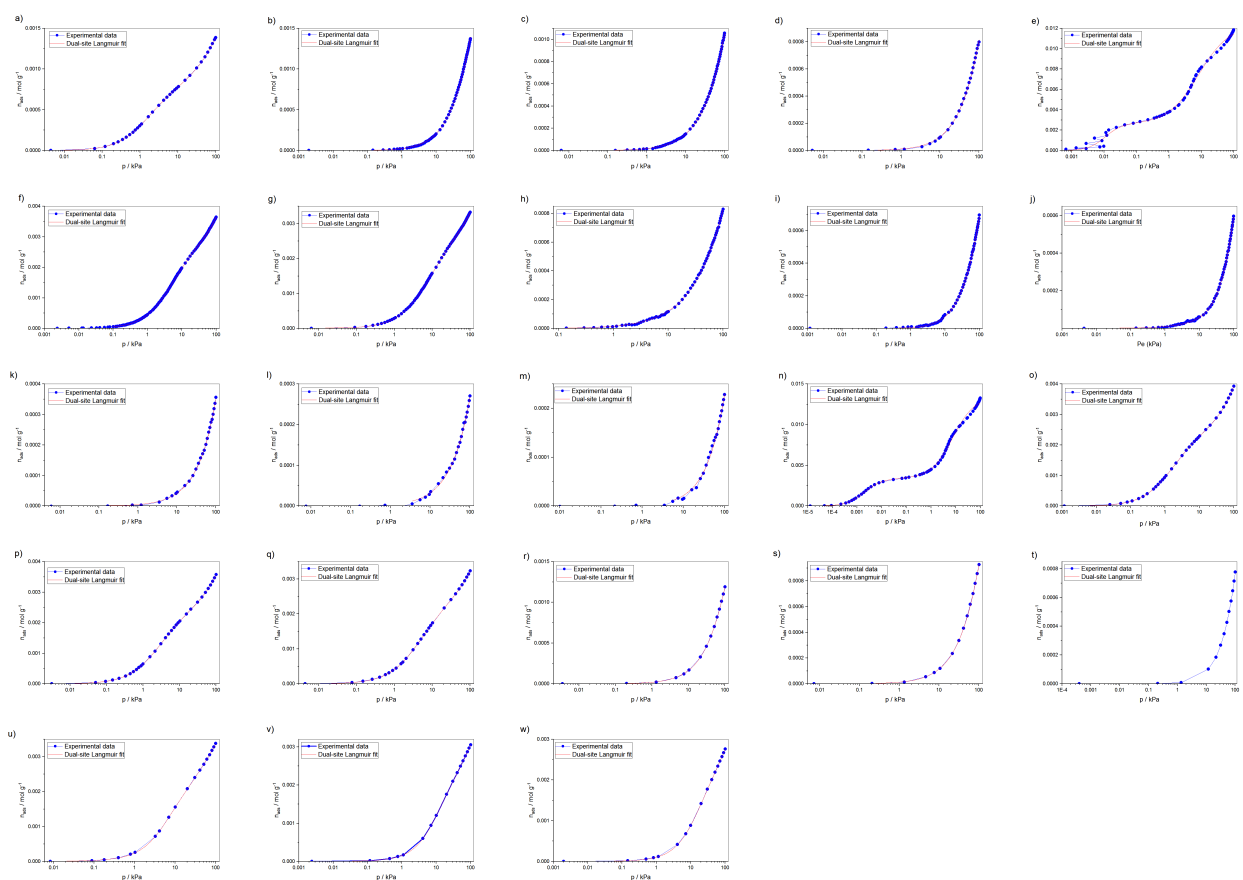
Figure C.5: Dueal-site Langmuir model fitted to experimental data for CPO-54-Co. **a)** CH_4 195 K, **b)** CH_4 278 K, **c)** CH_4 288 K, **d)** CH_4 298 K, **e)** CO_2 195 K, **f)** CO_2 278 K, **g)** CO_2 288 K, **h)** CO_2 298 K, **i)** N_2 278 K, **j)** N_2 288 K, **k)** N_2 298 K, **l)** O_2 278 K, **m)** O_2 288 K, **n)** O_2 298 K, **o)** N_2O 195 K, **p)** N_2O 278 K, **q)** N_2O 288 K, **r)** N_2O 298 K, **s)** Kr 278 K, **t)** Kr 288 K, **v)** Kr 298 K, **v)** Xe 288 K and **w)** Xe 298 K.

Table C.5: Parameters from the dueal-site Langmuir model fitted to experimental data for CPO-54-Co.

Gas / Temp	q1	b1	v1	q2	b2	v2	R-squared
CH4, 195 K	0.0055 ± 0	0.00588 ± 3.42163E-4	0.69418 ± 0.00984	0.0055 ± 0	0.62909 ± 0.00634	1.07722 ± 0.00782	0.99999
CH4, 278 K	0.0055 ± 0	0.00458 ± 7.09453E-5	0.93322 ± 0.00367	0.0055 ± 0	9.05493E-19 ± 0	0.411 ± 0	0.99971
CH4, 288 K	0.0055 ± 0	0.0033 ± 5.02802E-5	0.92571 ± 0.00448	0.0055 ± 0	6.05783E-13 ± 1.4932E-11	4.65948 ± 4.96465	0.99991
CH4, 298 K	0.0055 ± 0	0.00204 ± 1.04316E-4	0.96252 ± 0.01085	0.0055 ± 0	7.62941E-15 ± 5.12008E-4	3.65427E-9 ± 0	0.99951
CO2, 195 K	0.0055 ± 0	0.14351 ± 0.02095	0.91554 ± 0.0782	0.0055 ± 0	0.00261 ± 1.97569E-4	1.69296 ± 0.43635	0.9991
CO2, 278 K	0.0055 ± 0	4.18071E-4 ± 9.73502E-5	1.31464 ± 0.04348	0.0055 ± 0	0.17772 ± 0.00178	1.01857 ± 0.00437	0.99996
CO2, 288 K	0.0055 ± 0	1.36592E-4 ± 3.25474E-5	1.46467 ± 0.04446	0.0055 ± 0	0.1041 ± 6.72947E-4	1.01412 ± 0.00329	0.99999
CO2, 298 K	0.0055 ± 0	0.00287 ± 8.4523E-5	0.89395 ± 0.00618	0.0055 ± 0	0.16366 ± 0	26.03327 ± 0	0.99972
N2, 278 K	0.0055 ± 0	3.74589E-4 ± 0.01527	1.16546 ± 5.61962	0.0055 ± 0	0.00703 ± 0.00388	1.1386 ± 2.57129	0.9997
N2, 288 K	0.0055 ± 0	0.00178 ± 1.31495E-4	0.65479 ± 0.10598	0.0055 ± 0	3.07367E-4 ± 1.85152E-4	1.58174 ± 0.19333	0.99969
N2, 298 K	0.0055 ± 0	0.14351 ± 0.02095	0.69418 ± 0.00984	0.0055 ± 0	7.62941E-15 ± 5.12008E-4	1.69296 ± 0.43635	0.99983
O2, 278 K	0.0055 ± 0	4.19558E-33 ± 1.57898E-32	14.72282 ± 0.2531	0.0055 ± 0	8.757E-4 ± 3.56004E-5	0.94071 ± 0.00997	0.99952
O2, 288 K	0.0055 ± 0	1.85384E-14 ± 6.09199E-4	2.21176E-4 ± 3542668.56685	0.0055 ± 0	6.8611E-4 ± 1.02165E-4	0.93504 ± 0.03053	0.9997
O2, 298 K	0.0055 ± 0	1.16703E-19 ± 0	1.67776E-8 ± 0	0.0055 ± 0	3.58546E-4 ± 3.59706E-5	1.03989 ± 0.02299	0.9996
N2O, 195 K	0.0055 ± 0	0.00284 ± 1.73786E-4	1.05109 ± 0.01105	0.0055 ± 0	0.59778 ± 0.0052	0.96162 ± 0.00421	0.99999
N2O, 278 K	0.0055 ± 0	0.00284 ± 1.73786E-4	1.05109 ± 0.01105	0.0055 ± 0	0.00249 ± 1.42017E-5	0.59778 ± 0.0052	0.99999
N2O, 288 K	0.0055 ± 0	0.00242 ± 2.30179E-4	1.02093 ± 0.01667	0.0055 ± 0	0.00246 ± 2.02186E-5	0.34179 ± 0.00309	0.99999
N2O, 298 K	0.0055 ± 0	0.0018 ± 2.44923E-4	1.02445 ± 0.0234	0 ± 0	0.20084 ± 0.00177	1.01349 ± 0.00401	1
Kr, 278 K	0.0055 ± 0	0.0034 ± 7.75732E-5	0.95241 ± 0.0053	0 ± 0	2.91309 ± 0	1.24516 ± 0	0.99988
Kr, 288 K	0.0055 ± 0	0.00225 ± 4.41539E-5	0.97549 ± 0.00454	0 ± 0	1.95987 ± 0	1.97037 ± 0	0.99992
Kr, 298 K	0.0055 ± 0	3.45762E-16 ± 4.75666E-5	0.83025 ± 7.67561E10	0 ± 0	0.00199 ± 1.75014E-4	1.03588 ± 0.01303	0.99996
Xe, 278 K	0.0055 ± 0	0.02359 ± 0.00397	0.6801 ± 0.0151	0.0055 ± 0	0.08666 ± 0.0084	1.38157 ± 0.08249	0.99996
Xe, 288 K	0.0055 ± 0	0.01539 ± 0.00162	0.69743 ± 0.00928	0.0055 ± 0	0.04897 ± 0.0029	1.31828 ± 0.0397	0.99999
Xe, 298 K	0.0055 ± 0	0.01008 ± 9.4725E-4	0.72315 ± 0.00798	0.0055 ± 0	0.03061 ± 0.00134	1.26174 ± 0.0272	1

Appendix D

pyIAST Code

This code were written for Python 3 to run the pyIAST package and calculate the separation coefficients.

IAST calculations

The IAST code with a binary mixture of CO2 and N2 adsorbed in metal-organic framework.

Pure-component adsorption isotherms at same temperature should be provided in a form of .csv files:

- `ES-1-048_N2_278K.csv`
- `ES-1-048_CO2_278K.csv` , where "Pressure" is in bar and "Gas uptake" in mmol/g.

At the first step, the experimental pure-component adsorption isotherms is uploaded.

At the second step, the experimental pure-component adsorption isotherms are fitted using different models. In order to pront the fit of the data using dual-site Langmuir model, one can use M and K Langmuir model parameters, if needed.

```python
import pyiast
import pandas as pd
import numpy as np
import matplotlib.pyplot as plt

# Matplotlib settings
plt.style.use('bmh')
%matplotlib inline
%config InlineBackend.rc = {'font.size': 15, 'lines.linewidth':3, 'axes.facecolor':'w', 'legend.numpoints':1}

# colors to use for plots
color_key = {'N2':'g', 'CO2':'r'}
```

Load experimental pure-component isotherm data as Pandas dataframes

N2

```python
df_N2 = pd.read_csv("ES-1-048_N2_278K_bar.csv"    , skiprows=[1,]) #skiprows specify rows that are skipped in the csv
df_N2.head()
```

CO2

```
In [ ]: df_CO2 = pd.read_csv("ES-1-048_CO2_278K_bar.csv", skiprows=[1]) #skiprows specify rows that are skipped in the csv file
        df_CO2.head()
```

Plot isotherm data

in order to make sure that the date was uploaded correctly

```
In [ ]: fig, ax = plt.subplots()

        plt.scatter(df_CO2['Pressure (bar)'], df_CO2['Uptake (mmol/g)'],
                    label='CO2', color=color_key['CO2'], s=50)
        plt.scatter(df_N2['Pressure (bar)'], df_N2['Uptake (mmol/g)'],
                    label='N2', color=color_key['N2'], s=50, marker='s')

        plt.xlabel('Pressure (bar)')
        plt.ylabel('Gas uptake (mmol/g)')

        plt.xlim([-0.01, 1.05])
        plt.ylim([0, 7])


        plt.legend(loc='upper left')

        plt.tight_layout()
        plt.savefig("pure_component_isotherms.pdf", format='pdf')
        plt.savefig("pure_component_isotherms.png", format='png', dpi=250)
        plt.show()
```

Fit experimental pure-component isotherm data using theoretical model

Interpolator isotherm for N2

```
In [ ]: #N2_isotherm = pyiast.InterpolatorIsotherm(df_N2, loading_key="Uptake (mol/g)",
        #                                           pressure_key="Pressure (kPa)",
        #                                           fill_value=df_N2["Uptake (mol/g)"].max())
        #pyiast.plot_isotherm(N2_isotherm)
```

Langmuir isotherm for N2

```
In [ ]: N2_isotherm = pyiast.ModelIsotherm(df_N2,
                                            loading_key="Uptake (mmol/g)",
                                            pressure_key="Pressure (bar)",
                                            model="DSLangmuir" ,
                                            param_guess={"M1": 6.8, 'K1': 1, "M2": 0.8, 'K2': 1}, #starting parameters for dual-
                                            optimization_method='Powell'
                                            )
        pyiast.ModelIsotherm.print_params(N2_isotherm) # output parameters of the model
        pyiast.plot_isotherm(N2_isotherm)
```

Interpolator isotherm for carbon dioxide

```
In [ ]: #CO2_isotherm = pyiast.InterpolatorIsotherm(df_CO2, loading_key="Uptake (mmol/g)",
        #                                           pressure_key="Pressure (bar)",
        #                                           fill_value=df_CO2["Uptake (mmol/g)"].max())
        #pyiast.plot_isotherm(CO2_isotherm)
```

Langmuir isotherm for carbon dioxide

```
In [ ]: O2_isotherm = pyiast.ModelIsotherm(df_CO2,
                                   loading_key="Uptake (mmol/g)",
                                   pressure_key="Pressure (bar)",
                                   #model="Quadratic" ,
                                   model="DSLangmuir" ,
                                   param_guess={"M1":6.8 , 'K1':1 , "M2":6.8 , 'K2':1}, #starting parameters for dual-s
                                   optimization_method='Powell'
                                   )

        yiast.ModelIsotherm.print_params(CO2_isotherm) # output parameters of the model
        yiast.plot_isotherm(CO2_isotherm, xlogscale=False)
```

Perform IAST calculations

```
In [ ]: nsteps = 100
        iast_component_loadings = np.zeros((2, nsteps))
        partial_pressure = np.zeros((2, nsteps))

        y = np.array([, ]) # input gas mole fractions here. CO2 is component 0, N2 is component 1 in the array.
        tot_pressure =  # input total pressure (bar) here

        for i in range(1 , nsteps):
            partial_pressure[0, i] = y[0]*tot_pressure / nsteps * i
            partial_pressure[1, i] = y[1]*tot_pressure / nsteps * i

            iast_component_loadings[:, i] = pyiast.iast(partial_pressure[:,i],
                                   [CO2_isotherm, N2_isotherm],
                                   verboseflag=False)
```

Output results of calculations

Loading CO2

```
In [ ]: iast_component_loadings[0, :] #loading CO2
```

Loading N2

```
In [ ]: iast_component_loadings[1, :] #Loading N2
```

Partial pressure CO2

```
In [ ]: partial_pressure[0, :] #part pressure CO2
```

Partial pressure N2

```
In [ ]: partial_pressure[1, :] #part pressure N2
```

Selectivity CO2

```
In [ ]: (iast_component_loadings[0, :]/partial_pressure[0, :])/(iast_component_loadings[1, :]/partial_pressure[1, :]) #selecti
```

Results are combined in array

```
In [ ]: output_array = np.zeros((6, nsteps))

        for i in range(1 , nsteps):
            output_array[0, i] = iast_component_loadings[0, i] #loading CO2
            output_array[1, i] = iast_component_loadings[1, i] #Loading N2
            output_array[2, i] = partial_pressure[0, i] #part pressure CO2
            output_array[3, i] = partial_pressure[1, i] #part pressure N2
            output_array[4, i] = partial_pressure[0, i] + partial_pressure[1, i] #total pressure
            output_array[5, i] = (iast_component_loadings[0, i]/partial_pressure[0, i])/(iast_component_loadings[1, i]/partial_
```

```
In [ ]: output_array
```

Output results of calculations as .xls file

```
In [ ]: li = ['Uptake CO2 / mmol g-1','Uptake N2 / mmol g-1','part pressure CO2 / bar', 'part pressure N2 / bar', 'total pressu
        IASTfile = pd.DataFrame(output_array, dtype='str', index=li)
        IASTfile.to_excel("IAST_N2-CO2_CPO-54-Mg_278K.xls")
```

134

Appendix E

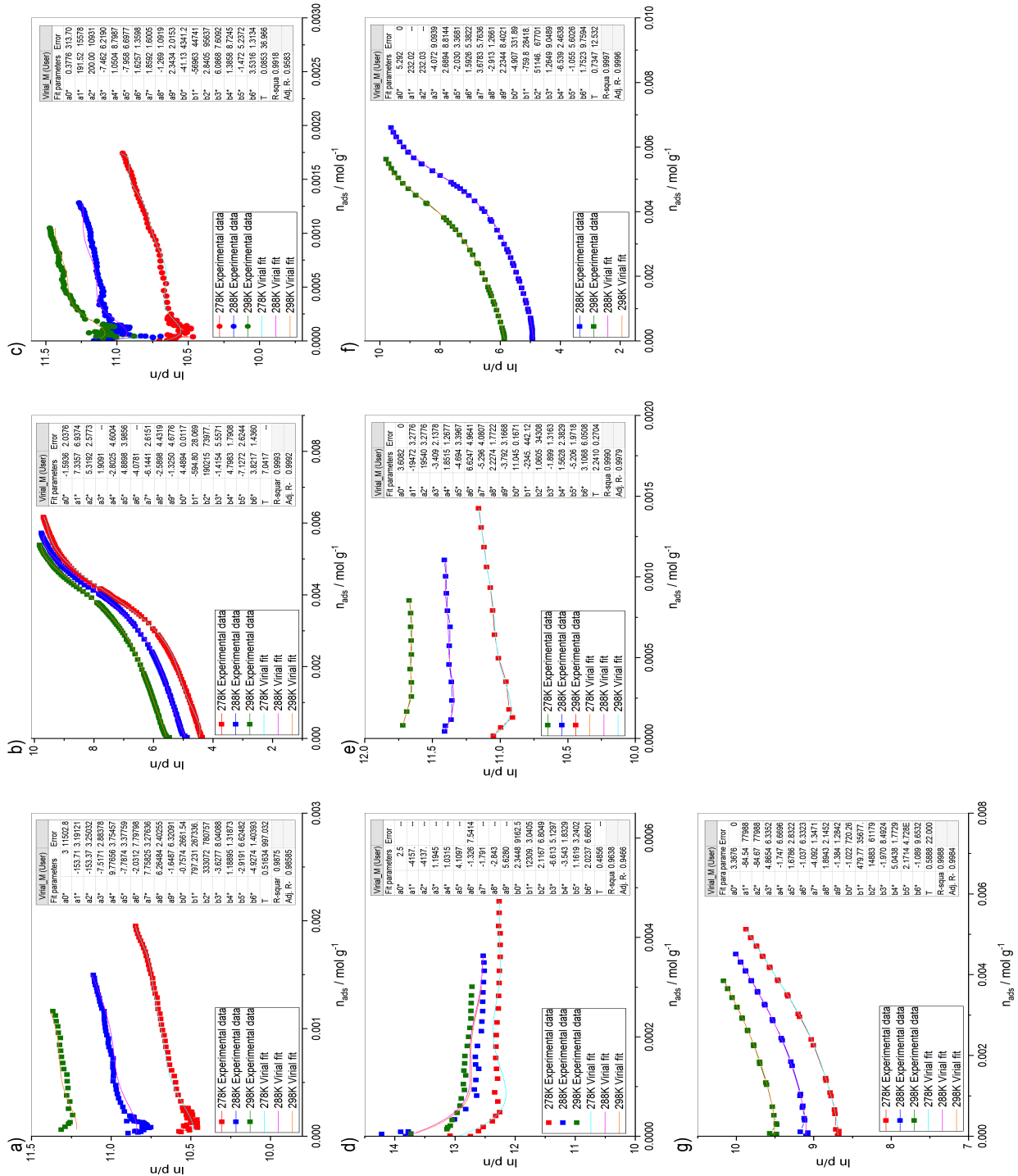# Fits of a virial equation to the experimental data

Figure E.1: Virial equation fitted to the standard-pressure experimental data for CPO-54-Mg. **a)** CH_4, **b)** CO_2, **c)** N_2, **d)** O_2, **e)** Kr, **f)** N_2O and **g)** Xe.
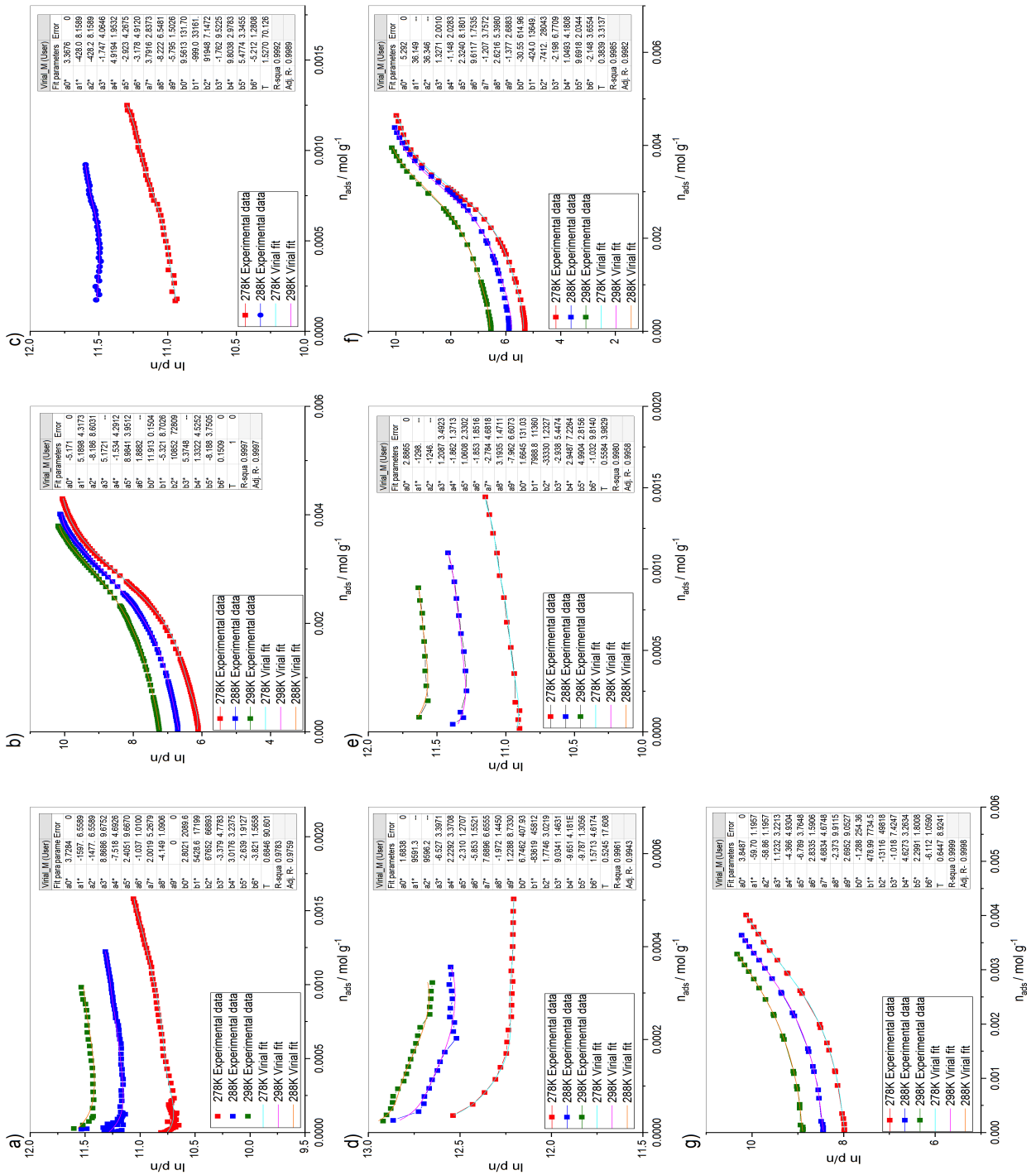
Figure E.2: Virial equation fitted to the standard-pressure experimental data for CPO-54-Ni. **a)** CH_4, **b)** CO_2, **c)** N_2, **d)** O_2, **e)** Kr, **f)** N_2O and **g)** Xe.

Figure E.3: Virial equation fitted to the high-pressure experimental data for CPO-54-Ni. **a)** CH_4, **b)** CO_2, **c)** N_2 and **d)** O_2.

Figure E.4: Virial equation fitted to the standard-pressure experimental data for CPO-54-Co. **a)** CH_4, **b)** CO_2, **c)** N_2, **d)** O_2, **e)** Kr, **f)** N_2O and **g)** Xe.
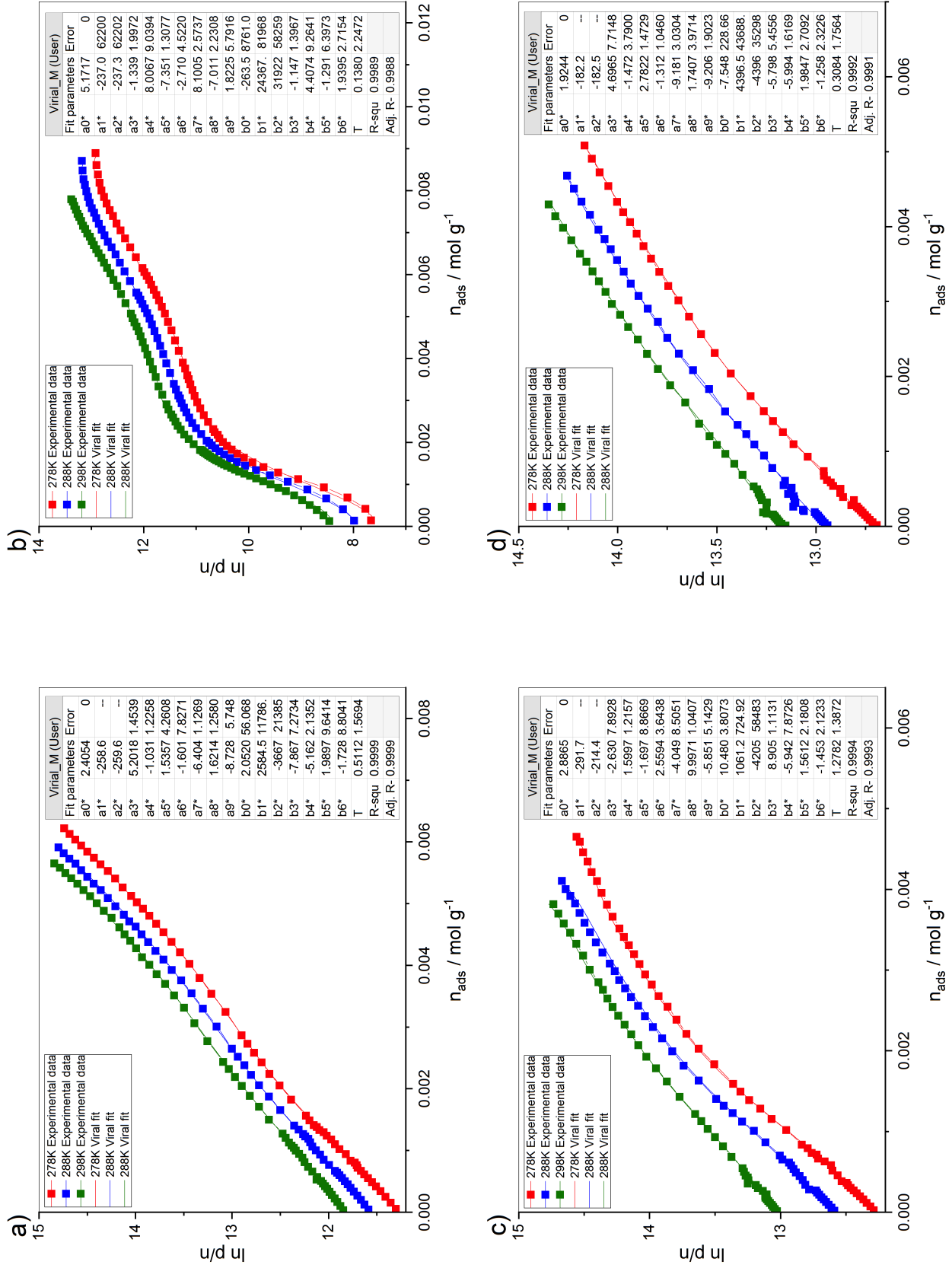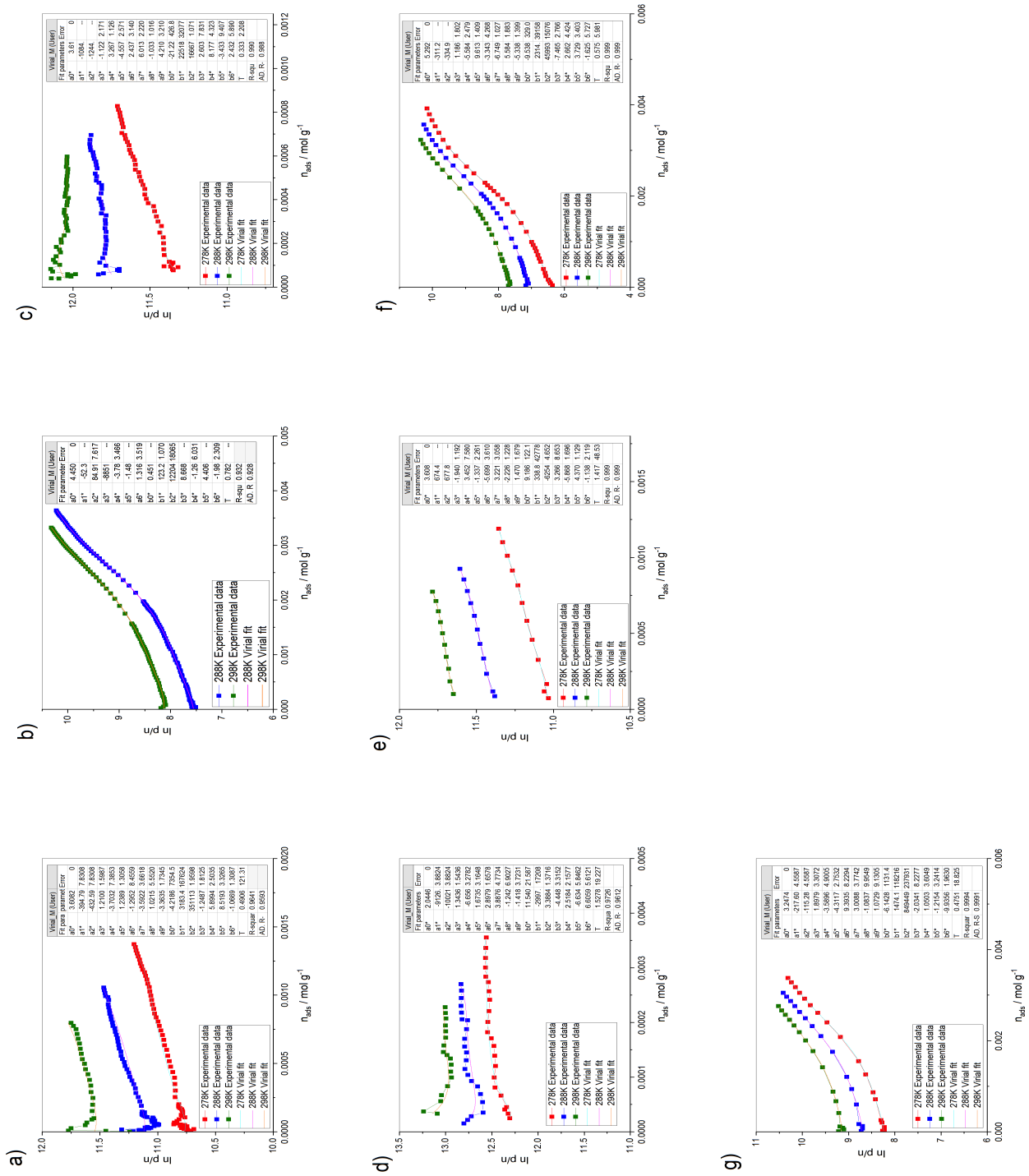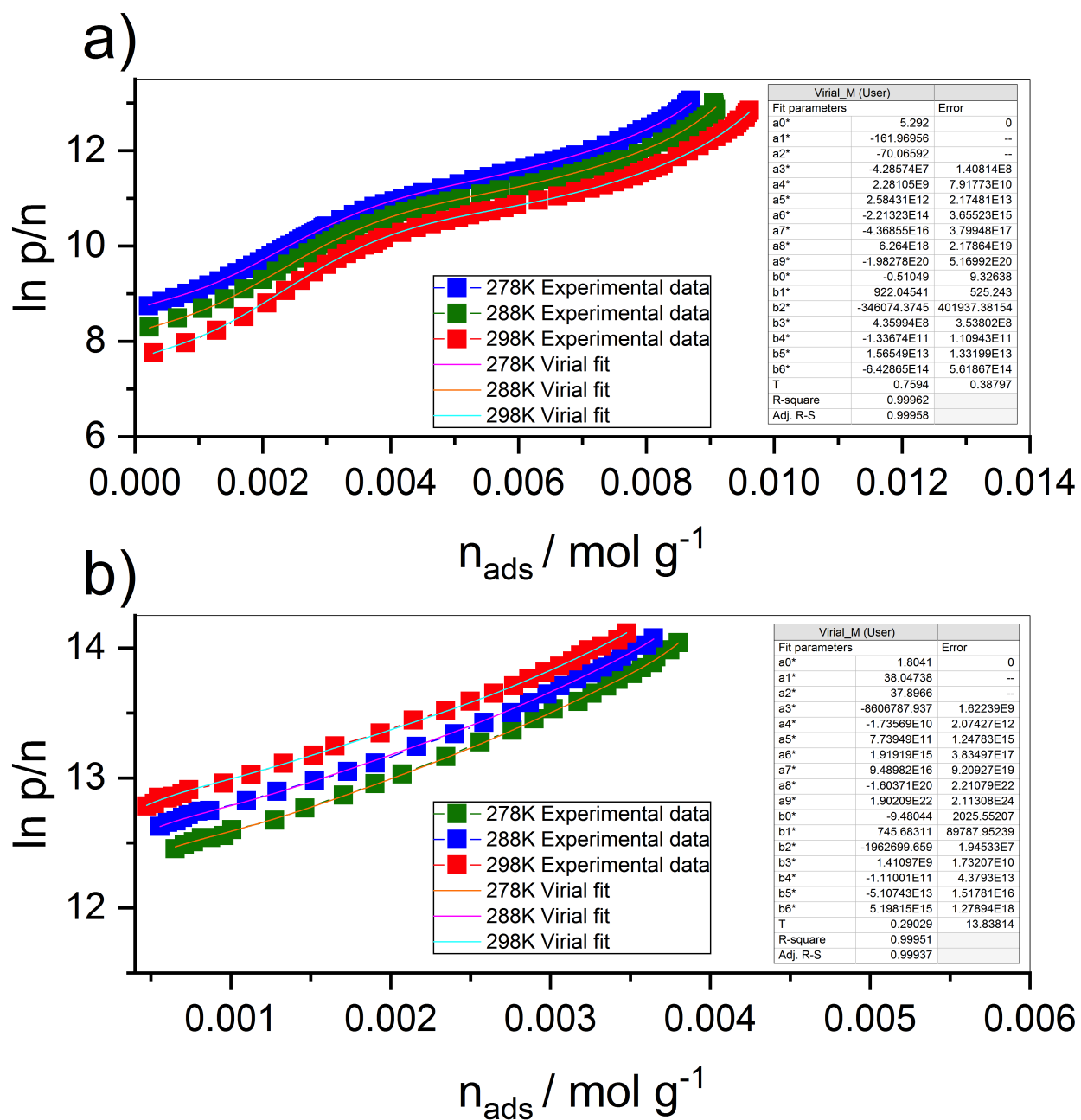
Figure E.5: Virial equation fitted to the high-pressure experimental data for CPO-54-Mn. **a)** CO_2 and **b)** N_2.

Bibliography

[1] V. Masson-Delmotte, P. Zhai, H. O. Pörtner, D. Roberts, J. Skea, P. R. Shukla, A. Pirani, W. Moufouma-Okia, C. Péan, R. Pidcock, S. Connors, J. B. R. Matthews, Y. Chen, X. Zhou, M. I. Gomis, E. Lonnoy, T. Maycock, M. Tignor, and T. Waterfield. Summary for policymakers. in: Global warming of 1.5°c. an ipcc special report on the impacts of global warming of 1.5°c above pre-industrial levels and related global greenhouse gas emission pathways, in the context of strengthening the global response to the threat of climate change, sustainable development, and efforts to eradicate poverty. *IPCC Special Report*, pages 6–7, 2018.

[2] UNFCCC. Paris agreement, September 2018.

[3] National Oceanic and Atmospheric Administration. Trends in atmospheric carbon dioxide, June 2019.

[4] Helge Drange. Norges co2-utslipp: På kollisjonskurs med paris-avtalen. *Norwegian Climate Foundation*, 5:1–20, October 2018.

[5] Jan Zalasiewicz, Colin N Waters, Colin P Summerhayes, Alexander P Wolfe, Anthony D Barnosky, Alejandro Cearreta, Paul Crutzen, Erle Ellis, Ian J Fairchild, Agnieszka Gałuszka, et al. The working group on the anthropocene: Summary of evidence and interim recommendations. *Anthropocene*, 19:55–60, 2017.

[6] Ottmar Edenhofer. *Climate change 2014: mitigation of climate change*, volume 3. Cambridge University Press, 2015.

[7] Bob Dudley et al. Bp statistical review of world energy 2018. *London, UK*, 2017.

[8] National Research Council et al. *America's energy future: technology and transformation.* National Academies Press, 2010.

[9] Nan Zhou. China's energy and carbon emissions outlook to 2050. 2011.

[10] FG Nielsen, K Argyriadis, N Fonseca, M Le Boulluec, P Liu, H Suzuki, J Sirkar, NJ Tarp-Johansen, SR Turnock, J Waegter, et al. *[Report of] Specialist Committee V. 4: ocean, wind and wave energy utilization.* Seoul National University, 2009.

[11] Nathan S Lewis. Research opportunities to advance solar energy utilization. *Science*, 351(6271):aad1920, 2016.

[12] Sigmund Ø Størset, Grethe Tangen, David Berstad, Peder Eliasson, Karl Anders Hoff, Øyvind Langørgen, Svend Tollak Munkejord, Simon Roussanaly, and Malin Torsæter. Profiting from ccs innovations: A study to measure potential value creation from ccs research and development. *International Journal of Greenhouse Gas Control*, 83:208–215, 2019.

[13] J. Owen-Jones. Grand opening of climeworks commercial dac plant, gasworld, 2017, 2017.

[14] Mai Bui, Claire S Adjiman, André Bardow, Edward J Anthony, Andy Boston, Solomon Brown, Paul S Fennell, Sabine Fuss, Amparo Galindo, Leigh A Hackett, et al. Carbon capture and storage (ccs): the way forward. *Energy & Environmental Science*, 11(5):1062–1176, 2018.

[15] Lesley E Smart and Elaine A Moore. *Solid state chemistry: an introduction.* CRC press, 2016.

[16] Stuart R Batten, Neil R Champness, Xiao-Ming Chen, Javier Garcia-Martinez, Susumu Kitagawa, Lars Öhrström, Michael O'Keeffe, Myunghyun Paik Suh, and Jan Reedijk. Terminology of metal–organic frameworks and coordination polymers (iupac recommendations 2013). *Pure and Applied Chemistry*, 85(8):1715–1724, 2013.

[17] Pascal DC Dietzel, Vasileios Besikiotis, and Richard Blom. Application of metal–organic frameworks with coordinatively unsaturated metal sites in storage and separation of methane and carbon dioxide. *Journal of Materials Chemistry*, 19(39):7362–7370, 2009.

[18] Decai Yu, A Ozgur Yazaydin, Joseph R Lane, Pascal DC Dietzel, and Randall Q Snurr. A combined experimental and quantum chemical study of co2 adsorption in the metal–organic framework cpo-27 with different metals. *Chemical Science*, 4(9):3544–3556, 2013.

[19] Liqing Ma, Carter Abney, and Wenbin Lin. Enantioselective catalysis with homochiral metal–organic frameworks. *Chem. Soc. Rev.*, 38(5):1248–1256, 2009.

[20] Alexander Kraft et al. On the discovery and history of prussian blue. *Bull. Hist. Chem*, 33(2):61–67, 2008.

[21] Dietmar Seyferth. Reviews-((c2h4) ptcl3)-, the anion of zeise's salt, k ((c2h4) ptcl3)-h2o. *Organometallics*, 20(1):2–6, 2001.

[22] OM Yaghi and Hailian Li. Hydrothermal synthesis of a metal-organic framework containing large rectangular channels. *Journal of the American Chemical Society*, 117(41):10401–10402, 1995.

[23] Hailian Li, Mohamed Eddaoudi, Michael O'Keeffe, and Omar M Yaghi. Design and synthesis of an exceptionally stable and highly porous metal-organic framework. *nature*, 402(6759):276, 1999.

[24] Mohamed Eddaoudi, Jaheon Kim, Nathaniel Rosi, David Vodak, Joseph Wachter, Michael O'keeffe, and Omar M Yaghi. Systematic design of pore size and functionality in isoreticular mofs and their application in methane storage. *Science*, 295(5554):469–472, 2002.

[25] Nathaniel L Rosi, Jaheon Kim, Mohamed Eddaoudi, Banglin Chen, Michael O'Keeffe, and Omar M Yaghi. Rod packings and metal- organic frameworks constructed from rod-shaped secondary building units. *Journal of the American Chemical Society*, 127(5):1504–1518, 2005.

[26] Pascal DC Dietzel, Yusuke Morita, Richard Blom, and Helmer Fjellvåg. An in situ high-temperature single-crystal investigation of a dehydrated metal–organic framework compound and field-induced magnetization of one-dimensional metal–oxygen chains. *Angewandte Chemie International Edition*, 44(39):6354–6358, 2005.

[27] Pascal DC Dietzel, Rune E Johnsen, Helmer Fjellvåg, Silvia Bordiga, Elena Groppo, Sachin Chavan, and Richard Blom. Adsorption properties and structure of co 2 adsorbed on open coordination sites of metal–organic framework ni 2 (dhtp) from gas adsorption, ir spectroscopy and x-ray diffraction. *Chemical communications*, (41):5125–5127, 2008.

[28] Alistair C McKinlay, Bo Xiao, David S Wragg, Paul S Wheatley, Ian L Megson, and Russell E Morris. Exceptional behavior over the whole adsorption- storage- delivery cycle for no in porous metal organic frameworks. *Journal of the American Chemical Society*, 130(31):10440–10444, 2008.

[29] Norbert Stock and Shyam Biswas. Synthesis of metal-organic frameworks (mofs): routes to various mof topologies, morphologies, and composites. *Chemical reviews*, 112(2):933–969, 2011.

[30] Ashlee J Howarth, Aaron W Peters, Nicolaas A Vermeulen, Timothy C Wang, Joseph T Hupp, and Omar K Farha. Best practices for the synthesis, activation, and characterization of metal–organic frameworks. *Chemistry of Materials*, 29(1):26–39, 2016.

[31] Ryan A Dodson, Antek G Wong-Foy, and Adam J Matzger. The metal–organic framework collapse continuum: Insights from two-dimensional powder x-ray diffraction. *Chemistry of Materials*, 30(18):6559–6565, 2018.

[32] Omar K Farha, Ibrahim Eryazici, Nak Cheon Jeong, Brad G Hauser, Christopher E Wilmer, Amy A Sarjeant, Randall Q Snurr, SonBinh T Nguyen, A Özgür Yazaydın, and Joseph T Hupp. Metal–organic framework materials with ultrahigh surface areas: is the sky the limit? *Journal of the American Chemical Society*, 134(36):15016–15021, 2012.

[33] Kenji Sumida, David L Rogow, Jarad A Mason, Thomas M McDonald, Eric D Bloch, Zoey R Herm, Tae-Hyun Bae, and Jeffrey R Long. Carbon dioxide capture in metal–organic frameworks. *Chemical reviews*, 112(2):724–781, 2011.

[34] Jason S Lee, Bess Vlaisavljevich, David K Britt, Craig M Brown, Maciej Haranczyk, Jeffrey B Neaton, Berend Smit, Jeffrey R Long, and Wendy L Queen. Understanding small-molecule

interactions in metal–organic frameworks: Coupling experiment with theory. *Advanced Materials*, 27(38):5785–5796, 2015.

[35] Stephen R Caskey, Antek G Wong-Foy, and Adam J Matzger. Dramatic tuning of carbon dioxide uptake via metal substitution in a coordination polymer with cylindrical pores. *Journal of the American Chemical Society*, 130(33):10870–10871, 2008.

[36] Pascal DC Dietzel, Barbara Panella, Michael Hirscher, Richard Blom, and Helmer Fjellvåg. Hydrogen adsorption in a nickel based coordination polymer with open metal sites in the cylindrical cavities of the desolvated framework. *Chemical Communications*, (9):959–961, 2006.

[37] Thomas M McDonald, Jarad A Mason, Xueqian Kong, Eric D Bloch, David Gygi, Alessandro Dani, Valentina Crocella, Filippo Giordanino, Samuel O Odoh, Walter S Drisdell, et al. Cooperative insertion of co 2 in diamine-appended metal-organic frameworks. *Nature*, 519(7543):303, 2015.

[38] Tae-Hyun Bae and Jeffrey R Long. Co 2/n 2 separations with mixed-matrix membranes containing mg 2 (dobdc) nanocrystals. *Energy & Environmental Science*, 6(12):3565–3569, 2013.

[39] Thomas M McDonald, Deanna M D'Alessandro, Rajamani Krishna, and Jeffrey R Long. Enhanced carbon dioxide capture upon incorporation of n, n'-dimethylethylenediamine in the metal–organic framework cubttri. *Chemical Science*, 2(10):2022–2028, 2011.

[40] Ranjani V Siriwardane, Ming-Shing Shen, Edward P Fisher, and James A Poston. Adsorption of co2 on molecular sieves and activated carbon. *Energy & Fuels*, 15(2):279–284, 2001.

[41] Praveen K Thallapally, Jay W Grate, and Radha Kishan Motkuri. Facile xenon capture and release at room temperature using a metal–organic framework: a comparison with activated charcoal. *Chemical communications*, 48(3):347–349, 2012.

[42] Seung-Joon Lee, Ki Chul Kim, Tae-Ung Yoon, Min-Bum Kim, and Youn-Sang Bae. Selective dynamic separation of xe and kr in co-mof-74 through strong binding strength between xe atom and unsaturated co2+ site. *Microporous and Mesoporous Materials*, 236:284–291, 2016.

[43] Xiaoping Zhang, Wenjie Chen, Wei Shi, and Peng Cheng. Highly selective sorption of co 2 and n 2 o and strong gas-framework interactions in a nickel (ii) organic material. *Journal of Materials Chemistry A*, 4(41):16198–16204, 2016.

[44] P. D. C. Dietzel, M. Fröseth, R. Blom, R. E. Johnsen, and H. Fjellvåg. A new series of isoreticular honeycomb-like coordination polymers with high density of open metal sites. In *2nd International Conference on Metal-Organic Frameworks and Open Framework Compounds*, 2010.

[45] A Dąbrowski. Adsorption—from theory to practice. *Advances in colloid and interface science*, 93(1-3):135–224, 2001.

[46] Kenneth SW Sing. Reporting physisorption data for gas/solid systems with special reference to the determination of surface area and porosity (recommendations 1984). *Pure and applied chemistry*, 57(4):603–619, 1985.

[47] Irving Langmuir. The adsorption of gases on plane surfaces of glass, mica and platinum. *Journal of the American Chemical society*, 40(9):1361–1403, 1918.

[48] Stephen Brunauer, Paul Hugh Emmett, and Edward Teller. Adsorption of gases in multimolecular layers. *Journal of the American chemical society*, 60(2):309–319, 1938.

[49] Matthias Thommes, Katsumi Kaneko, Alexander V Neimark, James P Olivier, Francisco Rodriguez-Reinoso, Jean Rouquerol, and Kenneth SW Sing. Physisorption of gases, with special reference to the evaluation of surface area and pore size distribution (iupac technical report). *Pure and Applied Chemistry*, 87(9-10):1051–1069, 2015.

[50] Jean Rouquerol, Françoise Rouquerol, Philip Llewellyn, Guillaume Maurin, and Kenneth SW Sing. *Adsorption by powders and porous solids: principles, methodology and applications*. Academic press, 2013.

[51] AL Myers and JM Prausnitz. Prediction of the adsorption isotherm by the principle of corresponding states. *Chemical Engineering Science*, 20(6):549–556, 1965.

[52] Rajamani Krishna and Jasper M van Baten. In silico screening of metal–organic frameworks in separation applications. *Physical Chemistry Chemical Physics*, 13(22):10593–10616, 2011.

[53] Cory M Simon, Berend Smit, and Maciej Haranczyk. pyiast: Ideal adsorbed solution theory (iast) python package. *Computer Physics Communications*, 200:364–380, 2016.

[54] Jose Carlos Guerrero. Nmr nodes - uib, July 2019.

[55] Wendy L Queen, Matthew R Hudson, Eric D Bloch, Jarad A Mason, Miguel I Gonzalez, Jason S Lee, David Gygi, Joshua D Howe, Kyuho Lee, Tamim A Darwish, et al. Comprehensive study of carbon dioxide adsorption in the metal–organic frameworks m 2 (dobdc)(m= mg, mn, fe, co, ni, cu, zn). *Chemical Science*, 5(12):4569–4581, 2014.